PHYSICAL SYSTEMS FOR THE ACTIVE CONTROL OF TRANSFORMER NOISE

Xun Li

This thesis is presented for the degree
of Ph.D. of Engineering
of The University of Adelaide,
Department of Mechanical Engineering

November 2000

CONTENTS

APPENDICES

ABSTRACT

Traditional means of controlling sound radiated by electrical power transformers involve the construction of large expensive barriers or full enclosures, which cause maintainability and cooling problems. One promising alternative is to use active noise control to cancel the noise.

This thesis is concerned with one of the many problems which need to be investigated to develop a practical active noise cancellation system for transformers. This work, in particular, is concerned with the physical system design which includes the selection of the control source types and the evaluation of the near-field sensing strategies.

Loudspeakers have been widely used in the past as an acoustic source for canceling transformer noise. The principal disadvantage of using loudspeakers is that to achieve global noise control, a large number, driven by a multi-channel controller, are required. However, if large panels are used in place of loudspeakers as control sources, it is possible that the number of the control sources and complexity of the controller could be reduced substantially. In addition to reducing the number of control sources and simplifying their application, panel sound sources could also overcome some disadvantages of the loudspeakers, such as limited life and deterioration due to the weather. Thus, part of the work described in this thesis is concerned with the development of a resonant curved panel with a backing cavity as an acoustic type source. The advantages of using a curved panel rather than a flat panel are twofold: first a curved panel is more easily excited by the extensional motion of the piezoelectric patch actuators; and second, it is more difficult to adjust the resonance frequencies of the efficient modes of a flat panel than of a curved panel. The analytical models for the design of the panel cavity systems have been developed. As an example, a resonant curved panel with a backing cavity system was constructed and the sound radiation of the system was measured. Results show that a resonant panel-cavity sound source could be used as an alternative to a number of loudspeakers for active cancellation of electric power transformer noise. Due to the advantages of using the vibration type control sources, two types of vibration control sources (inertial electrodynamic shakers and piezoelectric patch actuators) were considered and the mechanical output of the inertial shakers has been compared with that of the piezoelectric actuators. In contrast with the piezoelectric actuators, the resonance frequencies of the inertial shakers can be tuned to the frequencies of interest using simple tuning procedures, so that the output efficiency of the shakers can be increased. The output performance was evaluated for two types of actuators by measuring the structural response of either a panel or a transformer when excited by the actuators at half their rated voltage input. Results demonstrated that a much larger output amplitude at the frequency of interest can be achieved by the tuned inertial type actuators.

Two near-field sensing strategies, the minimization of the sum of the sound intensities and the minimization of the sum of the squared sound pressures, have been studied. A quadratic expression was derived for the minimization of the sum of the sound intensities in the near-field. To evaluate the control performances achieved using both sensing strategies, a flat-panel was modelled with a harmonic point force disturbance and several point force control sources. Simulation results show that the control performance could be improved by minimizing the sum of the sound intensities in the hydrodynamic near-field, provided that a very large number of error sensors were used, otherwise better results were achieved using near-field squared pressure sensing.

Both sensing strategies were used to predict the noise reductions that resulted for the active noise control of a small transformer in the laboratory environment and for a large electrical power transformer on site. To optimize the locations of the control sources (for the large transformer on site) and the locations of the error sensors (for the small transformer in the laboratory environment), a genetic algorithm (GA), which is an evolutionary optimization technique, was employed as a search procedure to optimize the control source and error sensor locations. The results showed that the control source locations and/or the error sensor locations must be optimized to achieve the maximum sound reduction for either error sensing strategy, especially for the sound intensity minimization; otherwise, the sound field level may increase after control due to the character of the cost function (the sum of the sound intensities).

The simulation results were experimentally validated for the small transformer in the laboratory environment. Due to the limitation of the number of controller channels, the control performance was only evaluated for squared pressure minimization. The results demonstrated that for the case of 8 control sources and 8 error sensors, at 100 Hz, an average sound pressure reduction of 15.8 dB was achieved when evaluated at 528 monitoring locations at 0.25 m intervals on a surface that surrounded the transformer.

DECLARATION

The work presented in this thesis has not been submitted, in full or in part, for another degree at this or any other institution. The contribution of others to the content of this thesis and all previously published material has been fully acknowledged. I give consent to this copy of my thesis, when deposited in the University Library, being available for loan and photocopying.

Xun Li

ACKNOWLEDGMENTS

Firstly, I would like to thank my supervisor, Professor Colin H Hansen, for his supervision, encouragement and guidance throughout this entire project.

I am also very grateful to the Electricity Supply Association of Australia Ltd, the Australian Research Council and Electricity Trust of South Australia for financial support.

I am thankful to Mr. Ron Jager, Anthony Sherry and George Osborne, the workshop technicians, for support of my experiments. I am appreciative to Dr. Xiaojun Qiu and Mr. Yianting Ai for help carrying out the experiments and willingness and interest to discuss areas of work.

I would also like to express gratitude my son, John C Li, for helping with programming.

Last but not the least, I would like to thank my wife for encouraging me to finish my thesis.

LIST OF FIGURES

LIST OF TABLES

CHAPTER 1 GENERAL INTRODUCTION

1.1 Introduction

In this thesis a physical system design strategy for the active control of large electrical power transformer noise is investigated. In general, the physical system design for active control of noise radiated from structures deals with:

(I) the evaluation of error sensing strategies, i.e. what cost function should be minimized;

(II) the selection of types of control actuators, i.e. what type of control source should be used: vibration or acoustic. Also, for a practical system, the modification or special design of the actuators needs to be considered to increase their output efficiency;

(III) the optimization of the system, i.e. the optimization of the locations and the number of the actuators and error sensors.

In this project two near-field sensing strategies are studied both theoretically and experimentally. They are the minimization of the sum of the sound intensities and the minimization of the sum of the squared sound pressures in the near-field.

As a potential acoustic control source, a model of resonant curved panels with a backing cavity is developed. The main task is to investigate a curved panel with a backing cavity sound source, which could replace loudspeakers in an active noise cancellation system for electrical transformers. In general, there may be less sound reduction when using acoustic control sources than when using vibration control sources, especially if the structural dimensions are approximately equal to (or larger than) the acoustic wavelength at the frequency of interest. Thus it is worthwhile to develop a vibration control source to cancel the noise radiated by large transformers with structural dimensions larger than the acoustic wavelength at the frequency of interest. For this purpose, a comparison of the output performance of conventional piezoelectric patch actuators with that of inertial electrodynamic actuators was made.

For optimizing the physical system arrangement (location and the number of the control sources and the error sensors), a genetic algorithm (GA), which is an evolutionary optimization technique, is employed as a search procedure to optimize the control source and error sensor layout in Chapter 6 and Chapter 7.

1.2 Control sources for active control of noise radiated by structures

1.2.1 Curved panel sources

In Chapter 3, an analytical model of a curved panel with a backing cavity is described. The backing cavity is used to prevent the interaction and cancellation of the sound radiation from the two sides of the panel. To increase the sound radiation efficiency at the frequencies of interest, the panel-cavity system was designed so that its resonance frequencies coincided with the transformer dominant noise frequencies of 100 Hz and 200 Hz.

To optimize the design procedure, both the effects of variations in the cavity geometry size and the additions of point masses to the panel, on the resonance frequencies of the panel-cavity system were determined analytically. By using these analytical models, a resonant curved panel with a backing cavity was designed so that the resonance frequencies of the first two acoustically efficient modes coincided with the two dominant noise radiation frequencies of the transformer.

To fine tune the resonance frequencies of the system after construction, facilities were provided for attaching mass to the panel and changing the depth of the backing cavity.

1.2.2 Tunable inertial shakers

Piezoelectric patch actuators have been widely used for active structural acoustic control because they are compact and light-weight. However, in general, piezoelectric patch actuators provide high force but low displacement output. This phenomenon may be a disadvantage for some low frequency active control applications, which require significant displacements from the actuators. In Chapter 4, an inertial electrodynamic shaker is introduced. Performances of both piezoelectric patch actuators and inertial electrodynamic shakers are compared. To increase the mechanical output force, the resonance frequency of the inertial shakers was tuned to the frequency of interest using a simple tuning procedure. This procedure is beneficial for some low frequency active control applications, for example, active control of noise radiated from a large power transformers at the fundamental frequency of 100 Hz or 120 Hz. At these low frequencies, piezoelectric actuators are ineffective because of the large dynamic stiffness of the transformer tank at low frequencies.

1.3 Error sensing in the near-field for active control of noise radiated by structures

In Chapter 5, two near-field error sensing strategies are studied. These are the minimization of the sum of the sound intensities and the minimization of the sum of the squared sound pressures. A quadratic expression is derived for the minimization of the sum of the sound intensities in the near-field. Formulation is expressed in terms of transfer functions from the control source inputs to the error sensor outputs and the primary sound field. Thus, the expressions can be used to predict the noise reduction due to active noise control for any complex problem where the control source to error sensor transfer functions and primary sound fields are known. As a theoretical simulation, a flat panel is modeled with a harmonic point force excitation and several point force control sources. In the numerical simulation, in order to evaluate the influence of the noise source size on the control performance, the noise source is either defined as a small source or as an extended source based on the source dimension normalized with respect to an acoustic wavelength. The variation of control results with the distance of the error sensors to the source is discussed as well.

1.4 Applications of active noise control techniques to transformer noise control

In Chapter 6, the noise attenuation for a small transformer is predicted using error sensing strategies proposed in Chapter 5. The transformer was located in an anechoic room in the Department of Mechanical Engineering, The University of Adelaide. For the sake of safety, the transformer was not connected to a power source; instead, the transformer tank was excited by an inertial shaker, which was mounted on the transformer. Transfer functions from 8 control source (inertial shaker) locations to 492 potential error sensor (sound intensity probe constructed with two microphones) locations and the sound field excited by a primary shaker were measured. These data were used to predict the global sound field reduction associated with optimum error sensing locations which were determined using the genetic algorithm (GA). The control results corresponding to optimum locations and non-optimum locations of error sensors are compared.

To verify predicted results, experiments were carried out using a 10 channel active noise controller which was specially developed for transformer noise control by the Department of Mechanical Engineering, The University of Adelaide. The global control performance associated with 8 control sources and 8 error sensors at 100 Hz is evaluated at 528 monitoring points.

In Chapter 7, as a practical application, the sound reduction for a large electrical transformer is predicted. A large zone substation transformer (160 MVA) located at Cherry Gardens, South Australia was selected for the tests. The dimensions of the transformer are 4.6×4.0×4.0 m (not including the insulating rod). The maximum operating load of the transformer is 160 MVA and the usual operating load is 44 MVA (160A, 275KV). The sound field radiated by the transformer alone was measured with the transformer energized. Transfer functions from control source inputs (at around 350 possible locations for loudspeaker control sources, 35 locations for curved panel control sources and 200 locations for vibration type control sources) to error sensor outputs (96 sensors around the transformer including the top) were measured. Data so acquired were used to predict the sound field reduction associated with the optimum control source locations. The objectives of the optimization process were to minimize either the sum of the sound intensities or the sum of the squared sound pressures at error sensors in the near-field. The sound field attenuation achieved using different types of control sources (loudspeakers, curved panels and forces) are compared.

1.5 What is new in this thesis

- Development of an analytical model of the curved panel-cavity source as a potential acoustic control source for the transformer noise control; construction of the prototype of the curved panel-cavity source and evaluation of the sound radiation level of the system in an anechoic room and on site;
- Evaluation of the feasibility of using the inertial shakers as vibration control actuators for a transformer tank;
- Derivation of the expression for minimizing the sum of the sound intensities at multiple error sensors using multiple control sources in the near-field; numerical evaluation of the effect of different near-field sensing strategies on the control performance;
- Derivation of strategies for determining the number of control sources and error sensors required to achieve a particular level of control;
- Prediction of the sound reduction level for a small transformer based on transfer function measurements and control noise with a ten channel controller in an anechoic room environment;
- Prediction of the sound reduction level for a large substation transformer using force type control sources, loudspeakers and curved panel-cavity sources, based on transfer function measurements on site.

CHAPTER 2 PREVIOUS WORK

2.1 Introduction

The aim of the work described in this thesis is to undertake the fundamental investigations needed to design and optimize the physical part of an active system for the reduction of electrical transformer noise. It involved a feasibility study of alternative sensing strategies, the design of new types of control actuators and the evaluation of the control performance at the optimal locations of control actuators and error sensors. Work done previously by others is discussed in this chapter.

2.2 Active control of structurally radiated noise

2.2.1 Near-field sensing strategies

When modeling an active noise control system for the control of sound radiated from a structure, it is considered undesirable to use error sensors located in the near field. This is because minimizing the sound pressure level in the near field does not necessarily result in a reduction of far field sound. On the other hand, for low frequency sound radiation from a large source, the near field extends a long way from the source, and error sensors placed at large distances from the control sources cause controller instability and convergence problems. Thus, there is some interest in investigating the feasibility of using near field sound intensity as a cost function for an active control system.

Wang and Fuller (1992) reported on a theoretical study of the near-field pressure and intensity distributions of actively controlled panel-radiated sound. In their work, a control system consisted of a single control force and a single error sensor, and the cost function to be minimized was the sum of the squared sound pressures in the near-field. Controlled sound fields, in terms of the sound pressure and the normal time-averaged sound intensity, were calculated on a plane 20 mm above the vibrating plate. Although limited to the 3,1 mode resonance case, it was found that the application of control led to an overall fall in the magnitudes of the near-field pressure and intensity vectors, while the complexity of the sound radiation pattern was increased.

Sommerfeldt and Nashif (1994) have developed two energy-based control algorithms for a predominantly standing wave field in an enclosure and a predominantly propagating wave field. This energy-based control approach included energy density control and acoustic intensity control respectively. The proposed approach was based on sensing and controlling the energy in the sound field, rather than a single acoustic parameter such as the pressure, so that better global control performance could be achieved. As an example, a 5.6 m long closed circular duct with a diameter of 0.116 m was modeled and tested to compare an acoustic pressure cost function with an acoustic energy density cost function. The 200 Hz tonal primary sound field was generated by a loudspeaker located at one end of the duct and the control loudspeaker was arbitrarily located in the duct. A single error sensor was positioned near to the mid point of the duct. Both the predicted results and the measured results were presented and compared. They concluded that in this application, the energy-based control method resulted in greater global control of the enclosed field when compared to using a pressure squared cost function. It is interesting to note that the control performance achieved by the energy-based control was not sensitive to the error sensor locations.

In the work of McLoughlin et al (1994), an active system for canceling the noise radiated from a small transformer (7.5 MVA), using the near-field sensing of the sound intensity was presented. For 120 Hz and 240 Hz tones, an average reduction of 10-15 dB was achieved in the far-field. However, no theoretical analysis was provided.

Lee and Park (1996) reported on the evaluation of the near-field sensing strategies for the noise control of a fluid-loaded plate. Quadratic expressions for the minimization of the near-field surface acoustic intensity and the minimization of the near-field surface reactive intensity were derived. For comparison, a total of four active control strategies were involved in their study, which included:

1. the integral of the near-field surface sound intensity over the plate surface;
2. the integral of the squared sound pressure over a hemisphere in the far field;
3. the integral of the near-field surface reactive intensity over the plate and
4. the integral of the squared velocity over the plate surface.

The results from numerical simulations showed that for the fluid-loaded plate, the optimal result achieved by minimizing the radiated sound power in the near-field was quite similar to that achieved by minimizing the sound power in the far-field and the control result obtained by the minimization of the reactive power was almost the same as that obtained by the minimization of the vibration energy. The sound power level reduction achieved using vibration minimization was much lower than that obtained by near-field active intensity minimization.

Lee and Park (1996) concluded that minimizing the vibration level of the oscillating plate led to the reduction of the near-field pressure level but gave less sound power level reduction in the far-field. This was because the sound pressure in the near-field consists of a combination of a propagating energy component and non-propagating energy component and therefore reducing the near-field sound pressure may not necessarily minimize the sound power in the far-field.

In this thesis, the use of near-field sensing is investigated thoroughly by analysing the control performances that were achieved using both sound pressure minimization and active intensity minimization.

Qiu et al (1998) presented a theoretical comparison of several near-field error sensing strategies for active control of harmonic free-field sound radiation. In their work, sensing strategies included the minimization of the acoustic potential energy density, acoustic kinetic energy density, total acoustic energy density, the mean active sound intensity at a point and the minimization of the sum of each cost function at a number of error sensing points in the near-field. These error sensing strategies were evaluated for the active control of harmonic free-field sound radiated from a monopole primary source and from a dipole-like pair of primary sources, associated with a single monopole control source. The distance between the primary source and the control source was one tenth of an acoustic wavelength for the monopole source and one third of an acoustic wavelength for the dipole-like source. Multiple error sensors were used and the effect of the number of error sensors associated with the variation of the error sensor locations on the control performance was studied. Results showed that the most appropriate near-field error sensing strategy was minimizing the sum of the mean active sound intensities provided that a large number of the error sensors were used. However, their models were limited to a single control output and multi error inputs. A formulation for sound intensity minimization with multi inputs and multi outputs is derived in Chapter 5, using the two microphone technique to define the intensity.

Berry et al (1999) and Berry (1999) numerically compared the control performances achieved by intensity minimization and squared pressure minimization in the near-field. An optimal minimization of the sum of the near-field sound intensities was derived, based on a Green's function implementation. A simply supported plate with a baffle was modeled as a noise source. Two different primary source cases were considered: one where the acoustic wavelength was longer than the source size and the other where the acoustic wavelength was shorter than the source size. In the numerical simulation, multiple acoustic control sources and error sensors were used. They concluded that when the error sensor plane was very close to the noise source, squared sound pressure minimization gave decreasing performance as the sensing plane approached the source, but sound intensity minimization did not significantly improve the control results. They believed that this was because in the near-field, the sum of the sound intensities could be large and negative.

Li et al (1999c, 2000), as part of the work in this thesis, have reported a theoretical analysis for the active control of structurally radiated noise by minimizing the sum of the sound intensities in the near-field. A formulation for the minimization of the sum of the sound intensities was derived by means of a quadratic optimization technique. During the derivation of the formulation, the calculation of the sound intensity was implemented by means of a two-microphone technique. The formulation was expressed in terms of transfer functions from control inputs to the sound field outputs at each microphone or sound intensity probe (error sensors) and the primary sound pressure. Thus, the expression could be used to solve any practical complex problem where the control source to error sensor transfer functions and primary sound fields were given, such as the prediction of sound reduction from a large power transformer. As an example, a flat panel was modeled with a harmonic point force excitation and several point force control sources. The control performance achieved by intensity minimization in the near-field was compared with that achieved by squared pressure minimization. The simulation results demonstrated that in the near-field, the control results could be improved by intensity minimization, but only if a large number of error sensors were used. Otherwise, better results were obtained by squared pressure minimization. They also found that more error sensors were required to minimize the sound field from a small source than to minimize the sound field from an extended source for a given frequency of sound radiation. The model was expressed as an numerical formulation and no experimental results were presented in their work. Therefore, in chapters 6 and 7, the model derived in Chapter 5 is verified experimentally by minimizing the noise field that was radiated by a small transformer structure and a large transformer. The transfer functions that were measured in the experiment were used in a quadratic optimization procedure to minimize the cost function.

Several near-field error sensing techniques involving structural vibration sensing have been developed for the minimization of structurally radiated sound. Clark and Fuller (1991,1992a) have presented the results of some experiments for the control of noise radiated from a rectangular flat panel. In their work, several sets of piezoelectric actuators bonded to a plate were used as control actuators, and microphones were located in the acoustic far-field as the error sensors. To evaluate the feasibility of using polyvinylidene fluoride (PVDF) piezoelectric distributed type sensors as error sensors for the active control of structurally radiated noise, two unshaped narrow strip PVDF sensors bonded to the panel were used as the error sensors. The results showed that for both on and off resonant excitation, the sound field attenuation achieved by using the PVDF type material as the error sensors was the same order of magnitude to that achieved by using error microphones in the far-field. However, by analyzing the control mechanisms, Clark and Fuller (1992a) found that for the PVDF type error sensors, the extent of the modal rearrangement which can be achieved was limited so that the sound field reduction was also limited. They suggested that this could be improved by optimizing the positions of the PVDF sensors on the plate. At about same time, Clark et al (1993) presented a procedure for designing shaped PVDF type sensors for general two–dimensional structures. They evaluated theoretically and experimentally the procedure for a beam model and analytically for a plate because physical implementation of a shaped PVDF sensor was not easily obtained for a plate at that time. Results indicated that the residual sound field achieved by using shaped PVDF sensors resulted in the identical acoustic directivity pattern obtained when using acoustic transducers as error sensors in the far-field. As a result, they addressed several disadvantages of using PVDF type error sensors. The most noticeable disadvantage was the sensitivity of the optimum sensor shape to the relative modal weighting of the plate response. This is because the strain for the beam and the plate varies as a function of the square of the mode order so that large errors in response can result from small errors in the shape of the sensor and the location of the sensor on the structure. Thus, for practical complex structure, the best design approach tends to optimize size and location of simple rectangular strip sensors to optimize the control performance, rather than optimizing the sensor shape for modal weighting of the structure response.

Snyder et al (1993a, b) used shaped PVDF error sensors to measure the transformed modal velocity for attenuating the structurally radiated sound power. Using analytical and experimental methods, they concluded that it was important to weight these signals, which are orthogonal sets of structural modes, in order to minimize the radiated acoustic power. The results demonstrated that this approach was straightforward for the problem of minimizing the sound field radiated into a free field, although it was complicated for attenuating the sound transmitted into the coupled enclosures.

Following the work of Snyder et al (1993a, b), Elliott and Johnson (1993) expressed structurally radiated sound power in terms of independent surface velocity distributions, which they termed radiation modes (or transformed modes (Snyder et al (1993b)). A review of minimizing structurally radiated sound power by sensing radiation modes was given by Hansen (1997). Because radiation modes are orthogonal (in terms of sound radiation) with all other radiation modes (independent), the reduction of the amplitude of one radiation mode will guarantee some reduction in the structurally radiated sound power.

Tanaka et al (1996a, b) presented the evaluation of using a distributed parameter sensor (PVDF strip sensor) to attenuate an acoustic and structural disturbance. In their work, they derived the models for designing the sensors. They found that a one-dimensional strip sensor was more practical, but did not satisfy the condition sufficiently for sensing an acoustic power mode. They suggested that this problem could be overcome by using multiple strip sensors at appropriate positions on the structure.

Maillard and Fuller (1998) compared the control performance that was achieved when using either of two structural sensing strategies, i.e. discrete structural acoustic sensing (DSAS) and discrete structural volume acceleration sensing (DSVAS). Both sensing strategies used vibration signals as error signals, which were measured using an array of accelerometers. For DSAS, the signals were weighted so that the far-field radiated pressure could be estimated using these signals for a given direction. The results demonstrated that DSAS gave good reductions of sound power radiated by a baffled panel over the entire bandwidth (including the first ten structural modes) with a very small amount of spillover. In contrast to DSAS, the discrete structural volume acceleration sensing (DSVAS) could only achieve a high sound power reduction in the low frequency range with a high level of spillover at some higher frequencies.

All of the above work regarding the minimization of the sound field by vibration sensing was performed both theoretically and experimentally on simple structures, e.g. simple rectangular panels. However, these techniques are not really practical for complex structures such as large transformer. Some problems still exist and need to be solved. For example: how to accurately shape PVDF sensors and how to optimize the locations of the sensors on the complex structure. These topics are outside the scope of this thesis but they may be interesting research topics for future work.

2.2.2 Control actuators

Piezoelectric (PZT) actuators have been widely used in active structural acoustic control (ASAC) as control actuators, particularly for light weight structures because they are compact and light-weight.

Fuller et al (1991) experimentally investigated the feasibility of using piezoelectric actuators as control sources for active noise control systems. The experiment was carried out in an anechoic room where a simply supported steel panel with a rigid wooden baffle was constructed as the noise source. The panel was driven by non-contacting exciters on its rear. One piezoelectric actuator was bonded to the panel as a control actuator and one microphone was located in the radiated field to sense the error signals. To simplify the experimental procedure, the phase and amplitude of the control actuator input was manually adjusted, relative to the primary exciter input. To measure structural response, an array of accelerometers were fixed on the panel, and a microphone mounted on a polar traverse was used to measure the radiated sound field in the far-field. In their work, two structural modes, the 1,1 mode and the 3,1 mode (corresponding to resonance frequencies of 88 Hz and 352 Hz respectively) were considered. For the case of the excitation of the 1,1 mode, a global sound field reduction of 45 dB was achieved and the structural vibration was attenuated in all modes. Similar results were obtained for the 3,1 mode excitation.

Dimitriadis et al (1991) presented a feasibility study of using the thin patch type piezoelectric actuators bonded to the structure to excite two dimensional thin structures. The objective of this work was to demonstrate that it was possible to excite two dimensional structures with patch type piezoelectric actuators and how the actuator shape and location affected the structural response to the actuator excitation, rather than optimizing the actuator shape or location to optimally excite the structures. In their work, a simply supported rectangular panel was excited by a pair of piezoelectric actuators which were bonded to the plate (one on each side). The results showed that it was possible to excite modes in two dimensional structures using patch type actuators. For both on-resonance and off-resonance cases, the modal responses of the structures were strongly affected by actuator location, and the modal distribution was sensitive to the actuator shape for the off-resonance excitation case.

Wang et al (1991a) studied the active control of noise radiated from a modally responding panel using multiple independently control piezoelectric actuators. Effects of the size, number and location of actuators on the sound power reduction in the far-field were evaluated. The work demonstrated that increasing the number of actuators resulted in an improvement of the control results, and the locations of actuators significantly affected the sound field reduction. They found that the size of the actuators strongly affected the optimal inputs of the actuators, but did not significantly affect the noise attenuation. At about same time, Wang et al (1991b) presented a study of the active control of sound transmitting through a panel, using multiple piezoelectric patch actuators and point forces. A harmonic plane wave incident on a simply supported panel with a rigid baffle was considered as a primary noise source. The actuators were applied to the panel as control sources to attenuate the sound transmission through the panel. The control performances achieved by both type control sources were compared. The results showed that the control performances could be improved by properly choosing the sizes, numbers and locations of the actuators. They also found that, based on their system configuration, higher sound reduction could be achieved using point force type control sources.

Kim and Jones (1991) have reported a generalized approach for the optimization of piezoactuator-structure coupling for active noise and vibration control. A formulation of the effective bending moment generated by the actuators on the structure was given in terms of the properties and thicknesses of the actuators and the structure respectively. A comparison of this model with some previous work (Crawley and de Luis (1987) and Dimitriadis and Fuller (1989)) was discussed. They found that for a steel plate, there was an obvious difference between their model and the model of Crawley and de Luis, when the actuator thickness was increased beyond a quarter of the plate thickness. They believed that this was because uniform strain across the actuator layer, rather than as a linear function of the thickness, was assumed in Crawley and de Luis' model and generally, this assumption is invalid for the thicker structures. The results demonstrated that there was an optimum value of the ratio of actuator thickness to structure thickness for generating the maximum bending moment in the structure. For commercially available piezoelectric actuators, this optimum ratio is approximately 0.5 for a steel structure and 0.25 for an aluminum structure. After Kim and Jones' work, some researchers (Hansen et al (1998b), Hansen (1999) and Li et al (1999a)) suggested that a desirable value of the actuator thickness is one quarter (0.25) of the structure thickness for a steel structure and one eighth (0.125) of the structure thickness for an aluminum structure, because the power requirement can be reduced by half, while the applied moment is not reduced by much (less than 2 dB) compared with the applied moment generated by an actuator of optimum thickness.

Clark and Fuller (1992b) provided experimental results for the active control of structurally radiated sound using multiple piezoelectric actuators. As a source, a simply supported rectangular plate with a point force disturbance was constructed. Several microphones were located in the far-field to sense the error signals. A three channel adaptive controller, based on an adaptive LMS algorithm was implemented. The effects of the number and locations of actuators (not optimal locations) on the control results were experimentally evaluated. The number of the actuators (control sources) varied from one to three and two configurations of the control actuator locations were considered. The results demonstrated that for off-resonance cases, the control performance was significantly improved by increasing the number of control actuators but it did not improve as much for on-resonance cases. This is because for off-resonant excitation, the sound radiation resulted from a high density structural mode pattern, rather than a single resonance mode, so that the sound field was much more complex than that for on-resonance cases. Thus, this more complex response pattern required more control actuators to optimally adjust the phase and amplitude between actuators to increase the sound reduction. In addition, the control results were much more sensitive to the control actuator locations on the plate when the plate was excited at a non-resonance frequency.

In general, piezoelectric actuators provide high force, but low displacement output. This phenomenon may be a disadvantage for some low frequency active control applications which require significant displacements from the actuators. Thus, effort has been directed towards increasing displacements generated by piezoelectric actuators.

Garcia-Bonito et al (1998) and Brennan et al (1999) reported some investigation of actuator technologies for active vibration control. Garcia-Bonito et al (1998) developed a high-displacement piezoelectric actuator. The device consisted of a PZT ring (as the active component) filled with a fluid that was used to amplify the motion of the PZT element and then drove the piston hydraulically. The results suggested that a more refined design of a PZT ring element driving a small section piston through a hydraulic mechanism can effectively be used to produce high forces and relatively high displacements.

Li et al (1999a) reported a feasibility study of using inertial type shakers as control actuators for active structural acoustic control. The shaker was constructed of a housing, a moveable mass which consisted of a permanent magnet and a core, flexible diaphragms as spring and a coil. The shakers can be bonded to a structure through the housing so that no backing mass is required. One of the advantages of using this kind of shaker was that the resonance frequency of the shaker was tunable by modifying the stiffness of diaphragms so that the mechanical output of the shaker at the frequency of interest could be maximized. Experiments were carried out to compare the mechanical outputs generated by both an inertial shaker and a piezoelectric patch type actuator on a plate. The results demonstrated that a large amplitude output at the frequency of interest could be achieved using inertial type actuators by tuning their resonance frequency. Around 40 dB higher mechanical outputs could be achieved by the tuned shaker than by the PZT actuator at low frequencies. In Chapter 4, the mechanical output efficiency of this particular type of shaker on a transformer tank was evaluated experimentally.

2.3 Active control of noise radiated by electrical transformers

The hum of transformers is caused by magnetostriction in the core and by magnetic force between the windings. These effects cause tank vibration resulting in radiated noise. The transformer noise can be characterized by pure tones at even harmonics of the fundamental frequency (100, 200, 300 ⋯ ⋯ Hz or 120, 240, 360 ⋯ ⋯ Hz, twice the line frequency). Large transformers radiate low frequencies very efficiently.

Traditional means of controlling noise radiated by large electrical power transformers involve the construction of large barriers or full enclosures which result in maintainability and cooling problems. To overcome these disadvantages, one promising alternative is to use active sound cancellation to reduce the noise. The first published attempt to control electrical transformer noise was reported by Conover (1956). In his work, the amplitudes and phases of the individual signals which were used to cancel the noise at 120 Hz, 240 Hz and 360 Hz respectively, were adjusted manually using a variable gain amplifier and phase shifter until the sound at an error microphone was minimized. He found that although noise reductions of up to 25 dB at the error microphone could be achieved, this reduction was restricted to a very small angle from the line joining the error microphone to the center of the tank wall against which the loudspeaker was placed. In other directions, the overall noise level invariably increased with the control loudspeaker turned on. He also found that as the transformer noise varied from day to day, the system had to be adjusted regularly. He suggested that this might be done automatically but did not follow this up.

After Conover’s work, Ross (1978) reported on an experiment in which transformer noise was cancelled actively. In his work an almost identical system to Conover’s was used to minimize noise from two transformers. One error microphone was placed close to one of the transformers. To evaluate the control results, he monitored the sound field at six positions in an office adjacent to the transformers. During the control, the loudspeaker location was shifted and he found that the control results were strongly affected by the loudspeaker position. The tone of 100 Hz was locally attenuated by up to 28 dB and not less than 10 dB at monitoring points elsewhere. Poor control performances were obtained at the higher frequencies. At about same time, Hesselmann (1978) experimentally demonstrated an active control system for canceling noise from a small transformer (100 kVA) in an anechoic room. Acoustic control sources were chosen and located adjacent to the transformer. The control system consisted of a set of phase shifters with an adjustable phase value, a ten–channel amplifier with a digitally remote controlled gain adjustment and a phase inversion. The results demonstrated that global control could be achieved in an anechoic room using a large number of loudspeakers around the transformer.

Angevine (1981) presented the results from an experimental investigation of minimizing transformer noise in a laboratory environment. In his experiment, a transformer tank was located in a laboratory and the noise was generated by a loudspeaker inside the tank. A number of ‘tripole’ control sources were located around the transformer at a distance of 0.5 m from the transformer. One microphone was located adjacent to each control source as an error sensor and independent single channel controllers were used to minimize the sound pressure level in the vicinity of each control source. The results demonstrated a 16 dB reduction in the sound pressure level at 125 Hz (noise source frequency). In his work, it was found that the attenuation was strongly dependent on the control source locations and it was difficult to achieve significant control at higher frequencies.

Berge et al (1987,1988) reported an attempt to actively control electrical transformer noise using an approach similar to that of Conover (1956). In their work, an active control system for canceling noise from a real transformer was investigated. The aim of this study was to develop an adaptive algorithm to compensate for random fluctuations that occurred due to changes in the environmental conditions. The active control system consisted of a signal processor, a microphone and a loudspeaker with an amplifier, and a computer. The gains and phases of the individual frequency components (100 Hz and 200 Hz) were automatically adjusted to minimize a r.m.s. signal at the error microphone located in the far field by means of an iterative algorithm which updated the gains and phases every 1 to 4 minutes. Using only one loudspeaker control source, they found that significant noise reduction could only be achieved over a very narrow zone – 2 m to each side of the error microphone for a 100 Hz tone and 1 m for a 200 Hz tone.

Angevine and Wright (1990), and Angevine (1992, 1995) demonstrated some success using multiple loudspeaker type control sources, to minimize the transformer noise. Eight loudspeakers were arranged in two rows of four in front of a transformer tank and 8 error microphones were located at 10 meters away from the transformer tank (at the same side of the transformer with loudspeakers). In their work, an adaptive controller was used to continuously adjust the magnitude and phase of the signal supplied to each control source. The results showed that significant noise reductions over a wide area (15 to 20 dB over an azimuth angle of 35 to 40 degrees) could be achieved.

In 1994, McLoughlin et al (1994) published some encouraging noise reduction results for a 7.5 MVA transformer. In their work, Active Structural Acoustic Control (ASAC) was implemented. Thirty two piezoelectric actuators were bonded to the transformer tank as vibration control sources; sixty four error sensors were located in the near-field to sense the error signals. The control system consisted of a PC–based controller, multi input/output filters and a set of amplifiers. The entire system with the 64 inputs and 32 outputs, computed and adapted to changes in the system and the system environment. With this active control system, they found that tonal reductions of up to 20 dB could be achieved at some monitor points in the far-field, with an average reduction in the tones of 10-15 dB. This was the first report of using ASAC to minimize transformer noise in practice but no theoretical analysis was given.

Brungardt et al (1997) reported a commercial application of active control of noise generated by transformers. In this work, a hybrid control source system consisted of piezoelectric actuators and acoustic actuators. They used measured vibration data to optimize the piezoelectric actuator locations and the resonant acoustic actuators were attached at locations that required a force larger than that which could be efficiently applied by piezoelectric actuators. Electret microphones were used as error sensors to sense the sound field in the far-field. The multi-channel controllers with 64 inputs and 48 outputs ran with self-calibrating and adaptive algorithms. The typical sound reduction was about 15 dB at the fundamental frequency (120 Hz) and 10-12 dB at the first harmonic (240 Hz).

In general, the use of far-field error sensors causes controller instability and convergence problems, especially for the low frequency sound radiated from a large source, because the error sensors are located at long distances from the control sources (which must be close to the primary sources for global control). Thus, the challenge is how to effectively cancel the noise radiated by large transformers when using near-field error sensors. This investigation is a core issue of this thesis.

Martin and Roure (1996,1997,1998) implemented an active noise control system to cancel the transformer noise. A small industrial transformer (630 kVA) was selected for the experiment and was located in an anechoic room. Spherical harmonic expansion and a genetic algorithm were employed to estimate the number and locations of actuators and error microphones. The results demonstrated that at 100 Hz, global sound reduction of 10–25 dB was achieved using 8 loudspeaker control sources and 10 error sensors. For the case of 200 Hz, a 30 dB reduction was achieved at some locations, but at other locations 5-10 dB increase was observed. They suggested that the control results could be improved by using more control sources and decreasing the distance of the control sources to the transformer.

More recently, Li et al (1999a) and Qiu et al (1999) reported predictions of the noise reduction from large transformers. In Li et al's (1999a) work, a large zone substation transformer (160 MVA) with the dimensions of 4.6×4.0×4.0 m was tested and the active noise control technique was employed to cancel the transformer noise. The average noise reduction at the error sensors was predicted using measured data which were the transfer functions from the control inputs to error sensor outputs and the primary sound field. The cost function that was minimized was the sum of the squared sound pressure in the near-field. Ninety six error sensors were evenly arranged around the transformer. The results demonstrated that, in the near-field using 80 vibration control sources, the average sound pressure reduction achievable at the error sensors was 23.1 dB, 16.0 dB and 16.0 dB for 100 Hz, 200 Hz and 300 Hz respectively. When 80 loudspeaker sources were used, the average achievable sound pressure reduction at the 96 error sensors was 19.6 dB, 12.8 dB and 10.3 dB for 100 Hz, 200 Hz and 300 Hz respectively.

2.4 Physical system optimization for active noise and vibration control

The physical system design for active noise and vibration control system involves several stages. One of these stages is to optimize the control source locations and the error sensor locations corresponding to the minimum cost function. One of the reasons for optimizing these parameters is that the achievable control performance is strongly dependent on the control actuator and error sensor arrangements and these issues are unrelated to the signal processing aspects of the problem (Hansen et al (1999)). To optimize the control source and error sensor locations, a genetic algorithm (GA), which is an evolutionary optimization technique, was employed as a search procedure even though it was not a focal point of the research work in this thesis.

The genetic algorithm (GA) as an optimization search procedure was documented by Goldberg (1989). This search algorithm is based on the mechanics of natural selection and natural genetics. The application of the genetic algorithm as a optimization search procedure in active noise and vibration control was thoroughly studied by Baek (1993); Baek and Elliott (1993) and Baek and Elliott (1995). In their work, GA search procedures were employed to optimized loudspeaker control source locations in aircraft interiors to minimize the pure tone interior sound. Thirty two error microphones and 16 loudspeakers acting as control sources were located in a wooden laboratory mock-up of 2.2×2.2×6 m to demonstrate an active noise cancellation system for the aircraft. The primary sound field was generated by a loudspeaker in the enclosure. The results showed that the genetic algorithm provided efficient and robust search procedures, which appear very difficult or impossible to obtain by conventional optimization techniques based on gradient descent methods. The attenuation was within about 0.5 dB of the best possible.

Simpson and Hansen (1996) developed an efficient and robust genetic algorithm search technique for optimizing vibration actuator placements on a cylinder with floor structure for the purpose of actively controlling interior noise levels. In their work, the steady state genetic algorithm was given to provide a more focused search procedure for new solutions than the traditional genetic algorithm. As an example, a cylinder with a floor was modeled to represent 3 m long aircraft fuselage, with an inner-radius of 0.45 m and a wall thickness of 0.001 m. Ten harmonic point forces were applied to the exterior surface of the cylinder to present the primary disturbance. During the optimization search, 16384 possible locations were considered for four control sources to achieve the maximum total interior acoustic potential energy reduction. With several optimization runs, an interior potential energy reduction of 28 ± 0.5 dB was achieved.

At the same time, other work (Tsahalis at al (1993), Katsikas et al (1993) and Manolas at al (1996)) reported the use of GA search procedures to optimize control actuator locations, for canceling interior noise in aircraft models. They concluded that the GA search procedure could provide a promising and efficient optimization technique to solve the positioning actuator problems in an active noise control system. They also highlighted that using the GA search, more than one configuration of the control actuators with near optimal average noise reduction could be found. This was very important for practical applications because engineering constraints would be met in actual systems.

Wang et al (1994) and Wang (1993,1996) improved the control performance by optimizing the locations of the control sources and error microphones. Wang (1996) employed a genetic algorithm as an optimal search procedure to find optimal locations of the control actuators and error microphones corresponding to the minimum sound radiation by a simply supported beam. In the simulation, the total radiated sound power was first defined as the cost function to be minimized using quadratic optimization theory. The locations of the control actuators and error microphones were then determined by the optimal search procedure. The results showed that better control performance could be achieved by using the optimal control actuator and error sensor locations rather than using arbitrary locations. Especially for off-resonance cases, control spillover could be limited by optimizing the actuator and microphone locations.

The optimization of the parameters and arrangement of the PZT actuators for minimizing the sound radiated by the clamped plates has been reported by Kim et al (1994, 1995, 1996) and Varadan et al (1995, 1997). In their work, a finite element method was used to model the actuators and the structures. In the models, the structures were modeled with 2-D elements to avoid too much stiffness in the structure model and 3-D elements were used to model the actuators. To connect these two kinds of elements, transition elements were adopted. The cost function to be minimized was total sound power, which was measured on a hemispherical surface above the vibrating plate. The optimization variables were the sizes, locations of the piezoelectric actuators and the voltages applied to the actuators. The results showed that the optimum locations of the piezoelectric actuators to minimize sound radiation were near the corners rather than the center of the plates. This is because the edges and corners of flat plates contributed most to the radiated sound power at frequencies below the plate critical frequency, the frequency range of the results reported.

Snyder and Hansen (1991) reported an application of using multiple regression to optimize active noise control system design. It was concluded that the multiple correlation coefficient, a product of the multiple regression procedure, could be used to estimate the acoustic power reduction corresponding to optimum control for a given control source arrangement. The control source locations can be optimized using multiple regression in conjunction with a numerical search technique. The residual vector in multiple regression procedure, which represents residual sound field in an application of the active noise control system, can be used to optimally determine the error microphone locations which correspond to minimum residual values. One of the advantages of using multiple regression is high computational efficiency and it can be performed by means of a commercial multiple regression package.

In this thesis, a general genetic algorithm procedure was used to optimize the locations of the error sensors to achieve the maximum sound reduction for the small transformer radiation (Chapter 6) and to optimize the locations of the control sources for canceling the noise that was radiated by a large transformer (Chapter 7).

CHAPTER 3 CURVED PANEL SOURCES FOR ACTIVE NOISE CONTROL

3.1 Introduction

This chapter is concerned with the design and application of a resonant curved panel with a backing cavity as an acoustic control source. For this purpose, an analytical model has been developed to design a resonant curved panel with a backing cavity system having resonance frequencies of 100 Hz and 200 Hz for the 1,1 mode and 1,3 mode respectively. Here an example configuration has been designed using the analysis described in this chapter and the result is verified by finite element analysis (FEA). To increase the sound radiation efficiency from the curved panel – backing cavity system at the frequencies of interest, simple optimization procedures for sizes and locations of piezoelectric actuators on the curved panel are investigated.

3.2 Model of the curved panel with a backing cavity

A model of a curved panel with a backing cavity is shown in Figure 3.1. The backing cavity prevents the interaction and cancellation of sound radiation from the two sides of the panel. All four sides of the panel were simply supported.

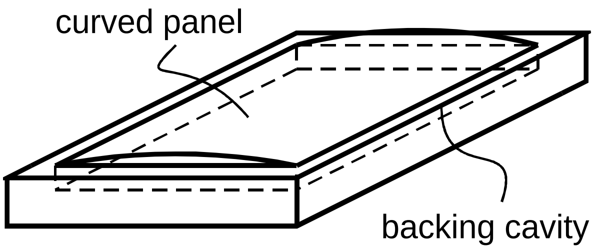

Figure 3.1 Curved panel with a backing cavity

According to Dowell (1977)'s work, in cases where there is a significant change in a flexible panel resonance frequency due to a backing cavity, the equation of motion of the flexible panel is

$$M_s(\ddot{q}_s + 2\xi_s\omega_s\dot{q}_s + \omega_s^2 q_s) = -(\rho_0 c_0^2 A_F^2 / V) L_{os}^2 q_s + \overline{Q}_s^E e^{i\omega_E t} \qquad (3.1)$$

Rearranging equation (3.1) gives

$$M_s(\ddot{q}_s + 2\xi_s\omega_s\dot{q}_s + \omega_s^{c\;2} q_s) = \overline{Q}_s^E e^{i\omega_E t} \qquad (3.2)$$

where

$$\omega_s^{c\;2} = \omega_s^2 + \rho_0 c_0^2 A_F^2 L_{os}^2 / (M_s V) \qquad (3.3)$$

Equation (3.3) represents the coupled panel-backing cavity system resonance frequency. The first term, ω_s, on the right-hand side of equation (3.3) is the resonance frequency of the panel and the second term is the panel–acoustic coupling term. The second term implies that the system resonance frequency is affected by the cavity parameters, i.e. the properties of the medium in the cavity and the dimensions of the cavity. In other words, the coupled panel–cavity system resonance frequency may be tuned by adjusting the volume of the cavity.

In the above mentioned equations: $M_s \equiv \int_{A_F} m_s \psi_s^2 dA$ is the panel generalized mass for the s^{th} mode, $m_s = \rho_s h$ is the panel mass per unit area, and ρ_s and h are the density and thickness of the panel respectively. The panel generalized mass, M_s, for a uniform thickness panel is expressed as:

$$M_s = \rho_s h \int_{A_s} \psi_s^2 dA \qquad (3.4)$$

where the quantity ψ_s is the s^{th} natural mode of the panel; ρ_0 and c_0 are the mean fluid density and sound velocity within the cavity respectively; A_F is the area of the panel and V is the volume of the cavity.

The quantity L_{0s} in equation (3.1) is the generalized panel exciting force and is defined by:

$$L_{0s} = \frac{1}{A_F}\int_{A_F} F_0 \psi_s dA \tag{3.5}$$

where F_0=1.

From Figure 3.2 some geometry parameters may be determined as follows:

$$\begin{gathered}
A_F = \theta_0 R a_0 \\
V = a_0 b_0 c + \frac{1}{2}R^2(\theta_0 - \sin\theta_0)a_0 \\
b_0 = 2R\sin\frac{\theta_0}{2} \\
z = \sqrt{R^2-(y-b_0/2)^2} - R\cos\frac{\theta_0}{2} + c \\
\theta = \arcsin\frac{(y-b_0/2)}{R} + \frac{\theta_0}{2}.
\end{gathered} \tag{3.6a-e}$$

where a_0 is the length of the cavity (not shown in Figure 3.2).

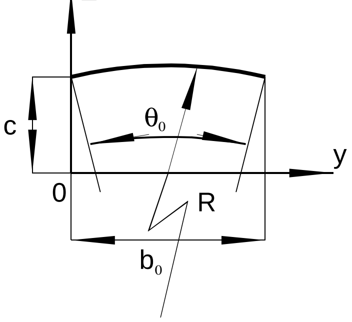

Figure 3.2 Front view of the curved panel

Soedel (1993) gives an expression for the mode shapes of a curved panel for which the boundary conditions are simply supported on all four edges as follows:

$$\psi_{mn}(x,\theta) = \sin\frac{m\pi x}{a_0}\sin\frac{n\pi\theta}{\theta_0} \tag{3.7}$$

where n is the number of axial node lines (plus one) and m is the number of circumferential node lines (plus one) on the shell. The quantities θ and θ_0 are defined in the Figure 3.2.

Using equation (3.7), equations (3.4) and (3.5) may be written as:

$$M_{mn} = \int_{A_F} \rho_s h \sin^2\frac{m\pi x}{a_0}\sin^2\frac{n\pi\left(\arcsin\frac{(y-b_0/2)}{R}+\frac{\theta_0}{2}\right)}{\theta_0}dA \tag{3.8}$$

$$L_{0mn} = \frac{1}{A_F}\int_{A_F}\sin\frac{m\pi x}{a_0}\sin\frac{n\pi\left(\arcsin\frac{(y-b_0/2)}{R}+\frac{\theta_0}{2}\right)}{\theta_0}dA \tag{3.9}$$

Integrating M_{mn} and L_{0mn} over A_F gives:

$$M_{mn} = \frac{\rho_s h a_0 \theta_0 R}{4} \tag{3.10}$$

$$L_{0mn} = \frac{2}{mn\pi^2}\sin^2\frac{n\pi}{2}(1-\cos(m\pi)) \tag{3.11}$$

The resonance frequency $\omega_{s,mn}$ of the curved panel is given by Soedel (1993):

$$\omega_{s,mn} = \frac{1}{R}\sqrt{\frac{(m\pi R/a_0)^4}{[(m\pi R/a_0)^2+(n\pi/\theta_0)^2]^2}+\frac{(h/R)^2}{12(1-\mu^2)}\left[\left(\frac{m\pi R}{a_0}\right)^2+\left(\frac{n\pi}{\theta_0}\right)^2\right]^2}\times\sqrt{\frac{E}{\rho_s}} \tag{3.12}$$

Substituting equations (3.10) and (3.11) and the square of equation (3.12) into equation (3.3) gives:

$$\omega_{s,mn}^{c\,2}=\frac{1}{R^2}\left(\frac{(m\pi R/a_0)^4}{[(m\pi R/a_0)^2+(n\pi/\theta_0)^2]^2}+\frac{(h/R)^2}{12(1-\mu^2)}\left[\left(\frac{m\pi R}{a_0}\right)^2+\left(\frac{n\pi}{\theta_0}\right)^2\right]^2\right)\frac{E}{\rho_s} \tag{3.13}$$

$$+\frac{16\rho_0 c_0^2 a_0\theta_0 R}{\rho_s h m^2 n^2\pi^4}\frac{\sin^4(n\pi/2)(1-\cos(m\pi))^2}{V}$$

By using equation (3.13) the curved panel with a backing cavity can be designed to be resonant at the required frequencies.

3.3 Example design

3.3.1 Specification of the geometry size of the system

In this section a resonant curved panel with a backing cavity is designed using the model described in the last section. The system is resonant at 100 Hz and 200 Hz corresponding to the 1,1 mode and 1,3 mode respectively. The material of the curved panel is aluminum and the cavity is made of medium density fiber (MDF) wood with a thickness of 25 mm. The parameters which represent the system properties are ρ_s=2700 $\mathrm{kg/m^3}$, E=70300 MPa, μ=0.345, ρ_0 = 1.21 $\mathrm{kg/m^3}$ and c_0=344 $\mathrm{m/s}$.

To help optimize the design of the system, the effect of variations in the cavity size on the coupled curved panel – cavity resonance frequencies for a panel thickness of 0.0016m is given in Figures 3.3 - 3.5.

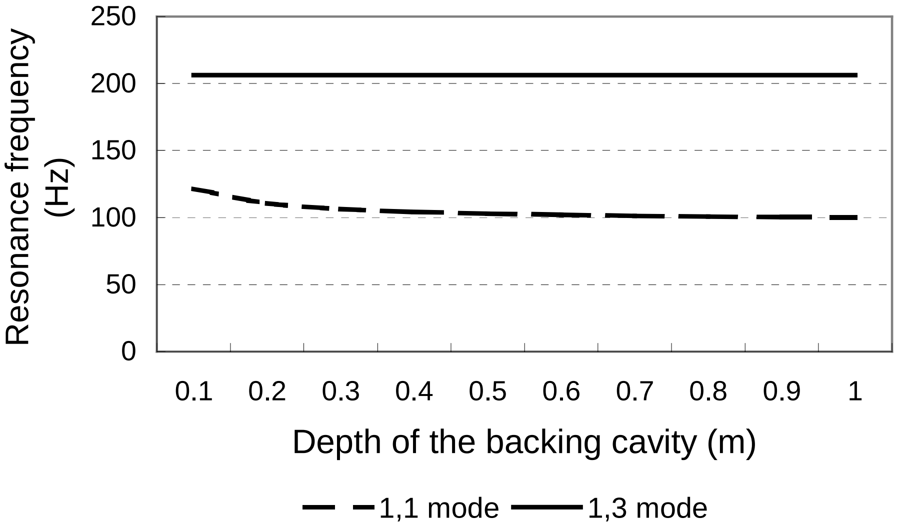

Figure 3.3 Variation of the resonance frequency of the panel-cavity system as a function of cavity depth, associated with cavity length of 0.985 m and width of 0.418 m.

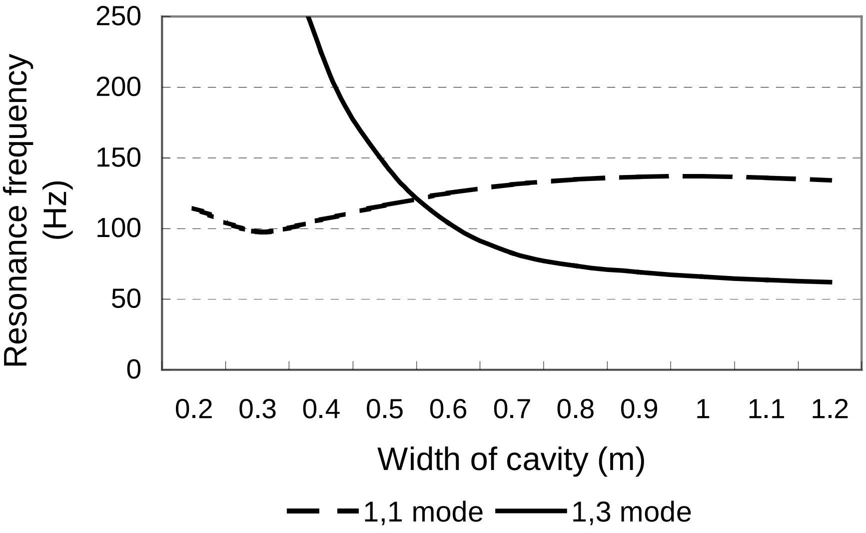

Figure 3.4 Variation of the resonance frequency of the panel-cavity system as a function of cavity width, associated with cavity length of 0.985 m and cavity depth of 0.25 m.

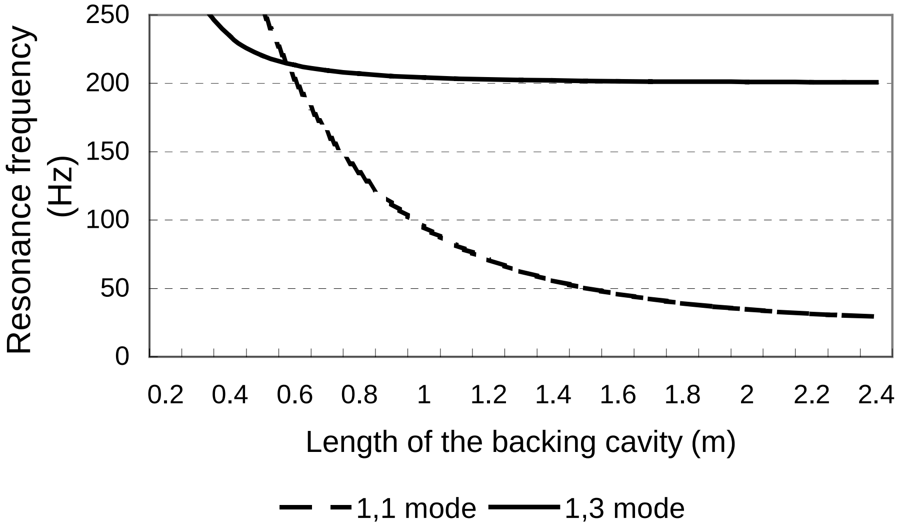

Figure 3.5 Variation of the resonance frequency of the panel-cavity system as a function of cavity length, associated with cavity width of 0.42 m and cavity depth of 0.25 m

According to Wallace (1972)'s work, the 1,1 and 1,3 modes for a simply supported panel have the highest radiation efficiencies at low frequencies; thus, these two modes have been selected for excitation on the curved panel. Here the intention is to design a curved panel so that the 1,1 mode resonance frequency occurs at 100 Hz and the 1,3 resonance frequency occurs at 200 Hz. The properties of the panel-cavity system which give $f_{1,1}$=108 Hz and $f_{1,3}$=206 Hz are given in Table 3.1.

Table 3.1. System property parameters

E (MPa)	ν	ρ (kg/m^3)	sizes (m)
70300	0.345	2700	R=1.33, a_0=0.985, h=0.0016, b_0=0.418, θ_0=18°.

The numerical frequencies have been selected to be higher than required as it is easier to reduce resonance frequencies in practice by adding mass to the panel, but it is not very easy to increase the frequencies by subtracting mass from the panel. The calculated resonance frequencies of the system are given in Table 3.2.

Table 3.2 Resonance frequencies of the curved panel with a backing cavity (Hz)

	n=1	n=2	n=3
m=1	108 (105)	98 (95)	206 (201)
m=2	259 (259)	141 (139)	223 (218)
m=3	382 (379)	217 (214)	256 (250)

Note: Data in brackets represent calculations made using ANSYS.

3.3.2 Verification of theoretical model by means of Finite Element Analysis (FEA)

To verify the theoretical model by means of Finite Element Analysis (FEA), the commercial ANSYS numerical computation package was used. For modeling the acoustic medium in the cavity, the FLUID30 3-D acoustic fluid element was used to couple with the SHELL63 elastic shell element representing the curved panel in the model. The resonance frequencies predicted using ANSYS are given in Table 3.2. It can be seen that results predicted using ANSYS agree closely (within 3%) with those predicted by theoretical model. The 1,1 mode shape and 1,3 mode shape are shown in Figures 3.7 – 3.8.

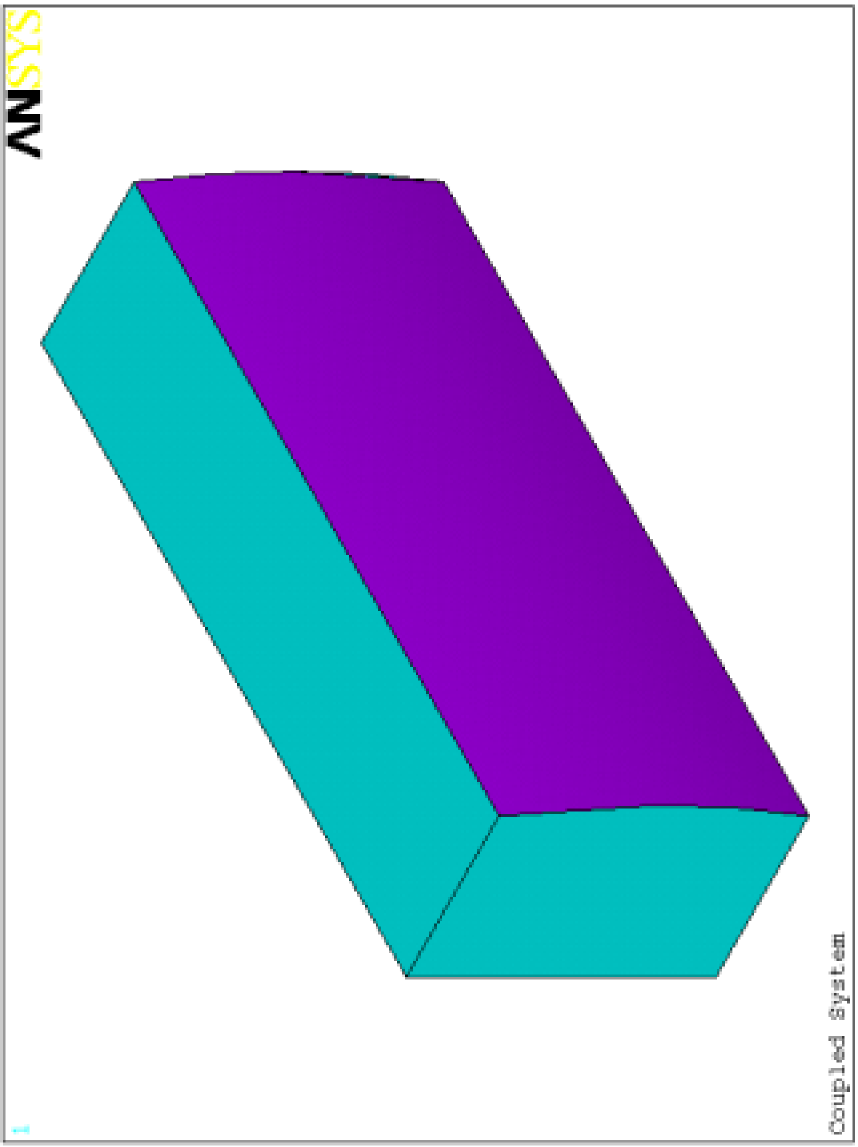

Figure 3.6 Curved panel with a backing cavity modeled by means of FEA (ANSYS R5.5)

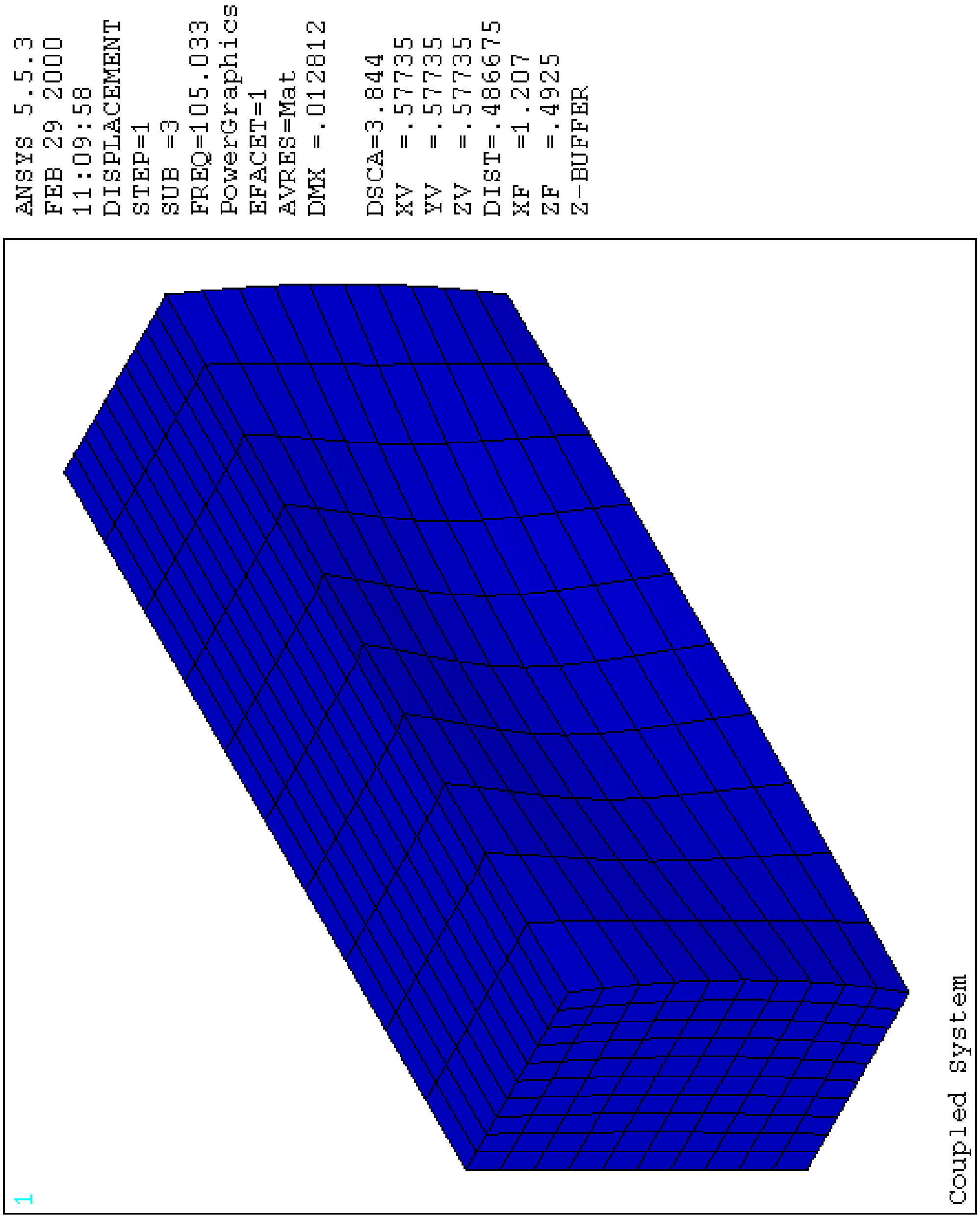

Figure 3.7 1,1 mode shape of the curved panel with a backing cavity modeled by means of FEA (ANSYS R5.5)

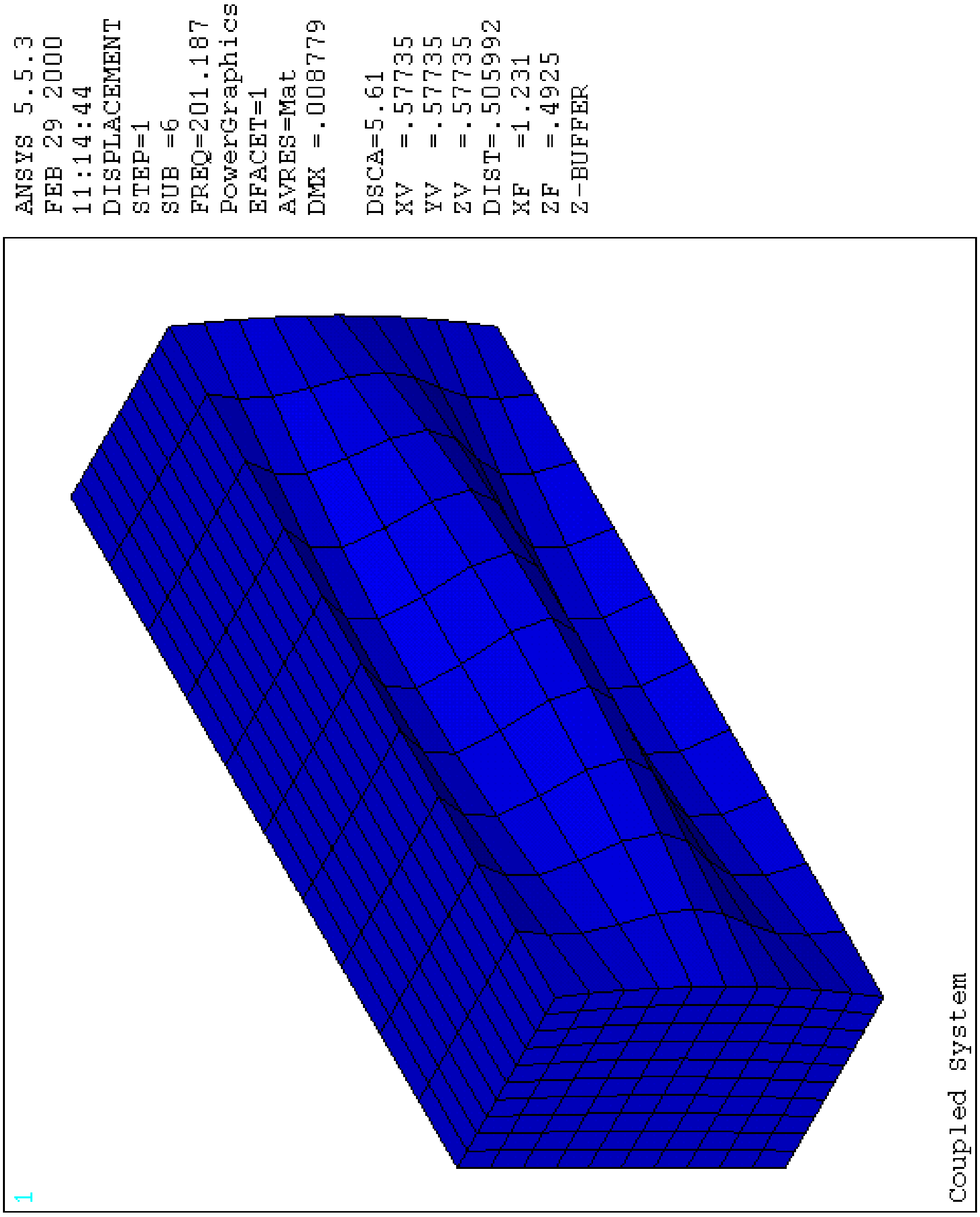

Figure 3.8 1,3 mode shape of the curved panel with a backing cavity modeled by means of FEA (ANSYS R5.5)

3.3.3 Tuning the resonance frequencies of the system

To obtain the required resonance frequencies ($f_{1,1}$=100 Hz and $f_{1,3}$=200 Hz) after the panel-cavity system is constructed, masses may be attached to the panel or the cavity depth may be adjusted. As shown in Figure 3.3, the 1,3 mode is much less sensitive than the 1,1 mode to the changes in the depth of the backing cavity and the 1,1 mode can be made relatively insensitive to the presence of point masses attached to the panel in properly chosen locations.

3.3.3.1 Mass attached to the curved panel

The characteristic equation for the curved panel with an attached mass (Soedel (1993)), M^*, is

$$\frac{4}{\rho_s h a_0 R\theta_0}\sum_{m=1}^{\infty}\sum_{n=1}^{\infty}\frac{1}{\omega_{mn}^2-\omega^2}\sin^2\frac{m\pi x^*}{a_0}\sin^2\frac{n\pi\theta^*}{\theta_0}-\frac{1}{M^*\omega^2}=0 \qquad (3.14)$$

where (x^*, θ^*) is the position of the attached mass and ω_{mn} is the original resonance frequency.

By rearranging equation (3.14), the equation for the system with a mass attached to the panel in the following form:

$$M^*=\frac{\rho_s h a_0 R\theta_0}{4\omega^2}\frac{1}{\sum_{m=1}^{\infty}\sum_{n=1}^{\infty}\frac{1}{\omega_{mn}^2-\omega^2}\sin^2\frac{m\pi x^*}{a_0}\sin^2\frac{n\pi\theta^*}{\theta_0}} \qquad (3.15)$$

Equation (3.14) has to be solved for its root, $\omega=\omega_0$, by a numerical procedure. However, in the case where the new resonance frequency ω_0 is not too different from the original resonance frequency ω_{mn}, the particular root ω_0 dominates all the others. Thus, when the mass is attached to a node line of the panel, the mass has no influence on that particular frequency. The largest influence that the mass can have on the mode happens if the mass is located on an anti-node line subject to the above assumption.

A mass $M^*_{1,1}$ of 0.0991 kg attached to a nodal line corresponding to the 1,3 mode, i.e. at $x^*= a_0/2$ and $\theta^* = \theta_0 / 3$, changes $f_{1,1}$ from 108 to 100 Hz, while the change of $f_{1,3}$ could be neglected. Another mass $M^*_{1,3}$ of 0.0296 kg located at the anti-node of the 1,3 mode, i.e. at $x^*= a_0/2$ and $\theta^* = \theta_0 / 6$, changes $f_{1,3}$ from 206 to 200 Hz but changes $f_{1,1}$ by less than 1%. The mode shapes with the masses added to the panel are slightly distorted as shown in Figure 3.9.

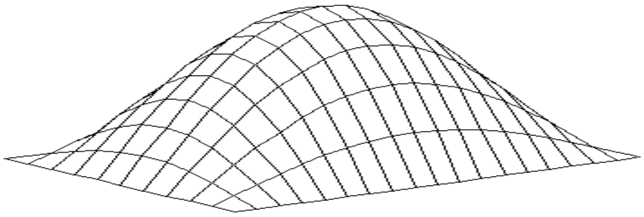

(a) 1,1 mode

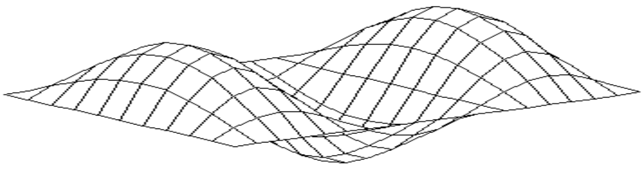

(b) 1,3 mode

Figure 3.9 Mode shapes in 1,1 mode and 1,3 mode with attached masses

3.3.3.2 Adjusting the depth of the backing cavity

As shown in Figure 3.3, the variation of the resonance frequency of the system with the depth of the cavity is obvious in mode 1,1 but not much in mode 1,3. Thus it is possible to tune the resonance frequency of the 1,1 mode by adjusting the cavity depth without affecting the resonance frequency of the 1,3 mode significantly.

3.3.4 Resonance frequency tests

3.3.4.1 Experimental set-up

The curved panel with a backing cavity was tested using experimental modal analysis to determine the resonance frequencies of the 1,1 mode and 1,3 mode. The modal testing technique involved the use of a Brüel & Kjær type 8202 impact hammer to excite the panel. Frequency response data were recorded using a Brüel & Kjær type 4394 accelerometer connected through a Brüel & Kjær type 2635 charge amplifier to a Brüel & Kjær type 2032 dual channel signal analyzer. Data were transferred into a personal computer in which the modal analysis software, PC Modal, was installed. The experimental set-up is shown in Figure 3.10.

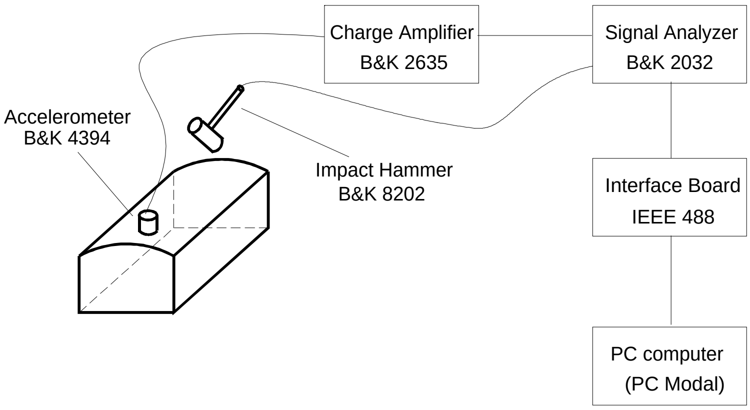

Figure 3.10 Experimental set-up for modal analysis testing

3.3.4.2 Experimental results

The measured frequency response of the panel is shown in Figure 3.11. The first peak (76 Hz) corresponds to the 1,1 mode resonance and the second peak (199 Hz) to the 1,3 mode resonance. These frequencies can be compared to the corresponding theoretical predictions of 108 Hz and 206 Hz respectively. Although the difference between measured and predicted resonance frequencies for the 1,3 mode is acceptably small, the difference for the 1,1 mode is unacceptably large. The reason for this is the high sensitivity of the 1,1 mode resonance frequency to errors in the radius of curvature of the panel and the difficulty in manufacturing panels of uniform and accurate radii of curvature.

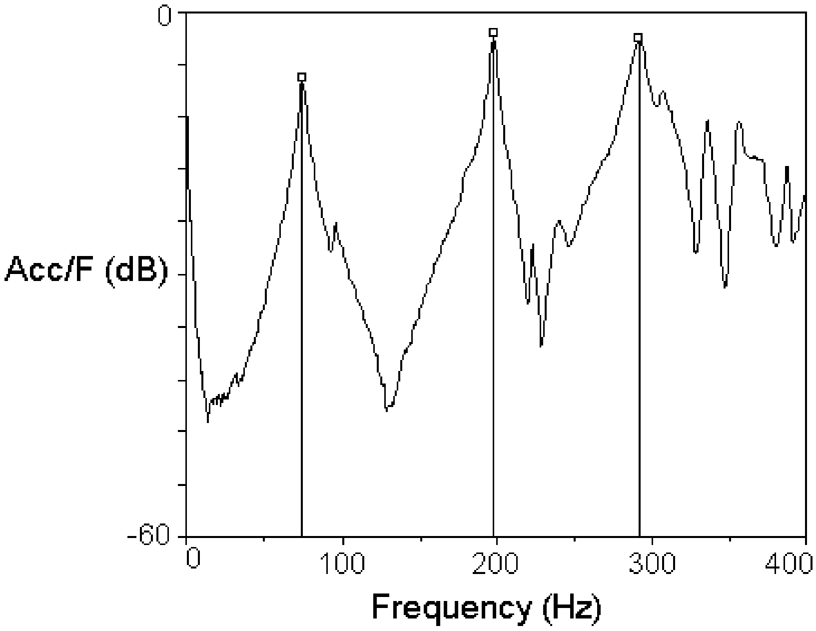

Figure 3.11 Frequency response of the curved panel with a backing cavity

However, as described theoretically in the previous section, the resonance frequency of the 1,1 mode may be tuned by adjusting the depth of the backing cavity without affecting the resonance frequency of the 1,3 mode significantly. This was verified experimentally and the effect of the backing cavity depth on the 1,1 and 1,3 mode resonance frequencies is shown in Figure 3.12.

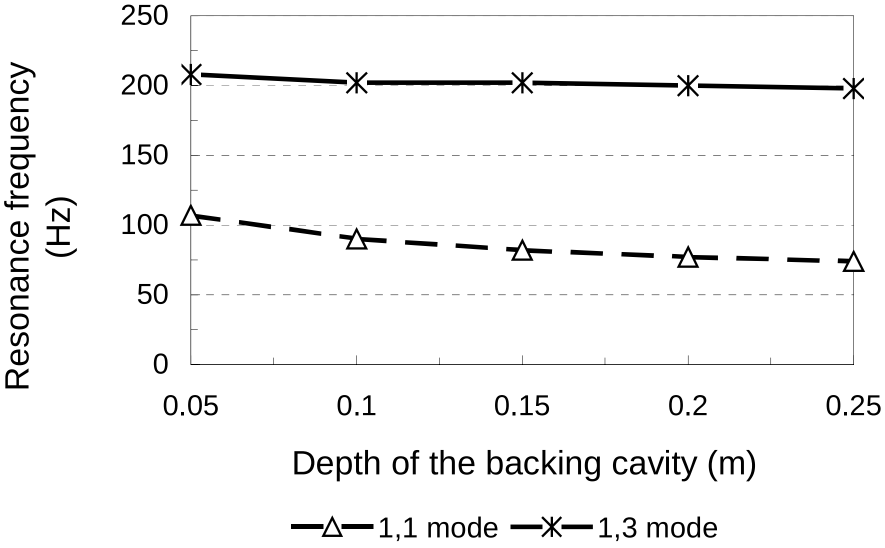

Figure 3.12 The effect of variations in backing cavity depth on the panel resonance frequency

From Figure 3.12 it can be seen that the required depth of the cavity for the 1,1 mode to be resonant at 100Hz is 58 mm. The resonance frequency of the 1,3 mode is only affected slightly by variations in the backing cavity depth as predicted theoretically in the previous section. In this case, the resonance frequency of the 1,3 mode was slightly above 200 Hz when the cavity depth was reduced to 58 mm. However this was reduced to 200 Hz by the addition of a 22 gram mass at $a_0/2$, $b_0/3$.

The measured frequency response for the panel with the backing cavity depth of 58 mm and a small mass of 22 grams fixed at $a_0/2$, $b_0/3$ is shown in Figure 3.13, where it can be seen that adjustment of the experimental model has resulted in the 1,1 mode being resonant at 100 Hz; the 1,3 mode being resonant at 200 Hz and the 3,1 mode being resonant at 295 Hz.

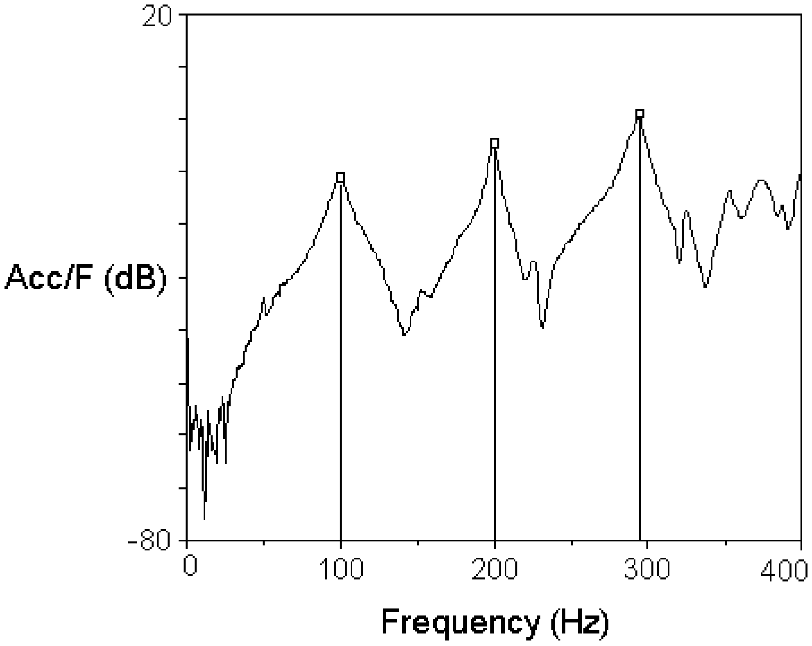

Figure 3.13 Frequency response of the adjusted curved panel with a backing cavity

3.4 Optimization of sizes and locations of piezoelectric actuators for curved panel sound sources

In this section the optimization of the sizes and locations of piezoelectric (PZT) actuators (which were used to drive the curved panel) is investigated. The objective of the optimization is to maximize the vibration level resulting from the bending moment generated by piezoelectric actuators on the panel.

Piezoelectric material has been widely used as an actuator material in active structural acoustic control. When a voltage is applied across the material, a mechanical strain in the material is induced. For thin patch actuators, the deformations of material, for instance extensions, as a result of an applied voltage are in a direction normal to the direction of polarization as shown in Figure 3.14.

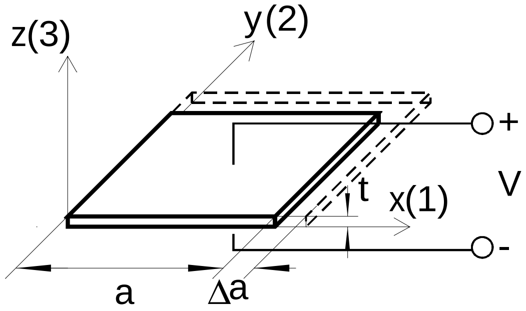

Figure 3.14 Extensions of a thin piezoelectric actuator under an applied voltage

If the piezoelectric actuator is bonded to a structure, extensions resulting from the applied voltage will be less than the free extensions due to the constraint between the actuator and the structure. This will cause bending moments in the structure which result in the movement of the structure. Mathematical models describing the behaviour of piezoelectric actuators bonded to a shell structure are described in APPENDIX A.

3.4.1 Response of the coupled structural/acoustic system

Due to weak coupling between the structural vibration and acoustic modes (this is allowed when the fluid medium is air), modal coupling theory (Pope (1971) and Hansen and Snyder (1997)) was used to derive the response expression for a structural/acoustic coupled system. In this case, the response of a structure coupled to an enclosure can be given in matrix form as follows (Hansen and Snyder (1997)):

$$\begin{bmatrix} V_1 \\ V_2 \\ \vdots \\ V_r \end{bmatrix} = \begin{bmatrix} Z_{I1,1} & Z_{I1,2} & \cdots & Z_{I1,r} \\ Z_{I2,1} & \ddots & & \\ \vdots & & \ddots & \\ Z_{Ir,1} & & & Z_{Ir,r} \end{bmatrix}^{-1} \begin{bmatrix} \gamma_1 \\ \gamma_2 \\ \vdots \\ \gamma_r \end{bmatrix} \tag{3.16}$$

where $V_i = V_{m,n}$ is the structural modal velocity amplitude corresponding to the $(m,n)^{\text{th}}$ structural mode resulting from the external force; $Z_{I\,i,j}$ is the structural modal input impedance, which can be defined as:

$$Z_{I\,i,j} = \begin{cases} \mathbf{j}\rho_0 A^2\omega\sum\limits_{\iota=1}^{n}\dfrac{B_{\iota,u}B_{\iota,u}}{\Lambda_\iota(\kappa_\iota^2 - k^2)} - \dfrac{\mathbf{j}M_u Z_u}{\omega} & i = j \\ \mathbf{j}\rho_0 A^2\omega\sum\limits_{\iota=1}^{n}\dfrac{B_{\iota,u}B_{\iota,v}}{\Lambda_\iota(\kappa_\iota^2 - k^2)} & i \neq j \end{cases} \tag{3.17}$$

where $u(m,n)$ and $v(m,n)$ refer to the structural mode indices; $Z_{I\,i,i}$ represents the velocity response of mode *u* to a unit excitation force and $Z_{I\,i,j}$ $(i \neq j)$ represents the response of mode *v* to a unit response of mode *u*; $B_{\iota,u}$ is the non-dimensional modal coupling coefficient between the ι^{th} acoustic mode and u^{th} structural mode and $B_{\iota,v}$ is similar to $B_{\iota,u}$; Λ_ι is the volume normalization of the acoustic mode ι; $\kappa_\iota = \omega_\iota/[c_0(1-\mathbf{j}2\xi_\iota)]$ is the eigenvalue of acoustic mode ι; *k* is the acoustic wavenumber at the excitation frequency ω. Moreover, M_u and Z_u in equation (3.17) are the modal mass and *in vacuo* structural input impedance of the u^{th} mode, which can be expressed as follows:

$$M_u = \int_A m(x,y)\psi_{m,n}^2(x,y)dA \tag{3.18}$$

$$Z_u = (\omega_{r,s}^2 + \mathbf{j}\eta_{m,n}\omega_{m,n}^2 - \omega^2) \tag{3.19}$$

where *m*(*x,y*) and $\psi_{m,n}(x,y)$ are the surface density and the mode shape of the structure at location (*x,y*) respectively; $\mathbf{j}=\sqrt{-1}$; ω_ι is the acoustic resonance frequency associated with acoustic mode ι and $\omega_{m,n}$ is the structural resonance frequency associated with the $(m,n)^{\text{th}}$ structural mode; ξ_ι is the viscous damping ratio associated with acoustic mode ι and $\eta_{m,n}$ is the hysteretic loss factor associated with the $(m,n)^{\text{th}}$ structural mode.

In equation (3.16), $\gamma_i = \gamma_{m,n}$ is the structural modal generalized force corresponding to the $(m,n)^{\text{th}}$ structural mode:

$$\gamma_i = \gamma_{m,n} = \int_A \psi_{m,n} p_{ext}(x,y)dA \tag{3.20}$$

where p_{ext} is the generalized external load in N/m^2 and here it is produced by the piezoelectric actuators.

3.4.2 Distributed external load produced by the piezoelectric actuator

In general, the moments generated in a plate by a piezoelectric actuator can be approximated by external line moments acting on the plate at the edges of the piezoelectric layer. However, for line moments on a cylindrical shell (see Figure 3.15), the distributed moments per unit area, T_x and T_θ, may be written as follows (Soedel (1993)):

$$T_x = M_x(\delta(x-x_1) - \delta(x-x_2))(u(\theta-\theta_1) - u(\theta-\theta_2)), \tag{3.21}$$

$$T_\theta = \frac{1}{R} M_\theta(\delta(\theta-\theta_1) - \delta(\theta-\theta_2))(u(x-x_1) - u(x-x_2)), \tag{3.22}$$

where $u(\ )$ and $\delta(\ )$ are the unit step function and Dirac delta function respectively; M_x and M_θ are the moments in the shell in x direction and θ direction in newton-meters per meter respectively; R is the radius of the shell; x_1, x_2, θ_1 and θ_2 are defined in Figure 3.15.

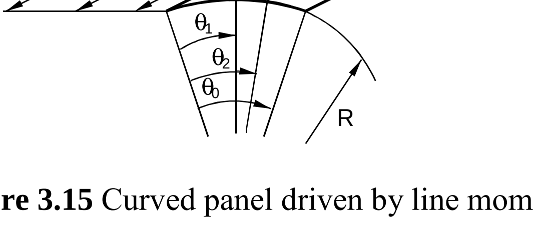

Figure 3.15 Curved panel driven by line moments

The equivalent distributed external load in newtons per square meter can be derived by differentiating equations (3.21) and (3.22) with respect to variables x and θ, i.e.:

$$\begin{aligned} p_{ext} &= M_x(\delta'(x-x_1)-\delta'(x-x_2))(u(\theta-\theta_1)-u(\theta-\theta_2)) \\ &+\frac{1}{R^2}M_\theta(\delta'(\theta-\theta_1)-\delta'(\theta-\theta_2))(u(x-x_1)-u(x-x_2)) \end{aligned} \tag{3.23}$$

In the case that the thickness of the shell is much smaller than the other shell dimensions and the panel is very shallow, the bending moment equations for M_x and M_θ generated by piezoelectric patch actuators on the panel may be written as:

$$M_x = \frac{h^2}{6}\frac{\frac{E_a\alpha_a t_a(h+t_a)}{2}\left(\left(\frac{h^2}{12}+\frac{2E_a}{hE_s}\alpha_a\beta_a\eta\right)\Lambda_x-\frac{2E_a}{hE_s}\alpha_a\gamma_a\eta\Lambda_\theta\right)}{\left(\frac{h^2}{12}+\frac{2E_a}{hE_s}\alpha_a\beta_a\eta\right)^2-\left(\frac{2E_a}{hE_s}\alpha_a\gamma_a\eta\right)^2} \tag{3.24}$$

$$M_\theta = \frac{h^2}{6}\frac{\frac{E_a\alpha_a t_a(h+t_a)}{2}\left(\left(\frac{h^2}{12}+\frac{2E_a}{hE_s}\alpha_a\beta_a\eta\right)\Lambda_\theta-\frac{2E_a}{hE_s}\alpha_a\gamma_a\eta\Lambda_x\right)}{\left(\frac{h^2}{12}+\frac{2E_a}{hE_s}\alpha_a\beta_a\eta\right)^2-\left(\frac{2E_a}{hE_s}\alpha_a\gamma_a\eta\right)^2} \tag{3.25}$$

where

$$\alpha_g = \frac{1}{\left(1-\mu_g^2\right)},\ \beta_g = 1-\mu_g\mu_s,\ \gamma_g = \mu_g-\mu_s,$$

$$\alpha_a = \frac{1}{\left(1-\mu_a^2\right)},\ \beta_a = 1-\mu_a\mu_s,\ \gamma_a = \mu_a-\mu_s, \tag{3.26a-i}$$

$$\eta = \frac{1}{4}h^2t_a+\frac{1}{2}ht_a^2+\frac{1}{3}t_a^3,$$

$$\Lambda_x = \frac{d_{31}V}{t_a} \text{ and } \Lambda_\theta = \frac{d_{32}V}{t_a}.$$

For the thin patch piezoelectric actuators $d_{31}=d_{32}$, thus:

$$M_x = M_\theta = \frac{h^2}{12}\frac{E_a\alpha_a t_a(h+t_a)\Lambda_x}{\left(\frac{h^2}{12}+\frac{2E_a}{hE_s}\alpha_a\beta_a\eta+\frac{2E_a}{hE_s}\alpha_a\gamma_a\eta\right)} \tag{3.27}$$

where d_{31} is the strain constant of the piezoelectric actuator and V is the applied voltage on the actuator. More details about the derivation of equations (3.24) and (3.25) are described in APPENDIX A.

For a simply supported curved panel, substituting equations (3.23) and (3.7) into (3.20) and using the properties of the Dirac function through integrating over the panel surface for the modal generalized force gives:

$$\gamma_{m,n} = -M_x\left(R\frac{\Delta_m}{\Delta_s}+\frac{1}{R}\frac{\Delta_s}{\Delta_m}\right)\left(\cos\Delta_m x_1-\cos\Delta_m x_2\right)\left(\cos\Delta_s\theta_1-\cos\Delta_s\theta_2\right) \tag{3.28}$$

where $\Delta_m = \frac{\pi m}{a_0}$ and $\Delta_n = \frac{\pi n}{\theta_0}$.

3.4.3 Numerical simulation

The parameters which represent the system properties have been given in Table 3.1. The cavity volume was $0.985\times0.418\times0.25$ m^3. The panel material was aluminum and the panel was simply supported on all four edges.

3.4.3.1 Optimal perimeter of piezoelectric actuators

In this case, a pair of PZT actuators was attached to the panel of length a_0 and width b_0. One was attached to the front of the panel and the other was attached to the back in same relative location as the one on the front. The actuators were driven 180 out of phase with an applied voltage of 100 V. To optimize the perimeter of the piezoelectric actuator, the modal generalized force of equation (3.28) is expressed in terms of the length *a* and width *b* of the PZT actuator, as follows:

$$\gamma_{m,n} = -M_x\left(R\frac{\Delta_m}{\Delta_n} + \frac{1}{R}\frac{\Delta_n}{\Delta_m}\right)\left(\cos[\Delta_m(a_0 - a)/2] - \cos[\Delta_m(a_0 + a)/2]\right) \\ \left(\cos[\Delta_n(\theta_0 - b/R)/2] - \cos[\Delta_n(\theta_0 + b/R)/2]\right) . \qquad (3.29)$$

By substituting equation (3.29) into equation (3.16), then differentiating the result with respect to the dimensions, *a* and *b*, of the piezoelectric actuator, and setting the result equal to zero, the equation for the optimal size of the PZT actuator in terms of maximizing the modal generalized force can be determined. That is,

$$\begin{bmatrix} V_1 \\ V_2 \\ \vdots \\ V_r \end{bmatrix}_{a,b}^{'} = \begin{bmatrix} Z_{I1,1} & Z_{I1,2} & \cdots & Z_{I1,\mathbf{r}} \\ Z_{I2,1} & \ddots & & \\ \vdots & & \ddots & \\ Z_{Ir,1} & & & Z_{Ir,r} \end{bmatrix}^{-1} \begin{bmatrix} \gamma_1 \\ \gamma_2 \\ \vdots \\ \gamma_r \end{bmatrix}_{a,b}^{'} = 0 . \qquad (3.30)$$

Figure 3.16 shows the variation of the structural response as a function of the size of the PZT actuator pair (one on the front and another on the back of the panel) for a constant input excitation voltage of 100 V at a frequency of *f*=207 Hz corresponding to the 1,3 mode. The center of the PZT actuator is at the center of the panel for all actuator sizes. The initial value of the actuator size was 52×26×0.3 mm. As can be seen from the figure, the structural response (velocity) of the simply supported curved panel excited by a pair of PZT actuators bonded to it is affected by the size of the PZT actuators and it is apparent from Table 3.3 that the maximum panel velocity occurs when the actuator width in the b_0 direction is about 1/3 of b_0 and the actuator length in the a_0 direction is equal to a_0. This implies that the optimal sizes of the PZT actuator for maximum structural response are about half of the wavelength of the structural vibration. It was found that the maximum structural response was achieved when the edges of the PZT actuator were coincident with the nodal lines of the structural mode.

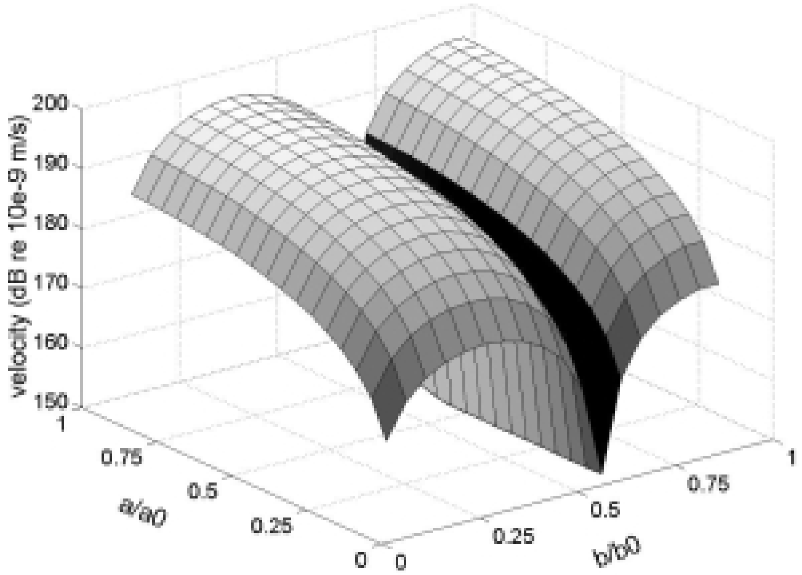

Figure 3.16 Variation of the structural response as a function of PZT actuator size for the 1,3 mode, using one pair of PZT actuators

Table 3.3. Velocity (dB re 10^{-9} m/s) of the system for the 1,3 mode (f=207 Hz) corresponding to a PZT input of 100 V, one pair of actuators

	b/b_0=1/9	2/9	3/9	4/9	5/9	6/9	7/9	8/9	9/9
a/a_0=1/9	177.0	181.8	183.0	181.8	177.0	150.0	176.9	181.7	182.7
2/9	182.9	187.7	188.9	187.7	182.9	150.0	182.8	187.6	188.6
3/9	186.2	191.0	192.3	191.0	186.3	150.0	186.1	190.9	191.9
4/9	188.5	193.2	194.5	193.2	188.5	150.0	188.4	193.2	194.1
5/9	190.0	194.8	196.1	194.8	190.1	150.0	190.0	194.8	195.7
6/9	191.2	196.0	197.2	196.0	191.2	150.3	191.1	195.9	196.8
7/9	192.0	196.8	198.0	196.8	192.1	152.0	191.9	196.7	197.7
8/9	192.5	197.3	198.6	197.3	192.6	153.3	192.4	197.2	198.2
9/9	192.8	197.6	198.9	197.6	192.9	154.1	192.7	197.5	198.5

In Figure 3.17 similar results are presented for input frequencies of *f*=107 Hz and 257 Hz corresponding to the 1,1 mode and 3,3 mode respectively. In Tables 3.4 and 3.5 numerical values of the structural velocities for various actuator sizes are presented. Odd-odd modes were chosen as they represent the most acoustically efficient modes.

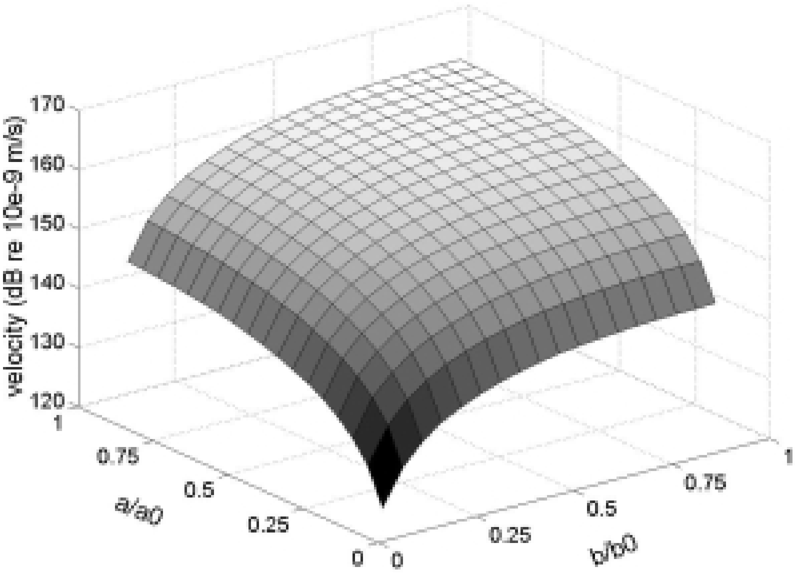

(a) 1,1 mode

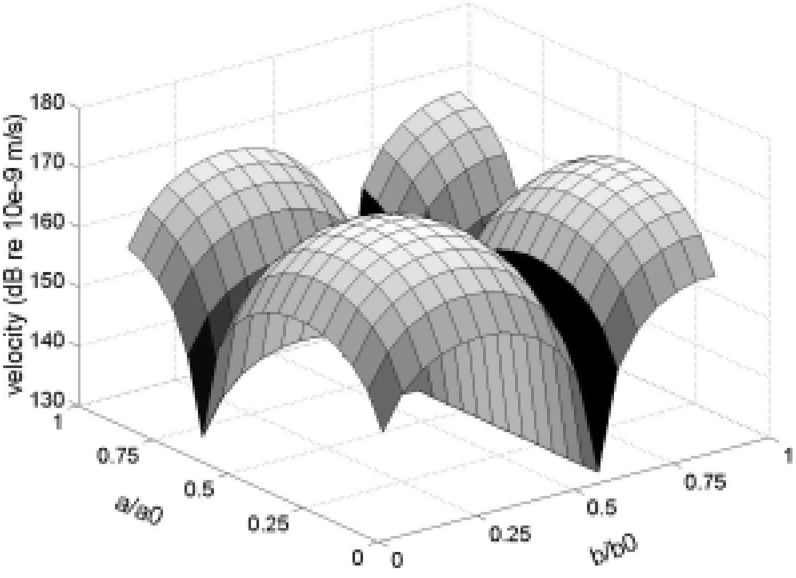

(b) 3,3 mode

Figure 3.17 Variation of the structural response as a function of PZT actuator size for the 1,1 and 3,3 modes, using one pair PZT actuators

Table 3.4. Velocity (dB re 10^{-9} m/s) of the system for the 1,1 mode (f=107 Hz) corresponding to a PZT input of 100 V, one pair of actuators

	b/b_0=1/9	2/9	3/9	4/9	5/9	6/9	7/9	8/9	9/9
a/a_0=1/9	135.7	141.5	144.7	146.7	147.9	148.7	149.1	149.3	149.4
2/9	141.7	147.5	150.6	152.6	153.8	154.6	155.0	155.3	155.3
3/9	145.0	150.8	154.0	155.9	157.2	158.0	158.4	158.6	158.6
4/9	147.3	153.1	156.2	158.2	159.4	160.2	160.6	160.8	160.9
5/9	148.9	154.7	157.8	159.8	161.0	161.8	162.2	162.4	162.4
6/9	150.1	155.9	159.0	161.0	162.2	162.9	163.3	163.5	163.5
7/9	151.0	156.8	159.9	161.8	163.0	163.7	164.1	164.3	164.3
8/9	151.6	157.3	160.5	162.4	163.6	164.2	164.6	164.8	164.8
9/9	151.9	157.7	160.8	162.7	163.9	164.5	164.9	165.0	165.1

Table 3.5. Velocity (dB re 10^{-9} m/s) of the system for the 3,3 mode (f=257 Hz) corresponding to a PZT input of 100 V, one pair of actuators

	b/b_0=1/9	2/9	3/9	4/9	5/9	6/9	7/9	8/9	9/9
a/a_0=1/9	157.9	162.6	163.9	162.6	157.9	130.0	157.8	162.6	163.6
2/9	162.9	167.6	168.9	167.6	162.9	130.0	162.8	167.6	168.6
3/9	164.5	169.3	170.6	169.3	164.5	130.0	164.5	169.3	170.3
4/9	164.1	168.9	170.1	168.9	164.1	130.0	164.1	168.9	169.8
5/9	161.4	166.1	167.4	166.1	161.3	130.0	161.4	166.2	167.1
6/9	153.5	158.3	159.5	158.3	153.4	130.0	153.9	158.6	159.5
7/9	150.2	155.0	156.2	155.0	150.4	130.0	149.3	154.3	155.2
8/9	160.4	165.2	166.4	165.2	160.5	130.0	160.0	164.9	165.8
9/9	163.7	168.4	169.7	168.4	163.7	130.0	163.4	168.2	169.2

Figure 3.18 and Table 3.6 show the variation of the structural response as a function of the size of the actuators for two pairs of PZT actuators at a frequency of f=207 Hz, corresponding to the 1,3 mode resonance. In this case, one pair of actuators was bonded at $\frac{1}{4}a_0,\frac{1}{2}b_0$ and the other pair at $\frac{3}{4}a_0,\frac{1}{2}b_0$; thus the size of the actuators along a_0 was limited to half the length of the panel. From Table 3.6, a similar conclusion could be drawn; namely, the maximum structural response will be achieved when the size of the PZT actuator is equal to half of the wavelength of the structural vibration. When comparing the results shown in Table 3.6 with those in Table 3.3 (for the same size of the actuator), one can see that under this configuration, the structural response did not increase much (less than 3 dB) when using two pairs of actuators than when using one pair of actuators. The reason for this is that for the test mode (1,3), the panel was easily excited with only one actuator at the center of the panel.

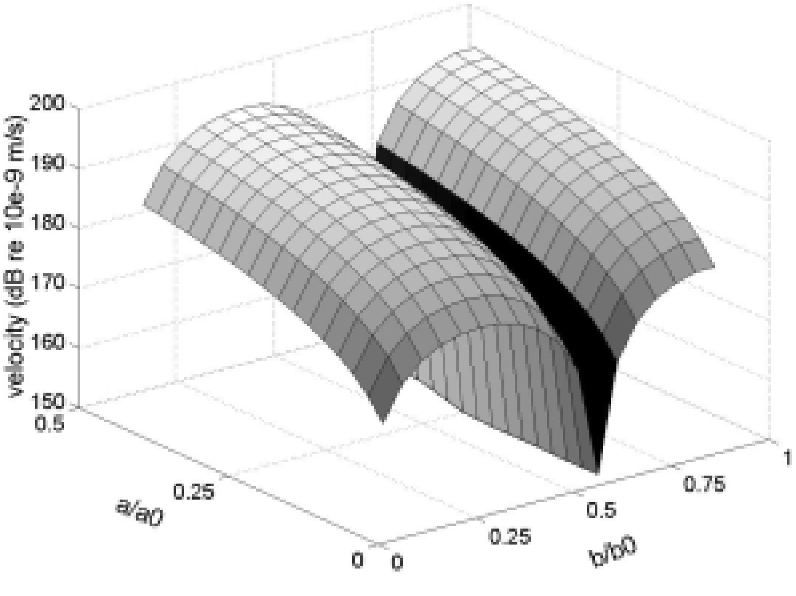

Figure 3.18 Variation of the structural response as a function of PZT actuator size for the 1,3, using two pairs of the PZT actuators

Table 3.6. Velocity (dB re 10^{-9} m/s) of the system for the 1,3 mode (f=207 Hz) corresponding to a PZT input of 100 V, two pairs of actuators

	b/b_0=1/9	2/9	3/9	4/9	5/9	6/9	7/9	8/9	9/9
a/a_0=2/18	177.4	182.2	183.5	182.2	177.5	150.0	177.3	182.1	183.1
3/18	181.8	186.6	187.9	186.6	181.9	150.0	181.7	186.5	187.5
4/18	184.7	189.5	190.7	189.5	184.8	150.0	184.6	189.4	190.3
5/18	186.8	191.6	192.9	191.6	186.9	150.0	186.7	191.5	192.4
6/18	188.5	193.2	194.5	193.3	188.5	150.2	188.3	193.1	194.1
7/18	189.8	194.6	195.8	194.6	189.9	151.5	189.7	194.5	195.4
8/18	190.9	195.7	197.0	195.7	191.0	152.6	190.8	195.6	196.6
9/18	191.9	196.6	197.9	196.7	191.9	153.5	191.7	196.5	197.5

3.4.3.2 Optimal locations of piezoelectric actuators on the panel

In this case two pairs of piezoelectric actuators (52×26×0.3 mm) were attached to the panel and were symmetrical about the center on the diagonal as shown in Figure 3.19. This size of the actuator will be selected for experiment described in section 3.5.

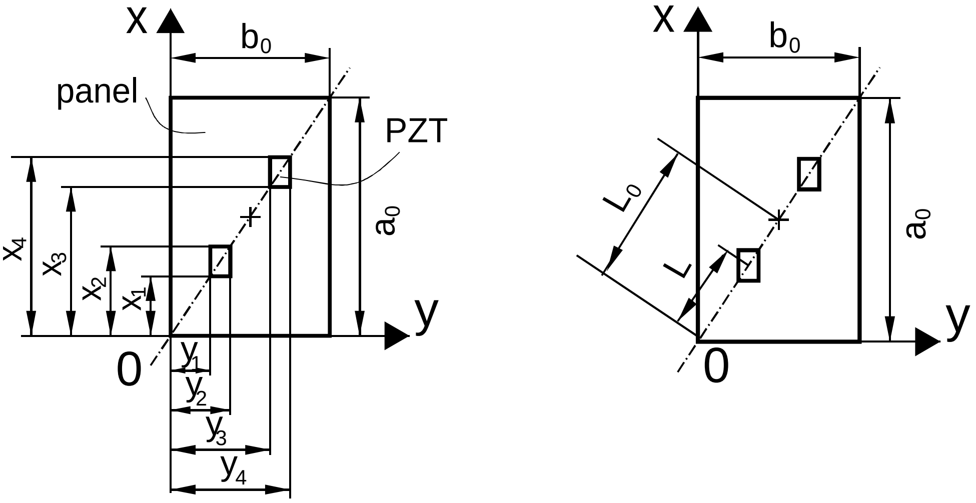

(a) coordinate system of PZT actuators on the panel

(b) path for optimization of location of PZT actuators

Figure 3.19 Top view of the configuration for optimizing locations of actuators

In Figure 3.19 L_0 is the distance between the center and the low left corner of the panel and L is the coordinate of the actuator pairs along the diagonal with an origin at the center of the panel.

The following constraint conditions for the optimization procedure have to be applied to confine the piezoelectric actuator locations inside the panel perimeter, i.e.:

$$x_1 > 0 \text{ and } y_1 > 0 \text{ for \#1 PZT}$$

$$x_4 < a_0 \text{ and } y_4 < b_0 \text{ for \#2 PZT.}$$

There are some other constraint conditions necessary for avoiding overlap between the actuators. However, as the actuators moved in opposite directions from their starting positions as shown in Figure 3.19, these additional constraint conditions are satisfied automatically.

The same frequencies as mentioned before were used to excite the panel at the resonances of the corresponding modes. Variations of the velocity amplitude of the panel as a function of the position of the PZT actuators on the panel are shown in Figure 3.20. The results are as expected, i.e. maximum panel velocities occur when the actuators are located on the anti-node lines and close to the center for odd-odd modes. This makes sense because the panel is more easily excited when the excitation is at the center. It can also be seen that velocity values strongly depend on the locations of the PZT actuators on the panel. For the 1,3 mode, the velocity response of the panel may vary by more than 30 dB depending on the PZT actuator locations. For the 1,1 and 3,3 modes, the variation may be more than this.

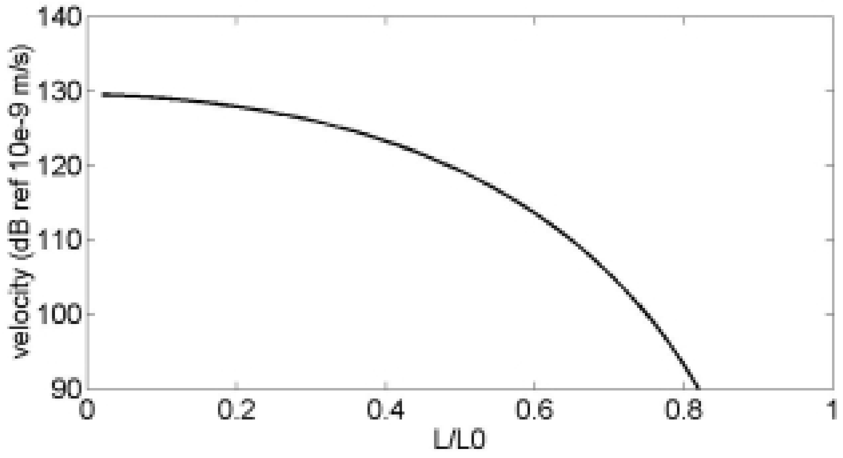

(a) 1,1 mode

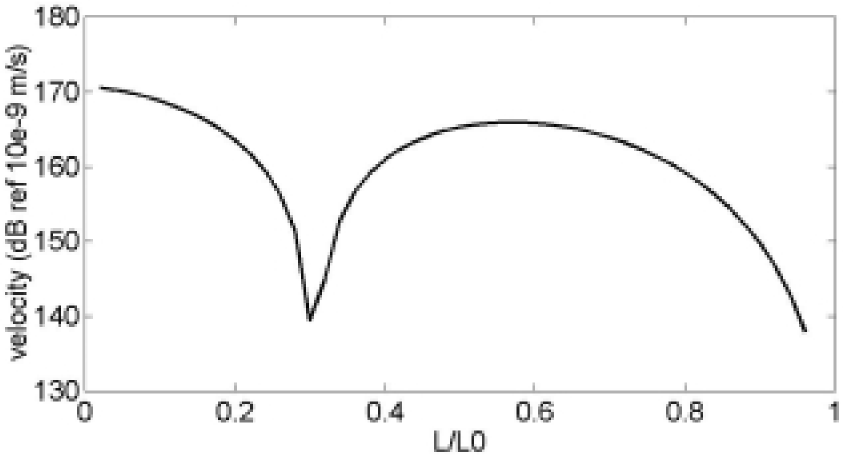

(b) 1,3 mode

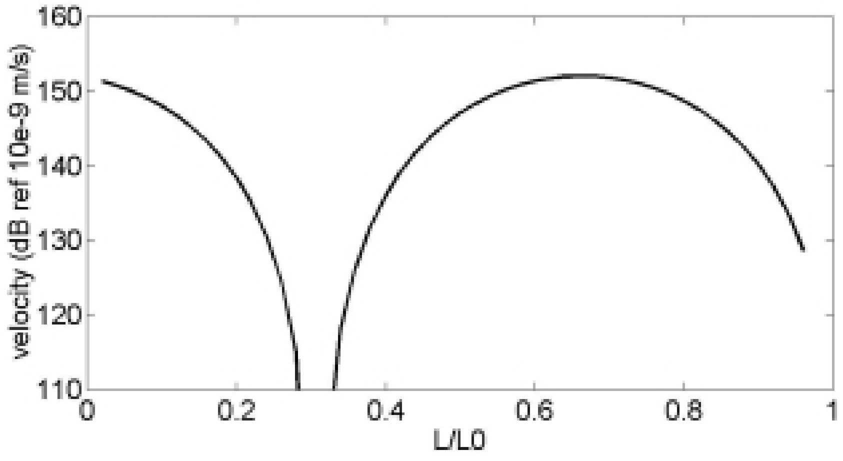

(c) 3,3 mode

Figure 3.20 Variations of the structural response as a function of positions of PZT actuators on the panel for a fixed actuator excitation voltage of 100 V

3.4.3.3 Optimal thickness of piezoelectric actuators

According to previous work (Kim and Jones (1991)), equation (3.27) implies that there is an optimum value of the ratio of the actuator thickness to the shallow shell thickness for generating the maximum bending moment in the structure. Figure 3.21 demonstrates that for the commercially available piezoelectric actuators, this optimum ratio is approximately 0.5 for a steel shallow shell and it is approximately 0.25 for an aluminum shallow shell.

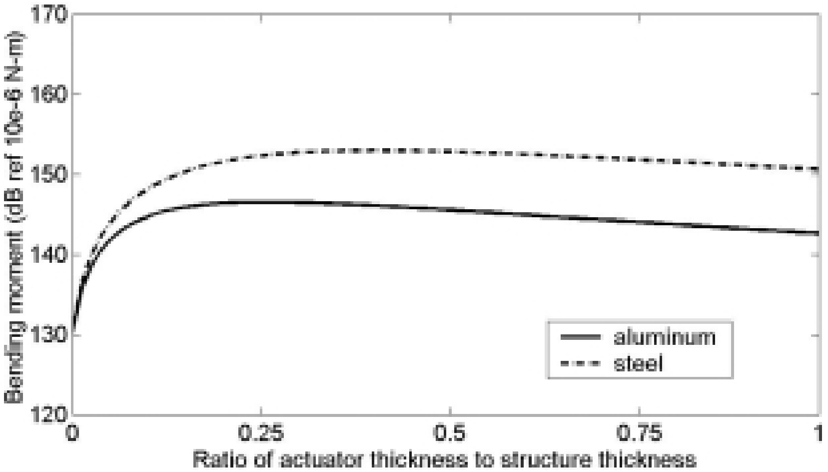

Figure 3.21 Bending moment induced in a structure as a function of the ratio of actuator thickness to shallow shell thickness

From equations (3.26) and (3.27) one can see that, to achieve the optimum bending moments in the curved panel, the required actuator thickness increases as the curved panel thickness increases, resulting in an increase in the required applied voltage as can be deduced from equation (3.26i). In other words, for a thick curved panel, a very high input voltage is required to drive the piezoelectric actuator to achieve the maximum bending moment in the structure, even though the power consumption may be quite low due to the high electrical impedance of the piezoelectric actuator. However, from Figure 3.21 it can be seen that the applied moment is not reduced by much (less than 2 dB) compared with the optimum value by making the actuator thickness around one quarter of the curved panel thickness for the steel structure and one eighth for the aluminum curved panel. For this sub-optimum ratio of the actuator thickness to the structure thickness, the power and voltage requirement can be reduced by half.

3.5 Sound radiation of the curved panel with a backing cavity

In this section the measurement procedures and results for sound radiation of the curved panel sound sources with a backing cavity are given. The 1,1 mode and the 1,3 mode resonance frequencies of the curved panel with a backing cavity were tuned to 100Hz and 200 Hz respectively as described in the previous section and sound radiation at 100 Hz and 200 Hz was measured.

3.5.1 Experimental set-up

The panel was excited by 6 piezoelectric patch actuators (52×26×0.3 mm). Three actuators were attached to each side and driven in phase but out of phase with the actuators on the other side. The actuators were driven by an oscillator which generated a sine wave signal through a transformer and Brüel & Kjær type 2706 power amplifier. An HP 54601A oscilloscope was used to detect the signal. Sound pressure level data were recorded by a Brüel & Kjær type 4177 microphone connected to a Brüel & Kjær type 2144 dual channel real-time frequency analyzer.

3.5.2 Experimental results

Figure 3.22 shows a comparison of the sound pressure level generated by the panel in a direction normal to its front face compared with measurements taken 1 m from an actual substation transformer.

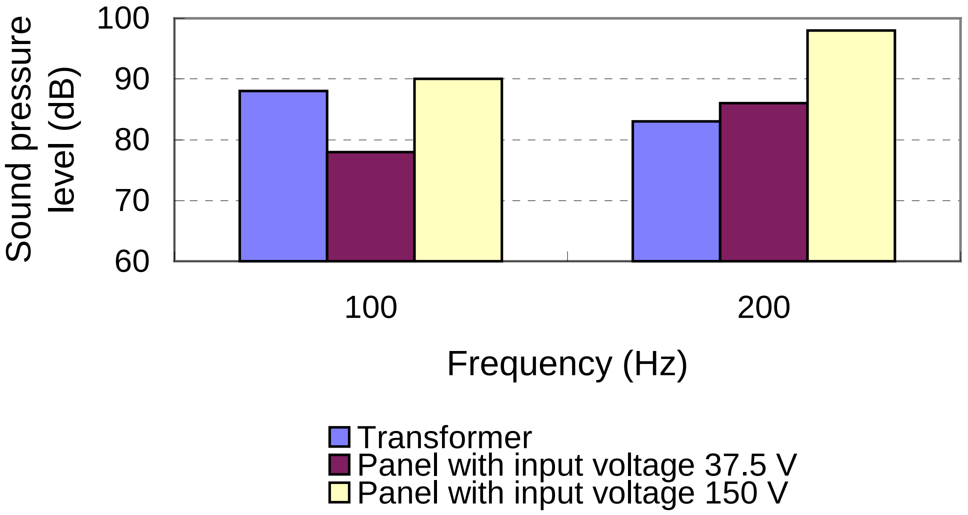

Figure 3.22 Comparison of sound pressure level of the panel-cavity system with a transformer, microphone at 1 m from sound sources, the panel being driven by 6 actuators.

From Figure 3.22, it can be seen that the sound pressure level generated by the panel-cavity system with driven voltage V_p=37.5 V at 200 Hz is higher than that generated by the transformer but the sound pressure level generated by the panel system at 100 Hz is lower than required. However, if it is assumed (as expected) that the sound pressure level generated by the panel-cavity system increases by 6 dB as the input voltage of the actuators is doubled, there is no doubt that the sound radiation levels generated by the panel-cavity system at all frequencies of interest will be higher than those generated by the transformer for an input voltage V_p of 150 V (less than the maximum allowed) as shown in Figure 3.22.

3.6 Conclusions

The work described here has demonstrated that a curved panel with backing cavity sound source could be used as an alternative to a number of loudspeakers for active cancellation of electric power transformer noise. Furthermore, it has been shown here that a single panel may be tuned to resonate at 100 Hz and 200 Hz, thus enabling one source type to control the two dominant noise radiating frequencies of the transformer. As described in section 3.5.2, the sound radiation levels corresponding to 100 Hz and 200 Hz for the panel-cavity system were high enough for noise cancellation for the test transformer. Thus, it may be concluded that the current design curved panel with a backing cavity sound source could replace loudspeakers in a practical active noise cancellation system for electric power transformers.

The effect of piezoelectric actuator size and location on the velocity response of a simply supported curved panel has been quantified for one pair and two pairs of actuators. The results provide a useful guide for optimizing the trade-off between actuator size and panel response. Although the maximum panel response is achieved when the actuator size is half of a structural wavelength, substantial response can also be achieved with much smaller actuators. For the case of optimizing the piezoelectric actuator thickness, a desirable value of the actuator thickness is one quarter of the panel thickness for a steel structure (one eighth of the panel thickness for an aluminum structure). These thicknesses do not correspond to the maximum moment generation; they produce slightly smaller moments but they require half of the driving power and voltage that are required by the actuators of optimum thickness.

CHAPTER 4 VIBRATION CONTROL SOURCES

4.1 Introduction

In the field of active structural acoustic control (ASAC), one of the important considerations is the optimal design and selection of the vibration actuators. Typical vibration actuators include piezoelectric patches, electromagnetic actuators and magnetostrictive actuators. Here the performance of piezoelectric patch type actuators and inertial electrodynamic type actuators are compared for ASAC on a transformer structure. Results demonstrate that a large amplitude output at the frequency of interest can be achieved by the inertial actuators by tuning their resonance frequency, thus allowing them to be effective even on large transformer structures at 100 Hz or 120 Hz as well as at higher frequencies.

4.2 Piezoelectric patch type actuators

Piezoelectricity is the phenomenon in which certain crystalline substances physically deform in the presence of an electric field, or conversely, develop an electric field when subjected to pressure forces. Thus, due to this property, piezoelectric (PZT) materials have been widely used in active structural acoustic control (ASAC) as actuators, particularly for light structures, because they are compact and light-weight. Here the task is to experimentally study the feasibility of using piezoelectric patch actuators to excite a heavy structure, for instance, a transformer tank. Table 4.1 shows the parameters which represent the actuator properties (type P-42 <P$_{(ZT)}$ - F>) in this chapter.

Table 4.1 Piezoelectric actuator specifications

Type	**P-42 <P(ZT) - F>**
Coupling coefficient	$K_{33}=0.68$ $K_{31}=0.34$
Piezoelectric strain coefficient (m/V)	$d_{33}>260\times10^{-12}$ $d_{31}>100\times10^{-12}$
Piezoelectric voltage coefficient (Vm/N)	$g_{33}>24\times10^{-3}$ $g_{31}>11.5\times10^{-3}$
Coercive field[†] (V/m)	400×10^{3}
Density (kg/m)	$>7.5\times10^{3}$
Mechanical Q for a thin disc	>600
Elastic constant (m^2/N)	$S^{E}_{11}=12\times10^{-12}$
Curie temperature (°C)	> 320
Loss factor	$\tan\delta<0.04$

4.3 Inertial shaker

An inertial shaker is constructed of a housing, a moveable mass which consists of a permanent magnet and a core, flexible diaphragms as springs and a fixed coil, as shown in Figure 4.1.

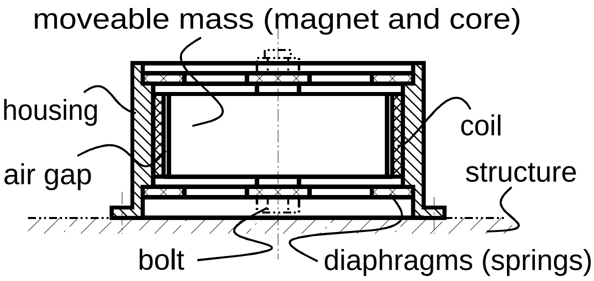

Figure 4.1 Inertial shaker

[†] Coercive field is the maximum anti-poling field a piece can withstand without experiencing depolarization.

The mass is supported on two diaphragms which are fixed to the housing. Each diaphragm is bolted to each side of the mass. When a sinusoidal voltage is applied to the coil that is fixed to the housing, the polarity and strength of the coil magnetic field changes in phase with the applied voltage, thus producing a force of attraction between the permanent magnet and the coil, resulting in axial movement of the mass. The spring force resulting from the displacement of the mass produces an axial force on the housing of the unit which is transmitted through the mounting interface to the structure.

Specifications of the low cost inertial shaker chosen for testing are shown in Table 4.2 (Cazzolato (1999)).

Table 4.2 Inertial actuator specifications

Impedance (Ω)	3.8
Maximum input voltage (Vrms)	8.3
Resonance frequency (Hz)	44.5
Quality factor	13
Total mass (kg)	0.64
Dynamic mass (kg)	0.4
Overall diameter (mm)	120
Inner mass diameter (mm)	80
Height (mm)	30
Cost	$12 AUD
Manufacturer	Aura System Inc

The unloaded frequency response of the unit at room temperature was measured by mounting the shaker through the housing to a heavy block (>50 kg) as shown in Figure 4.2.

Figure 4.2 A photograph of the test shaker mounted on a 50 kg mass

The response of the movable mass was recorded using a Brüel & Kjær type 4394 accelerometer connected to a Brüel & Kjær type 2816 data acquisition unit via a Brüel & Kjær type 2635 charge amplifier. The shaker was driven by a Brüel & Kjær type 3107 generator via a power amplifier. The force sensitivity was calculated by multiplying the acceleration sensitivity by the dynamic mass which is shown in Table 4.2. Figure 4.3 shows the unloaded frequency responses of the unit.

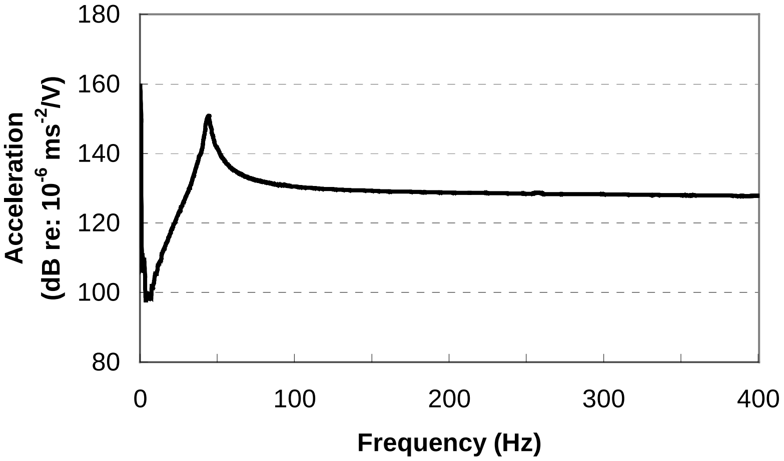

(a) acceleration of moving mass vs excitation frequency

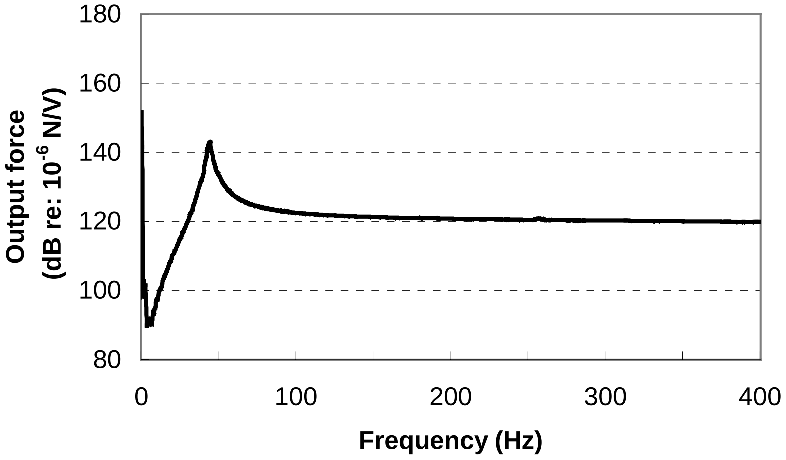

(b) force output vs excitation frequency

Figure 4.3 Frequency response of the inertial shaker for an input voltage of 1 Vrms

4.4 Tuning the resonance frequency of the inertial shaker

One of the advantages of using the inertial shakers is that the resonance frequency of the unit is tunable so that the mechanical output of the unit at the frequency of interest may be maximized. In general, the resonance frequency of a unit can be tuned by modification of the spring stiffness or modification of the mass of the moveable element. But as far as increasing the resonance frequency is concerned, modification of the spring stiffness is easier than modification of the moveable mass, so the former modification is undertaken for the shakers discussed here. A major assumption was that the shaker could be modeled as a spring-mass system, which is shown in Figure 4.4. The effective spring stiffness for such system can be increased either by increasing the actual spring stiffness or by modifying the configuration of the spring, i.e. adding a spring in parallel with the original spring.

4.4.1 Modification of the spring arrangement

The resonance frequency of the spring-mass system shown in Figure 4.4 is expressed as:

$$f = \frac{1}{2\pi}\left(\frac{k}{m}\right)^{\frac{1}{2}} \tag{4.1}$$

where: k is the stiffness of the spring and m is the mass of the moveable unit.

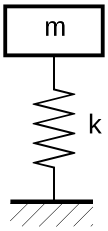

Figure 4.4 Spring-mass system

The resonance frequency of a unit with two springs in parallel, as shown in Figure 4.5 is given as follows:

$$f = \frac{1}{2\pi}\left(\frac{k_1 + k_2}{m}\right)^{\frac{1}{2}}. \tag{4.2}$$

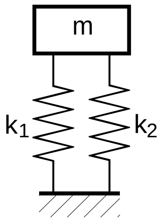

Figure 4.5 Two springs in parallel

For a diaphragm spring, the stiffness is proportional to the cube of the diaphragm thickness (Soedel (1993)), i.e. $k \propto h^3$, so equation (4.2) can be rewritten as:

$$f = f_1\left(1 + \left(\frac{h_2}{h_1}\right)^3\right)^{\frac{1}{2}} \tag{4.3}$$

where f_1 is the resonance frequency of the unit associated with spring 1 only, and h_1, h_2 are the thicknesses of diaphragms 1 and 2 respectively. The required diaphragm thickness corresponding to a resonance frequency f can be estimated using the following equation:

$$h_2 = h_1\left(\left(\frac{f}{f_1}\right)^2 - 1\right)^{\frac{1}{3}} \tag{4.4}$$

In order to verify equation (4.3), two additional diaphragms were clamped to the housing of the unit (one on each side of the mass) for producing the configuration represented by Figure 4.5. The thickness of the additional diaphragm was the same as the original one. Figure 4.6 shows the frequency responses of the shaker with its original diaphragms and with the additional new diaphragms. It can be seen that the resonance frequency has increased from about 44.5 to 62 Hz. From equation (4.3), one would expect the resonance frequency of the unit to increase by $\sqrt{2}$, i.e. to 63 Hz which is close to that measured.

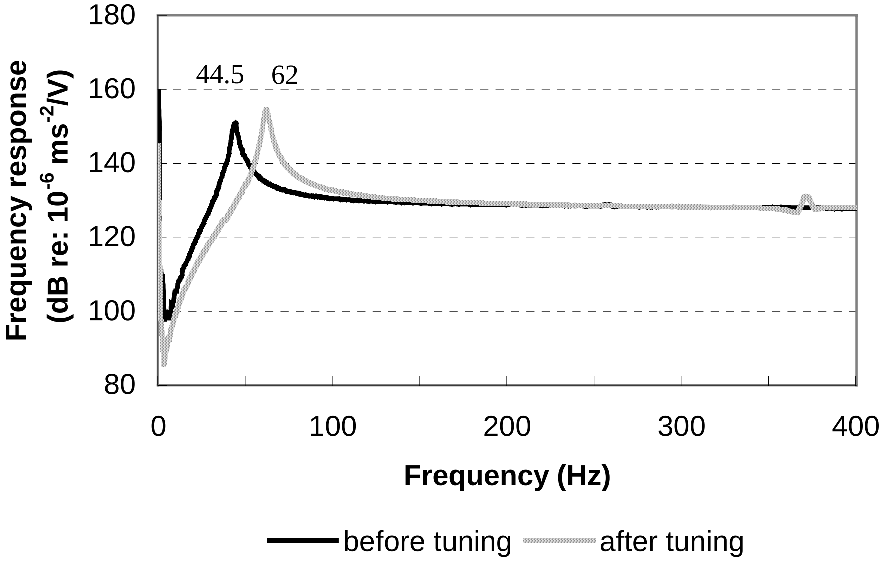

Figure 4.6 Frequency response of the inertial shaker before and after adding two additional diaphragms

4.4.2 Modification of the thickness of the diaphragm

For a diaphragm spring, the stiffness is proportional to the cube of the thickness, i.e.:

$$k \propto h^3 \tag{4.5}$$

Substituting equation (4.1) into (4.5) gives:

$$f \propto h^{\frac{3}{2}} \tag{4.6}$$

The resonance frequency of a shaker after modifying the thickness of the diaphragm can be expressed as:

$$f = f_0 \left(\frac{h}{h_0} \right)^{\frac{3}{2}} \tag{4.7}$$

where f_0 is the resonance frequency of the original unit associated with the diaphragm thickness of h_0; $h = h_0 + \Delta h$; Δh is the required additional thickness that can be calculated by:

$$\mathit{\Delta} h = h_0 \left(\left(\frac{f}{f_0} \right)^{\frac{2}{3}} - 1 \right) \tag{4.8}$$

In order to verify equation (4.7), the original diaphragm thickness of h=1.6 mm was replaced by a diaphragm with a thickness of h=2.4 mm. The predicted value of the resonance frequency was 81.8 Hz for the modified diaphragm thickness. The reason for choosing this diaphragm thickness was simply to verify equation (4.7), rather than optimize the thickness for the transformer application. The acceleration of the unit was measured while the shaker was mounted on a mass of 50 kg. The results are shown in Figure 4.7, where it can be seen that the resonance frequency of the shaker increases from 44.5 Hz to 84 Hz (as the diaphragm thickness is increased) which is close to that predicted.

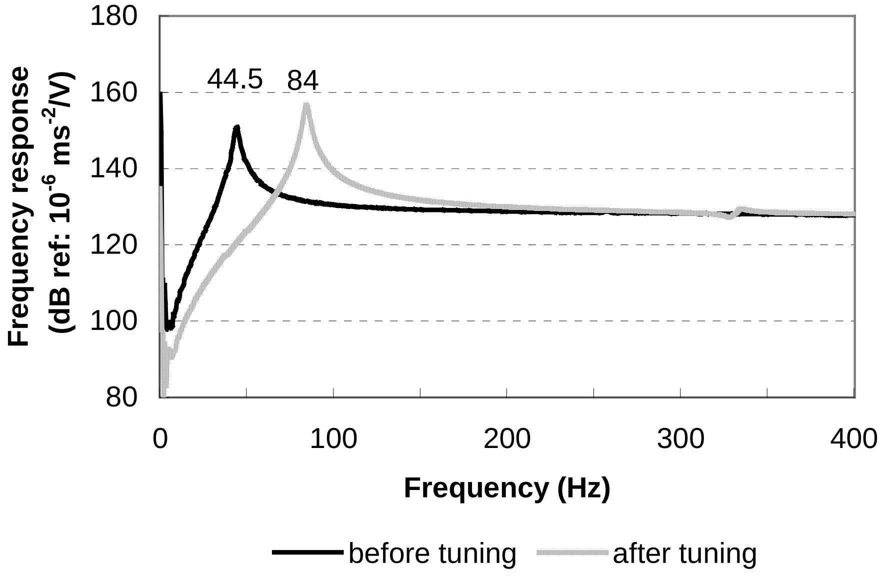

Figure 4.7 Frequency response of the inertial shaker before and after modifying the diaphragm thickness

4.4.3 Effect of the temperature on the resonance frequency of the shaker

The stiffness of a fiber glass diaphragm changes with temperature and this directly affects the resonance frequency of the shaker. Thus, the influence of the temperature of the shaker on the resonance frequency of the unit was tested. The shaker was driven continuously at 50 Hz with a maximum input voltage of 8.3 V_{rms} (Cazzolato (1999)) and the temperature of the shaker was monitored. After running for 19 hours, the temperature of the shaker peaked at approximately 48 C in an ambient temperature environment of approximately 22 C. Ambient temperatures of 42 C are typical for a South Australian summer and could result in the shaker reaching temperatures of up to 68 C. Therefore, it was necessary to investigate the behaviour of the shaker at a high temperature, representative of typically hot Australian summer.

Figure 4.8 shows the frequency response of the shaker for a range of temperatures of the shaker housing. Here, the shaker was driven using the same testing procedure that was described in Section 4.3, except that the input voltage was 12 V_{rms}. The reason for choosing an over loaded input voltage was so that a higher shaker temperature could be reached at a room temperature of approximately 22 C. In the figure, the values in the legend show the temperature in degrees Celsius.

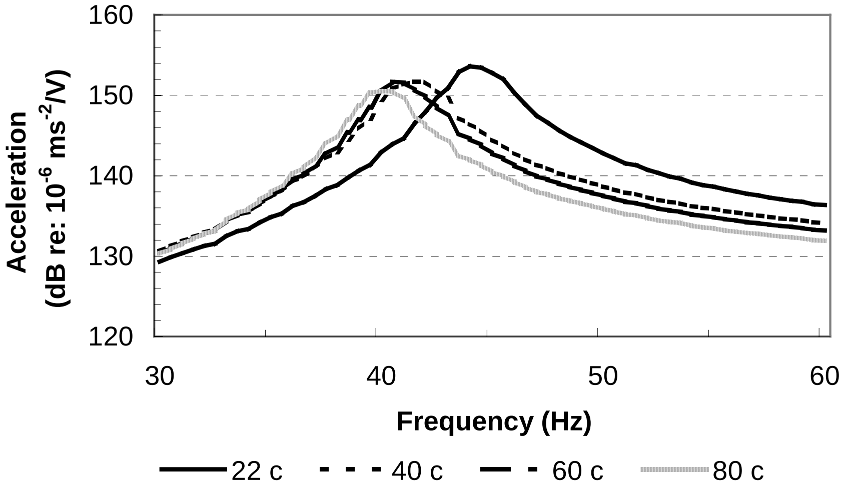

Figure 4.8 Influence of the temperature of the shaker on the resonance frequency (after Cordioli 1999).

From Figure 4.8 it can be seen that the resonance frequency of the shaker decreases as the temperature of the shaker increases. This is because the diaphragm becomes softer as the temperature increases and so the stiffness of the diaphragm (the spring element) decreases. Thus, the resonance frequency of the shaker reduced to 39 Hz when the temperature was 80 C from 44.5 Hz when at 22 C. This was a change in resonance frequency of 5.5 Hz (approximately 12%). Thus, it is suggested that the resonance frequency of the shaker at room temperature, after tuning, should be approximately 15% higher than the frequency of interest, so that the shaker operating frequency can still be near to its resonance frequency when it is operated at a higher temperature.

4.5 Comparison of the vibration performance of the inertial shaker with the piezoelectric patch type actuator

4.5.1 Experimental set-up

To compare the vibration performance of the inertial shakers with the piezoelectric patch type (PZT) actuators in terms of the vibration amplitude that could be generated on the structures, the mechanical vibration generated by the PZT actuators and the inertial shakers on a flat panel and a transformer tank were measured respectively. The general experimental set-up for both measurements is shown in Figure 4.9.

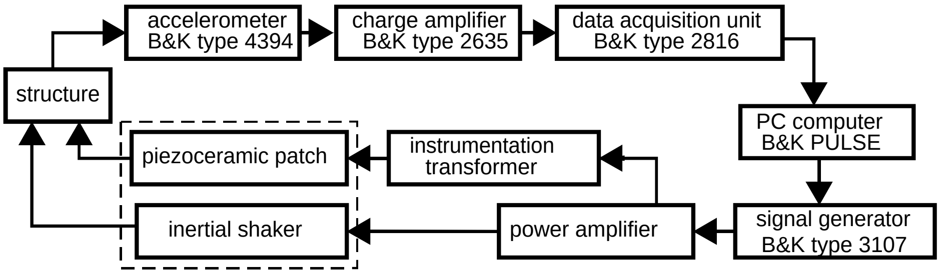

Figure 4.9 Block diagram of the experimental set-up

For measuring the vibration amplitude, a Brüel & Kjær type 4394 accelerometer was connected through a Brüel & Kjær type 2635 charge amplifier to a Brüel & Kjær type 2816 data acquisition unit with a Brüel & Kjær type 3022 4-channel input module (not shown in Figure 4.9). Data were transferred into a PC in which Brüel & Kjær PULSE LabShop V. 4.1 was installed. Both types of actuators were driven by a Brüel & Kjær type 3107 generator module which generated the signals through a power amplifier. To amplify the signals for the piezoelectric patch type actuator an additional instrumentation transformer was used in series with the power amplifier.

4.5.2 Results

4.5.2.1 Evaluation of vibration on a panel

To evaluate the vibration performance generated by both types of actuators on the flat panel, the actuators were mounted on a steel panel (872×788×8 mm), supported at 4 corners). A PZT actuator with a diameter of 70 mm and a thickness of 2 mm was bonded on to the panel using epoxy adhesive. A metal ring was stuck on the panel around the PZT actuator for supporting the shakers. Both actuators were driven by the Brüel & Kjær type 3107 generator module, which generated a random noise, at half their rated maximum voltages. The resulting vibration levels were measured at various locations on the panel as shown in Figure 4.10. Actuator mechanical properties are listed in Table 4.3.

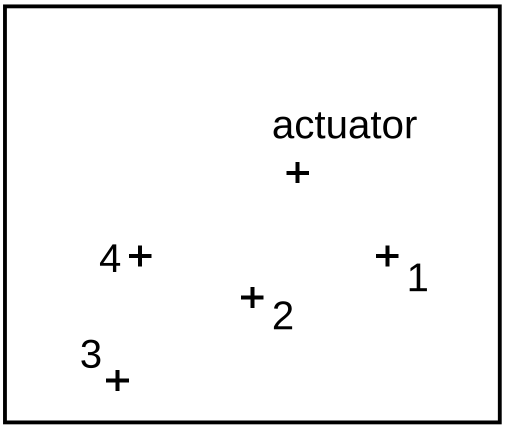

Figure 4.10 Locations of the accelerometers and actuator on the panel

Table 4.3 Mechanical properties of the piezoelectric patch actuator

Young’s modulus (GPa)	63
Poisson’s ratio	0.35
Diameter (mm)	75
Thickness (mm)	2

According to the results shown in Figure 3.21, the piezoelectric patch thickness listed in Table 4.3 is not optimum. However, the reduction in the excitation force available to excite the panel as a result of the sub-optimal thickness of the actuators is less than 2 dB. Also as discussed in Chapter 3, the vibration level generated by a piezoelectric actuator on a structure will increase as the diameter of the actuator disc increases. But the diameter presented corresponding to the thickness of 2 mm in the table is the maximum that can be manufactured easily. This configuration represents a practical case of what could be used on a large transformer tank. The maximum allowed input voltage to the piezoelectric patch is 800 V_{p-p}. Figure 4.11 shows a comparison between vibration levels of the panel excited by an inertial shaker with a resonance frequency of 44.5 Hz and a piezoelectric actuator at the position shown in Figure 4.10.

From Figure 4.11 it can be seen that the inertial shaker always produced higher panel vibration levels throughout the test frequency band even though there were no great differences at frequencies greater than 300 Hz. Around the shaker untuned resonance frequency of 44.5 Hz, vibration levels excited by the inertial shaker were about 30 dB higher than those excited by the piezoelectric actuator.

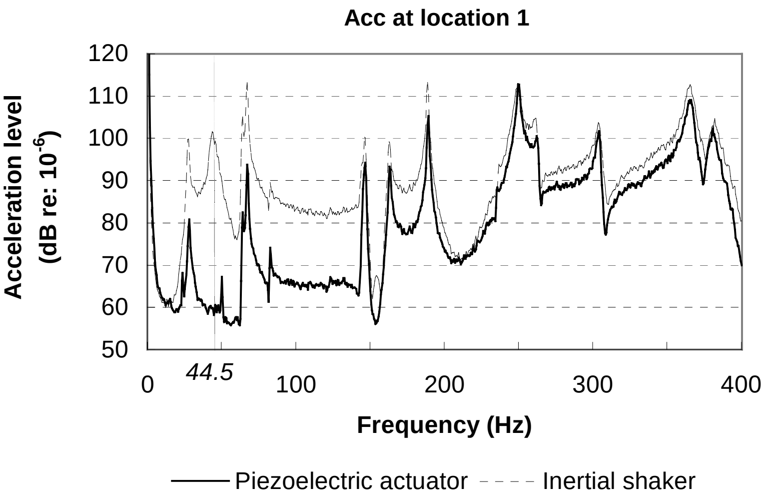

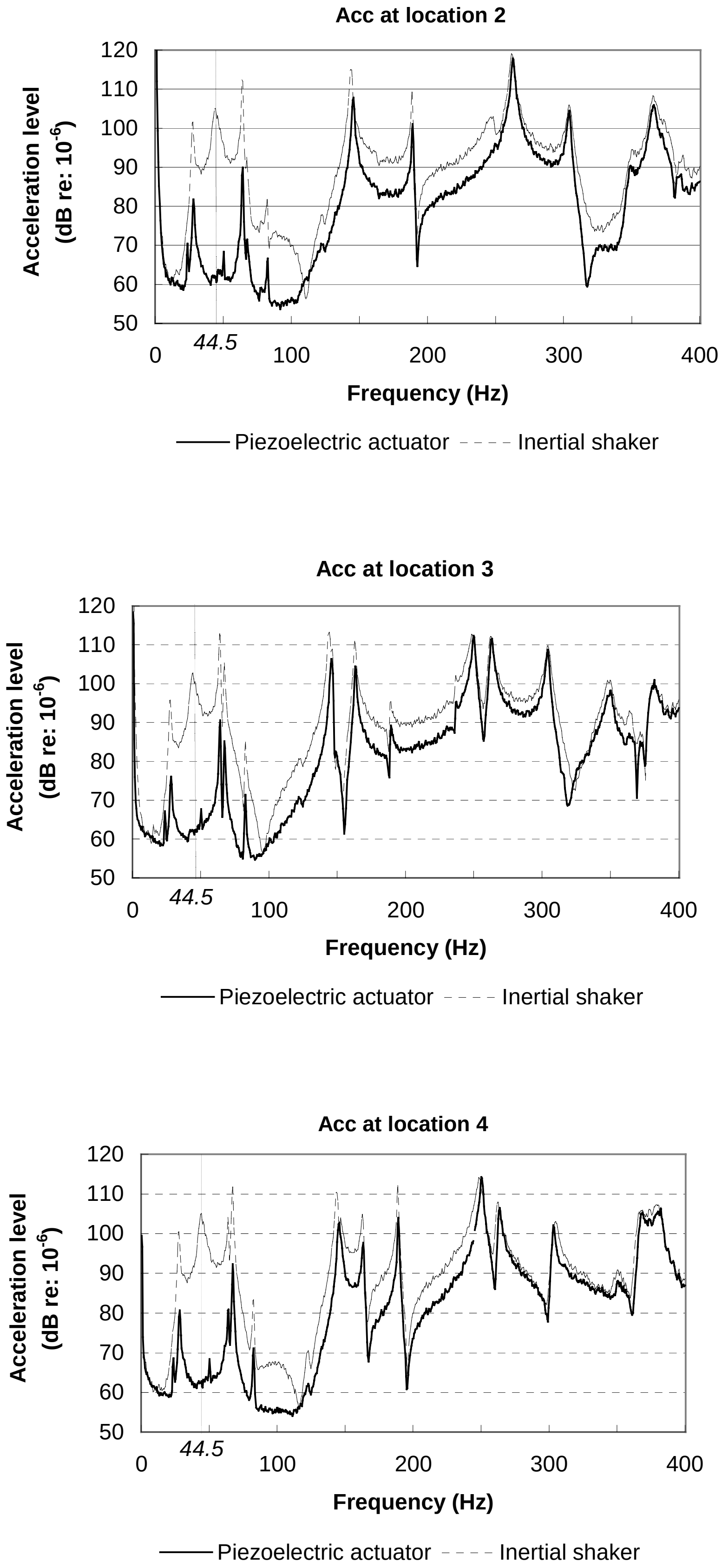

Figure 4.11 Comparison of the acceleration levels of the panel excited by the inertial shaker and the piezoelectric actuator at half the rated input. (the resonance frequency of the shaker is 44.5 Hz).

To evaluate the vibration levels excited by a tuned inertial shaker, a shaker tuned to a resonance frequency of 84 Hz was tested. Vibration levels are shown in Figure 4.12. From the following figures it is obvious that vibration levels throughout the test frequency band have increased, particularly around the resonance frequency of 84 Hz, where the inertial shaker produced approximately 40 dB higher vibration levels in the panel than the piezoelectric actuator did.

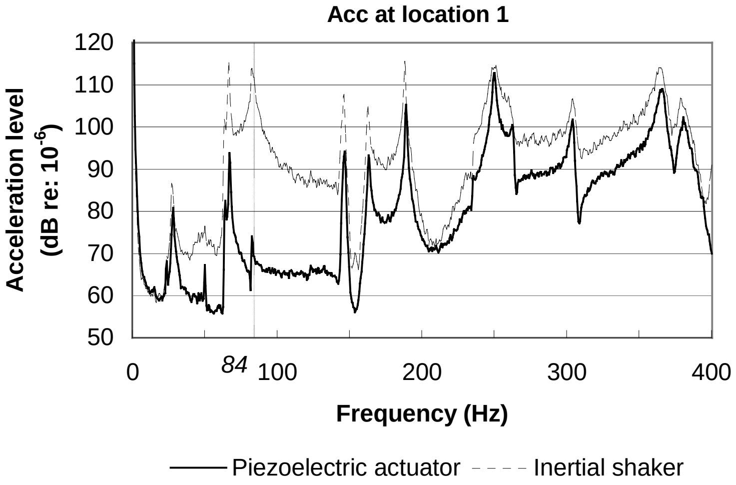

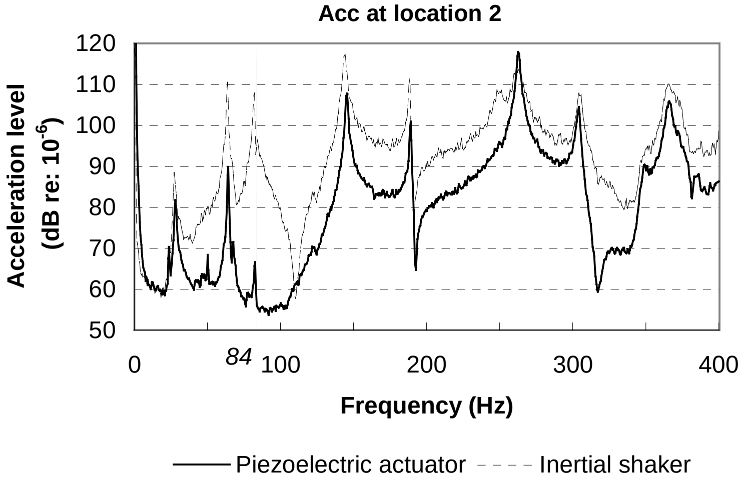

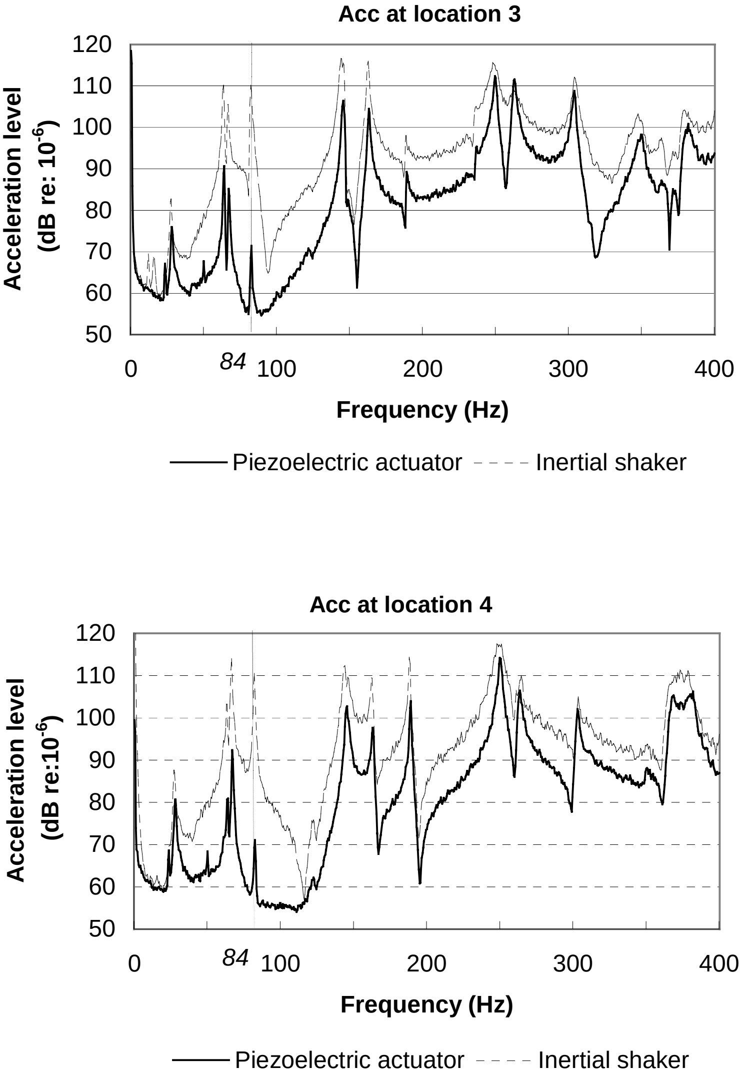

Figure 4.12 Comparison of the acceleration levels of the panel excited by the inertial shaker and the piezoelectric actuator is half the rated input, (the resonance frequency of the shaker is 84 Hz).

4.5.2.2 Evaluation of vibration on a transformer tank

To compare the vibration levels generated by the inertial shakers with that generated by the piezoelectric actuator on the transformer tank, a small transformer tank as shown in Figure 4.13 was individually excited by both actuators at 100 Hz, 200 Hz and 300 Hz, which are the fundamental frequency and two harmonic frequencies of transformer noise, respectively. The experimental set-up is shown in Figure 4.9.

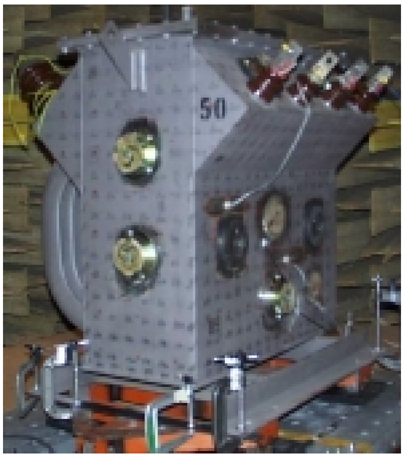

Figure 4.13 A photograph of a small transformer

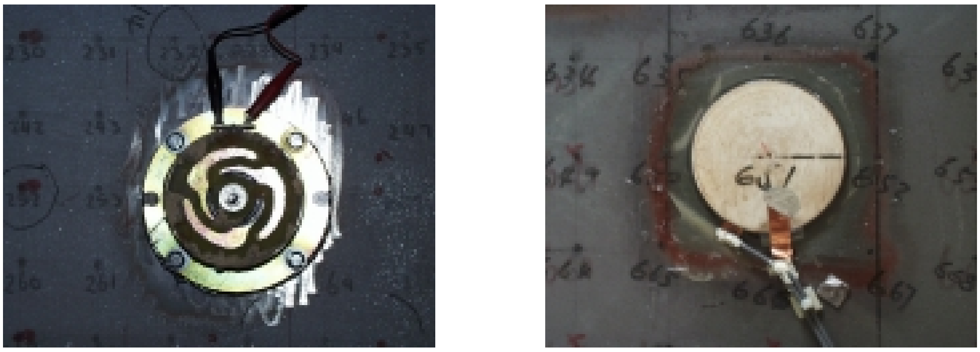

(a) an inertial actuator

(b) a piezoelectric patch actuator

Figure 4.14 Vibration control sources

To increase the output of the shakers as shown in Figure 4.14(a) at frequencies of interest, resonance frequencies of three inertial actuators were tuned at 114 Hz, 215 Hz and 312 Hz respectively at room temperature corresponding to 100 Hz, 200 Hz and 300 Hz excitation respectively. The reason that the tuned resonance frequencies of the shakers were selected to be higher than the operating values was addressed in Section 4.4.3. The unloaded frequency response of the shakers at room temperature was measured following the procedure shown in Figure 4.2. The frequency responses are shown in Figure 4.15.

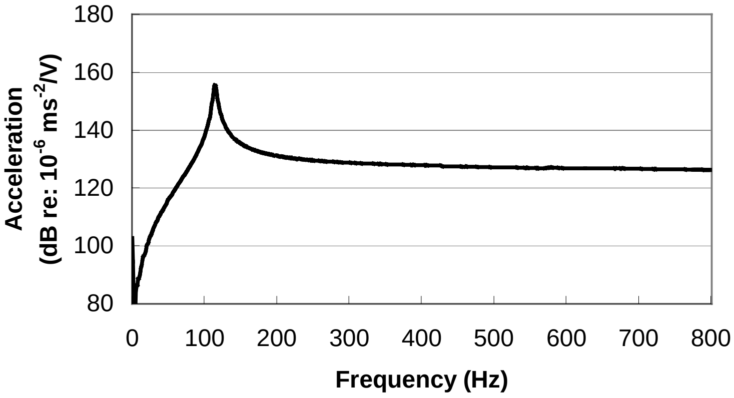

(a) A shaker resonance at 114 Hz

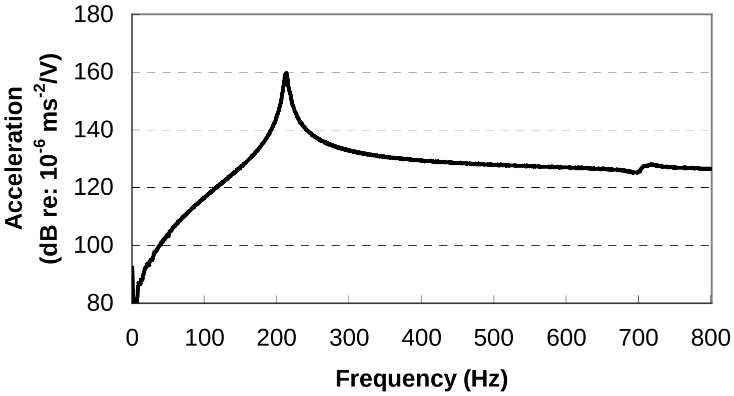

(b) A shaker resonance at 215 Hz

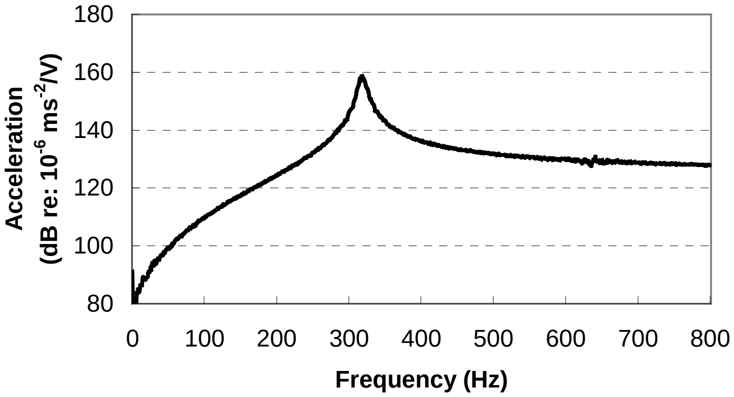

(c) A shaker resonance at 312 Hz

Figure 4.15 Frequency response of inertial shakers

Dimensions of the piezoelectric actuator shown in Figure 4.14(b) are a diameter of 76 mm and a thickness of 3.5 mm, and the material properties of the actuator are shown in Table 4.2. The structural responses (acceleration) were measured at 3 locations as shown in Figure 4.16.

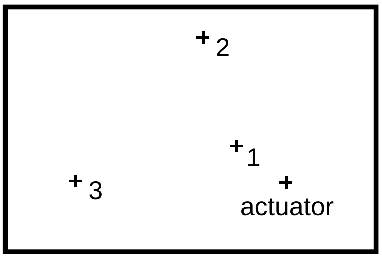

Figure 4.16 Locations of the accelerometers and actuator on the transformer wall

The comparisons of the acceleration levels excited by both inertial and piezoelectric actuators in the transformer structure at 100 Hz, 200 Hz and 300 Hz are shown in Figure 4.17. It can be seen that the vibration levels in the transformer tank, generated by the inertial shaker, are much higher than those generated by the piezoelectric actuator, especially at 100 Hz where the vibration level produced by the inertial shaker is approximately 36 dB higher than that produced by the piezoelectric actuator.

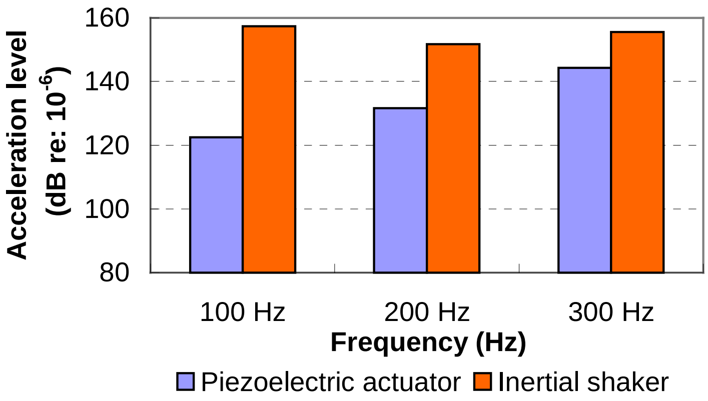

(a) Acc at location 1

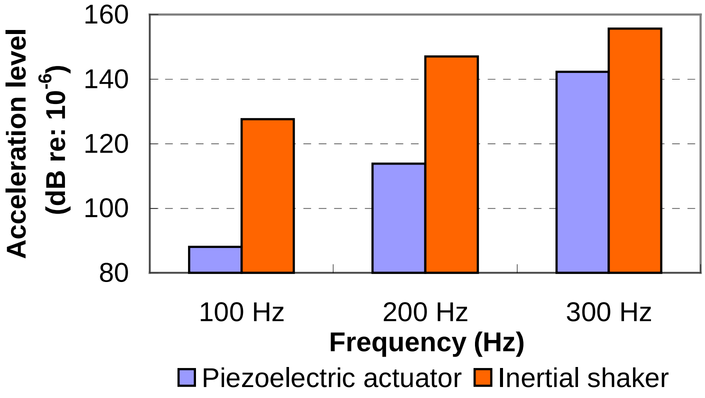

(b) Acc at location 2

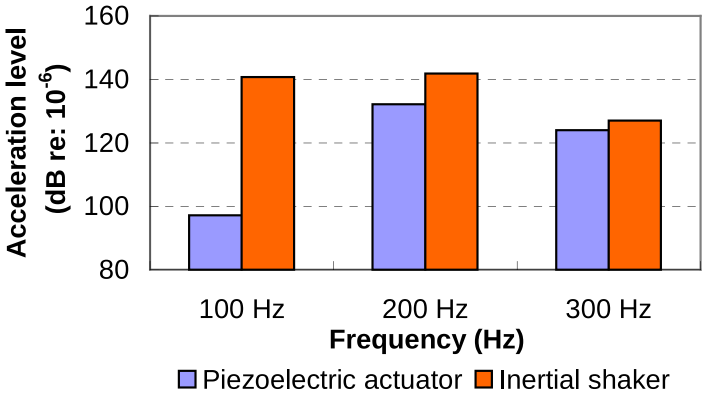

(c) Acc at location 3

Figure 4.17 Comparison of the acceleration levels of the transformer excited by the inertial shakers and the piezoelectric actuator at half the rated maximum voltages of the actuators.

4.5.3 Harmonic distortion in actuators

Linearity (or absence of harmonic distortion) is an important property of ideal control actuators. Thus the total harmonic distortion (THD) was measured at several input voltages for the piezoelectric actuator and the inertial shakers, that were used in section 4.5.2.2. The actuators were mounted on the transformer tank (as shown in Figure 4.16) and twenty harmonics were included in the THD calculation. The rated maximum voltages were 8.3 V_{rms} and 495 V_{rms} for the inertial shakers and piezoelectric actuator respectively. The total harmonic distortions measured at several voltages for both actuators are shown in Tables 4.4-4.7.

Table 4.4 Total harmonic distortion (%) for the PZT actuator

Driving frequency	100 V_{rms}	200 V_{rms}	300 V_{rms}	400 V_{rms}
100 Hz	2.6	3.0	3.2	5.5
200 Hz	1.5	1.7	1.9	2.1
300 Hz	6.0	6.9	8.0	9.3

Table 4.5 Total harmonic distortion (%) for the inertial shaker tuned to 100 Hz

Driving frequency	2.1 V_{rms}	4.2 V_{rms}	6.3 V_{rms}	8.4 V_{rms}
100 Hz	3.0	4.5	6.2	7.7

Table 4.6 Total harmonic distortion (%) for the inertial shaker tuned to 200 Hz

Driving frequency	2.1 V_{rms}	4.2 V_{rms}	6.3 V_{rms}	8.4 V_{rms}
200 Hz	1.2	2.2	3.3	4.0

Table 4.7 Total harmonic distortion (%) for the inertial shaker tuned to 300 Hz

Driving frequency	2.1 V_{rms}	4.2 V_{rms}	6.3 V_{rms}	8.4 V_{rms}
300 Hz	0.5	0.36	1.4	5.2

When comparing the results in Tables 4.4 - 4.7 respectively, it can be seen that the harmonic distortion of the shakers is higher than that of the PZT actuators, except for the 300 Hz example. For example, at 100 Hz and at around half the rated maximum voltages (4.2 V_{rms} for the inertial shaker and between the 200 and 300 V_{rms} for the PZT actuators), the total harmonic distortion in the inertial shaker was approximately 1.5% higher than that in the PZT actuator. However, as shown in Figure 4.17, at 100 Hz the inertial shaker can produce approximately 36 dB more vibration than the piezoelectric actuator, at half the rated maximum voltages. On the other hand, when the piezoelectric actuator was driven at the maximum rated voltage (i.e. doubled), only a further 6 dB of vibration level can be generated. However, the harmonic distortion produced by the piezoelectric actuator at the maximum voltage is higher than that produced by the inertial shaker at the half maximum voltage, as shown in Tables 4.3 and 4.4. Consequently, when the harmonic distortion is the same, higher vibration levels can be produced when using the tuned inertial shaker than when using the piezoelectric actuator.

4.6 Conclusions

A comparison has been made between the performance of low cost inertial shakers and piezoelectric patch actuators in terms of their effectiveness in exciting a steel panel and an electrical transformer tank respectively. Results show that the inertial shakers are more effective and their effectiveness can be further increased by a simple tuning procedure that allows the shaker resonance to be aligned with the excitation frequency. Different shakers can be tuned to different frequencies so a range of frequencies may be covered. This is particularly beneficial for active control of noise radiated by large power transformers at the fundamental frequency of 100 or 120 Hz, because piezoelectric actuators cannot generate sufficient vibration levels at this frequency due to the much greater dynamic stiffness of the transformer tank than at higher frequencies.

CHAPTER 5 SENSING STRATEGIES FOR THE ACTIVE NOISE CONTROL IN THE NEAR-FIELD

5.1 Introduction

In this chapter, two near-field error sensing strategies are evaluated. They are the minimization of the sum of the sound intensities[+] and the minimization of the sum of the squared sound pressures. A quadratic expression is derived for the minimization of the sum of the sound intensities in the near-field. The derivation is based on a two-microphone technique, and the formulation is expressed in terms of the transfer functions from the control inputs to the error sensor outputs, and the primary sound field. This has practical advantages because all data required to evaluate the analytical expressions are contained in the measurements and no physical controller is necessary to determine the degree of control that is possible for the experimental situation.

To evaluate the near-field sensing strategies by numerical simulation, a flat panel with a rigid baffle is modeled as a primary source with a point force disturbance and 4 point force control sources. The control performance achieved using both near-field sensing strategies is evaluated in the far-field.

[+] Previous research has studied the minimization of the sum of the squared sound intensities. Here however, the cost function to be minimized is in a non-quadratic form so that multiple minima may be found. In other words, one must be able to determine whether the result is a local or global minimum. Therefore, in this project, minimizing the sum of the squared sound intensities won’t be considered.

5.2 Minimization of the sum of the sound intensities in the near-field

5.2.1 Derivation of the theoretical model

The sound power, W, radiated from a structure can be expressed as:

$$W = \int_S I dS \tag{5.1}$$

where S is the area of the structure; I is the time-averaged sound intensity, which can be written as:

$$I = \frac{1}{2}\mathbf{Re}\left\{\boldsymbol{p}(\mathbf{r})\boldsymbol{u}^*(\mathbf{r})\right\} \tag{5.2}$$

where $\boldsymbol{u}(\mathbf{r})$ and $\boldsymbol{p}(\mathbf{r})$ are the complex particle velocity at the error sensing location and the complex pressure at the error sensing location, $\mathbf{r}$, respectively; $*$ indicates the complex conjugate and **Re** indicates the real part of a complex quantity.

For calculating the radiated sound power, the surface integral in equation (5.1) may be replaced by the sum of products of the sound intensities and associated areas at discrete sensing locations:

$$W = \sum_{\boldsymbol{i}=1}^{\boldsymbol{n}} I_i \Delta S_i \tag{5.3}$$

Note that the quantity n in the above equation should be sufficiently large for an acceptably small error. In equation (5.3) an assumption is made that the elemental area ΔS_i is constant so that the subscript can be dropped and equation (5.3) may be rewritten as:

$$W = \Delta S \sum_{i=1}^{\boldsymbol{n}} I_i \tag{5.4}$$

Thus the minimization of the sum of the sound intensities at a finite number of error sensing locations implies the minimization of the sound power provided that a sufficient number of points is used. The error criterion J_I, which is the sum of the sound intensities at a set of discrete error sensing locations, can be written in matrix form as:

$$J_I = \frac{1}{2}\mathbf{Re}\left\{\boldsymbol{P}^{\mathrm{T}}(\mathbf{r})\boldsymbol{U}^{*}(\mathbf{r})\right\} \tag{5.5}$$

where $\boldsymbol{U}(\mathbf{r})$ is the $(N_e \times 1)$ vector of particle velocities at a set of error sensing locations, $[\boldsymbol{u}(\mathbf{r}_1), \boldsymbol{u}(\mathbf{r}_2), \cdots\cdots, \boldsymbol{u}(\mathbf{r}_{N_e})]^{\boldsymbol{T}}$; $\boldsymbol{P}(\mathbf{r})$ is the $(N_e \times 1)$ vector of complex sound pressures radiated by a source to the error sensing locations, $[\boldsymbol{p}(\mathbf{r}_1), \boldsymbol{p}(\mathbf{r}_2), \cdots\cdots, \boldsymbol{p}(\mathbf{r}_{N_e})]^{\boldsymbol{T}}$. **T** is the transpose of the matrix and N_e is the number of error sensors.

For calculating the sound intensity, the two-microphone technique reported by several researchers (Kristiansen (1981); Krishnappa and McDougall (1989); Fahy (1995)) was employed. In this case, the sound pressure midway between two closely spaced sensing points for a tonal sound can be approximately expressed:

$$\boldsymbol{P}_{12} \approx \frac{\boldsymbol{P}_1 + \boldsymbol{P}_2}{2} \tag{5.6}$$

and the particle velocity is:

$$\boldsymbol{U}_{d_{12}} \approx \frac{-\left(\boldsymbol{P}_2 - \boldsymbol{P}_1\right)}{\mathbf{j}\rho_a \omega d_{12}} \tag{5.7}$$

where ρ_a is density of the acoustic medium; ω is the circular frequency of excitation; d_{12} is the distance between two microphone acoustic centers in the acoustic intensity probe and **j**=$\sqrt{-1}$.

The arrangement for the calculation of the sound intensity using the two-microphone technique is shown in Figure 5.1,

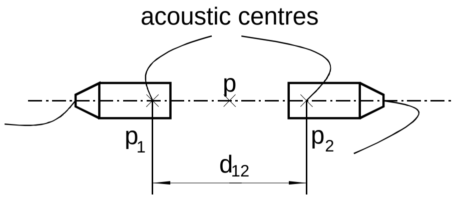

Figure 5.1 Sound intensity probe set up

Thus, for tonal noise, the sum of the sound intensities at point p can be expressed approximately in terms of the sound pressures at points p_1 and p_2.

Substituting equations (5.6) and (5.7) into (5.5) gives:

$$J_I = \frac{-1}{4\rho_a \omega d_{12}} \mathbf{Re}\left\{(\boldsymbol{P}_2 + \boldsymbol{P}_1)^{\mathrm{T}} (\boldsymbol{P}_2 - \boldsymbol{P}_1)^* \ \mathbf{j}\right\} \tag{5.8}$$

and rearranging the equation gives:

$$J_I = \frac{1}{4\rho_a \omega d_{12}} \mathbf{Im}\left\{\boldsymbol{P}_1^{\mathrm{T}} \boldsymbol{P}_2^* - \boldsymbol{P}_2^{\mathrm{T}} \boldsymbol{P}_1^*\right\} \tag{5.9}$$

It is obvious that a systematic error is introduced due to the approximations inherent in equations (5.6) and (5.7). However, one of the advantages of the two-microphone technique when control of tonal noise is the objective is that the cost of the sound intensity probe which can be constructed using two electret microphones is very low. This is because the phase and amplitude of the frequency response of each of the two microphones does not have to be matched. They can be calibrated for each tonal frequency and provided that the response is stable with time and with temperature variations, any differences can be accounted for in the controller software. This practical advantage makes it possible to minimize sound radiation by the minimization of the sum of the sound intensities in an actual control system. A complete error analysis of the inaccuracies associated with estimating sound intensity using the two-microphone technique is discussed elsewhere(Fahy (1995)).

Sound pressures, $\boldsymbol{P}_1 = \boldsymbol{P}_{1\mathbf{R}} + \mathbf{j}\boldsymbol{P}_{1\mathbf{I}}$ and $\boldsymbol{P}_2 = \boldsymbol{P}_{2\mathbf{R}} + \mathbf{j}\boldsymbol{P}_{2\mathbf{I}}$, in equation (5.9) are complex quantities and equation (5.9) can be expressed as,

$$J_{\boldsymbol{I}} = \frac{1}{4\rho_a \omega d_{12}}\left\{-\boldsymbol{P}^{\mathrm{T}}{}_{1\mathbf{R}}\boldsymbol{P}_{2\mathbf{I}} + \boldsymbol{P}^{\mathrm{T}}{}_{1\mathbf{I}}\boldsymbol{P}_{2\mathbf{R}} + \boldsymbol{P}^{\mathrm{T}}{}_{2\mathbf{R}}\boldsymbol{P}_{1\mathbf{I}} - \boldsymbol{P}^{\mathrm{T}}{}_{2\mathbf{I}}\boldsymbol{P}_{1\mathbf{R}}\right\} \tag{5.10}$$

Due to $\boldsymbol{P}_{\mathbf{I}}$ and $\boldsymbol{P}_{\mathbf{R}}$ being vectors, thus:

$$\boldsymbol{P}_{\mathbf{I}}^{\mathrm{T}}\boldsymbol{P}_{\mathbf{R}} + \boldsymbol{P}_{\mathbf{R}}^{\mathrm{T}}\boldsymbol{P}_{\mathbf{I}} = 2\boldsymbol{P}_{\mathbf{I}}^{\mathrm{T}}\boldsymbol{P}_{\mathbf{R}} \tag{5.11}$$

and

$$J_{\boldsymbol{I}} = \frac{1}{2\rho_a \omega d_{12}}\left(\boldsymbol{P}_{1\mathbf{I}}^{\mathrm{T}}\boldsymbol{P}_{2\mathbf{R}} - \boldsymbol{P}_{2\mathbf{I}}^{\mathrm{T}}\boldsymbol{P}_{1\mathbf{R}}\right). \tag{5.12}$$

In a linear system, the superposition principle implies that the sound pressure at a sensing location in a sound field is the linear sum of the contributions from all significant noise sources. For an active noise control system, the sound pressure at a sensing location $\mathbf{r}$ is classified as the sum of the primary source and control source sound pressures; that is:

$$\boldsymbol{P}(\mathbf{r}) = \boldsymbol{P}_p(\mathbf{r}) + \boldsymbol{P}_c(\mathbf{r}). \tag{5.13}$$

where $\boldsymbol{P}_p(\mathbf{r})$ is the $(N_e \times 1)$ vector of complex sound pressures radiated by the primary sources at the error sensing locations, $[\boldsymbol{p}_p(\mathbf{r}_1), \boldsymbol{p}_p(\mathbf{r}_2), \cdots\cdots, \boldsymbol{p}_p(\mathbf{r}_{N_e})]^{\mathrm{T}}$ and $\boldsymbol{P}_c(\mathbf{r})$ is the $(N_e \times 1)$ vector of complex sound pressures radiated by the control sources at the error sensing locations, $[\boldsymbol{p}_c(\mathbf{r}_1), \boldsymbol{p}_c(\mathbf{r}_2), \cdots\cdots, \boldsymbol{p}_c(\mathbf{r}_{N_e})]^{\mathrm{T}}$.

Substituting equation (5.13) into equation (5.12) gives:

$$J_{\boldsymbol{I}} = \frac{1}{2\rho_a \omega d_{12}} \left[\left(\boldsymbol{P}_{c1\mathbf{I}} + \boldsymbol{P}_{p1\mathbf{I}} \right)^{\mathrm{T}} \left(\boldsymbol{P}_{c2\mathbf{R}} + \boldsymbol{P}_{p2\mathbf{R}} \right) - \left(\boldsymbol{P}_{c2\mathbf{I}} + \boldsymbol{P}_{p2\mathbf{I}} \right)^{\mathrm{T}} \left(\boldsymbol{P}_{c1\mathbf{R}} + \boldsymbol{P}_{p1\mathbf{R}} \right) \right] \tag{5.14}$$

Rearranging equation (5.14) gives:

$$J_{\boldsymbol{I}} = \left(\mathrm{I} + \mathrm{II} + \mathrm{III} + \mathrm{IV} \right) \tag{5.15}$$

where

$$\mathrm{I} = \frac{1}{2\rho_a \omega d_{12}} \left(\boldsymbol{P}_{c1\mathbf{I}}^{\mathrm{T}} \boldsymbol{P}_{c2\mathbf{R}} - \boldsymbol{P}_{c1\mathbf{R}}^{\mathrm{T}} \boldsymbol{P}_{c2\mathbf{I}} \right)$$

$$\mathrm{II} = \frac{1}{2\rho_a \omega d_{12}} \left(\boldsymbol{P}_{p1\mathbf{I}}^{\mathrm{T}} \boldsymbol{P}_{c2\mathbf{R}} - \boldsymbol{P}_{p1\mathbf{R}}^{\mathrm{T}} \boldsymbol{P}_{c2\mathbf{I}} \right)$$

$$\mathrm{III} = \frac{1}{2\rho_a \omega d_{12}} \left(\boldsymbol{P}_{c1\mathbf{I}}^{\mathrm{T}} \boldsymbol{P}_{p2\mathbf{R}} - \boldsymbol{P}_{c1\mathbf{R}}^{\mathrm{T}} \boldsymbol{P}_{p2\mathbf{I}} \right)$$

$$\mathrm{IV} = \frac{1}{2\rho_a \omega d_{12}} \left(\boldsymbol{P}_{p1\mathbf{I}}^{\mathrm{T}} \boldsymbol{P}_{p2\mathbf{R}} - \boldsymbol{P}_{p1\mathbf{R}}^{\mathrm{T}} \boldsymbol{P}_{p2\mathbf{I}} \right) \tag{5.16a-d}$$

The sound pressure, $\boldsymbol{P}_c(\mathbf{r})$, radiated from the control sources can be expressed in terms of the transfer functions from the control sources to the error sensors, and the control source strengths; that is,

$$\boldsymbol{P}_c(\mathbf{r}) = \boldsymbol{Z}_{QP} \boldsymbol{Q}_c \tag{5.17}$$

where $\boldsymbol{Z}_{QP}$ is the $\left(N_e \times N_c \right)$ matrix of transfer functions from the control source inputs to the error sensor outputs; $\boldsymbol{Q}_c$ is the $\left(N_c \times 1 \right)$ vector of complex control source strengths and N_c is the number of control sources.

For the case of a primary sound field generated by a vibrating structure, the control sound field, $\boldsymbol{P}_c(\mathbf{r})$ in equation (5.13), can be generated by a set of acoustic sources or vibration sources attached directly to the structure. Thus, for the acoustic control sources, source strength $\boldsymbol{Q}_c$ represents the volume velocity of the acoustic control sources; and for the vibration control sources, $\boldsymbol{Q}_c$ represents the excitation force of the vibration control sources.

Here the quadratic optimization technique (Nelson and Elliott (1995); Lütkepohl (1993)) is used to derive expressions for the minimization of the sum of the sound intensities with respect to the optimum strength of the control sources. Thus, the sum of the sound intensities needs to be expressed as a function of the control source strengths. To do this, substituting equation (5.17) into equation (5.16) and rearranging it gives:

$$\mathrm{I} = \frac{1}{2\rho_a \omega d_{12}} \Big(\boldsymbol{Q}_{c\mathbf{I}}^{\mathrm{T}} \,\mathbf{Re}\{\boldsymbol{Z}_{QP1}^{\mathrm{H}} \boldsymbol{Z}_{QP2}\} \boldsymbol{Q}_{c\mathbf{R}} - \boldsymbol{Q}_{c\mathbf{I}}^{\mathrm{T}} \,\mathbf{Im}\{\boldsymbol{Z}_{QP1}^{\mathrm{H}} \boldsymbol{Z}_{QP2}\} \boldsymbol{Q}_{c\mathbf{I}}$$

$$- \boldsymbol{Q}_{c\mathbf{R}}^{\mathrm{T}} \,\mathbf{Im}\{\boldsymbol{Z}_{QP1}^{\mathrm{H}} \boldsymbol{Z}_{QP2}\} \boldsymbol{Q}_{c\mathbf{R}} - \boldsymbol{Q}_{c\mathbf{R}}^{\mathrm{T}} \,\mathbf{Re}\{\boldsymbol{Z}_{QP1}^{\mathrm{H}} \boldsymbol{Z}_{QP2}\} \boldsymbol{Q}_{c\mathbf{I}} \Big)$$

$$\mathrm{II} = \frac{1}{2\rho_a \omega d_{12}} \Big(- \mathbf{Im}\{\boldsymbol{P}_{p1}^{\mathrm{H}} \boldsymbol{Z}_{QP2}\} \boldsymbol{Q}_{c\mathbf{R}} - \mathbf{Re}\{\boldsymbol{P}_{p1}^{\mathrm{H}} \boldsymbol{Z}_{QP2}\} \boldsymbol{Q}_{c\mathbf{I}} \Big),$$

$$\mathrm{III} = \frac{1}{2\rho_a \omega d_{12}} \Big(\boldsymbol{Q}_{c\mathbf{I}}^{\mathrm{T}} \,\mathbf{Re}\{\boldsymbol{Z}_{QP1}^{\mathrm{H}} \boldsymbol{P}_{p2}\} - \boldsymbol{Q}_{c\mathbf{R}}^{\mathrm{T}} \,\mathbf{Im}\{\boldsymbol{Z}_{QP1}^{\mathrm{H}} \boldsymbol{P}_{P2}\} \Big),$$

$$\mathrm{IV} = \frac{1}{2\rho_a \omega d_{12}} \Big(- \mathbf{Im}\{\boldsymbol{P}_{p1}^{\mathrm{H}} \boldsymbol{P}_{p2}\} \Big). \tag{5.18a-d}$$

Substituting equation (5.18) into equation (5.15) gives:

$$J_I = - \boldsymbol{Q}_{c\mathbf{R}}^{\mathrm{T}} \boldsymbol{a}_{\mathbf{I}} \boldsymbol{Q}_{c\mathbf{R}} - \boldsymbol{Q}_{c\mathbf{R}}^{\mathrm{T}} \boldsymbol{a}_{\mathbf{R}} \boldsymbol{Q}_{c\mathbf{I}} - \boldsymbol{Q}_{c\mathbf{I}}^{\mathrm{T}} \boldsymbol{a}_{\mathbf{I}} \boldsymbol{Q}_{c\mathbf{I}} + \boldsymbol{Q}_{c\mathbf{I}}^{\mathrm{T}} \boldsymbol{a}_{\mathbf{R}} \boldsymbol{Q}_{c\mathbf{R}} \tag{5.19}$$

$$- \boldsymbol{b}_{1\mathbf{I}} \boldsymbol{Q}_{c\mathbf{R}} - \boldsymbol{b}_{1\mathbf{R}} \boldsymbol{Q}_{c\mathbf{I}} + \boldsymbol{Q}_{c\mathbf{I}}^{\mathrm{T}} \boldsymbol{b}_{2\mathbf{R}} - \boldsymbol{Q}_{c\mathbf{R}}^{\mathrm{T}} \boldsymbol{b}_{2\mathbf{I}} - \boldsymbol{c}_{\mathbf{I}}$$

thus,

$$J_I = \mathbf{Im}\{\boldsymbol{Q}_c^{\mathrm{H}} \boldsymbol{a} \boldsymbol{Q}_c + \boldsymbol{b}_1 \boldsymbol{Q}_c + \boldsymbol{Q}_c^{\mathrm{H}} \boldsymbol{b}_2 + c\} \tag{5.20}$$

where

$$\boldsymbol{a} = \frac{-1}{2\rho_a \omega d_{12}} \boldsymbol{Z}_{QP1}^{\mathrm{H}} \boldsymbol{Z}_{QP2}$$

$$\boldsymbol{b}_1 = \frac{-1}{2\rho_a \omega d_{12}} \boldsymbol{P}_{p1}^{\mathrm{H}} \boldsymbol{Z}_{QP2}$$

$$\boldsymbol{b}_2 = \frac{-1}{2\rho_a \omega d_{12}} \boldsymbol{Z}_{QP1}^{\mathrm{H}} \boldsymbol{P}_{p2}$$

$$c = \frac{-1}{2\rho_a \omega d_{12}} \boldsymbol{P}_{p1}^{\mathrm{H}} \boldsymbol{P}_{p2} \qquad (5.21\text{a-d})$$

Equation (5.20) is the quadratic form defining the sum of the sound intensities (Lee and Park (1996)). Furthermore, it demonstrates that it is possible to minimize the sum of the sound intensities with respect to the optimum control source strengths by means of quadratic optimization. The minimum sum of sound intensities can be obtained by differentiating the sum of the sound intensities J_I in equation (5.19) with respect to $\boldsymbol{Q}_{c\mathbf{R}}$ and $\boldsymbol{Q}_{c\mathbf{I}}$, and then setting the resultant gradient expressions equal to zero:

$$\frac{\partial J_I}{\partial \boldsymbol{Q}_{c\mathbf{R}}} = -\left(\boldsymbol{a}_{\mathbf{I}} + \boldsymbol{a}_{\mathbf{I}}^{\mathrm{T}}\right)\boldsymbol{Q}_{c\mathbf{R}} - \boldsymbol{a}_{\mathbf{R}}\boldsymbol{Q}_{c\mathbf{I}} + \boldsymbol{a}_{\mathbf{R}}^{\mathrm{T}}\boldsymbol{Q}_{c\mathbf{I}} - \boldsymbol{b}_{1\mathbf{I}}^{\mathrm{T}} - \boldsymbol{b}_{2\mathbf{I}} = 0$$

$$\frac{\partial J_I}{\partial \boldsymbol{Q}_{c\mathbf{I}}} = -\left(\boldsymbol{a}_{\mathbf{I}} + \boldsymbol{a}_{\mathbf{I}}^{\mathrm{T}}\right)\boldsymbol{Q}_{c\mathbf{I}} - \boldsymbol{a}_{\mathbf{R}}^{\mathrm{T}}\boldsymbol{Q}_{c\mathbf{R}} + \boldsymbol{a}_{\mathbf{R}}\boldsymbol{Q}_{c\mathbf{R}} - \boldsymbol{b}_{1\mathbf{R}}^{\mathrm{T}} + \boldsymbol{b}_{2\mathbf{R}} = 0 \qquad (5.22\text{a,b})$$

By solving this set of equations for $\boldsymbol{Q}_{c\mathbf{R}}$ and $\boldsymbol{Q}_{c\mathbf{I}}$ and combining the results for the vector of control source strengths $\boldsymbol{Q}_c = \boldsymbol{Q}_{c\mathbf{R}} + \mathbf{j}\boldsymbol{Q}_{c\mathbf{I}}$, the optimum strengths of the control sources $\boldsymbol{Q}_{c,opt}$ can be obtained,

$$\boldsymbol{Q}_{c,opt} = -\boldsymbol{A}^{-1}\boldsymbol{B} \qquad (5.23)$$

where

$$\boldsymbol{A} = \boldsymbol{a} - \boldsymbol{a}^{\boldsymbol{H}}$$

$$\boldsymbol{B} = \boldsymbol{b}_2 - \boldsymbol{b}_1^{H} \qquad (5.24\text{a,b})$$

Comparing this to the previous work of Berry et al. (1999) has shown that the principal advantage of using the above approach is that in order to predict the noise reduction achieved by minimizing the cost function, it is only necessary to measure (or calculate) the sound pressures at the error sensors that result from the primary sources and the control sources, rather than measuring (or calculating) the sound pressures and the particle velocities at the error sensors. This advantage implies that for an actual practical active noise control system, intensity probes can be constructed using low cost electret microphones. In Berry et al. (1999)'s work, an exact expression for intensity minimization was derived based on sound pressure and particle velocity calculations at the error sensors by means of the acoustic Green's function. In practice, the transducers for measuring sound intensities are usually constructed using two pressure transducers so that Berry et al.'s model is unsuitable for application in practice. Another approach regarding intensity minimization was reported by Sommerfeldt and Nashif (1994). However, their work was concerned with the development of adaptive algorithms for minimizing the energy-based quantities in the time domain, rather than an algorithm for sound intensity minimization defined by means of the quadratic optimization theory in the frequency domain as investigated in this thesis.

The minimum sum of the sound intensities at the error sensing locations can be obtained by substituting equations (5.23) and (5.24) into equation (5.20) provided that the coefficient of the quadratic term is positive definite. However, it should be noted that the coefficient of the quadratic term in equation (5.20) is not guaranteed to be positive definite due to the characteristics of the sound intensity. Mathematically, the solution of equation (5.20) corresponding to the solution of equation (5.23) may represent a maximum (Lütkepohl (1993)). In physical terms, this phenomenon can result in the sound radiation increasing at the error sensors after control (Koehler and Snyder (2000)). To improve this, a sufficient number of error sensors should be used; and because the coefficient of the quadratic term depends only on the transfer functions between the control source inputs and error sensor outputs, the poor control performance can be avoided by careful arrangement of the control sources and error sensors. This may be done by optimizing the control source locations and/or error sensor locations. The optimization procedure is discussed in Chapter 6.

5.3 Minimization of the sum of the squared sound pressures

In general, the sum of the squared sound pressures at a finite number of points can be expressed as:

$$J_p = \sum_{i=1}^{N_e} | p_i |^2 = \sum_{i=1}^{N_e} p_i {*} p_i = \boldsymbol{P}^{\mathrm{H}} \boldsymbol{P} \tag{5.25}$$

where $\boldsymbol{P}$ is the sum of the primary source and control source sound pressures at the error sensors as described in equation (5.13). Thus equation (5.25) may be expressed as:

$$J_p = \boldsymbol{P}^{\mathrm{H}} \boldsymbol{P} = \boldsymbol{P}_c^{\mathrm{H}} \boldsymbol{P}_c + \boldsymbol{P}_c^{\mathrm{H}} \boldsymbol{P}_p + \boldsymbol{P}_p^{\mathrm{H}} \boldsymbol{P}_c + \boldsymbol{P}_p^{\mathrm{H}} \boldsymbol{P}_p \tag{5.26}$$

In a similar way to equation (5.17), the sound field generated by the control sources may be expressed in terms of the transfer functions from the control source inputs to the error sensor outputs and the control strengths as:

$$\boldsymbol{P}_c(\mathbf{r}) = \boldsymbol{Z}_{QP} \boldsymbol{Q}_c \tag{5.27}$$

Substituting equation (5.27) into equation (5.26) and rearranging it gives:

$$J_p = \boldsymbol{Q}_c^{\mathrm{H}} \boldsymbol{A} \boldsymbol{Q}_c + \boldsymbol{Q}_c^{\mathrm{H}} \boldsymbol{b} + \boldsymbol{b}^{\mathrm{H}} \boldsymbol{Q}_c + c \tag{5.28}$$

where

$$\boldsymbol{A} = \boldsymbol{Z}_{QP}^{\mathrm{H}} \boldsymbol{Z}_{QP}$$

$$\boldsymbol{b} = \boldsymbol{Z}_{QP}^{\mathrm{H}} \boldsymbol{P}_p \tag{5.29a-c}$$

$$c = \boldsymbol{P}_p^{\mathrm{H}} \boldsymbol{P}_p$$

Equation (5.28) is a quadratic form defining the sum of the squared sound pressures; thus, by means of quadratic optimization, the optimum values of the control source strengths are given as (Nelson and Elliott (1992)):

$$\boldsymbol{Q}_{c,opt} = -\boldsymbol{A}^{-1}\boldsymbol{b} \tag{5.30}$$

Substituting equation (5.30) into equation (5.28) and rearranging it gives the following expression for the minimum sum of the squared sound pressures:

$$J_{prs,min} = c + \boldsymbol{b}^{\mathrm{H}} \boldsymbol{Q}_{c,opt} \tag{5.31}$$

The coefficient of the quadratic term defined in equation (5.28) is positive definite (Nelson and Elliott (1992)); thus the cost function for squared sound pressure minimization has a unique global minimum.

5.4 Numerical simulation

In this section, two near-field sensing strategies, i.e. minimizing the sum of the sound intensities and minimizing the sum of the squared sound pressures in the near-field, are evaluated numerically. As a source, a simply supported steel flat panel, mounted in an infinite rigid baffle surrounded with air, was modeled with a harmonic point force excitation as shown in Figure 5.2. Young's modulus of the panel was E=209 MPa; Poisson's ratio ν =0.29 and density ρ_s =7870 kg/m^3. Sound speed in air is c_0 =343 m/s and the air density is ρ_a =1.21 kg/m^3. The distance of the error sensor plane from the vibrating panel was normalized as $\gamma = 2z/L$, where L is the characteristic panel dimension and z is the distance between the error sensing plane and the vibrating panel. In the work described here, the diagonal of the panel, L_{xy}, was selected as the characteristic panel dimension for normalizing. The noise source dimension was normalized as $\kappa = \pi L / \lambda$, where λ is the acoustic wavelength. Thus, the noise source was defined as a *small source* for $\kappa << \pi$ and as an *extended source* for $\kappa > \pi$.

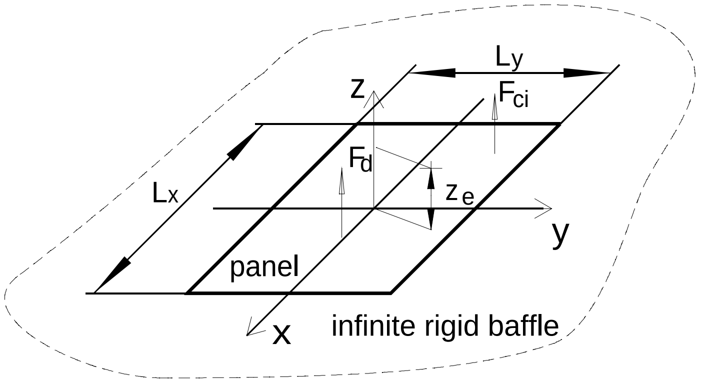

Figure 5.2 Physical system arrangement

5.4.1 Transfer functions from control inputs to error sensing outputs

In general, when predicting the minimized sound field radiated from a structure using equations (5.20), (5.23), (5.30) and (5.31), the transfer function $\boldsymbol{Z}_{QP}$ and the primary sound field $\boldsymbol{P}_p$ can be directly measured on site or be modeled theoretically or numerically for simple systems. In this section, in order to evaluate the near-field sensing strategies theoretically, a simply supported panel mounted in an infinite rigid baffle was modeled as the primary source associated with a point force disturbance, and several point forces were applied on the panel as control sources.

For vibration control sources, the transfer function $\boldsymbol{Z}_{QP}$ can be expressed as (Hansen and Snyder (1997)):

$$\boldsymbol{Z}_{QP} = \boldsymbol{Z}_r \boldsymbol{Z}_I^{-1} \Psi_c \tag{5.32}$$

For a simply supported panel mounted in an infinite rigid baffle as shown in Figure 5.3, the modal radiation transfer function, $\boldsymbol{Z}_r$, can be written in matrix form as:

$$\boldsymbol{Z}_r = \begin{bmatrix} z_{rad,1}(\mathbf{r}_1) & \cdots & z_{rad,N}(\mathbf{r}_1) \\ \vdots & z_{rad,j}(\mathbf{r}_i) & \vdots \\ z_{rad,1}(\mathbf{r}_{N_e}) & \cdots & z_{rad,N}(\mathbf{r}_{N_e}) \end{bmatrix} \tag{5.33}$$

where the subscript j is the structural mode index corresponding to the m,n mode and j=1, 2 … N.

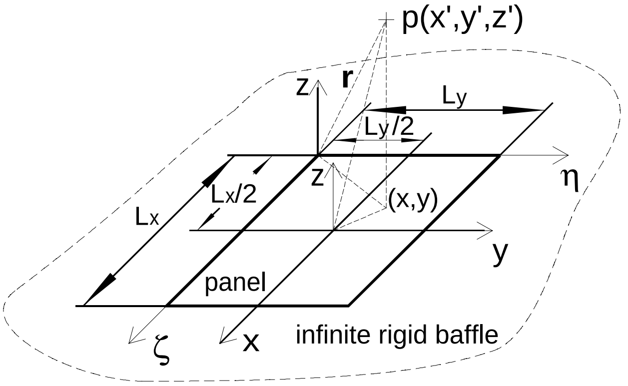

Figure 5.3 Coordinate system of a vibrating plate

In equation (5.33), the modal radiation function for the j^{th} mode at observer point (x',y',z') with the origin at the panel corner is expressed as:

$$z_{rad,j}(x',y',z') = \frac{\mathbf{j}\omega\rho_a}{2\pi}\int_0^{L_y}\int_0^{L_x}\frac{\sin(\alpha_m\zeta)\sin(\beta_n\eta)e^{-\mathbf{j}k\mathbf{r}_i}}{\mathbf{r}_i}d\zeta d\eta \tag{5.34}$$

where $\alpha_m = \frac{m\pi}{L_x}$ and $\beta_n = \frac{n\pi}{L_y}$; $k = \frac{c}{\omega}$ is acoustic wavenumber; c is speed of sound and the subscript i=1, 2… N_e. By means of the coordinate transformation, equation (5.34) can be rewritten as:

$$z_{rad,j}(x',y',z') = \frac{\mathbf{j}\omega\rho_a}{2\pi}\int_{-L_x/2}^{L_y/2}\int_{-L_y/2}^{L_x/2}\frac{\sin(\alpha_m(x+\frac{L_x}{2}))\sin(\beta_n(y+\frac{L_y}{2}))e^{-\mathbf{j}k\sqrt{(x'-x)^2+(y'-y)^2+z^2}}}{\sqrt{(x'-x)^2+(y'-y)^2+z^2}}dxdy$$

(5.35)

In equation (5.35), the origin of the coordinate system x, y is at the panel center and the equation must be evaluated numerically in the near-field.

The second term in equation (5.32), modal impedance $\mathbf{Z}_I$, is the ($N \times N$) diagonal matrix,

$$\mathbf{Z}_I = \begin{bmatrix} z_{I1,1} & \cdots & 0 \\ \vdots & z_{I\,j,j} & \vdots \\ 0 & \cdots & z_{I\,N,\mathbf{N}} \end{bmatrix} \tag{5.36}$$

where the modal impedance of the j^{th} mode, $z_{I\,j,j}$, can be expressed as:

$$z_{I\,j,j} = \frac{\rho_s hS}{4}\left(\omega_j^2(1+\mathbf{j}\eta_j) - \omega^2\right) \tag{5.37}$$

where ρ_s is the density of the structure; h is the thickness of the structure; η_j is the loss factor of the j^{th} structural mode; ω_j is the resonance frequency of the j^{th} structural mode and is defined as:

$$\omega_j = \left(\frac{D}{\rho_s h}\right)^{1/2}\left(\left(\frac{m\pi}{L_x}\right)^2 + \left(\frac{n\pi}{L_y}\right)^2\right) \tag{5.38}$$

where $D = \dfrac{Eh^3}{12(1-\nu^2)}$ is the structure bending stiffness.

The mode shape function of the panel at the control force input locations, Ψ_c , is:

$$\Psi_c = \begin{bmatrix} \psi_{c\,1,1} & \cdots & \psi_{c\,1,N_c} \\ \vdots & \psi_{c\,j,l} & \vdots \\ \psi_{c\,N,1} & \cdots & \psi_{c\,N,N_c} \end{bmatrix} \tag{5.39}$$

where the subscript l=1, 2 … N_c. The mode shape function, $\psi_{c\,j,l}$, of the j^{th} structural mode associated with the l^{th} control force at location (ζ_l, η_l), with the origin at the panel corner, is expressed as:

$$\psi_{c\,j,l} = \sin(\alpha_m \zeta_l)\sin(\beta_n \eta_l) \tag{5.40}$$

By means of a coordinate transformation, the mode shape function at the control force input location (x_l, y_l) with the origin at the panel center can be written as:

$$\psi_{\boldsymbol{c}\,j,l} = \sin(\alpha_{\boldsymbol{m}} (x_l + \frac{L_x}{2}))\sin(\beta_{\boldsymbol{n}} (y_l + \frac{L_y}{2})) \tag{5.41}$$

In this case, the primary sound field may be expressed as:

$$\boldsymbol{P}_p = \boldsymbol{Z}_r \boldsymbol{Z}_I^{-1} \Psi_p f_p \tag{5.42}$$

In equation (5.42), the mode shape function evaluated at the primary disturbance locations can be calculated theoretically by employing equation (5.39) and replacing the subscript c with p.

5.4.2 Simulation results

Table 5.1 presents the coordinates of a primary disturbance and 4 control forces that were applied to the panel.

Table 5.1 Coordinates of forces on the panel

Disturbance	$\bar{\boldsymbol{l}}_d$ (L_x/4, 0)
Control forces	$\bar{\boldsymbol{l}}_{c1}$ (L_x/4, L_y/4); $\bar{\boldsymbol{l}}_{c2}$ (L_x/4, -L_y/4); $\bar{\boldsymbol{l}}_{c3}$ (-L_x/4, L_y/4); $\bar{\boldsymbol{l}}_{c4}$ (-L_x/4, -L_y/4).

Small source ($\kappa = \pi L_{xy} / \lambda \approx 1.2$)

In this case, the panel was 1.5×1×0.006 m in size. The panel oscillated at 73 Hz corresponding to the 3,1 mode resonance, the radiated sound field was calculated at 441 error sensing points (21×21 grid) at 0.2 m intervals on a plane γ =0.17 above the panel, and the control results were evaluated using 1297 sensors distributed over a test hemisphere in the far-field (10 m from the panel) for each test case.

The calculated sound pressure and intensity distributions characterizing the primary sound field are shown in Figures 5.4 and 5.5. Since the panel was excited at 73 Hz, corresponding to the 3,1 mode resonance, the sound radiation patterns in Figures 5.4 and 5.5 represent the 3,1 mode shape of the panel. It should be noted that negative intensities in the scale in Figure 5.5 indicate the negative energy flow, i.e. energy flowing into the panel, but not negative intensity level.

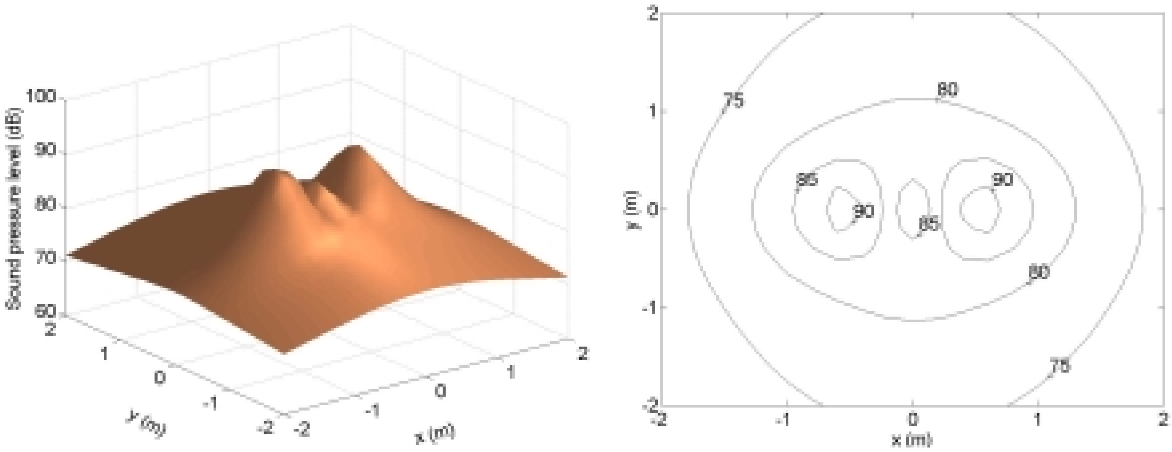

Figure 5.4 Distribution of sound pressure level without control; error sensors at 441 points at 0.2 m intervals on a plane γ =0.17 above the panel

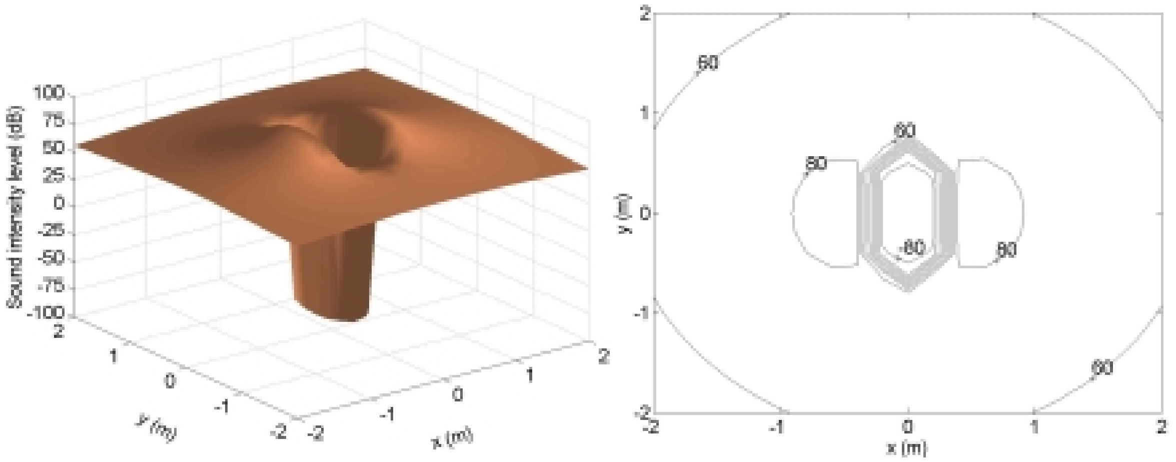

Figure 5.5 Distribution of sound intensity level without control; error sensors at 441 points at 0.2 m intervals on a plane γ =0.17 above the panel

Figure 5.6 (a) shows the distribution of sound intensity levels after point force control. The sum of the sound intensities over all 441 error sensing points was chosen as the cost function. One can see that intensity levels at all sensing points decrease in the near-field, the total sound power reduction is around 66 dB in the far-field and the average intensity reduction at the error sensors is around 65 dB.

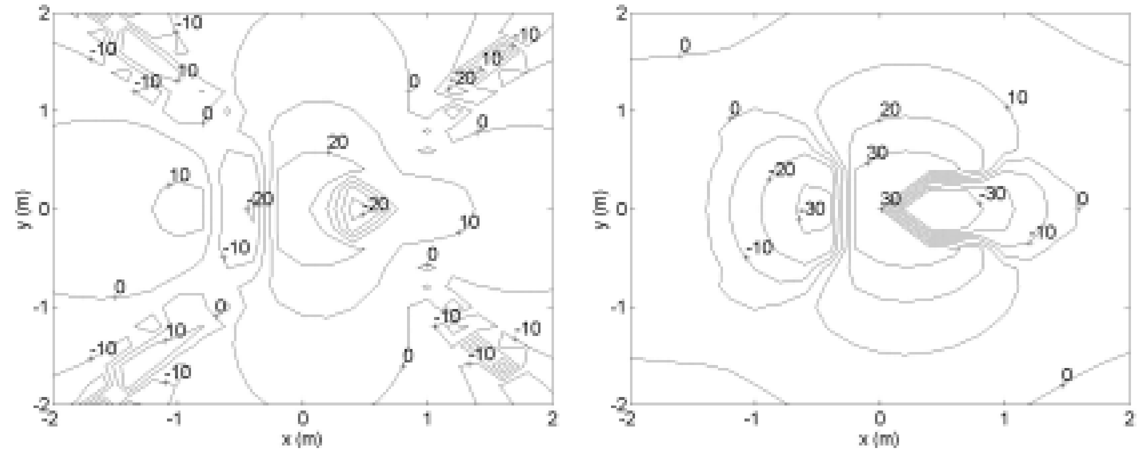

(a) sound intensity minimization (b) squared pressure minimization.

Figure 5.6 Distribution of sound intensity level after point force control (4 control sources); error sensors at 441 points at 0.2 m intervals on a plane γ =0.17 above the panel

To evaluate the control performance achieved by the minimization of the sum of the squared sound pressures in the near-field, first the sum of the squared sound pressures was chosen as the cost function to obtain optimal control forces. These control forces were then used to calculate the sound power reduction in the far-field and to plot the distribution of sound intensity levels in the near-field as shown in Figure 5.6(b). For this situation the total sound power was reduced by about 59 dB in the far-field, which is 7 dB less than that achieved using sound intensity minimization, even though sound intensity levels were reduced at all the monitoring points in the near-field, as shown in Figure 5.6(b). In this case, the average squared sound pressure reduction is around 52 dB at the error sensors.

When comparing the controlled near-field sound intensity level distribution patterns shown in Figures 5.6(a) and 5.6(b), one can see that the complexity of the sound radiation pattern in Figure 5.6(a) is increased in comparison to the field shown in Figure 5.6(b). This more complicated sound field thus seems to be less able to propagate sound energy to the far-field because areas of opposite phase are small and close together, allowing fluid to move back and forth without propagating energy.

Figure 5.7 shows the variation of the sound power reduction in the far-field as a function of the normalized distance ($\gamma = 2z/L_{xy}$) of the error sensor plane from the surface of the primary source. The sound power reduction achieved by minimizing the sum of the squared sound pressures increases as the separation distance between the error sensor plane and the vibrating panel increases until the maximum sound power reduction was achieved. In this case, the γ value for this maximum value was 0.7. In the figure, values in brackets represent the actual distances between the error sensor planes and the panel source, and the units are meters.

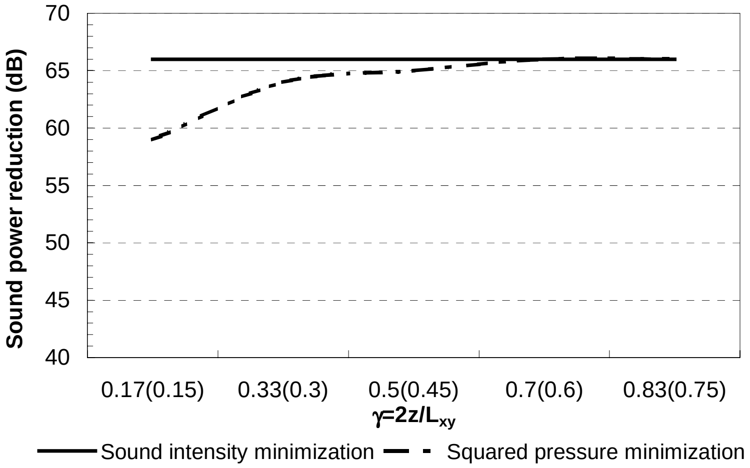

Figure 5.7 Variation of the sound power reduction in the far-field as a function of the distance between the error sensors and the panel for 441 error sensors; $\kappa \approx 1.2$.

For a source radiating sound in a free field, the near-field consists of a hydrodynamic near-field adjacent to the source and a geometric near-field between the hydrodynamic near-field and the far-field (Bies and Hansen (1996)) (referring Figure 5.12). In the hydrodynamic near-field, the sound pressure is out of phase with local particle velocity, but sound propagation to the far-field is only associated with the in-phase components of pressure and particle velocity; thus measurements of the sound pressure give no indication of the sound power radiated by the source. In other words, the measurement of the sound pressure in this region represents a combination of the propagating energy and non propagating energy, unlike the measurement of the time-averaged sound intensity which is only sensitive to the propagating energy. Therefore, in the case of squared sound pressure minimization, the control effort tends to minimize the propagating and non propagating energy, rather than focusing on minimizing the propagating energy only. This is why, for the case shown in Figure 5.7, a poorer far field control performance was obtained by minimizing the sum of the squared sound pressures in the region of γ =0.7 associated with $\kappa \approx 1.2$.

To compare the sound field reduction between the far-field and the error sensors (in the near-field), both proposed control strategies were used to obtain optimal control forces. The control forces were then used to calculate the sound field reduction in the far-field and at the error sensors respectively, as shown in Figure 5.8. The results demonstrated that the average squared pressure reduction in the near-field did not indicate the sound power reduction in the far-field because of the complexity of the sound field in the near-field.

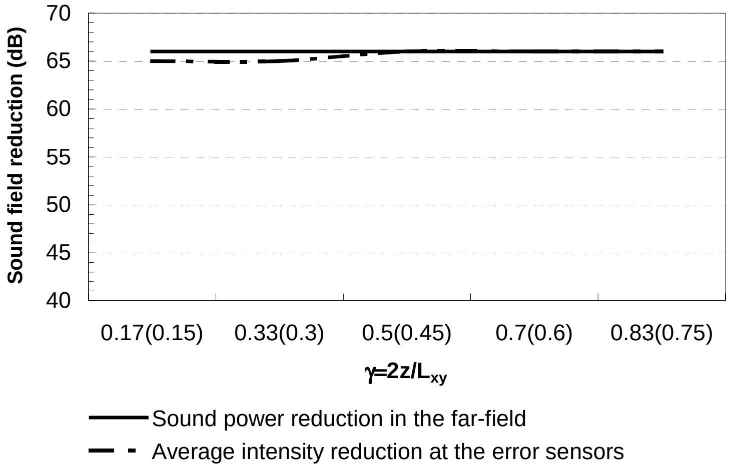

(a) Intensity minimization

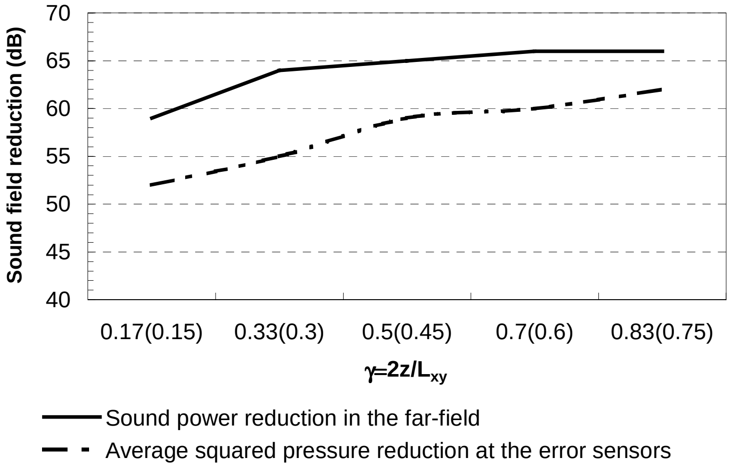

(b) Squared pressure minimization

Figure 5.8 Comparison of the sound field reduction in the far-field and at the error sensors; 441 error sensors; $\kappa \approx 1.2$.

Due to the complexity of the distribution of the sound energy in the near-field, the number of error sensors required to achieve control performance using near-field sensing strategies may be quite large (Berry et al. (1999), Li et al (1999a-b, 2000)). Thus, the effect of the number of the error sensors on the control performance was evaluated. In this case, 36 error sensors (6×6 grid) at 0.8 m intervals on a plane above the panel were used. The results evaluated in the far-field are shown in Figure 5.9. From the figure one can see that for the case of the minimization of the sum of the sound intensities in the hydrodynamic near-field (γ =0.7), the sound power reduction decreased as the error sensing plane became close to the primary source panel. The results from the minimization of the sum of the sound intensities at a less than optimum number of error sensors were worse (for near-field error sensor locations) than those achieved by minimizing the sum of the squared sound pressures. This is because the cost function associated with minimizing the sum of the sound intensities is more sensitive to the accurate measurement of the sound field, as the sound intensity varies much more drastically with location than does the sound pressure.

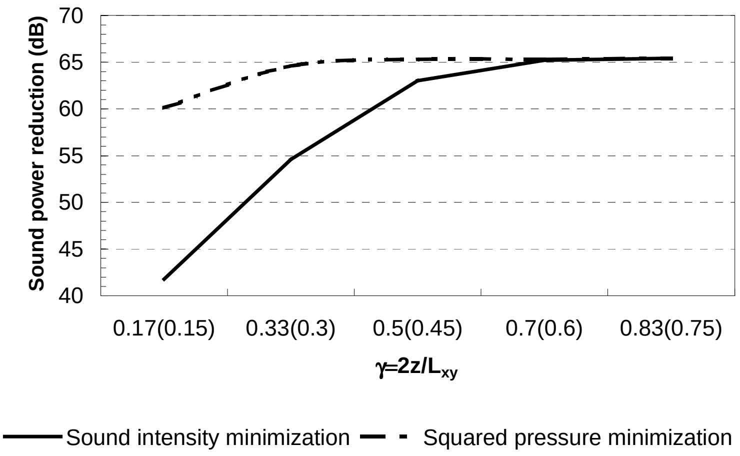

Figure 5.9 Variation of the sound power reduction as a function of the distance between the error sensors and the panel for 36 error sensors; $\kappa \approx 1.2$.

To investigate the effect of the number of error sensors on the control performance in the near-field, the sound pressure field was calculated as a function of the number of error sensors on error sensing planes γ=0.17 (hydrodynamic near-field) and γ=0.83 (transition region) above the panel respectively. The results are shown in Figures 5.10. The figure shows that the sound power reduction achieved by both sensing strategies fluctuated in the hydrodynamic near-field until a sufficient number of error sensors were used (441 error sensors in this case). This is because the cost function is the sum of the sound intensities (or the sum of the squared sound pressures) so that the optimum result is an average of values sensed at the error sensors. Thus, it does not follow that the sound power reduction will increase as the number of error sensors increases when an insufficient number of error sensors are used to sense the sound field in the hydrodynamic near-field. When comparing results shown in Figures 5.10(a) and (b), one can see that a greater number of error sensors were required to achieve the maximum sound reduction in the hydrodynamic near-field than in the transition region due to the complexity of the distribution of the sound energy in the hydrodynamic near-field.

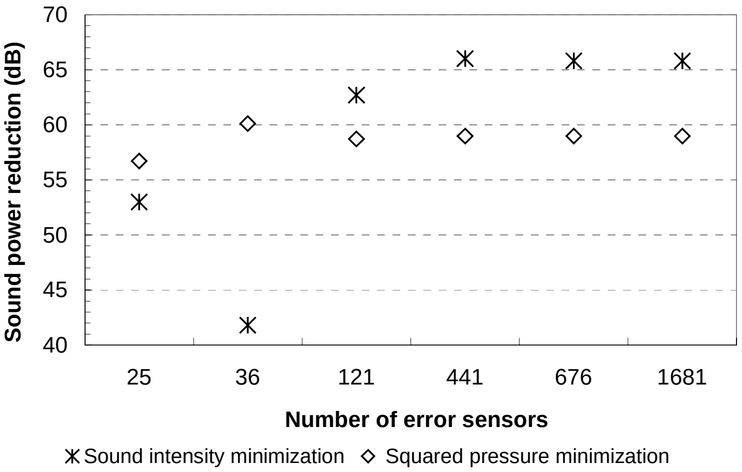

(a) γ =0.17

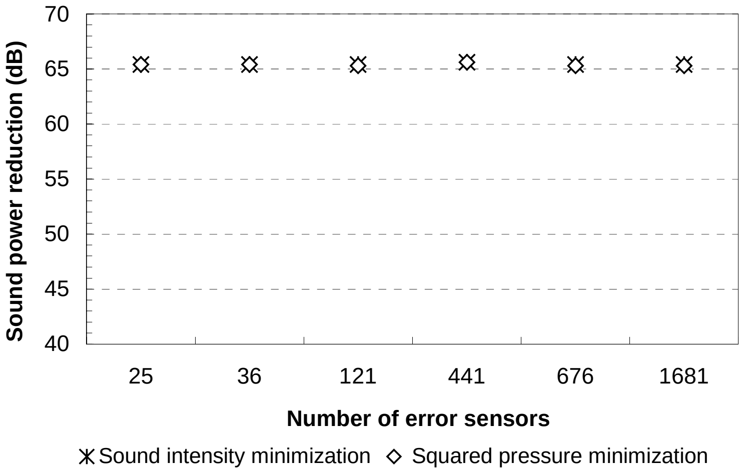

(b) γ =0.83

Figure 5.10 Variations of the sound power reduction as a function of the number of error sensors associated with $\kappa \approx 1$.

Extended source ($\kappa = \pi L_{xy} / \lambda \approx 3.77$)

According to the definition of the region of a sound field (Bies and Hansen (1996)), characteristics of the sound field not only depend on the normalized separation distance between the sensing locations and the surface of the source ($\gamma = 2z/L_{xy}$), but also depend on the normalized source dimension ($\kappa = \pi L_{xy} / \lambda$). To evaluate the effect of the normalized source dimension on the sound power reduction, an extended source associated with $\kappa \approx 3.77$ was considered. In this case, the panel thickness increased to 10 mm and the panel oscillated at 230 Hz corresponding to the 1,3 mode resonance. Four control forces attached to the panel and 441 error sensors (21×21 grid) at 0.2 m intervals were used. The coordinates of forces on the panel were shown in Table 5.1. The variations in the sound power reduction as a function of the normalized distance between the error sensing plane and the panel, γ, are shown in Figure 5.11.

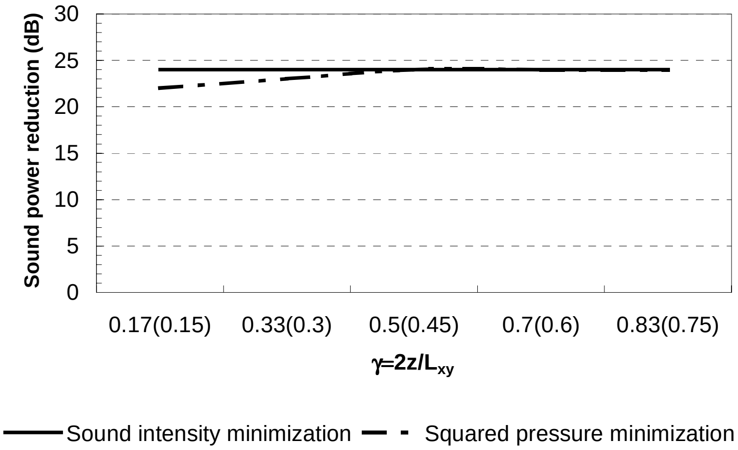

Figure 5.11 Variation of the sound power reduction in the far-field as a function of the distance between the error sensor plane and the panel for 441 error sensors; $\kappa \approx 3.77$.

The results demonstrate that the sound power reduction achieved by minimizing the sum of the squared sound pressures was close to the maximum achievable sound power reduction, even though the sensing plane was near to the primary source, γ =0.17**.** The biggest difference is around 2 dB at γ =0.17. When comparing results shown in Figure 5.7 with those shown in Figure 5.11, one can see that for the case of using squared sound pressure minimization, at a constant distance of the error sensor plane to the noise source, the calculated control result for the extended source is closer to the maximum achievable sound reduction than that for the small source. In this case, the maximum achievable sound reduction represents the sound power reduction that can be achieved using intensity minimization in the far-field as shown in Figures 5.7 and 5.11. This can be explained from characteristics of the sound field. As mentioned at the beginning of this section, the characteristics of the sound field were determined by both the normalized distance of the sensing point to the noise and the normalized source dimension. This is defined in Figure 5.12.

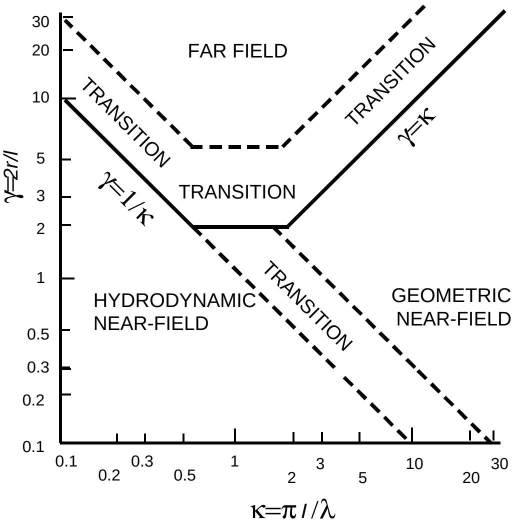

Figure 5.12 The radiation field of a source
(after Bies and Hansen (1996))

From Figure 5.12, in contrast to the case of $\kappa \approx 1.2$ (Figure 5.7), the sound field associated with $\kappa \approx 3.77$ (Figure 5.11) corresponding to the distance range γ =0.17-0.83, moves from the hydrodynamic near-field through the transition field to the geometric near-field. In general, in the geometric near-field (and some parts of the transition field) the pressure and the particle velocity are in–phase as for waves in the far-field. Thus, the radiated sound power can be accurately determined by a sufficient number of sound pressure measurements in the geometric near-field. This is why good far-field control performance was achieved by minimizing the sum of the squared sound pressures in this ‘near-field’ region when a large number of error sensors was used.

Figure 5.13 shows the comparisons of the sound field reduction in the far-field and at the error sensors associated with 441 error sensors and $\kappa \approx 3.77$ (geometric near-field). The results show that the sound field reduction at the error sensors is close to the sound power reduction achieved using sensors in the far-field for both minimizing the sound intensity and minimizing the squared sound pressure. When comparing the results shown in Figures 5.8 (b) and 5.13 (b), one can see that the sound field reduction achieved by minimizing the squared sound pressure in the geometric near-field is closer to the sound power reduction achieved by minimizing the signal from far-field sensors than it is to that achieved by minimizing the signal from sensors in the hydrodynamic near-field. Again, this can be explained because in the geometric near-field, a sufficient number of sound pressure measurements can determine the radiated sound power in the far-field. Thus, in the geometric near-field, the sound pressure reduction at a large number of error sensors may represent the sound power reduction in the far-field.

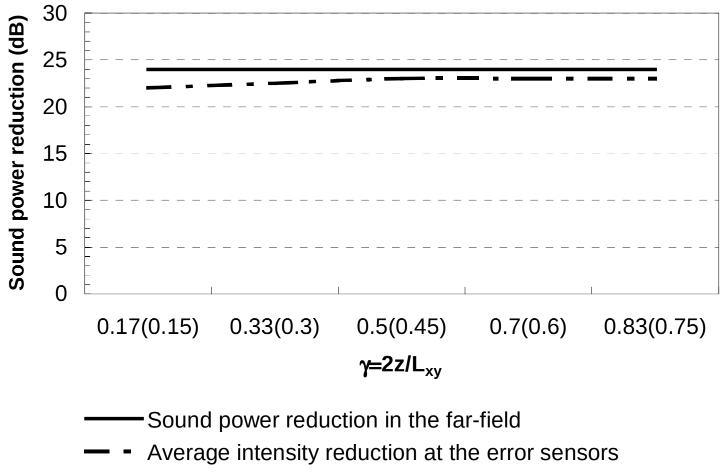

(a) Intensity minimization

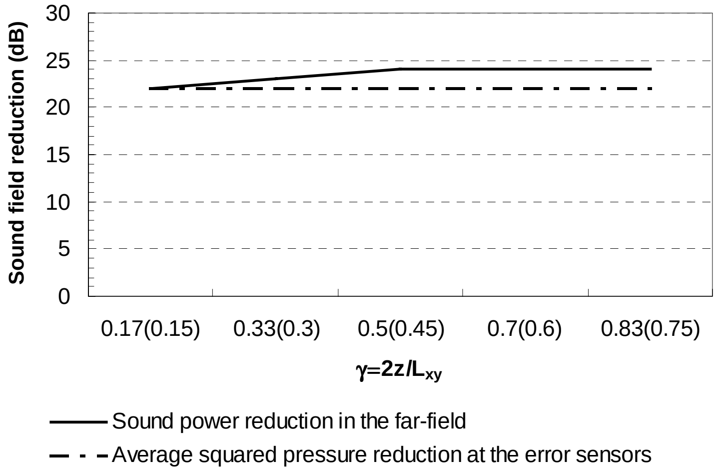

(b) Squared pressure minimization

Figure 5.13 Comparison of the sound field reduction in the far-field and at the error sensors; 441 error sensors; $\kappa \approx 3.77$.

Figure 5.14 shows the control performances achieved using the two proposed sensing strategies with 36 error sensors (6×6 grid) at 0.8 m intervals on a plane above the panel. The variations in the sound power reduction as a function of the number of error sensors on planes γ=0.17 and γ=0.83 above the panel are shown in Figure 5.15. Here, it should be noted that the maximum achievable sound power reduction in the far-field for the case of $\kappa = \pi L_{xy} / \lambda \approx 3.77$ is much smaller than for the case of $\kappa = \pi L_{xy} / \lambda \approx 1.2$, as more control sources are needed to control high frequency radiation.

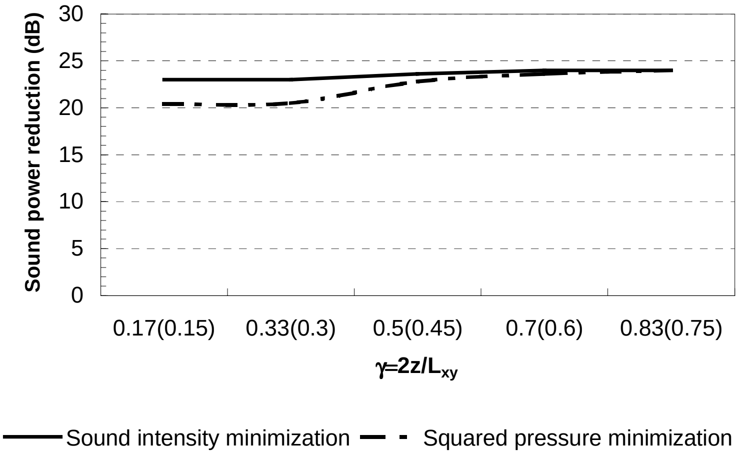

Figure 5.14 Variation of the sound power reduction as a function of the distance between the error sensing plane and the panel for 36 error sensors; $\kappa \approx 3.77$.

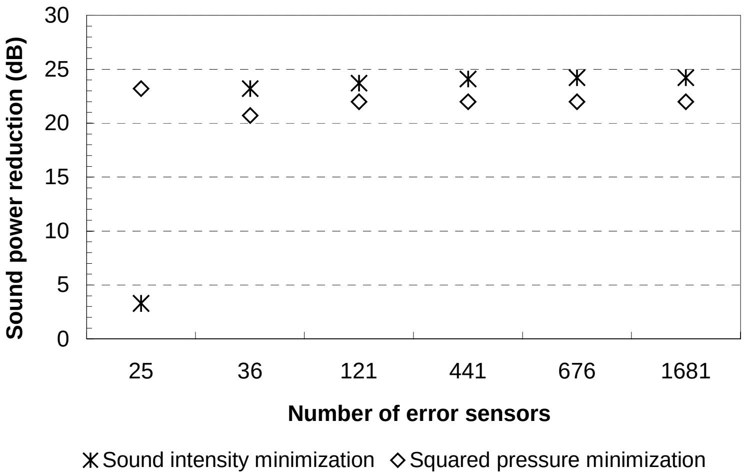

(a) γ =0.17

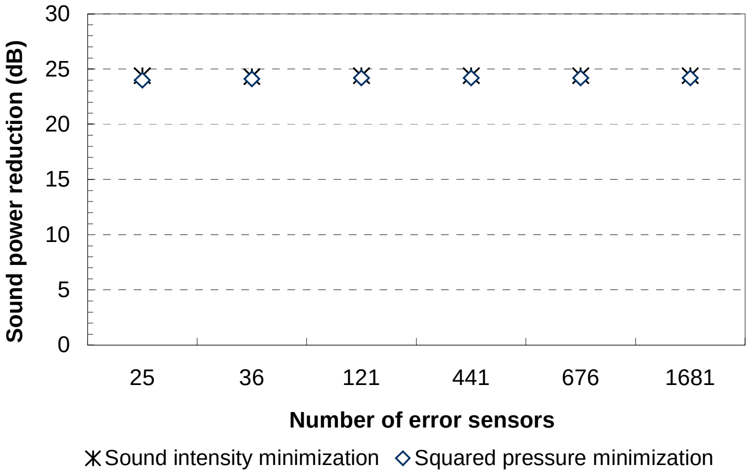

(b) γ =0.83

Figure 5.15 Variations of the sound power reduction as a function of the number of error sensors associated with $\kappa \approx 3.77$

By comparing results shown in Figure 5.9 with those in Figure 5.14, one can see that a smaller number of error sensors were required to maximally reduce the sound field radiated by the extended source ($\kappa \approx 3.77$) than required to maximally reduce the sound field radiated by the small source ($\kappa \approx 1.2$) when the error sensors were close to the vibrating panel . From Figure 5.12, it can be seen that for the case of γ =0.33, the sound fields radiated by the small source and the extended source were characterized as the hydrodynamic near-field and the transition region respectively. Thus, the sound radiation pattern from the small source was more complex and higher order than that from the extended source, as shown in Figure 5.16. In general, a finer resolution is required to adequately plot more complex radiation patterns and therefore more sensors (or measurement positions) will be required. This is why in this case study, a larger number of error sensors were required to maximally reduce the sound field radiated by the small source than that required to reduce the sound field radiated by the extended source.

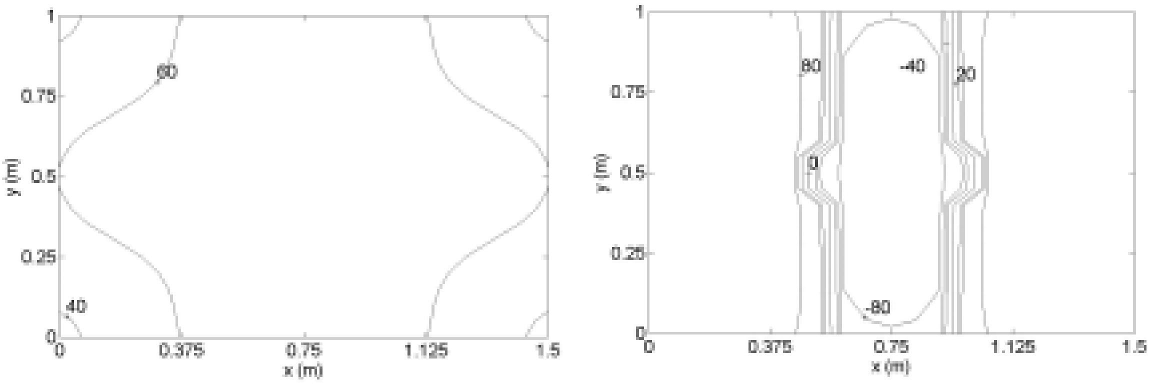

(a) extended source ($\kappa \approx 3.77$) (b) small source ($\kappa \approx 1.2$)

Figure 5.16 Distribution of the primary sound intensity field on a plane above the panel, γ =0.33

5.5 Conclusions

The aim of this chapter was to evaluate near-field sensing strategies for the active control of noise radiated by a vibrating structure in free field. To do this, a flat panel was modeled with a harmonic point force excitation and several point force control sources. Two sensing strategies, sound intensity minimization and sound pressure minimization were considered. A quadratic expression was derived for the minimization of the sum of sound intensities.

To evaluate the effect of the size of the noise source on the control performance, both a small source and an extended source were investigated. The general near field was characterized as the hydrodynamic near-field and the geometric near-field. The results demonstrated that the control performance can be improved (over that achievable by minimizing squared sound pressures) by minimizing the sum of the sound intensities in the hydrodynamic near-field provided that a very large number of error sensors are used. If insufficient error sensors are used, better results are achieved using near-field pressure squared sensing. In other words, good control performance may be achieved by minimizing the sum of the squared sound pressures in the geometric near-field and the squared sound pressure reduction at the error sensors may indicate the sound power reduction in the far-field. It was concluded that less near-field error sensors are required to satisfactorily minimize the sound field radiated by an extended source than to minimize the sound field radiated by a small source for a given frequency of sound radiation.

CHAPTER 6 ACTIVE CONTROL OF SOUND RADIATION FROM A SMALL TRANSFORMER

6.1 Introduction

In this chapter, an active control system for the cancellation of noise radiated from a small transformer was evaluated. The aim is to study the effect of the near-field error sensing strategies on the control performance and the influence of the error sensor arrangement (number and location) on the global control results. To do this, the transfer functions from the control inputs to error outputs, and the primary sound field from the transformer are measured and then data are substituted into the theoretical models for predicting the noise reduction. The cost functions to be minimized are the sum of the sound intensities[†] and the sum of the squared sound pressures in the near-field. The control results are evaluated by measuring the sound field on an enclosed surface surrounding the transformer. A genetic algorithm is employed as a search procedure to optimize the error sensor layout. To verify the numerical simulation, experiments are carried out. Only 8 error sensors and 8 control sources are used due to the limitations of the controller, and the results are evaluated at a large amount of monitor sensors. Both predicted and test results are given.

[†] Due to the limitation of the number of controller channels, only predicted results were presented.

6.2 Prediction of the sound field reduction at discrete locations using measured data

6.2.1 Measurement of sound field

The arrangement for measuring the sound field radiated by a small transformer, which was located in an anechoic room in the Department of Mechanical Engineering at The University of Adelaide, is shown in Figure 6.1. For the sake of safety, the transformer was not energized. Thus, to generate noise, the transformer was excited by an inertial type shaker at 100 Hz, 200 Hz, 300 Hz and 400 Hz. It was found that this excitation provided a sufficiently complex vibration pattern on the transformer tank (see figures shown in Section 6.4). For measuring the sound field, the transformer was surrounded with a frame for holding sound intensity probes around all four sides and over the top. The distance of the frame from the transformer tank was 0.8 m. Six intensity probes were fixed on a beam for sensing the sound field. Noise radiated by the transformer was measured at 492 sensing locations at 0.25 intervals by sliding the beam along the frame during the data acquisition. Eight inertia type shakers, acting as control sources, were mounted on the transformer tank.

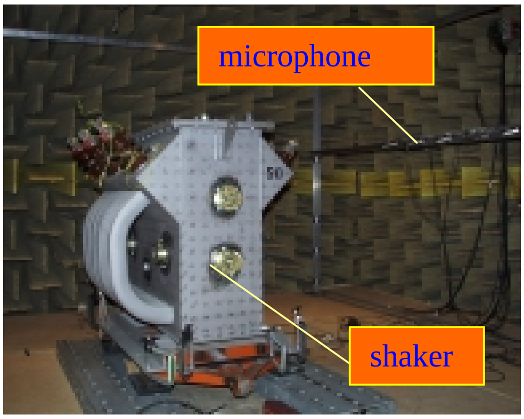

Figure 6.1 A test transformer in the anechoic room

The transfer functions from each shaker input to the sound intensity probe outputs were measured. Each shaker was driven through a power amplifier by a Brüel & Kjær type 3107 signal generator that produced sine waves at frequencies of 100 Hz, 200 Hz, 300 Hz and 400 Hz. For collecting acoustic data, sound intensity probes were connected through microphone pre-amplifiers to a Brüel & Kjær type 2816 multi data acquisition unit with four Brüel & Kjær type 3022 4-channel input modules (not shown in the figure). Data were transferred into a PC computer in which Brüel & Kjær PULSE LabShop V.4.1 was installed. For analyzing the control mechanisms, structural responses to shakers were measured at 224 sensing points as well. Vibration data were recorded using three Brüel & Kjær type 4394 accelerometers connected through Brüel & Kjær type 2635 charge amplifiers to the data acquisition system. A photograph of the experimental set-up is shown in Figure 6.2 and a block diagram of the experimental set-up is shown in Figure 6.3.

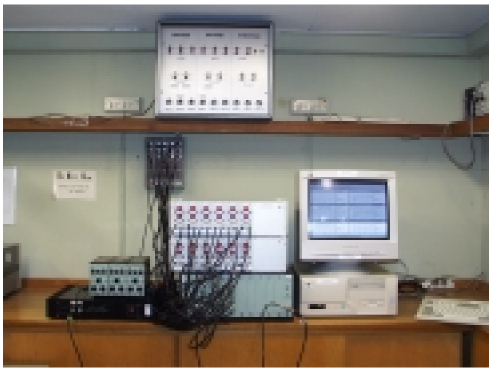

Figure 6.2 The experimental set-up in a control room

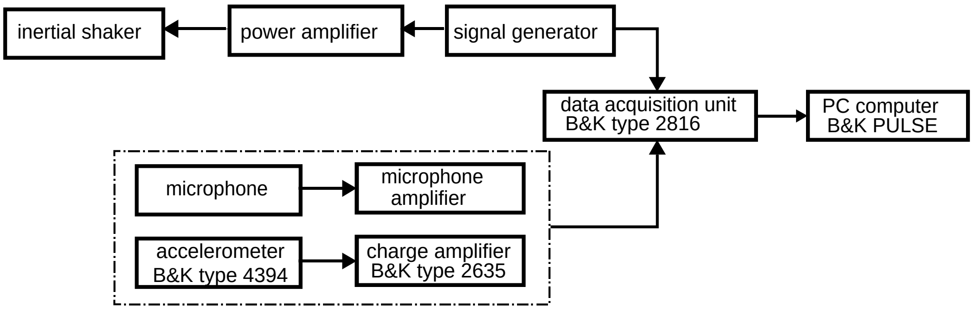

Figure 6.3 Block diagram of the experimental set-up

In general, for sound intensity measurements associated with the pressure sensors, two highly phase–matched microphones are required, which can imply a relatively high cost for the sensors. However, to minimize the cost of a control system which requires a large amount of sensors, particularly for minimizing a tonal sound, low cost microphones can be used. In this case, the amplitude and phase of each microphone must be calibrated at each tone. Here two low cost electret microphones were mounted close together in a support structure to construct a sound intensity probe in a face to face configuration as shown in Figure 6.4. A calibration procedure of the sound intensity probes is discussed in Appendix B.

Figure 6.4 A photograph of the sound intensity probe constructed by two electret microphones

For control sources, as suggested in Chapter 4, several inertial type shakers were used and are shown in Figure 6.5. Due to the great dynamic stiffness of the transformer tank at 100 Hz, the resonance frequencies of the shakers were tuned to approximately 100 Hz to increase their output efficiency at this frequency. After being tuned, the shakers were calibrated on a heavy mass (50 kg) following the procedure that is described in Chapter 4. The force sensitivities of the shakers are given in Appendix C.

Figure 6.5 A photograph of an inertial shaker

6.2.2 Predicted results

To evaluate how the control performance is influenced by the number of the error sensors and whether the error sensors are evenly spaced or optimally located, the average noise reduction at 492 monitor sensors was calculated as a function of the number and the arrangement of error sensors. One inertial shaker was used to excite the transformer tank and generate the primary sound field, while eight shakers (two on each of four sides) were used as control sources.

In the numerical simulations, the cost functions[‡] were first minimized at evenly spaced error sensors and the sound field was calculated at each monitor sensor for the resulting optimum control forces. The results were then compared to those obtained in numerical simulations where the error sensors were optimally located by means of a genetic algorithm search procedure. In this project, the *objective function* for optimizing the control source locations (or the error sensor locations) can be the average intensity (or

---

[‡] In this thesis, the term, *objective function* is used for optimizing the control source locations or the error sensor locations. In contrast with this, the term, *cost function* is used for optimizing the sum of the acoustic parameters (pressure squared or intensity) at the error sensors by means of quadratic optimization theory.

pressure) reduction at the *error sensors* (e.g. the case in Chapter 7), or the average noise reduction at the *monitor sensors* (e.g. the case in this chapter). For the former, the cost function that was defined using the quadratic optimization theory (QOT) was first optimized at the error sensors. The result was then used as a variable in an optimization search procedure to determine the optimal control source locations (or error sensor locations) for achieving the maximum average intensity (or pressure) reduction at the *error sensors*. Generally, this approach is suitable for optimizing the control source locations associated with the fixed error sensor arrangement (number and location). For the latter, the optimal control forces resulting in the minimization of the cost function at the error sensors by means of the QOT were employed to calculate the average noise reduction at the monitor sensors (the average noise reduction at these points can represent the global sound power reduction when sufficient monitor sensors are used). Then, this average noise reduction at the monitor sensing points was chosen as the variable in the optimal search procedure to determine the optimal control source locations or the error sensor locations corresponding to the maximum average noise reduction at these *monitor sensors*. It should be noted that because the average noise reduction at the monitor sensors is unrelated to the average field reduction at the error sensors, sometimes the average intensity reduction at the error sensors may be negative even though the maximum average noise reduction is achieved at the monitor sensors (e.g. some case shown in Figure 6.8). The following paragraphs include some definitions used in this chapter:

$$PR = -10\log_{10}\left(\frac{\sum_{i=1}^{N_e}\left|p_{c,i}\right|^2}{\sum_{i=1}^{N_e}\left|p_{p,i}\right|^2}\right)$$

$$IR = -10\log_{10}\left(\frac{\sum_{i=1}^{N_e} I_{c,i}}{\sum_{i=1}^{N_e} I_{p,i}}\right)$$

$$NR = -10\log_{10}\left(\frac{\sum_{i=1}^{492} I_{c,i}}{\sum_{i=1}^{492} I_{p,i}}\right) \qquad (6.1a\text{-}b)$$

where PR, IR and NR are the average pressure reduction at the error sensors, the average intensity reduction at the error sensors and the average sound intensity reduction at the 492 monitor sensors, respectively. Here the average sound intensity reduction at the 492 monitor sensors was calculated to evaluate the control performance. The reason for this is that the sound intensity reduction at a sufficient number of monitor sensors can represent the global sound power reduction. Subscripts c and p denote the controlled sound field and the primary sound field respectively. N_e is the number of error sensors. Value of 492 is the number of monitor sensors.

6.2.2.1 Control achieved by sound intensity minimization

In order to predict the noise reduction achieved by the minimization of the sum of the sound intensities at the discrete locations, the measured primary sound pressures at two microphones, $\boldsymbol{P}_{p1}$ and $\boldsymbol{P}_{p2}$, on the sound intensity probe and the transfer functions between the control sources and two microphones respectively, $\boldsymbol{Z}_{QP1}$ and $\boldsymbol{Z}_{QP2}$, were substituted into the models outlined in chapter 5. The optimal control forces resulting in the minimization of the cost function at the error sensors were then used to calculate the average noise reduction at 492 monitor sensors, defined in equation (6.1c). Figure 6.6 shows predicted results associated with *evenly* spaced error sensors.

From Figure 6.6, one can see that the noise reduction at 100 Hz achieved by sound intensity minimization using evenly spaced error sensors fluctuated wildly as a function of the number of error sensors unless a large amount of error sensors were used. As explained in Chapter 5, because the cost function is the sum of the sound intensities, the optimum result is an average of values measured at the error sensors. Thus, it does not follow that the noise reduction will increase as the number of error sensors increases when an insufficient number of error sensors are used to sense the sound field.

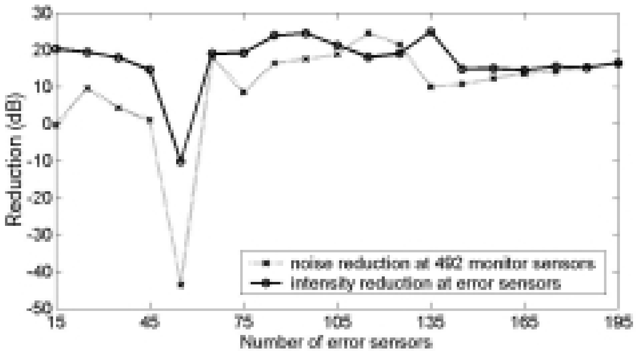

(a) at 100 Hz

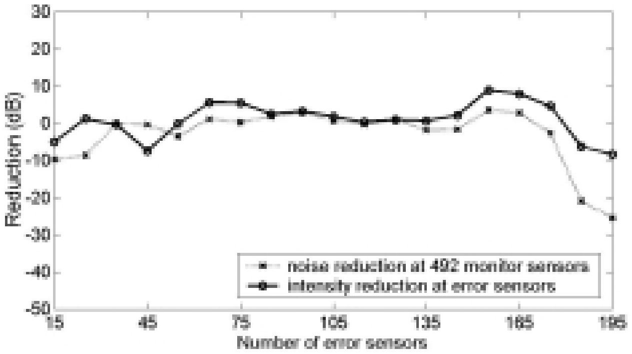

(b) at 200 Hz

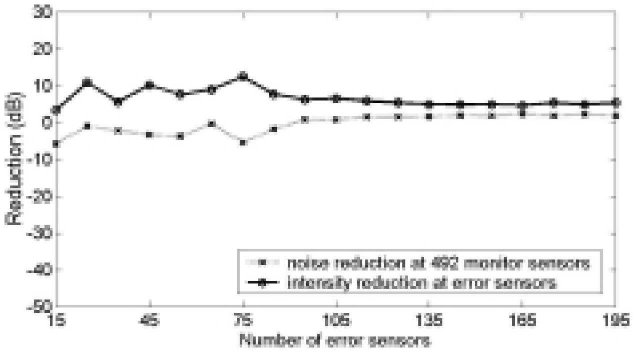

(c) at 300 Hz

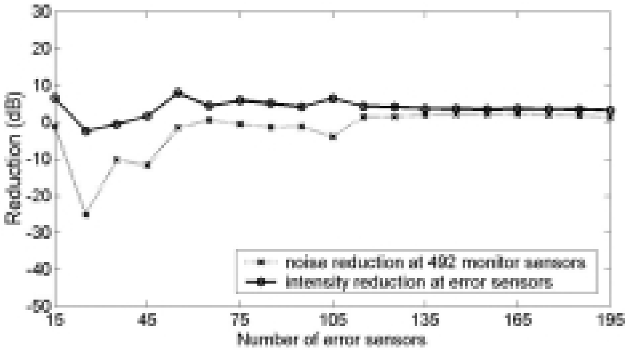

(d) at 400 Hz

Figure 6.6 Variation of the noise reduction level with the number of the error sensors, (sound intensity minimization at evenly spaced error sensors)

As mentioned previously in Chapter 5, although the cost function for minimizing the sum of the sound intensities at the error sensors can be expressed in a quadratic form, the coefficient of the quadratic term is not guaranteed to be positive definite, due to the characteristics of the sound intensity. Thus, the sum of the sound intensities at the *error sensors* resulting from the optimal control forces, $\boldsymbol{Q}_{c,opt}$, may be increased when the control is on. This is why in Figure 6.6, there are some negative reductions corresponding to the cost function, i.e. the sum of the sound intensities at the error sensors.

The elements in the coefficient matrix of the quadratic term, which represent the transfer functions from the control sources to the error sensors, depend on the relative positions between the control sources and the error sensors. In other words, the properties of this matrix can be changed by choosing properly the relative positions between the control sources and the error sensors, so that the coefficient matrix of the quadratic term in the cost function is positive definite. Thus the unexpected control performance at the error sensors may be avoided by optimizing the control source locations and/or the error sensor locations, to rearrange the transfer functions from the control sources to the error sensors. In this case, the object function for the optimizing the control source locations and the error sensor locations, is the maximum average intensity reduction at the error sensors because the objective is to improve the control performance at the error sensors. Figure 6.7 shows the maximum average intensity reduction at the error sensors as a function of the number of error sensors, when using the optimally located error sensors.

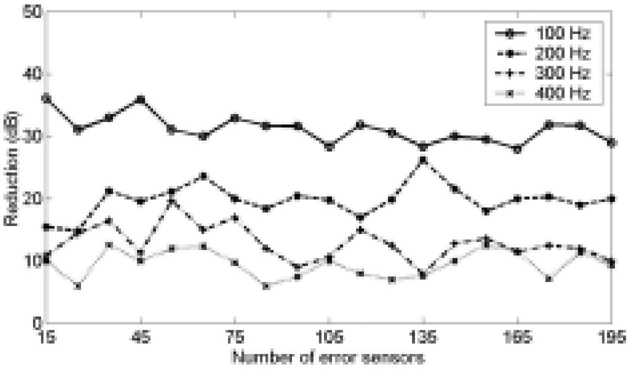

Figure 6.7 Variation of the average intensity reduction at the error sensors as a function of the number of error sensors, associated with the optimum error sensor locations that correspond to the maximum noise reduction at the error sensors

Comparing the results in Figure 6.7 with the respective error sensor measurements in Figure 6.6, one can see that the average intensity reductions at the error sensors were significantly improved after optimizing the error sensor locations that correspond to the average maximum sound intensity reduction at the error sensors. It should be emphasized that the maximum noise reduction at a finite number of error sensors does not necessarily imply that a maximum global noise reduction will be achieved. This is because generally, there is no inherent relation between the noise reduction at the error sensors in the near field and that at the monitor sensors used for evaluation of the control performance. However, evaluation of an active control system is usually based on the maximum global noise reduction, rather than the maximum noise reduction at the error sensors. Thus, the objective function for optimization of the error sensor locations in the work described in the following sections is the maximum average noise reduction at the monitor sensors.

Generally, the control source arrangement, which includes number and location, will determine the achievable noise reduction assuming that an ideal error sensor arrangement exists. The optimization of error sensor arrangement is directed at achieving the maximum reduction in the cost function set by the control source arrangement. In other words, the maximum achievable noise reduction is determined by the control source arrangement first and the error sensor arrangement second. In this chapter, due to the limitation of the potential locations of the control sources, an effort was made to improve the control results by optimizing the error sensor locations based on the fixed control source arrangement. In this case, the *objective function* for optimizing the error sensor locations is the maximum average noise reduction at the *monitor sensors*, rather than the average noise reduction at the *error sensors*. The optimal procedure was described at the beginning of the Section 6.2. The average noise reductions obtained by sound intensity minimization using the optimal error sensor locations are shown in Figure 6.8.

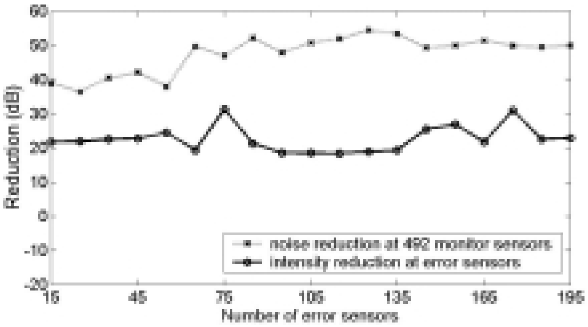

(a) at 100 Hz

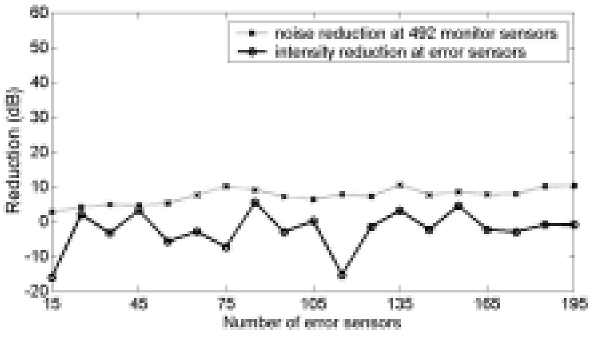

(b) at 200 Hz

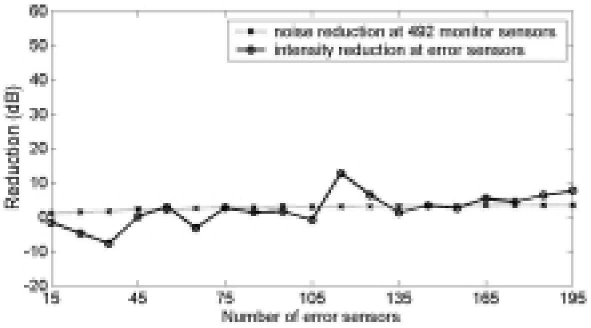

(c) at 300 Hz

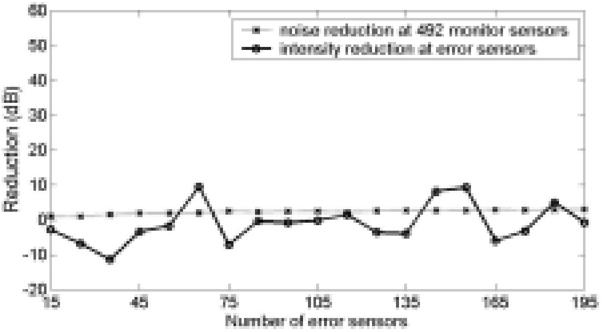

(d) at 400 Hz

Figure 6.8 Variation of the noise reduction level as a function of the number of error sensors, associated with the optimum error sensor locations that correspond to the maximum noise reduction at the monitor sensors (intensity minimization)

From Figure 6.8 it can be seen that for 100 Hz excitation, the average noise reduction at 492 monitor sensors was significantly achieved using the optimally located error sensors, even in the case of using a small number of error sensors. The figure shows that the average intensity reduction at the *error sensor*s is still negative (i.e. a sound power gain) for some of the control cases (for instance 15 error sensors at 200 Hz). This is because the *objective function* of optimizing the error sensor locations is the maximum average noise reduction at a total 492 *monitor sensors* rather than the average intensity reduction at the error sensors but, generally, the average noise reduction at the monitor sensors is unrelated to the average intensity reduction at the error sensors.

Figure 6.8 also shows that it is very hard to achieve a significant global noise reduction at 200 Hz, 300 Hz and 400 Hz even though error sensors were optimally located. As mentioned previously, by analyzing the cost functions to be minimized, one can see that for a certain noise source, the variables in the cost functions are the transfer functions between the control sources and the error sensors. In other words, once a cost function to be minimized has been chosen, the only way to improve the control performance is to rearrange the transfer functions from the control source inputs to the error sensor outputs, by optimizing control source locations and/or error sensor locations and the quantity of each. In fact, this optimization illustrates how the control mechanisms work for an active control system.

Generally, for an active structural acoustic control system, there are two control mechanisms for minimizing the sound field when vibration control sources are used (Snyder and Hansen (1991), Hansen and Snyder (1997)). One of control mechanisms is termed *modal control* and other one is called *modal rearrangement*. Unlike the modal control mechanism which always tends to reduce the sound field, the modal rearrangement mechanism is not effective if the acoustic wavelength at the frequency of interest is short compared to the structure dimensions. By analyzing the control results in terms of the control mechanisms, it is found that for these higher frequencies, *modal rearrangement* cannot effectively work and so the control only relied on *modal control* which cannot work properly with only a few control sources. In other words, it is not possible to reduce the noise at 200 Hz, 300 Hz and 400 Hz by reducing the overall the transformer tank vibration level with just few control actuators. More details about the control mechanisms are discussed in Section 6.4.

6.2.2.2 Control achieved by squared pressure minimization

In this section, the aim is to show the control performance achieved by minimizing the sum of the squared sound pressures at the monitor sensors using the optimum error sensing locations. To do this, the control forces resulting in the minimization of the squared pressure at the error sensors were used to calculate the average noise reduction that is defined in equation (6.1c). This noise reduction was then applied to the optimization search procedure to determine the optimal error sensor locations corresponding to the maximum average noise reduction at the monitor sensors. Figure 6.9 shows the average noise reduction associated with the optimal error sensor locations which corresponded to the maximum average noise reduction at monitor sensors.

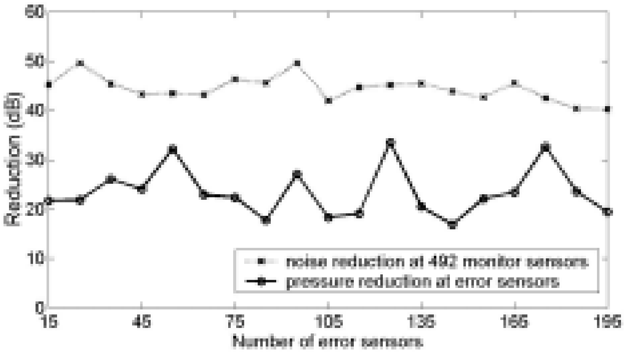

(a) at 100 Hz

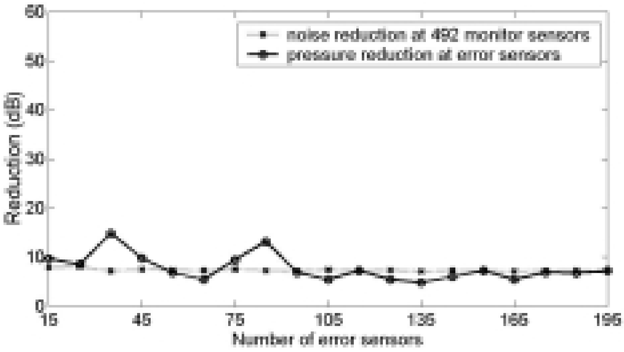

(b) at 200 Hz

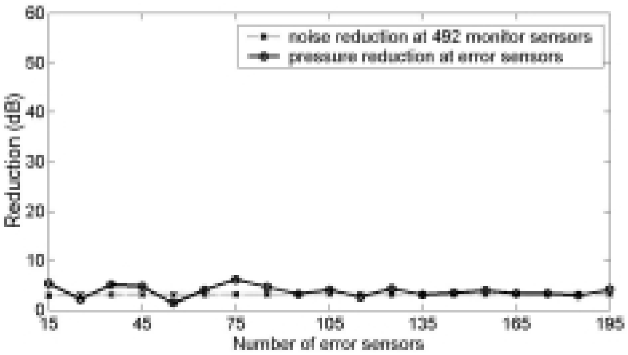

(c) at 300 Hz

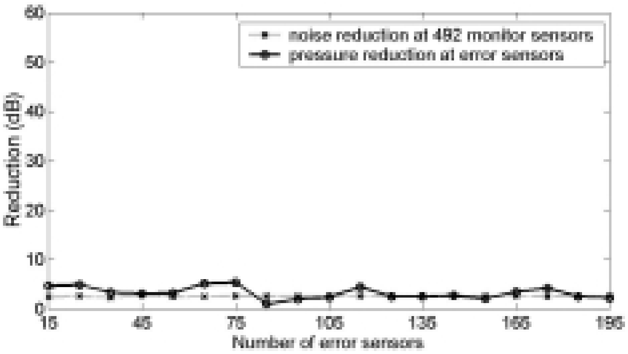

(d) at 400 Hz

Figure 6.9 Variation of noise reduction as a function of the number of error sensors, associated with the optimum error sensor locations that correspond to the maximum noise reduction at the monitor sensors (squared pressure minimization)

Similar to the case of intensity minimization, a significant noise reduction at the monitor sensors was achieved using the optimum error sensor locations at 100 Hz, but poor control results were obtained at higher frequencies. A comparison of the control performance achieved by the two sensing strategies is given in the following section.

6.2.2.3 Effect of error sensing strategies on the control performance

In order to verify the conclusions in Chapter 5, a comparison of the maximum average noise reduction achieved by intensity minimization with that achieved by squared pressure minimization was made. The results are the maximum average noise reduction at the 492 monitor sensors (associated with optimum error sensor locations). The comparison is shown in Figure 6.10.

Results shown in Figure 6.10 demonstrate that, in the experimental configuration tested, better control performance can be achieved by minimizing the sum of the squared sound pressures than can be achieved by minimizing the sum of the sound intensity when a small number of the error sensors are used. This is because a larger amount of the error sensing points are required to accurately describe the intensity field than the pressure field. This conclusion agrees with that reached using the theoretical analysis of Chapter 5.

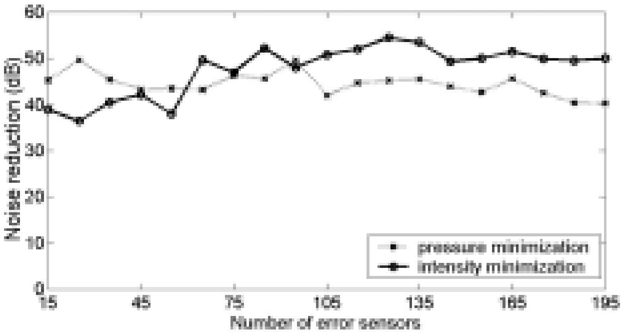

(a) at 100 Hz

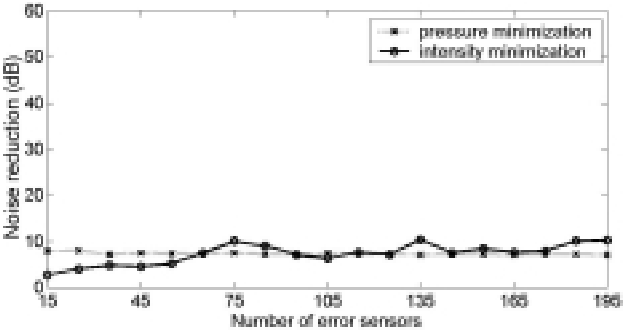

(b) at 200 Hz

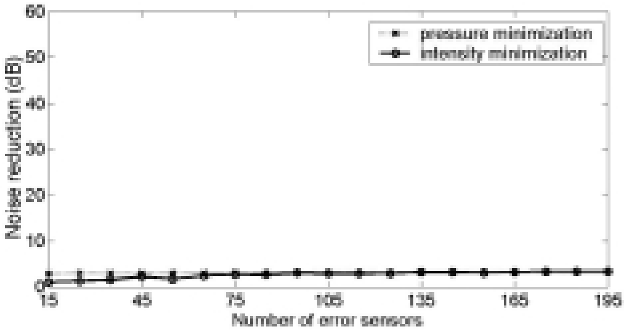

(c) at 300 Hz

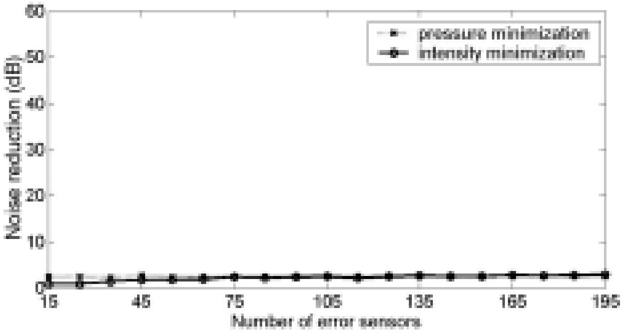

(d) at 400 Hz

Figure 6.10 Comparison of the noise reduction achieved by intensity minimization with that achieved by squared pressure minimization at monitor sensors (associated with optimum error sensor locations)

From Figure 6.10(a) one can see that if a large number of error sensors are used, the noise reduction achieved by intensity minimization at 100 Hz is approximately 10 dB higher than that obtained by squared pressure minimization. Again this result agrees with that in Chapter 5. The reason is that in the case of this physical system configuration, the sound field at 100 Hz is characterized as the *transition* region (between the *hydrodynamic* near field and the *geometric* near field) (Bies and Hansen (1996)). In this region of the sound field, due to the complexity of the sound field, the measurement of the sound pressure may not give an indication of the sound power radiated by the source. In other words, rather than squared pressure minimization, a good control result in this region may be achieved by sound intensity minimization but associated with a large number of error sensors.

6.3 Experimental results

6.3.1 Evaluation of control performance at monitor sensors

To verify the predicted results, experiments were carried out with a ten channel control system which was specially developed for the transformer noise control by the Department of Mechanical Engineering, The University of Adelaide. The control results at 100 Hz associated with 8 error sensors and 8 vibration control sources were evaluated at 528 *monitor sensing points* that were on a frame surrounding the transformer. The distance of the frame to the transformer was 0.8 m. The cost function that was minimized was the sum of the squared sound pressures at the error sensors. An inertial shaker with half rated input of 4.2 V_{rms} was used to excite the transformer for generating the primary sound field. Eight inertial type shakers were used as the control sources. Signals at error microphones were input to the controller through electret microphone amplifiers and the output signals from the controller were used to drive the control shakers through the power amplifiers. A Graphic User Interface (GUI) was used to communicate with the controller and to monitor the error signals while the control was on so that it was known if a maximum level of the noise reduction was reached, as shown in Figure 6.12.

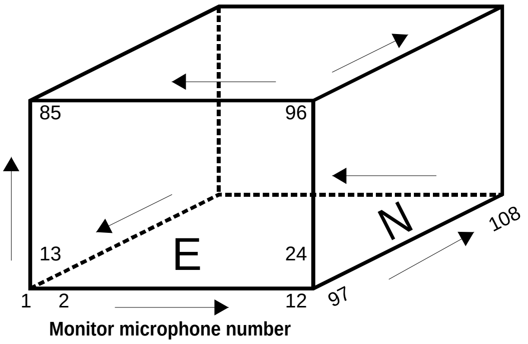

Figure 6.11 Coordinate system for monitor microphones

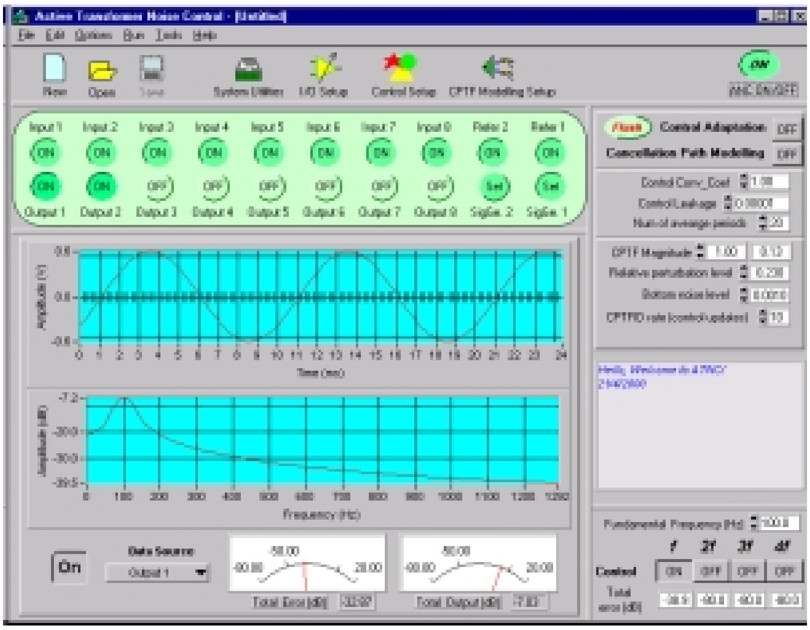

Figure 6.12 A Graphic User Interface of the controller

Once the minimum error signal which represented the sum of the squared sound pressures at the error sensors was reached, the control adaptation was set to *off*. Then the control shakers were constantly driven by the controller during the measurement of the sound field at 528 monitor locations (these 528 sensing points were around all 4 sides and over the top of the transformer). The auto-spectrum was recorded by a PC computer with Brüel & Kjær PULSE LabShop V.4.1 through the Brüel & Kjær type 2816 multi data acquisition unit with four Brüel & Kjær type 3022 4-channel input modules. The experimental set-up is shown in Figure 6.13.

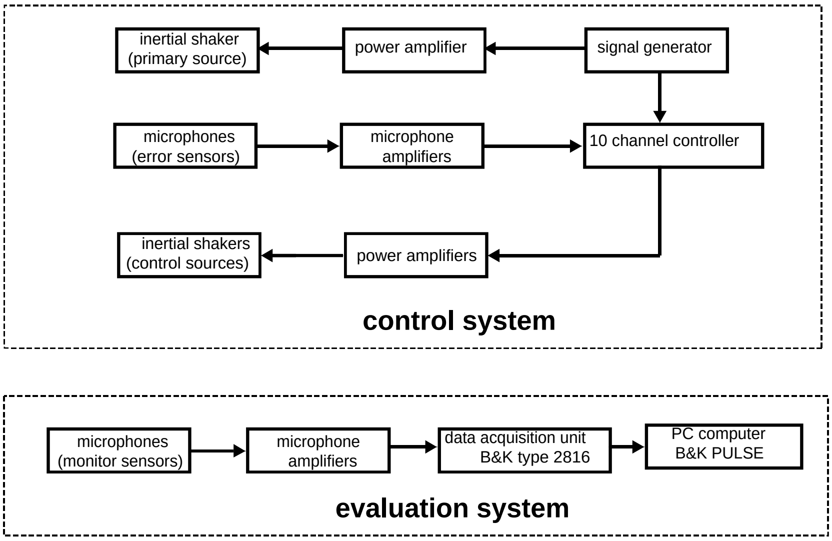

Figure 6.13 Experimental set-up for evaluating global control performance

Figure 6.14 shows the sound pressure reduction levels at the monitor sensing locations. From the figure it can be seen that noise was significantly reduced at most monitor sensing locations even though noise was increased at 3 sensing points. The largest overall sound pressure reduction level was approximately 32.7 dB and the largest overall increase of the sound pressure level was 2.7 dB. The average sound pressure reduction level at the monitor sensors locations was 15.8 dB. This result is similar to the predicted result of 18.7 dB, based on transfer function measurements. Figure 6.15 shows the distribution of the sound pressure level before and after control.

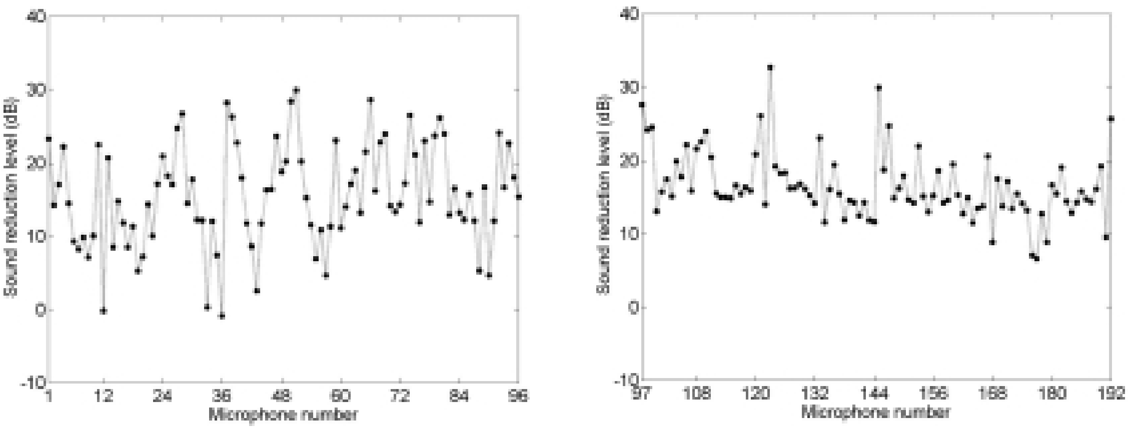

(a) east side of the sensing surface (b) north side of the sensing surface

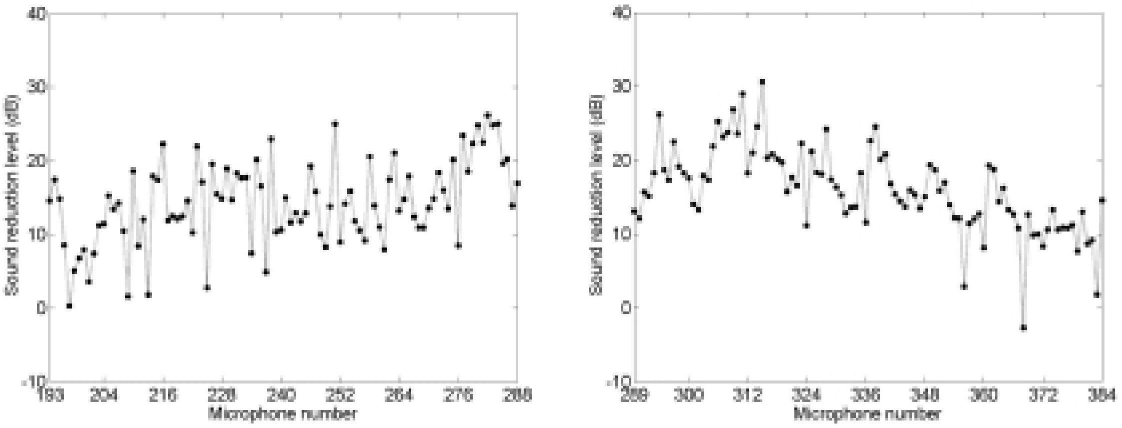

(c) west side of the sensing surface (d) south side of the sensing surface

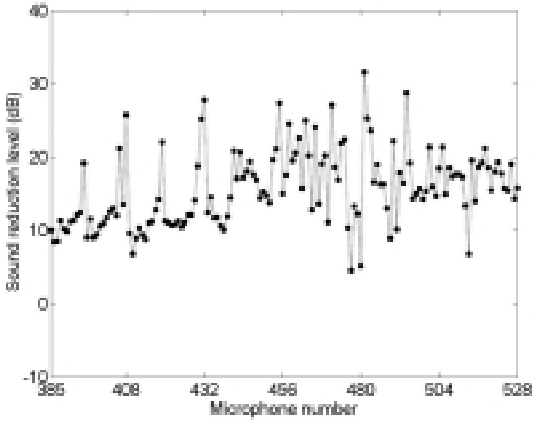

(e) top of the sensing surface

Figure 6.14 Sound pressure level reduction at monitor microphones at 100 Hz in the near-field (8 control sources and 8 error sensors)

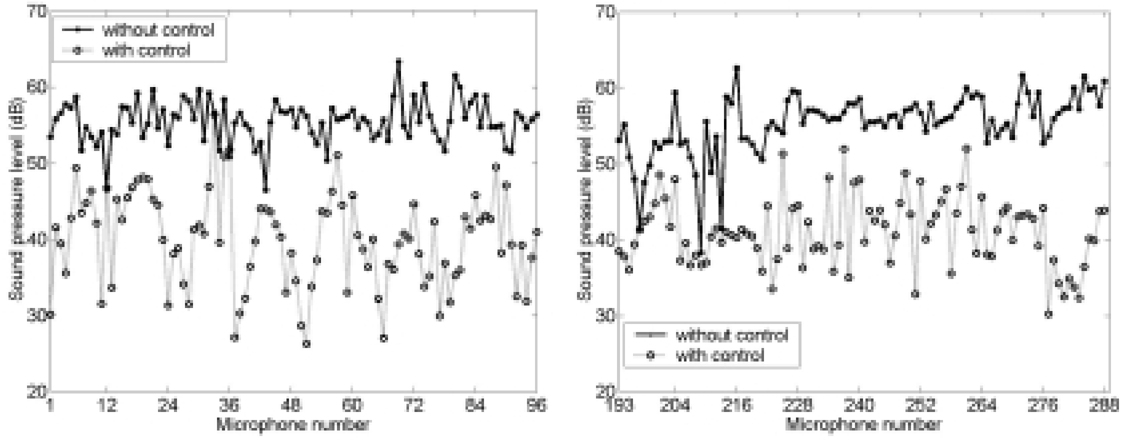

(a) east side of the sensing surface (b) north side of the sensing surface

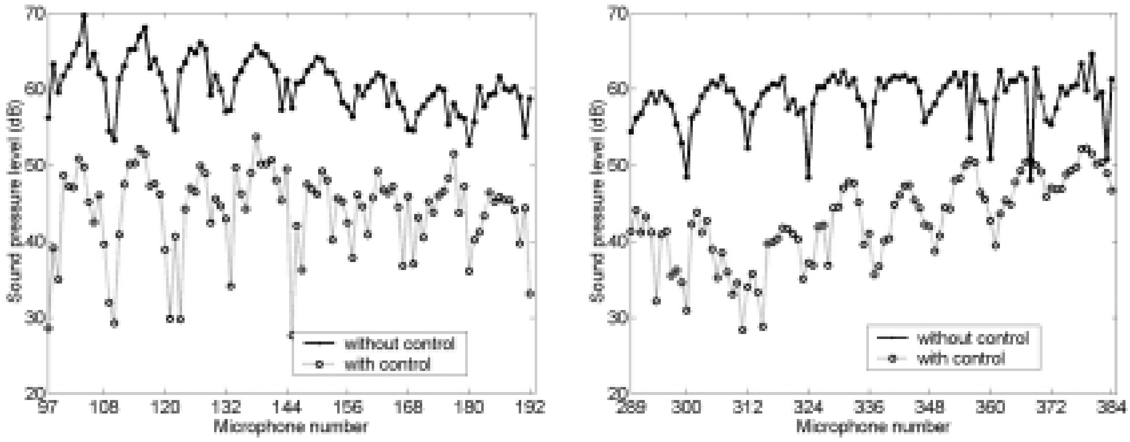

(c) west side of the sensing surface

(d) south side of the sensing surface

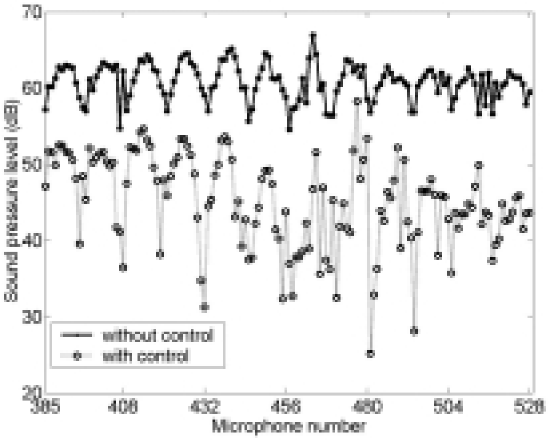

(e) top of the sensing surface

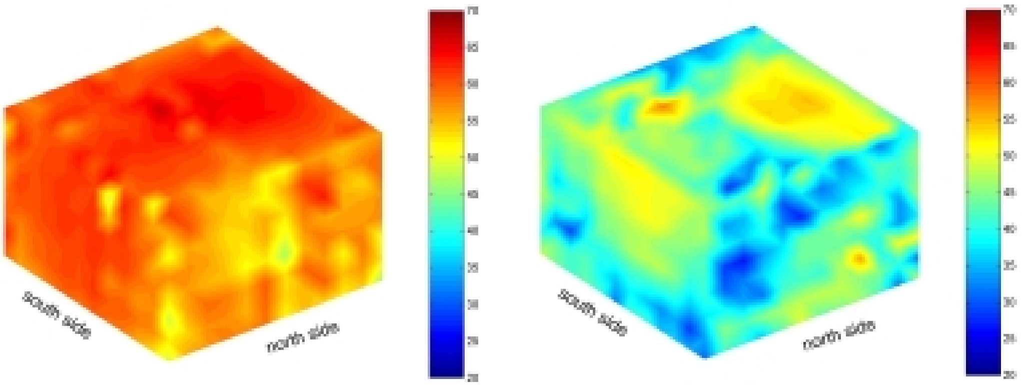

(f) before control

(g) after control

Figure 6.15 Distribution of sound pressure level at monitor microphones at 100 Hz before and after control (8 control sources and 8 error sensors)

6.3.2 Effect of the number of control sources on the control results

In this section, the effect of the number of control sources on the control performance at the *error sensors* is evaluated using measured data. Due to the limitation of the number of controller channels, only 8 error sensors were used so that the number of control sources were from one to eight, otherwise, an infinite number of 'optimum' control source strength vectors will be produced. For the case of using 8 control sources, the sound pressure reduction at the eight error sensors tends theoretically to an infinite value. In other words, the residual (controlled) sound field at the error sensors will be zero. To account for the influence of noise on the simulation results, a 1% error in the control forces was added. This results in the noise reduction predicted using 8 control sources and 8 error sensors dropping from an infinite value to 40 dB. The experimental procedure was the same as that described in section 6.3.1. Figure 6.16 shows predicted results and measured results.

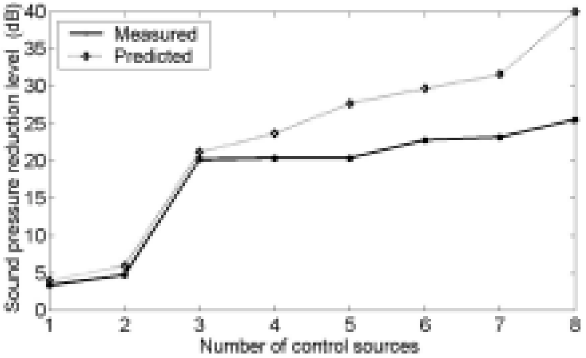

(a) at 100 Hz

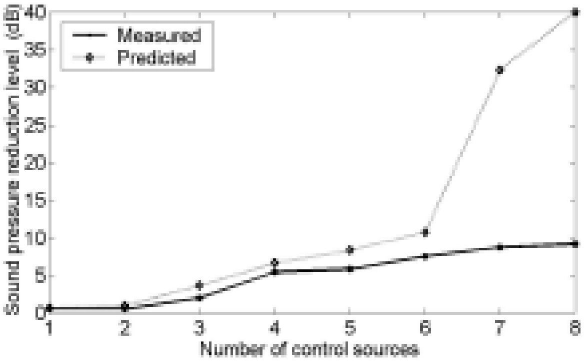

(b) at 200 Hz

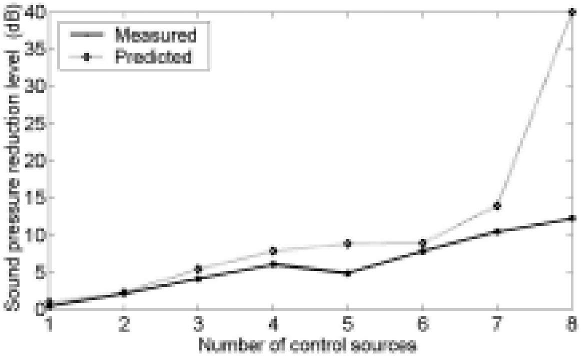

(c) at 300 Hz

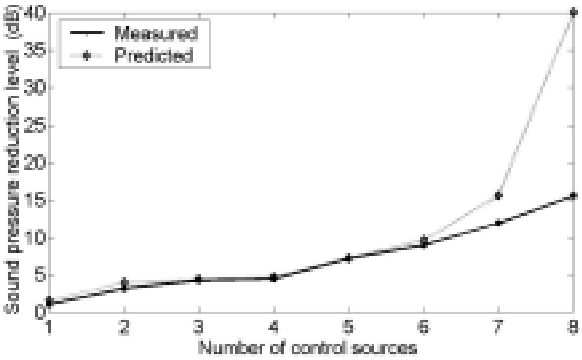

(d) at 400 Hz

Figure 6.16 Variation of the average noise reduction at the error sensors as a function of the number of the control sources, associated with 8 error sensors

As expected, the average sound pressure reduction level at the error sensors increased as the number of control sources increased for both predicted and measured results. Figure 6.16 shows a very good agreement between the predicted and measured results for a small number of control sources. However, the difference between predicted and measured values increased as the number of control sources increased, and it was worse at the lower frequencies. This may be due to some background noise from the measurement system.

6.4 Control mechanisms

Generally, for the active structural acoustic control system, there are two control mechanisms for attenuating the sound field when vibration control sources are used

(Snyder, S. D. and Hansen, C. H. (1991), Hansen, C. H. and Snyder, S. D. (1997)). The first is a reduction in the velocity levels of the principal offending modes. By this mechanism, termed *modal control*, the control effort is directed towards reducing the vibration levels of the structure, especially the modal vibration levels of the high radiation modes, so that the total sound power radiated by the vibrating structure will be attenuated. The other way for attenuating the radiated sound field is to reduce the radiation efficiency of the structure by changing the structure velocity distribution without necessarily reducing the structural velocity levels. Attenuating the sound field by altering the amplitude and phase relationship between modes to reduce the sound radiation efficiency has been named *modal rearrangement*. This section analyzes the control mechanisms for the control results achieved in Section 6.3 based on these concepts. The general mechanisms of active structural acoustic control by vibration control sources are discussed in more detail elsewhere (Hansen, C. H. and Snyder, S. D. (1997)).

To analyze the control mechanisms, structural responses to the shakers were measured at 224 points at 100 mm intervals on the transformer tank. Then the vibration levels of the transformer tank after control were calculated using resulting optimum force values from the minimization of the sum of the squared sound pressures at the *error microphones*. The associated vibration reduction levels at the sensing points are shown in Figure 6.17.

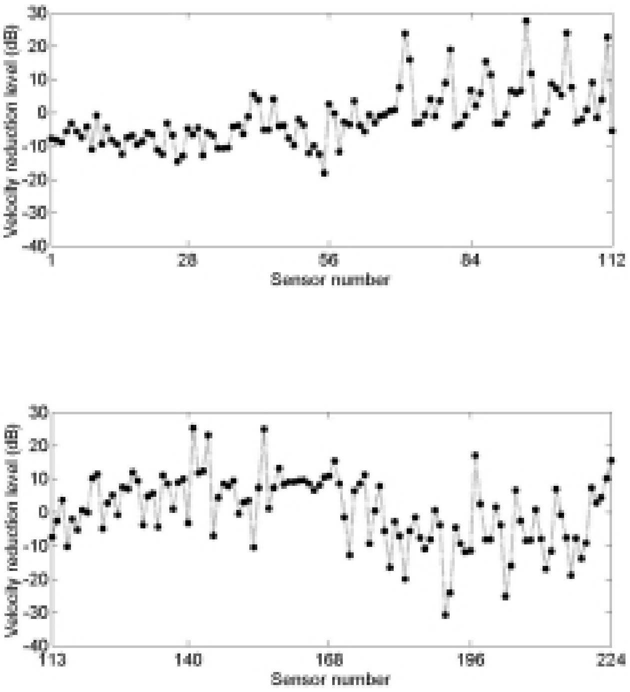

Figure 6.17 Vibration reduction level of the transformer tank at 100 Hz corresponding to the minimization of the sum of the squared sound pressures using 8 control sources and 8 error sensors.

The results demonstrate that the average squared structural velocity reduction level at the sensing points is 4.3 dB for 100 Hz excitation. By comparing this value with the predicted sound pressure reduction of 18.7 dB, it can be concluded that the sound field must be minimized by modal rearrangement of the transformer tank vibration. Figures 6.18-6.22 show the distribution of vibration levels on the transformer tank before and after control.

(a) before control

(b) after control

Figure 6.18 Distribution of velocity level on the transformer tank (top panel) corresponding to the minimization of the sum of the squared sound pressures using 8 control sources and 8 error sensors, at 100 Hz

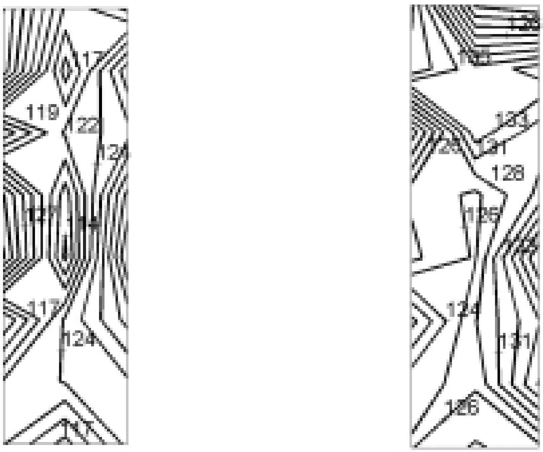

(a) before control (b) after control

Figure 6.19 Distribution of velocity level on the transformer tank (west panel) corresponding to the minimization of the sum of the squared sound pressures using 8 control sources and 8 error sensors, at 100 Hz

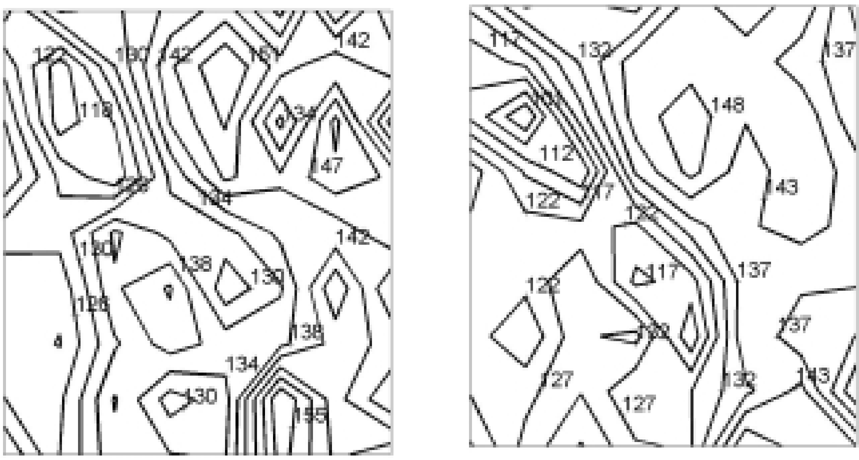

(a) before control (b) after control

Figure 6.20 Distribution of velocity level on the transformer tank (south panel) corresponding to the minimization of the sum of the squared sound pressures using 8 control sources and 8 error sensors, at 100 Hz

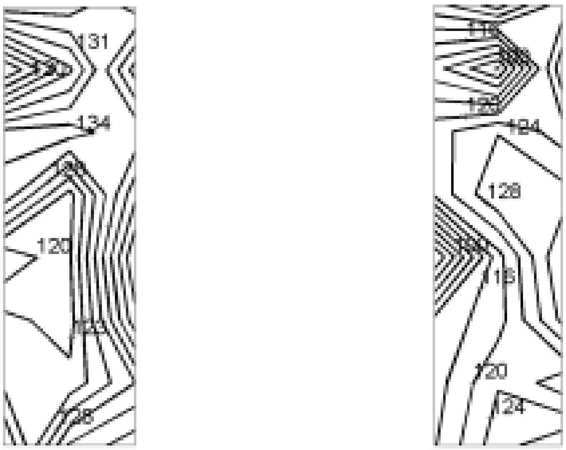

(a) before control (b) after control

Figure 6.21 Distribution of velocity level on the transformer tank (east panel) corresponding to the minimization of the sum of the squared sound pressures using 8 control sources and 8 error sensors, at 100 Hz

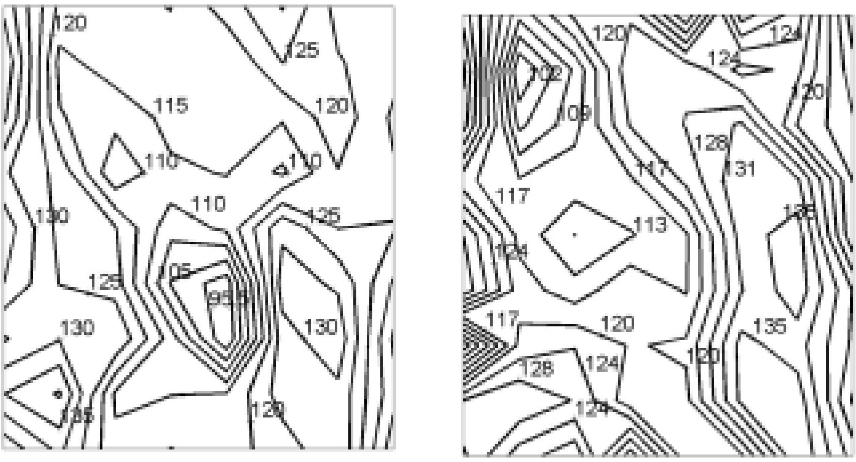

(a) before control (b) after control

Figure 6.22 Distribution of velocity level on the transformer tank (north panel) corresponding to the minimization of the sum of the squared sound pressures using 8 control sources and 8 error sensors, at 100 Hz

Figures 6.18-6.22 show that the structure vibration patterns were significantly changed after control. This alteration of the controlled vibration patterns resulted in decreasing sound radiation efficiency so that sound field was attenuated.

6.5 Conclusions

The aim of this chapter was to evaluate a physical system for the active control of noise radiated from a small transformer. The effect of error sensing strategies on the control performance and the optimization of the error sensor arrangement (number and location) were studied.

Two near-field error sensing strategies, the minimization of the sum of the sound intensities and the minimization of the sum of the squared sound pressures, were numerically evaluated using data measured on the small transformer. Results demonstrate that better control can be achieved using intensity minimization in the near-field, provided that there are a large amount of error sensors; otherwise, better results are obtained by using squared pressure minimization. This conclusion agrees with the theoretical results described in Chapter 5.

The numerical results show that for both sensing strategies, better control at the multiple monitor sensing positions can be achieved using optimally located error sensors than when using evenly spaced ones. Especially, for sound intensity minimization, a quite good result could be achieved using a small number of optimally located error sensors. For instance, when using 25 optimally located error sensors, approximately 37 dB reduction was achieved using sound intensity minimization, even though the result was around 15 dB less than that achieved using squared pressure minimization. However, the predicted results demonstrated that it was very difficult to minimize the sound field at higher frequencies, i.e. 200 Hz, 300 Hz and 400 Hz according to the control mechanisms.

The sound field radiated from the small transformer tank was minimized experimentally using 8 control sources and 8 sound pressure error sensors in an anechoic room. To generate the primary sound field, the transformer tank was excited by an inertial shaker at 100 Hz. Two inertial shakers were mounted to each side of the transformer (a total of eight) as the control sources and eight error sensors were located on a frame of 0.8 m from the transformer, as shown in Figure 6.1. The sound pressure reduction achieved using 8 control actuators and 8 error sensors was evaluated at 528 monitor sensing points over the frame surface. The results show that an average sound pressure reduction of 15.8 dB was achieved at the monitor sensing points using squared pressure minimization. This is similar to the predicted result of 18.7 dB, based on transfer function measurements. By analyzing the vibration patterns with and without control, it was shown that this sound reduction was mainly achieved by the modal rearrangement control mechanism. Due to the limitation of the number of controller channels, there were no measurements of the control performance for sound intensity minimization.

CHAPTER 7 PREDICTION OF THE SOUND FIELD RADIATED FROM A LARGE ELECTRICAL TRANSFORMER IN THE NEAR-FIELD

7.1 Introduction

In this chapter, predictions of the sound radiated from a large zone substation transformer were undertaken, with the aim of determining if it is possible to use active control to cancel the radiated noise. The test transformer, with the dimensions of 4.6×4.0×4.0 m (not including the insulating rod), was located at Cherry Gardens, South Australia. The maximum operating load of the transformer is 160 MVA and the usual operating load is 44 MVA (160A, 275KV). The transfer functions from the control source inputs (two acoustic type control sources and one vibration type control source) to error sensor outputs (sound intensity probes) and the sound filed radiated by the transformer alone were measured and these data were used to predict the noise reduction that could be achieved at the error sensor locations with an active noise control system. In the simulation, the cost functions to be minimized were squared sound pressure minimization and sound intensity minimization.

7.2 Measurement of transfer functions between control source inputs and error sensor outputs

A steel frame was constructed around the transformer to hold the sound intensity probes. It extended around all 4 sides and over the top of the transformer at a distance of 1 meter from the transformer as shown in Figure 7.1. Ninety six intensity probes (dual microphone type) at 1.5 m intervals were placed on the frame for sensing the sound field. Each sound intensity probe consisted of two electret microphones (and preamplifiers) that were calibrated for each tonal frequency, i.e. 100 Hz, 200 Hz and 300 Hz, as shown in Figure 7.2. A calibration procedure for the sound intensity probes is discussed in Appendix B.

Figure 7.1 The test transformer

Figure 7.2 Sound intensity probe

For measuring the primary sound field with the transformer energized, the intensity probes were connected through the microphone pre-amplifiers and a multiplexer to a Brüel & Kjær type 2816 multi data acquisition unit with four Brüel & Kjær type 3022 4-channel input modules. Data were transferred into a PC computer, in which Brüel & Kjær PULSE LabShop V. 4.1 was installed. As the sound pressure at each microphone on the intensity probe is a time dependent quantity, a reference signal is required to determine the phase. Microphone *A* on intensity probe #1 was used as this phase reference, and the transfer function from every microphone to this reference was measured. A photograph of the experimental set-up is shown in Figure 7.3.

Figure 7.3 A picture of the experimental set-up

Figure 7.4 A picture of a swing hammer

For measuring the transfer functions, $\boldsymbol{Z}_{QP(f)}$, from the force inputs to the error sensor outputs, a swing hammer (as shown in Figure 7.4) was used to impact the transformer tank at the potential locations of the vibration control sources (around 200 positions), while the transformer was switched off. For collecting impact force data, a Brüel & Kjær type 4394 accelerometer was fixed to the back of the hammer. A signal proportional to the impact force was measured using the accelerometer connected through a Brüel & Kjær type 2635 charge amplifier to the Brüel & Kjær type 2816 multi-channel data acquisition unit. The block diagram of the experimental set-up is shown in Figure 7.5.

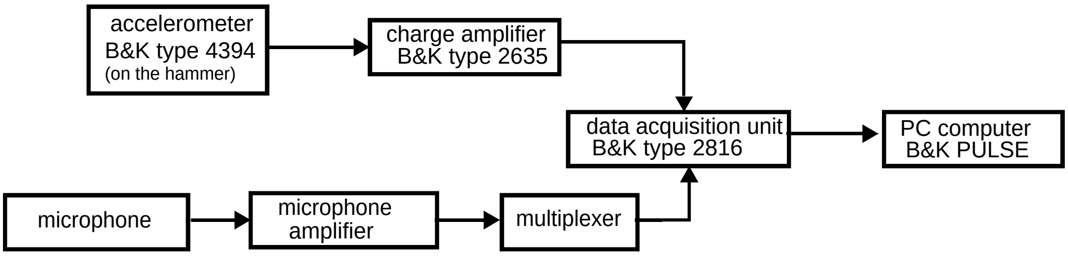

Figure 7.5 A block diagram of the experimental set-up of force source test

To measure the transfer functions, $\boldsymbol{Z}_{QP(a)}$, from the acoustic control sources (loudspeaker) to error sensor outputs, the sound field was generated by a loudspeaker at the potential positions of the acoustic control sources (around 350 locations). The loudspeaker, which was specially designed for the project application (Hansen et. al. (1998)), was driven by a signal generator which generated sine waves at the frequencies of interest, 100 Hz, 200 Hz and 300 Hz, through a power amplifier. The block diagram of the experimental set-up is shown in Figure 7.6.

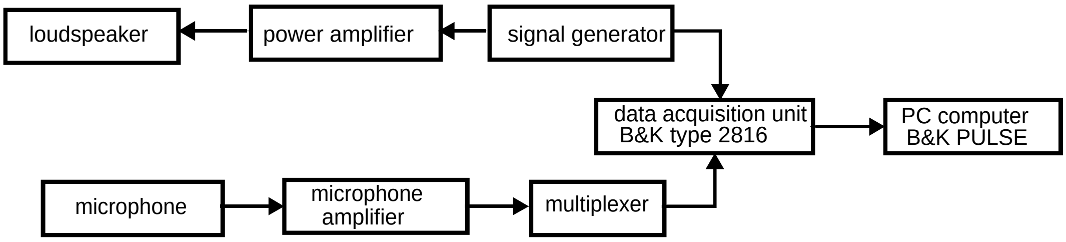

Figure 7.6 The experimental set-up of acoustic source test

For measuring the acoustic responses produced by the curved panel-cavity source, a curved panel-cavity source with the configuration described in Chapter 3 was used to generate a sound field. The experimental set-up was the same as that used for the loudspeaker test. However, because the opportunities for switching off the test transformer were limited by the electricity authority, only 35 potential locations (on one side of the transformer) were selected for measuring the transfer functions relating the curved panel-cavity inputs and the error sensor outputs.

7.3 Predicted results at the error sensors

The noise reduction at the *error sensors* for the large power transformer was predicted on the basis of transfer function measurements. To obtain the maximum achievable noise reduction at the error sensors, the control source locations were optimized by means of the genetic algorithm searching procedure. The optimization procedure follows the discussion of Chapter 6. The cost function defined by the quadratic optimization theory (QOT) was first optimized at the error sensors. The result was then used as a variable in the optimization search procedure to determine the control source locations corresponding to the maximum noise reduction at the error sensors. Three types of control sources were considered, i.e. the force type source, the loudspeaker source and the resonant curved panel-cavity source; and two near-field sensing strategies were considered, i.e. intensity minimization and squared pressure minimization. Due to insufficient data being available (as a result of the limited access to the transformer provided by the electricity authority), no evaluation of the control results in the far-field was given.

In general, for a practical active noise and vibration control system, the number and location of the actuators is limited and the configuration of these actuators should be suitable for minimizing the noise at all frequencies of interest. To obtain the control source locations corresponding to minimizing the cost function at the error sensors, which were suitable for all three frequencies discussed in this chapter, the optimization search procedure was first used to produce a group of optimal control positions at 100 Hz. The same locations were then used to calculate the noise reduction at 200 Hz and 300 Hz individually. Finally, the optimal control source configuration for each frequency was adjusted to achieve a balanced control performance for all three frequencies when using one common control source configuration, based on the ‘balance criterion’. To guarantee the control results, the balance criterion, which represents the departure from the maximum achievable reduction, must be reasonably small. In this chapter, this quantity was approximately 3 dB.

Figure 7.7 shows the sound field distributions radiated by the transformer alone at 1 meter from the transformer tank.

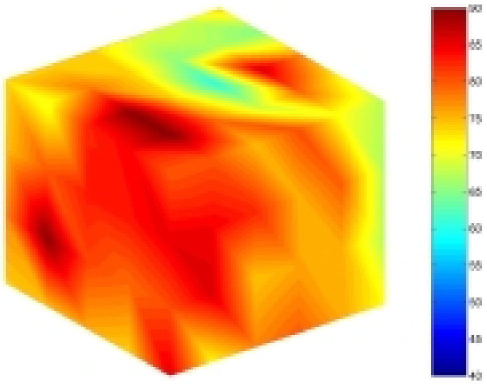

(a) at 100 Hz

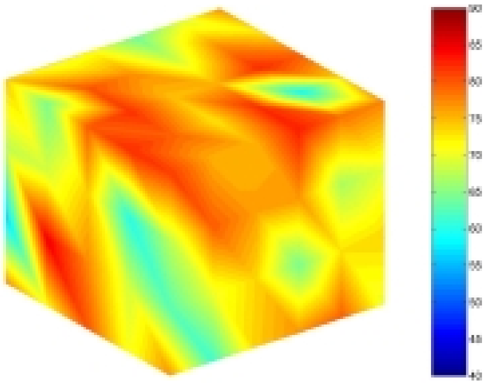

(b) at 200 Hz

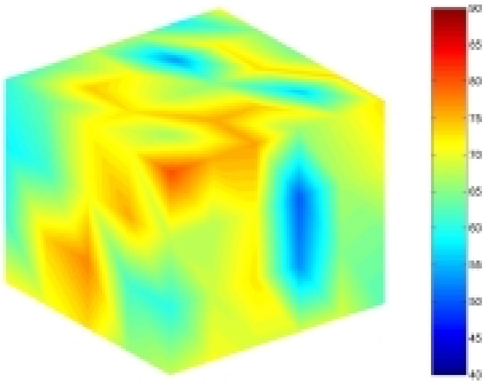

(c) at 300 Hz

Figure 7.7 Distribution of sound pressure level without control, one meter from the transformer

7.3.1 Results predicted by squared sound pressure minimization in the near-field

7.3.1.1 Force type control sources

Figure 7.8 shows the average sound pressure reduction at the error sensor locations for 100 Hz, associated with 80 optimally located control source (force type) and 96 fixed error sensors. From the figure, it can be seen that the sound pressure was significantly reduced at most error sensing locations even though the noise was increased at a few sensing locations (2 locations). The largest overall sound pressure reduction was approximately 56.3 dB and the largest overall increase of the sound pressure level was 0.9 dB for the force control sources. The average sound pressure reduction at the error sensors was 23.1 dB. Figure 7.9 shows the distribution of the sound pressure at the error sensors before and after control.

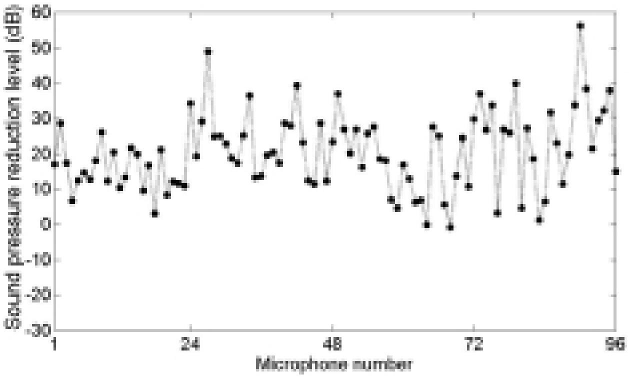

Figure 7.8 Sound pressure reduction level for 100 Hz at a distance of 1 meter from the transformer after force type source control (80 control sources at optimized locations).

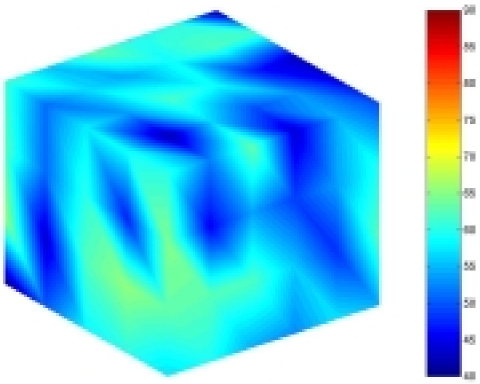

(a) distribution of sound pressure after force control at 100 Hz

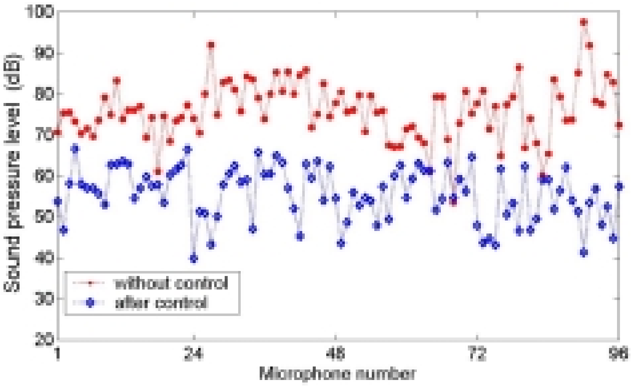

(b) comparison of sound pressures at error sensors
before and after force control at 100 Hz

Figure 7.9 Predicted distribution of sound pressure level for 100 Hz at a distance of 1 meter from the transformer without control and after force-source control (80 control sources at optimized locations).

The sound pressure reductions at the error sensors for 200 Hz and 300 Hz were calculated for fixed control source locations corresponding to the optimal control source locations at 100 Hz (‘compromised’ locations). Figure 7.10 shows the comparisons between the sound pressure reductions associated with optimized control source locations at 100 Hz or 200 Hz or 300 Hz and those associated with ‘compromised’ control source locations. In the figure, the columns labelled ‘optimum’ represent the average sound pressure reductions at the error sensors associated with the optimized control source locations at each frequency individually, and the columns labeled ‘compromised’ represent the average sound pressure reductions at the error sensors associated with the optimized control source locations at 100 Hz for each frequency. In this case, the maximum difference in the average sound pressure reductions between the 'optimum' and 'compromised' cases was 2.4 dB at 200 Hz. The average sound pressure reductions at the error sensors using the 'compromised' control source locations were 22.7 dB, 13.6 dB and 14.9 dB for 100 Hz, 200 Hz and 300 Hz respectively, and the average sound pressure reductions at the error sensors using the 'optimum' control sources were 23.1 dB, 16.0 dB and 16.0 dB for 100 Hz, 200 Hz and 300 Hz, respectively.

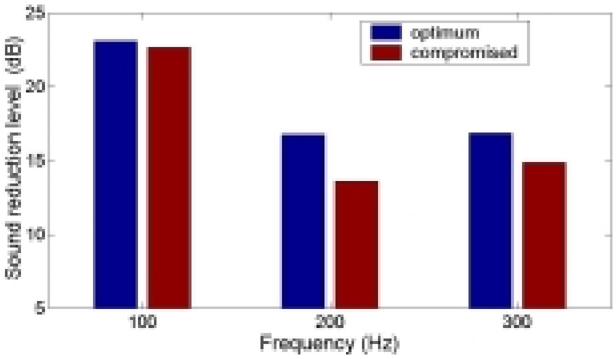

Figure 7.10 Comparisons between the average sound pressure reductions at the error sensors using optimized control source locations and 'compromised' control source locations, (80 force type control sources and 96 error sensors)

Figures 7.11-7.14 show the average sound pressure reductions and the sound pressure distributions for 200 Hz and 300 Hz, when using the 'compromised' control source locations. As with the case for 100 Hz, the sound pressure was reduced at most error sensing points, for both the frequencies of interest. However, the sound pressure at several points did increase. The largest overall increase of the sound pressure level was 13.1 dB for 200 Hz and 20.0 dB for 300 Hz. However, by observing Figures 7.12 and 7.14, one can see that in this study case, all pressure increases occur at sensing locations where the primary sound pressures are every low. So the controlled sound pressure at these locations was still quite low even though the sound pressure increased.

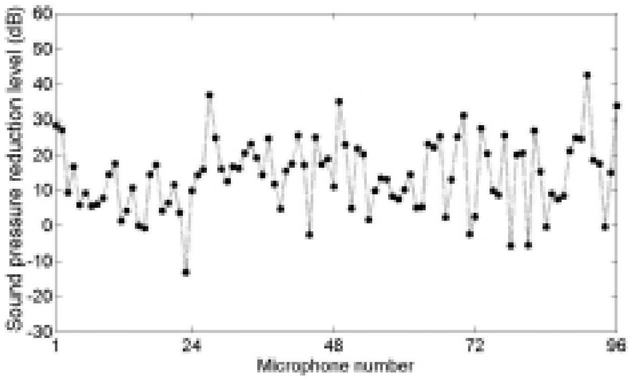

Figure 7.11 Sound pressure reduction level at the error sensors for 200 Hz at a distance of 1 meter from the transformer after force type source control (80 control sources at 'compromised' locations).

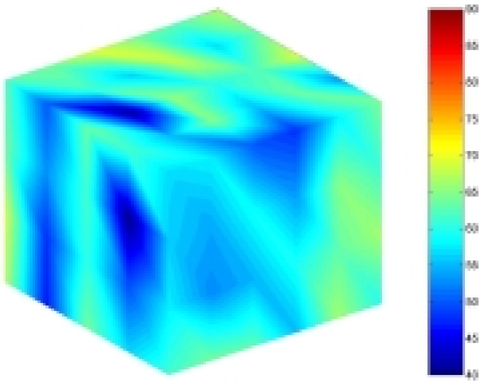

(a) distribution of sound pressure after force control at 200 Hz

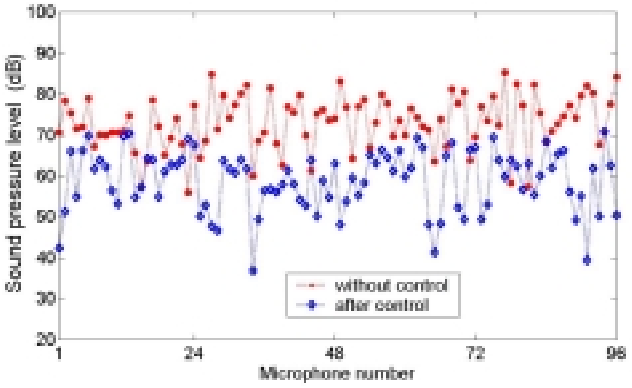

(b) comparison of sound pressures at error sensors
before and after force control at 200 Hz

Figure 7.12 Predicted distribution of sound pressure level for 200 Hz at a distance of 1 meter from the transformer without control and after force-source control (80 control sources at 'compromised' locations).

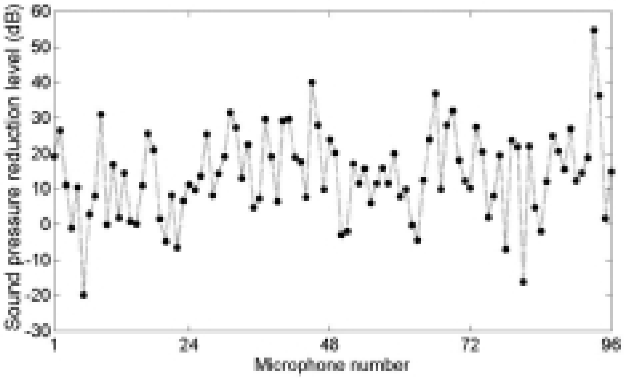

Figure 7.13 Sound pressure reduction level at the error sensors for 300 Hz at a distance of 1 meter from the transformer after force type source control (80 control sources at ‘compromised’ locations).

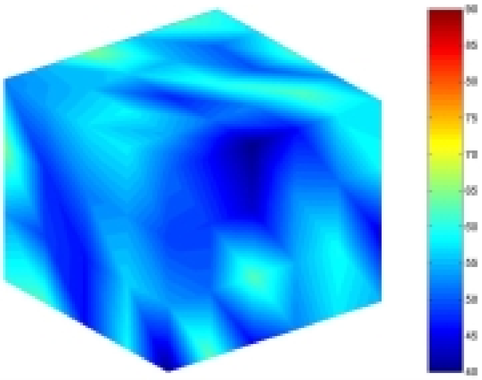

(a) distribution of sound pressure after force control for 300 Hz

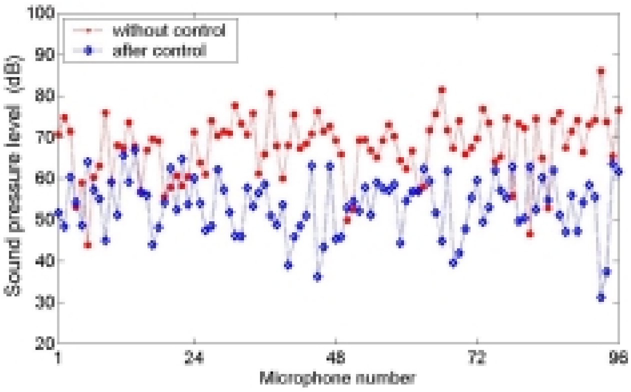

(b) comparison of sound pressures at error sensors
before and after force control for 300 Hz

Figure 7.14 Predicted distribution of sound pressure level at 300 Hz at a distance of 1 meter from the transformer without control and after force-source control (80 control sources at ‘compromised’ locations).

7.3.1.2 Loudspeaker type control sources

The sound pressure at the error sensors was also minimized using loudspeaker control sources. The prediction procedure used was the same as in section 7.3.1.1 for the force control sources. The average sound pressure reductions at the ‘compromised’ control source locations were 18.1 dB, 11.5 dB and 8.5 dB at 100 Hz, 200 Hz and 300 Hz respectively, and the average sound pressures reductions at the optimized control sources were 19.6 dB, 12.8 dB and 10.3 dB for 100 Hz, 200 Hz and 300 Hz respectively, as shown in Figure 7.15.

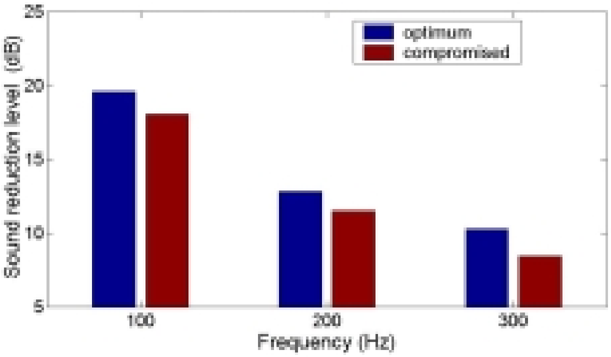

Figure 7.15 Comparisons between the average sound pressure reductions at the error sensors using the optimized control source locations and compromised control source locations, (80 loudspeaker type control sources and 96 error sensors)

By comparing Figure 7.15 with 7.9, for cases of the control associated with the optimized control source locations for each frequency individually, one can see that the maximum sound pressure reductions at the error sensors obtained using the force control sources are higher than those achieved using the loudspeaker control sources for each frequency. This is because, in general, the sound reduction levels achieved with each acoustic type control source may be less than those achieved with each vibration control source, especially if the structural dimensions of the noise source are approximately equal to (or larger than) the acoustic wavelength at the frequency of interest. A comparison of the average sound pressure reductions at the error sensors obtained using the vibration control sources with those obtained using the loudspeakers is shown in Figure 7.16.

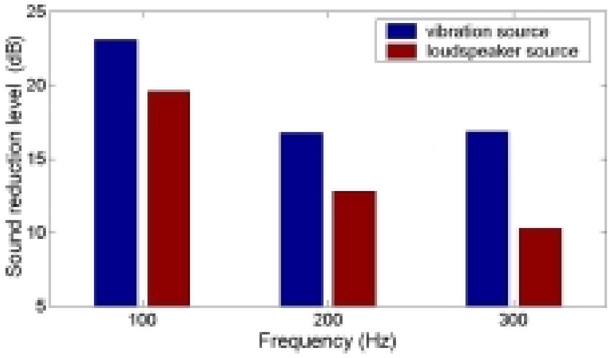

Figure 7.16 Average sound pressure reductions at the error sensors obtained using vibration control sources and loudspeakers, (80 control sources at optimized locations and 96 error sensors)

7.3.1.3 Curved panel type control sources

The aim of this section is to study the feasibility of using the curved panel-cavity sources to cancel the transformer noise. The prototype of the curved panel with a backing cavity designed in Chapter 3 was used to generate a sound field at 100 Hz and 200 Hz (the original design of the system was for these two frequencies), and the transfer functions from the curved panel inputs (35 potential locations) to the error sensor outputs were measured individually. Because 35 potential control source positions (on the south side wall of the transformer) were selected for testing, only 24 error sensors on the south side were considered for predicting the sound pressure reduction, otherwise, poor control results would be obtained if the control sources on one side are used to minimize the sound pressure at total 96 error sensors surrounding the transformer. The average pressure reduction at 24 error sensors was predicted based on these measurements. Figure 7.17 shows a comparison of the average sound pressure level reductions at 24 error sensors achieved using both the loudspeaker sources and the resonant curved panel sources. In this case, the control sources were evenly spaced and the average sound pressure reduction at 24 error sensors was calculated as a function of the number of control sources. From Figure 7.17, one can see that good control results at 24 error sensors can be obtained using the curved panel sources except for using 12 sources at 200 Hz. At 100 Hz, the sound pressure reduction achieved using 16 curved panel sources at 24 error sensors was 4 dB higher than that obtained using 16 loudspeakers. It was postulated that this was because the curved panel sources provided a larger radiation surface than the loudspeaker sources and might match the primary sound field better than the loudspeaker sources.

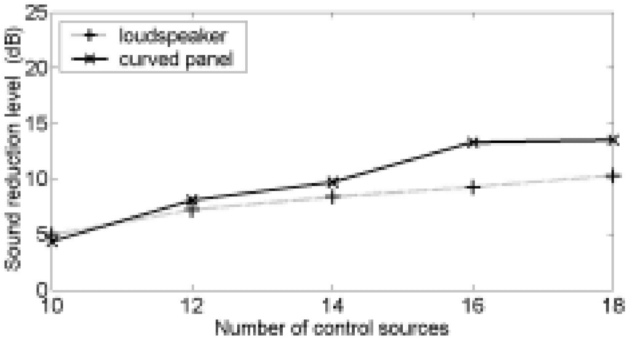

(a) 100 Hz

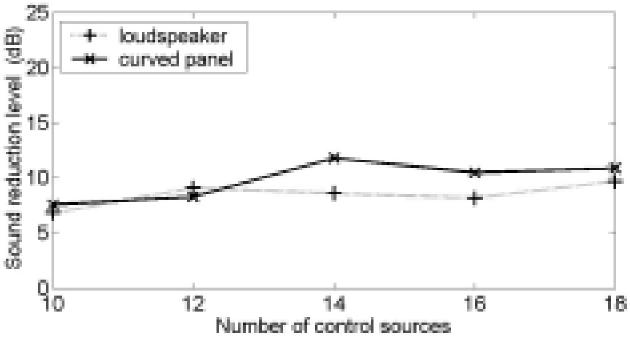

(b) 200 Hz

Figure 7.17 Comparison of the average sound pressure level reductions at the error sensors achieved using the curved panels with those achieved using the loudspeakers for the larger transformer noise control (using evenly spaced control sources and 24 error sensors)

Figure 7.18 shows that the average sound pressure reductions at 24 error sensors achieved using optimally located curved panel sources and loudspeaker sources. From Figure 7.18(a), it can be seen that in this case, better controls for 100 Hz were achieved using the loudspeakers. These results appear to be contrary to those shown in Figure 7.17. This is because there were many more potential locations of the loudspeaker sources (87 options) than those of the curved panel sources (35 options) during the optimization search. Increasing the number of options in the searching procedure provides a method for the optimization search procedure to more effectively adjust the phases and the magnitudes between the control sources to achieve the maximum noise reduction.

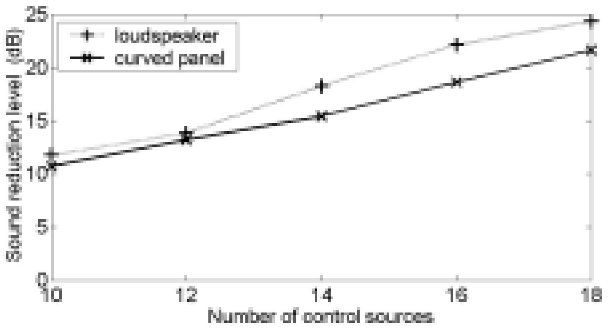

(a) 100 Hz

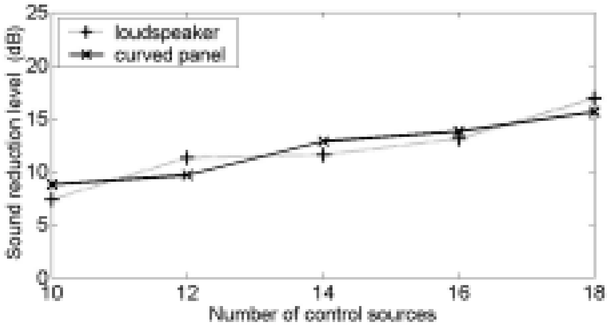

200 Hz

Figure 7.18 Average sound pressure reductions at 24 error sensors using both curved panels and loudspeakers for the larger transformer noise control (at optimized control source locations)

The results from Figure 7.18(b) show the control results at 200 Hz for both types of the control sources were quite similar. The reason for this is that in general, when using acoustic control sources to cancel the noise radiated from a panel with dimensions that are much larger than the acoustic wavelength (especially for higher frequencies), the important aspect of improving the control is the number of control sources, rather than the type of the acoustic control sources (Qiu and Hansen (2000)). Thus, there was no significant improvement of the control results at 200 Hz when using loudspeaker control sources over the use of curved panel type control sources in this case study.

7.3.2 Effect of the number and the locations of the control sources on the control performance

Previous work (Hansen et al (1999)) shows that the control source arrangement (number and location) will determine the achievable sound field reduction with an ideal error sensor arrangement. In this section, the effect of the numbers and the locations of the control sources on the control performance was evaluated. The average sound pressure reduction at 96 error sensors was calculated as a function of the number of control sources that were optimally located. Both vibration control sources and loudspeaker sources were used. The variation of the average sound pressure reduction at the error sensors with the number of control sources is shown in Figure 7.19 (based on 96 error sensors). As expected, the average sound pressure reduction at the error sensors increased as the number of control sources increased. For the frequencies of interest, the radiated sound resulted from the complex interaction of many structural modes, thus increasing the number of control sources allows the control procedure to more easily vary the phases and magnitudes between the control sources and the primary source.

By comparing Figure 7.19(a) and (b), one can see that to achieve the same sound pressure reduction, ten more sources were required when using the loudspeaker control sources than when using the force control sources. This is because in general, the sound reduction levels achieved using each vibration control source may be higher than those obtained using each acoustic control source, especially when the structural dimensions are larger than the acoustic wavelength at the frequency of interest. Thus, to achieve a certain sound level reduction at the frequency of interest, more acoustic control sources were required than vibration control sources.

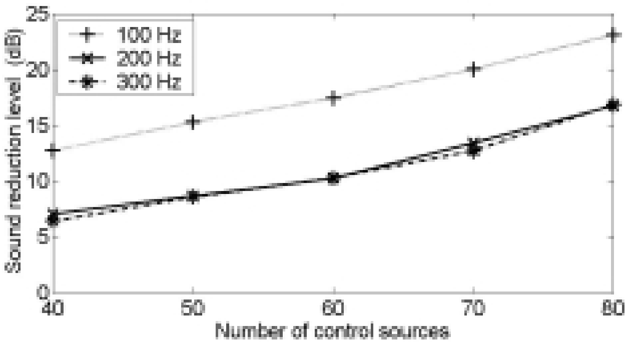

(a) force control sources

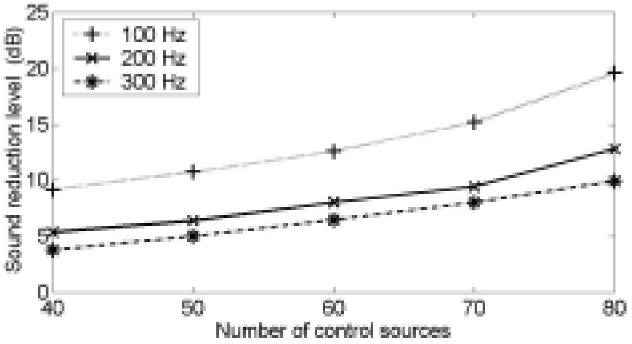

(b)loudspeaker sources

Figure 7.19 Variation of the average sound pressure reductions at 96 error sensors with the number of control sources; (a) force control sources, (b) loudspeaker sources

To evaluate the effect of the locations of the control sources on the control performance, the average sound pressure reductions at the error sensors were calculated using arbitrarily located control sources. Comparisons of these results with those achieved using optimally located control sources are given in Figures 7.20 and 7.21. In these cases, 80 control sources and 96 error sensors were used. From the figures, the control results were obviously improved when the control source locations were optimized. The maximum increase in the average sound pressure reduction at the error sensors is approximately 6 dB for both types of control source.

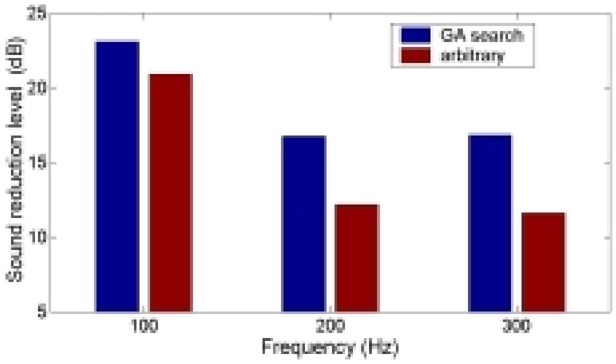

Figure 7.20 Comparisons of control results associated with optimum locations of control sources with those associated with arbitrarily selected locations; (80 vibration control sources and 96 error sensors)

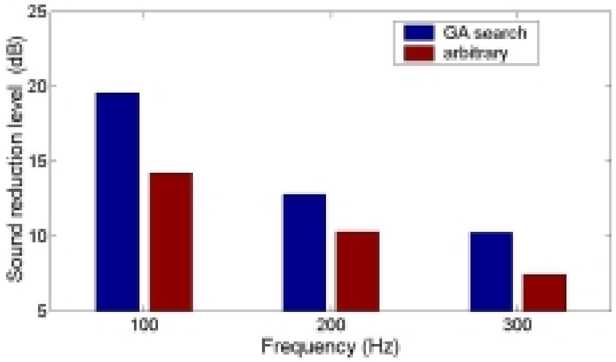

Figure 7.21 Comparisons of control results associated with the optimum locations of the control sources with those associated with arbitrarily selected locations; (80 loudspeaker control sources and 96 error sensors)

7.3.3 Results predicted by sound intensity minimization in the near-field

In this section, the average sound intensity reduction at the error sensors is predicted using data measured on site. Two types of the control sources, i.e. force type sources and loudspeaker sources, were used and the control source locations were optimized corresponding to the maximum average sound intensity reduction at the error sensors. Figure 7.22 shows the average sound intensity reduction at the error sensors for 100 Hz, 200 Hz and 300 Hz using individually optimized control source locations.

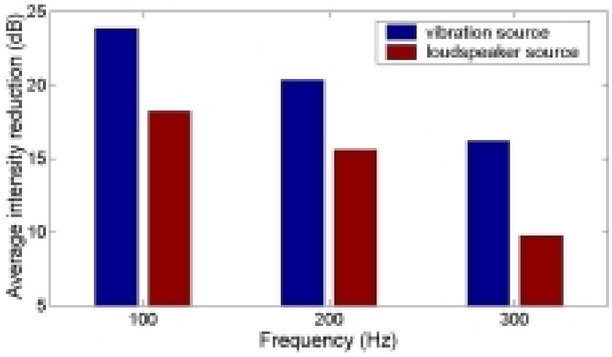

Figure 7.22 Average sound intensity reduction at the error sensors, associated with the optimized control source locations, (80 control sources and 96 error sensors)

Figure 7.22 shows that for the case of using the vibration control sources, average intensity reductions of 23.9 dB, 20.4 dB and 16.2 dB at the error sensors were achieved for 100 Hz, 200 Hz and 300 Hz respectively, and for the case of using the loudspeaker sources, 18.2 dB, 15.6 dB and 9.8 dB reduction at the error sensors was achieved for 100 Hz, 200 Hz and 300 Hz respectively. It should be emphasized that the minimization of the sum of the active intensities in the near-field does not necessarily result in the reduction of the sound pressure in the near-field which is a combination of the active energy and reactive energy. In Figure 7.23, the results show the sound pressure level reductions at the monitor sensors (near-field) before and after control.

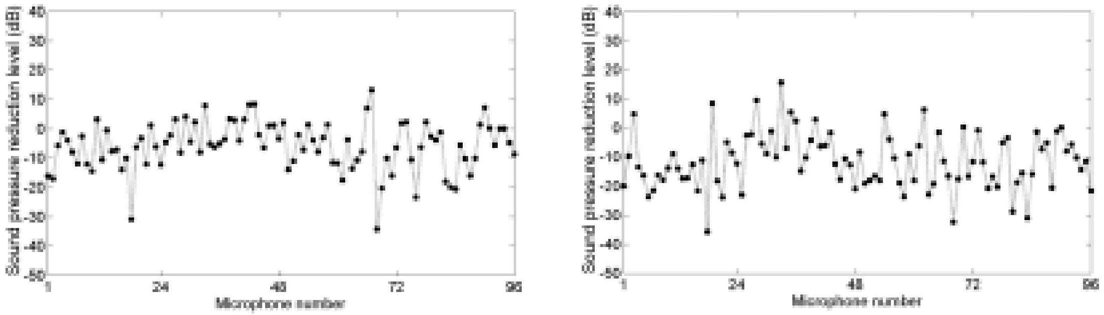

force type sources loudspeaker sources

(a) 100 Hz

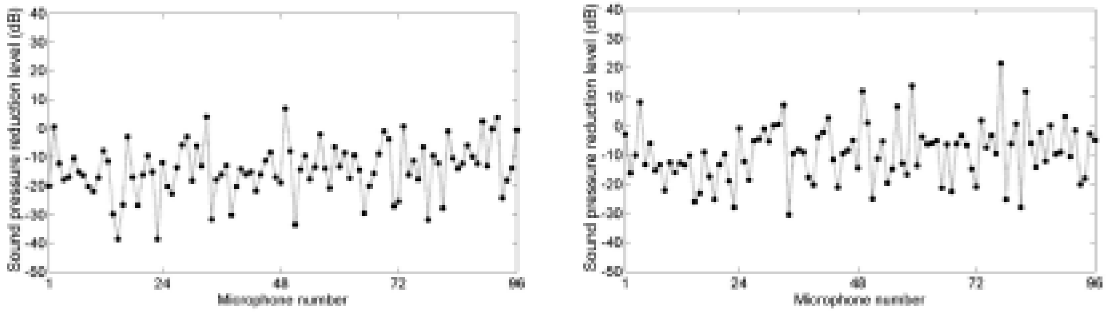

force type sources loudspeaker sources

(b) 200 Hz

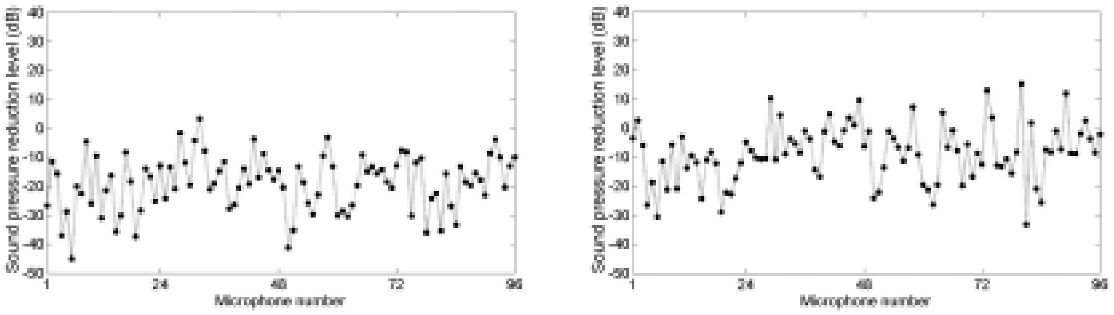

force type sources loudspeaker sources

(c) 300 Hz

Figure 7.23 Sound pressure reduction at the monitor sensors before and after intensity minimization in the near-field

In the figure, the controlled sound pressures at the monitor sensors were calculated using the control forces that produced the minimization of the sum of the active intensities at the error sensors, and the transfer functions relating these control sources to the monitor sensors. From Figure 7.23, it can be seen that for both types of control source, the sound pressures at the monitor sensors increased after minimizing the sum of the sound intensities at the error sensors, which were at the same locations as the monitor sensors. As discussed in Chapter 5, measurements of the sound pressures in the near-field consist of the propagating energy (active) and the non-propagating energy (reactive). In this case study, the cost function that was minimized was the sum of the sound intensities (active) at the error sensors in the near-field, which provided an indication of energy propagating to the far-field. Thus, this type of control cannot guarantee that the total energy at the error sensors (in the near-field), which is a combination of the propagating energy and non-propagating energy, can be minimized. The total energy in the near-field may increase after intensity minimization, resulting in an increase in the non-propagating energy and near-field sound levels.

7.4 Estimation of the global sound power reduction

Until now, only the prediction of the control results at the error sensors for the large transformer (due to the limitation of data) has been discussed. However, it may be interesting to estimate the global sound power reduction for the large transformer, based on the results on the small transformer described in Chapter 6. For this purpose, the following assumptions were made:

- in Chapter 6, the number of monitor sensors (492) for evaluating the control performance was sufficiently large so that the average sound intensity reduction at the monitor sensors could adequately represent the global sound power reduction;

- definition of the regions in a sound field radiated by a source was based on the classification given by Bies and Hansen (1996), namely, the type of sound field was defined according to the source size normalized by the acoustic wavelength and the distance between the source and sensing locations, which was normalized by the characteristic source dimension.

For comparing the reduction of noise radiated from different size transformers, the sound field was normalized as the hydrodynamic near-field, the geometric near-field and the far field (ref. Figure 5.13). To do this, the diagonal of the transformer tank, l_d, was selected as the characteristic source dimension for normalizing. Table 7.1 shows the characteristics of the sound fields at the error sensing locations for the frequencies of interest for both the large transformer and the small transformer.

Table 7.1 The characteristics of the sound fields radiated from transformers at error sensing locations

	100 Hz	200 Hz	300 Hz
large transformer	transition region	transition region	geometric near-field
small transformer	transition region	transition region	geometric near-field

Table 7.2 Average sound intensity reduction at the monitors sensors for the small transformer, using 8 force type control sources (dB)

cost function	sound pressure minimization			sound intensity minimization		
error sensor number	15	105	195	15	105	195
100 Hz	45.3	44.7	33.4	38.9	50.8	50
200 Hz	7.9	7.4	7.1	2.7	6.3	10.2
300 Hz	2.9	3.2	3.2	1.1	2.9	3.4

Note: the results in the table correspond to Figures 6.7 and 6.8.

The average sound reduction at the monitor sensors on the small transformer (achieved using both pressure minimization and intensity minimization) is summarized in Table 7.2 and used as a reference value for estimating the sound power reduction on the large transformer. For this case, eight control sources were used and error sensors were optimally located.

In general, more control sources may be required to reduce the noise radiated from a larger structure than the noise radiated from a smaller structure, if the characteristics of the sound fields are similar. Thus, referring Tables 7.1 and 7.2, one might expect a global sound power reduction of approximately 40 dB at 100 Hz by sound pressure minimization in the transition region, when using 80 force type control sources. If a sufficient number of error sensors are used, a global sound power reduction of approximately 45 dB at 100 Hz might be expected by using sound intensity minimization in the transition region, when using 80 force type control sources. For the higher frequencies, 200 Hz and 300 Hz, it is difficult to give estimated reduction values for the large transformer, due to poor reference values resulting from the control results on the small transformer.

It must be noted that the above results (estimated sound power reduction for the large transformer) were limited by following conditions:

- for the small transformer, the noise reductions at the monitor sensors were predicted using optimally located error sensors;
- the characteristics of the sound field were only defined by the normalized dimensions of the noise sources and the normalized distance between the source surface and the sensing locations; on the other hand, the complex distribution of the sound field at the sensing points, which might affect the control results, was not considered;

- noise radiated by the small transformer tank was generated by an inertial shaker, rather than an operating transformer.

7.5 Conclusions

This chapter presented the predicted reduction by active control of noise radiated from a large power transformer in the near-field, based on transfer function measurements made on site. To do this, the sound radiation from the transformer alone and the transfer functions between the control sources and the error sensors were measured. Ninety six error sensors were located on a steel frame that surrounded the transformer in the near-field. The distance of the frame from the transformer was 1 meter. The sound radiation at the error sensors was minimized using vibration type control sources, loudspeaker sources and curved-panel sources. The cost functions that were minimized were the sum of the squared sound pressures at the error sensors and the sum of the sound intensities at the error sensors. To obtain the maximum achievable noise reduction at the error sensors, the control source locations were optimized by the GA search procedure. The results demonstrated that for the case of squared sound pressure minimization, optimally located control sources resulted in better sound radiation control than arbitrarily selected ones. Tonal noise at 100 Hz, 200 Hz and 300 Hz could be reduced respectively by 23.1 dB, 16 dB and 16 dB for vibration control sources, and 19.6 dB, 12.8 dB and 10.3 dB for loudspeaker control sources, when using 80 control sources at the optimized locations and 96 error sensors. Also, the results showed that it was possible to find a set of control source locations where slightly sub optimal controls could be achieved for all three frequencies, for instance, for the vibration control sources, average pressure reductions of 22.7 dB, 13.6 dB and 14.9 dB could be achieved respectively, and 18.1 dB, 11.5 dB and 8.5 dB could be achieved for the loudspeaker sources, when using 80 control sources at the ‘compromised’ locations and 96 error sensors.

The capability of the curved panel-cavity sources for canceling transformer noise was evaluated using data measured on site. Only those transfer functions corresponding to the south side of the transformer tank (35 potential control source locations and 24 fixed error sensor locations) were used. The average sound pressure reductions at the error sensors were calculated using evenly spaced and optimally located control sources. By comparing these results with those achieved using the loudspeaker sources, it was found that for the case of evenly spaced control sources, higher sound pressure reduction at the error sensors could be obtained using the curved panel sources. But for the case of optimally located control sources, the results turned out contrary to the above. The reason for this is because there were more potential control source locations for the loudspeakers during the optimization search than for the curved panel sources. This large number of potential locations provided a method for the optimization search procedure to more effectively adjust the phase and amplitude between the control sources to achieve the maximum sound reduction.

Results from intensity minimization in the near-field demonstrated that the sound pressure at the monitor sensors (near-field) could increase when the average active intensity at the error sensors (same locations as the above monitor sensors) was minimized. This is because in the near-field, measurements of the active intensity only correspond to the propagating energy rather than to the total energy field which is defined as a combination of the propagating energy (active) and the non-propagating energy (reactive). Thus, intensity minimization does not guarantee the minimization of the non-propagating energy in the near-field so that the near-field sound level may increase, as a result of sound intensity minimization.

Finally, the global sound power reduction was estimated based on the predicted results on the small transformer, following several assumptions. The results demonstrated that it was possible to globally reduce noise radiated from large transformers at 100 Hz and results for 200 Hz and 300 Hz were inconclusive.

CHAPTER 8 CONCLUSIONS AND FUTURE WORK

8.1 Conclusions

The aim of the work described in this thesis was to develop a procedure for the design of the physical part of an active noise cancellation system for transformers. To realize this aim, two kinds of control actuators were developed and the output efficiency of each was evaluated by comparing it with that of conventional control actuators. A sensing strategy, involving the minimization of the sum of the near-field sound intensities at the error sensors, was also derived. The control performance achieved using this approach was evaluated by comparing with that which was attained when using sound pressure minimization in the near-field to control noise that was radiated from plates and transformers.

An acoustic type control actuator was developed that utilized a curved panel with a backing cavity. To optimize the design procedure, an analytical model of the actuator was developed, which was used to assess the effect of cavity size on the panel resonance frequencies. Mechanisms for tuning the resonance frequencies of the system after construction were developed. This involved attaching a mass to the panel and altering the depth of the cavity. A resonant curved-panel source system was constructed for testing. The system resonated at 100 Hz and 200 Hz corresponding to the 1,1 structural mode and the 1,3 structural mode. These modes have the highest radiation efficiencies for the system. To evaluate the radiation efficiency of the panel-cavity source as an acoustic control source, measurements of the sound radiation were taken in an anechoic room in the Department of Mechanical Engineering, The University of Adelaide. It was shown that the sound radiation levels corresponding to 100 Hz and 200 Hz for the panel-cavity source were high enough to cancel noise radiated by the test power transformer. The capability of the curved panel-cavity source for cancellation of the transformer noise was evaluated by comparing the predicted noise reduction at the error sensors for both the curved panel sources and the loudspeaker sources, based on transfer function measurements. The effect of the control source locations on the control performance was studied. The results demonstrated that for the case of evenly spaced sources, good control could be achieved using the curved panel sources. For the case of optimally located sources, higher sound reduction levels were obtained using the loudspeaker control sources than those obtained using the curved panel sources. This was because there were many more potential locations for the loudspeaker sources (due to their smaller size) than for the curved panel sources during the optimization search of the control source locations. This means that more effective adjustment of the phases and amplitudes between the control sources could be achieved for the case of using the loudspeaker control sources. It was observed that the 3,1 mode was resonant at 295 Hz, which was close to the second harmonic that was radiated from the transformer. Although this was not an intention of the original design, it was a useful fortuitous outcome, enabling the curved panel sound source to be effective in controlling the 100 Hz, 200 Hz and 300 Hz components simultaneously.

The feasibility of using inertial shakers as control actuators for active noise and vibration control was studied experimentally and the results are discussed in Chapter 4. Because inertial shakers could be directly bonded to a structure through the housing, no backing mass was required so that the system could be compact. Another advantage of using inertial shakers was that the resonance frequency of the shakers could be tuned by modifying the stiffness of the diaphragm (spring element) and hence the mechanical output of the shakers at the frequency of interest could be increased. To evaluate the mechanical output efficiency of the shakers, experiments were carried out to compare the mechanical outputs produced by the inertial shakers with those produced by the piezoelectric actuators on a steel plate and a transformer structure. The thickness of the PZT actuators was one quarter of the structure thickness which was not the optimum value (half of the structure thickness). However, the reduction in the excitation force available to excite the structure as a result of this sub-optimal thickness of the actuators was less than 2 dB. The results demonstrated that a large amplitude output at the frequency of interest could be achieved using the inertial shakers by tuning their resonance frequency to the test frequency. For the case of transformer excitation, up to 36 dB higher mechanical outputs could be achieved using the tuned shakers than using the PZT actuators. Because of the importance of the linearity in the actuators, the total harmonic distortion for each type of actuator was measured at several voltages. It was shown that for equivalent levels of harmonic distortion, higher vibration levels could be produced when using the tuned inertial shaker than when using the piezoelectric actuator. Thus it is desirable to replace PZT actuators with inertial shakers as control actuators for the transformer noise control systems, provided that weather proofing issues can be addressed satisfactorily.

In Chapter 5, an expression for the minimization of the sum of the sound intensities in the near-field was derived by means of quadratic optimization theory (QOT). Calculation of the sound intensities in the formulation was implemented by means of the face to face method, a two-microphone technique, based on a finite difference method. The sound pressure and particle velocity at the mid point of the separation distance between the two microphones can be approximately expressed as the local spatial gradient of sound pressure and an average of sound pressures at the two microphones respectively. As was expressed by Fahy (1995), a systematic error in the two-microphone technique is introduced into the calculation (or measurement) of the sound intensity due to the approximate method used to calculate the sound pressure and particle velocity. However, the noticeable advantage of using this technique to calculate the sound intensity for controlling tonal noise is that the cost of the sound intensity probes constructed using two electret microphones is very low. This is because each microphone on the sound intensity probes can be calibrated for each tonal frequency so that the frequency response of each microphone on the sound intensity probes can be identical at each frequency of interest in a sound field. This practical advantage makes it possible to minimize the sum of the sound intensities at a large number of error sensing points in an actual control system.

As described in Chapter 5, the formulation for minimizing the sum of the sound intensities at the error sensors was expressed in terms of the primary sound field and the transfer functions from the control inputs to the outputs at each microphone on the probes. In general, these quantities can be calculated analytically or numerically for simple structures or be directly measured on site. In other words, the analysis of Chapter 5 can be used to predict any practical problem where the transfer functions between the control sources and the error sensors and the primary sound field are known, no matter how complex the problem is. This potential advantage makes it possible to more accurately predict the achievable reduction in the noise radiated from a complex structure than using methods reported previously (Berry et al (1999)), which was implemented based on Green's function calculations.

Although the formulation was expressed in quadratic form as mentioned above, due to the characteristics of the sound intensity, the coefficient of the quadratic term in the expression is not guaranteed to be positive definite so that the optimal result achieved by the QOT may not correspond to a minimum at the error sensors. However, because this coefficient depends on the transfer functions from the control sources to the error sensors, this unexpected control result may be avoided by rearranging the control source locations and/or the error sensor locations, i.e. by optimizing the locations of the control sources and/or the error sensors. The objective for optimizing the arrangements of the control sources and the error sensors can be the maximum average noise reduction at the error sensors or the maximum average noise reduction at the monitor sensors. For the former, the solution of the cost function defined by the QOT at the error sensors was used as a variable in an optimization search procedure to determine the locations of the control sources corresponding to the maximum average noise reduction at the error sensors, e.g. in Chapter 7. In the latter case, the control forces corresponding to the minimization of the cost function at the error sensors were first used to calculate the average noise reduction at the monitor sensors. This average noise reduction at the monitor sensors was then applied to the optimization search procedure to find the locations of the error sensors corresponding to the maximum average noise reduction at the monitor sensors, e.g. in Chapter 6. If a sufficient number of monitor sensors are used, this maximum average noise reduction at the monitor sensors can represent the global sound power reduction. But it should be emphasized that for the case of sound intensity minimization, the average intensity reduction at the error sensors may be negative, even though a maximum average intensity reduction at the monitor sensors is achieved. This is because the objective is to achieve the maximum noise reduction at the monitor sensors, rather than a maximum reduction at the error sensors.

To evaluate how the near-field control strategies affect the control performance, both sound intensity minimization and squared sound pressure minimization were used to minimize sound radiated from a baffed flat plate with a single harmonic point disturbance. The effects of the numbers of error sensors and the normalized distance of the error sensors from the noise source ($\gamma = 2z/L_{xy}$) on the control performance were investigated.

Characterisation of a sound field depends on both the normalized distance separating the measurement position and the surface of the noise source ($\gamma = 2z/L_{xy}$) and the normalized source dimension ($\kappa = \pi L_{xy} / \lambda$). Therefore, both a small source ($\kappa << \pi$) and an extended source ($\kappa > \pi$) were considered in the numerical simulation.

The numerical results showed that when the error sensors were placed very close to the source plate, better control results could be achieved using intensity minimization than those obtained by squared pressure minimization, provided that a large number of error sensors were used. It is believed that in the hydrodynamic near-field, which is generally defined as a region within much less of a wavelength from the source surface, the sound pressure is out of phase with the local particle velocity; thus measurements of the sound pressure give no indication of the radiated sound power, which is only associated with the in-phase components of the pressure and particle velocity.

However, for the case of intensity minimization, a sufficient number of error sensors were required to achieve the satisfactory control results, otherwise better control could be obtained by minimizing the sum of the squared sound pressures in the hydrodynamic near-field. This is because the cost function associated with minimizing the sound intensity is more sensitive to the accurate measurement of the sound field, as the sound intensity changes much more with position than does the sound pressure. The conclusions drawn from Chapter 5 also demonstrated that for both sensing strategies, a smaller number of error sensors were required to reduce the sound field radiated from an extended source than those required to reduce the sound field radiated from a small source. The reason for this is because in this case study, unlike the region of the sound field from the extended source (the geometric near-field), the region of the sound field from the small source was characterized as the hydrodynamic near-field; thus more error sensors were required to achieve the maximum sound power reduction in this region which had a more complex sound field.

The near-field sensing strategies (sound intensity minimization and squared sound pressure minimization) proposed in Chapter 5 were evaluated experimentally by minimizing the sound field radiated from a small transformer tank in an anechoic room. An inertial shaker was used to generate the primary sound field and eight shakers were evenly mounted to the tank, acting as the control actuators. The intensity probes were mounted on a frame surrounding the transformer. The distance of the frame from the transformer was 0.8 m. The average noise reduction at the monitor sensors was calculated based on transfer function measurements. The influence of the number and locations of error sensors on the control performance was studied, associated with a limited number of fixed control sources. The number of error sensors was varied from 15 to 195 in steps of 10. The potential sensor locations for the optimization search were 492 and all of these sensors were used as the monitor sensors to evaluate the control results in the numerical simulation. The results demonstrated that for the case of using the optimally located error sensors, the average sound level reduction at the monitor sensors increased as the number of error sensors increased. For 100 Hz, a 35-55 dB average noise reduction at the monitor sensors was achieved by sound intensity minimization in the test error sensor number range and a 40-50 dB average noise reduction was achieved by squared pressure minimization. Poor control (less than 10 dB) were obtained at high frequencies, i.e. 200 Hz, 300 Hz and 400 Hz. This is because it was difficult to attenuate the sound field by reducing the overall tank vibration level with a small number of control sources at these frequencies and the modal rearrangement control mechanism could not work effectively because of the shorter structural wavelengths involved. By comparing control results obtained using both sensing strategies at 100 Hz, it was seen that when a small number of error sensors was used, a higher average noise reduction at the monitor sensors could be achieved by minimizing the sum of the squared sound pressures than minimizing the sum of the sound intensities. This is because for the particular experimental configuration, the sound field at the error sensors was characterized as being in the near-field so that for intensity minimization, a large number of error sensors were required to accurately describe the sound field.

In Chapter 6, experiments were carried out on the small transformer tank in the anechoic room using a ten channel active noise and vibration controller to verify the predicted results based on transfer function measurements. The transformer tank was excited by an inertial shaker at 100 Hz to generate the primary sound field. The control result achieved using 8 error microphones and 8 control shakers was evaluated at 528 monitor microphones which were positioned uniformly around the 4 sides and top of the transformer. The cost function to be minimized at the error sensors was the sum of the squared sound pressures. The results demonstrated that the measured noise reduction of 15.8 dB at the monitor sensors was similar to the predicted value of 18.7 dB. To investigate how the numbers of control actuators affected the control performance at the *error sensors*, the average sound pressure reduction at the error sensors was calculated as a function of the numbers of control shakers, associated with 8 error sensors. As expected, the average sound pressure reduction at the *error sensors* increased as the number of control shakers increased. By comparing the measured results and the predicted results, it was seen that the difference between them increased as the number of control shakers increased and this was more apparent at low frequencies. This might be caused by limitations of the controller when used with multiple channels.

In Chapter 7, the average noise reduction at the error sensors radiated from a large zone substation transformer was predicted, based on transfer function measurements made on site. The maximum operating load of the transformer is 160 MVA and the usual operating load is 44 MVA (160A, 275 KV). To measure the sound field, ninety six sound intensity probes (dual microphone type) were mounted on a frame at a distance of 1 meter from the transformer tank. Three types of the control sources were tested: 1) force type sources; 2) loudspeaker sources and 3) resonant curved pane-cavity sources; and two near field sensing strategies: squared sound pressure minimization at the error sensors and sound intensity minimization at the error sensors were evaluated. A genetic algorithm optimization search procedure was employed for optimizing the control source locations. During the optimization search, around 200 potential locations were considered for the vibration control sources and around 350 possible positions for the loudspeakers. Due to the limitation of the opportunities for switching off the transformer, only 35 potential locations (on the one side of the transformer tank) were supplied for the curved-panel sources during optimization search. The results demonstrated that the average sound pressure reductions at the error sensors were increased by increasing the number of control sources and optimizing the control source locations for all types of sources. This is because both increasing the number of control sources and rearranging the control source locations provided a method for the ‘controller’ to more effectively vary the phases and amplitudes between the control sources to achieve the maximum achievable sound reduction. The average predicted sound pressure reductions of tonal noise at 100Hz, 200 Hz and 300 Hz were 23.1 dB, 16.0 dB and 16.0 dB respectively for vibration type sources and 19.6 dB, 12.8 dB and 10.3 dB for loudspeaker sources, when using 80 optimally located control sources and 96 fixed error sensors. Also, the results showed that it was possible to arrange a set of common control source locations for all three frequencies corresponding to ‘sub optimum’ control. For instance, the average pressure reductions at the error sensors were

22.7 dB, 13.6 dB and 14.9 dB corresponding to 100 Hz, 200 Hz and 300 Hz respectively for the force type sources and 18.1 dB, 11.5 dB and 8.5 dB for the loudspeaker sources, when using 80 control sources at the ‘compromised’ locations and 96 error sensors.

For the large transformer noise control, it was found that the sound pressure levels at the monitor sensors (in the near-field) were predicted to increase when a control strategy of minimizing the sum of the sound intensities in the near-field was used. In general, the acoustic energy in the near-field can be considered as consisting of propagating energy (active energy) and non-propagating energy (reactive energy). Measurements of the active intensity only give an indication of the propagating energy rather than a measurement of both. In other words, the non-propagating energy is not necessarily minimized in the near-field when active intensity is used as an error signal in an active control system. This is why in this case study, average sound pressures at near-field monitor sensors increased after active intensity minimization, although the sound pressure level would decrease in the far-field.

8.2 Future work

A physical system for active control of large power transformer noise has been demonstrated using data measured on site. The system was implemented using 96 error sensors and 80 control sources. The cost functions were minimized by means of a simultaneous optimization (or centralized technique). Generally, physical controllers designed on such a basis can guarantee convergence and stability. However, the computational load for the processor in the controller can be large if a large number of error sensors and control actuators are used. Also the communication between the error sensors and the control actuators will result in a large number of connecting cables and long controller convergence times. Thus, a decentralized approach in which the total power radiated by a noise source could be minimized by creating a number of individual quiet zones around the noise source, could be investigated to overcome these problems.

In the work described in this thesis, the prediction of noise reduction for the large transformer was based on measurements of the sound field generated by both the transformer and the control sources on the site. One advantage of using this technique was that the effect of active control could be simulated if accurate measurements could be made. No structural responses were required in the model for calculating the sound radiation from the transformer structure so that numerical simulation could be easily carried out. However, it was not easy to accurately measure the outdoor sound field due to wind induced noise in the transducer signals. This is an inherent problem for control systems that are used for outdoor noise control based on acoustic measurements. To solve this problem, a windproof microphone housing needs to be designed. Effort should be expended to design adequate wind, rain and UV light guards. Other research directions could study the feasibility of sensing structural response to provide error signals proportional to sound radiation. This may involve using polyvinylidene fluoride (PVDF) piezoelectric distributed type sensors.

REFERENCES

Angevine, L., “Active Acoustics Attenuation of Electric Transformers”, *Proceedings of Internois’81*, pp 303-306, 1981.

Angevine, L., “Active Cancellation of the Hum of Large Electric Transformers”, *Proceedings of Internois’92*, pp 313-316, 1992.

Angevine, L., “Active Control of Hum from Large Power Transformers-the Real World”, *Proceedings of the Second Conference on Recent Advances in Active Control of Sound and Vibration*, Virginia Tech., Blacksburg, VA, US,. pp 279-290

Angevine, L., “Active Systems for Attenuation of Noise”, *International Journal of Active Control*, **1**, pp 65-78.

Baek, K. H., “Genetic algorithms for choosing source locations in active control system”, *M. Sc. Thesis*, University of Southampton, 1993.

Baek, K. H. and Elliott, S. J., “Genetic algorithms for choosing source locations in active control system”, *Proceedings of the Institute of Acoustics*, Vol. 15(3), pp437-445, 1993.

Baek, K. H. and Elliott, S. J., “Natural algorithms for choosing source locations in active control system”, *Journal of Sound and Vibration*, **186**(2), pp245-267, 1995.

Berge, Pettersen, O. Kr. ϕ and Sϕrsdal, S., “Active Noise Cancellation of Transformer Noise”, *Proceedings of Internois’87* , pp 537-540, 1987.

Berge, Pettersen, O. Kr. ϕ and Sϕrsdal, S., “Active Cancellation of Transformer Noise: Field Measurements”, *Applied Acoustics*, pp 309-320, 1988.

Berry, A., Qiu, X. and Hansen, C. H., “Near-field sensing strategies for the active control of the sound radiated from a plate”, *Journal of the Acoustical Society of America*, **106** (6), pp 3394-3406, 1999.

Berry, A., “Advanced sensing strategies for the active control of vibration and structural radiation”, Active 99, Fort Lauderdale, pp 73-90, 1999.

Bies, D. A. and Hansen, C. H., *Engineering Noise Control*, E & FN SPON, Second Edition, 1996.

Brennan, M. J., Garcia-Bonito, J., Elliott, S. J., David, A. and Pinnington, R. J., “Experimental investigation of different actuator technologies for active vibration control”, *Smart Materials and Structures,* **8,** pp 145-153, 1999.

Brungardt, K. Vierengel, J. and Weissman, K., “Active structural acoustic control of noise from power transformers"” *Noise-con 97,* pp 173-182, 1997.

Cazzolato, B. S., “Aura Shaker Specifications”, *internal technical report*, ANVC group, the Department of Mechanical Engineering, The University of Adelaide, 1999.

Clark, R. L. and Fuller, C. R., “Control of sound radiation with adaptive structures”, *Journal of Intelligent Material Systems and Structures*, Vol. 2, 431-452, 1991.

Clark, R. L. and Fuller, C. R., “Modal sensing of efficient acoustic radiators with polyvinylidene fluoride distributed sensors in active structural acoustic control approaches”, *Journal of the Acoustical Society of America,* **91** (6), pp 3321-3329, 1992a.

Clark, R. L. and Fuller, C. R., “Experiments on active control of structurally radiated sound using multiple piezoceramic actuators”, *Journal of the Acoustical Society of America,* **91** (6), pp 3313-3320, 1992b.

Clark, R. L. and Fuller, C. R., “Design approached for shaping polyvinylidene fluoride sensors in active structural acoustic control (ASAC)”, *Journal of Intelligent Material Systems and Structures,* Vol. 3, 354-365, 1993.

Conover, B., “Fighting Noise with Noise”, *Noise Control* **2**, pp78-82, 1956.

Cordioli, J., “Adaptation of aura shakers to be used as actuators for the project”, *internal technical report*, ANVC group, the Department of Mechanical Engineering, The University of Adelaide, 1999.

Crawley, E. F. and de Luis, J., “Use of piezoelectric actuators as elements of intelligent structures”, *AIAA journal*, Vol. 25, No. 10, pp 1373-1385, 1987.

Dimitriadis, E. K. and Fuller, C. R., “Piezoelectric actuators for noise and vibration control of thin plates”, 12th ASME conference on mechanical vibration and noise, Montreal, 1989.

Dimitriadis, E. K., Fuller, C. R. and Rogers, C. A., “Piezoelectric actuators for distributed vibration excitation of thin plates”, Transaction of the *ASME*, Vol. 113, pp 100-107, 1991.

Dowell et al, “Acoustoelasticity: General Theory, Acoustic Natural Modes and Forced Response to Sinusoidal Excitation, Including Comparisons with Experiment”, *Journal of Sound and Vibration* **52**(4), pp 519-542, 1977.

Elliott, S. J. and Johnson, M. E., “Radiation modes and the active control of sound power”, *Journal of the Acoustical Society of America*, **94** (4), pp 2194-2204, 1993.

Fahy, F. J., *Sound Intensity*, E & FN SPON, Second Edition, 1995.

Fuller, C. R., Hansen, C. H. and Snyder, S. D., “Experiments on active control of sound radiation from a panel using a piezoceramic actuator”, *Journal of Sound and Vibration*, **150**(2), pp 179-190, 1991.

Garcia-Bonito, J., Brennan, M. J., Elliott, S. J., David, A. and Pinnington, R. J., “A Novel High-Displacement Piezoelectric Actuator for Active Vibration Control”, *Smart Materials and Structures*, **7,** pp 31-42, 1998.

Goldberg, D. E., *Genetic Algorithm in Search, Optimization & Machine Learning*, Addison-Wesley, 1989.

Hansen, C. H., “Active noise control – from laboratory to industrial implementation”, *Noise-con 97*, pp 3-38, 1997.

Hansen, C. H. and Snyder, S. D., *Active Control of Noise and Vibration* E & FN SPON, 1997.

Hansen, C. H., Qiu, X. and Li, X., “Feasibility Study on Acoustic Noise Control of Power Transformers technical”, *research report for Electricity Supply Association of Australia Ltd*, Contract No.: 97007, 1997.

Hansen, C. H., Gu, R., Qiu, X. and Li, X., “Design and Construction of Weather Proof Control Source”, *research report for Electricity Supply Association of Australia Ltd*, contract No.: 97007, 1998a.

Hansen, C. H., Li, X and Qiu, X., “Feasibility Study of Using Thin Piezoelectric Patch Actuators to Control Transformer Noise”, *research report for Electricity Supply Association of Australia Ltd*, contract No.: 97007, 1998b.

Hansen, C. H., Li, X, Qiu, X. and Ai, Y., “Optimization of the Locations of the Control Sources and Error Sensors”, *research report for Electricity Supply Association of Australia Ltd*, contract No.: 97007, 2000.

Hansen, C. H., “Active noise control - extending the limits”, *Proceedings of Internois’98*, pp 1-30, 1998.

Hansen, C. H., Simpson, M. T. and Cazzolato, B. S, “Genetic algorithms for active sound and vibration control”, Proceedings of IEE Inter-Active'99, http://www.iee.org.uk/Control/active.htm, 1999.

Hesselmann, “Investigation of Noise Reduction on a 100 kVA Transformer Tank by Means of Active Methods”, *Applied Acoustics* **11**, pp 27-34, 1978.

Katsikas, S. K., Tsahalis, D. T., Manolas, D. A. and Xanthakis, S., “Genetic algorithms for active noise control”, *Noise-93,* pp167-171, 1993.

Koehler, R. and Snyder, S. D., “Near-field intensity error sensing in the active control of a free-field acoustic monopole source”, prepared for *Journal of Sound and Vibration,* 2000.

Kim, J, Varadan, V. V. and Varadan, V. K., “Finite element modeling of a finite piezoelectric sensor/actuator embedded in a fluid-load plate”, *SPIE* Vol. 2192, pp 273-280, 1994.

Kim, J, Varadan, V. V. and Varadan, V. K., “Finite element-optimization methods for the active control of radiated sound from a plate structure”, *Smart Mater. Struct.* **4**, pp 318-326, 1995.

Kim, J, Varadan, V. V. and Varadan, V. K., “Finite-element modelling of a smart cantilever plate and comparison with experiments”, *Smart Mater. Struct.* **5**, pp 165-170, 1996.

Kim, S. J. and Jones, J. D., “Optimal Design of Piezoactuators for Active Noise and Vibration Control”, *AIAA Journal,* Vol. 29, No. 12, 1991, pp 2047-2053.

Krishnappa, G. and McDougall, J. M., “Sound intensity distribution and energy flow in the near-field of a clamped circular plate”, *Journal of Vibration, Acoustics, Stress, and Reliability in Design* Vol. **111,** 465-471, 1989.

Kristiansen, U. R., “A numerical study of the acoustic intensity distribution close to a vibration membrane”, *Journal of Sound and Vibration* **76**(2), 305-309, 1981.

Lee, H. and Park, Y., “A near-field approach to active control of sound radiation from a fluid-loaded rectangular plate”, *Journal of Sound and Vibration* **196**(5), 579-593, 1996.

Li, X., Hansen, C. H. and Qiu, X., “Design of curved panel sources for active control of sound radiated by transformers”, FIFTH INTERNATIONAL CONGRESS ON SOUND AND VIBRATION, Adelaide, 1997a.

Li, X., Hansen, C. H. and Qiu, X., “Optimal sizes and locations of piezoelectric actuators for curved panel sound sources”, *International Journal of Acoustics and Vibration,* Vol. 2, pp161-166, 1997b.

Li, X., Cordioli, J., Cazzolato, B. S., Qiu, X. and Hansen, C. H., “Experiments on actuators for active structural acoustic control”, submitted to *International Journal of Acoustics and Vibration,* 1999a.

Li, X., Qiu, X., Gu, R., Köeheler, R. and Hansen, C. H., “Active control of large electrical transformer noise using near-field error sensing”, AAS Conference 99, Melbourne, 1999b.

Li, X., Qiu, X. and Hansen, C. H., “Active control of sound radiated from structures using near-field error sensing”, Active 99, Fort Lauderdale, pp 399-410, 1999c.

Li, X., Qiu, X. and Hansen, C. H., “A study of active control of noise radiated by structures using near-field sensing”, preparation for *International Journal of Acoustics and Vibration,* 2000.

Lütkepohl, H., *Introduction to Multiple Time Series Analysis,* Springer-Verlay, Second Edition, 1993.

Maillard, J. P. and Fuller, C. R., “Comparison of two structural sensing approaches for active structural acoustic control”, *Journal of the Acoustical Society of America,* **103**, pp 369-400, 1998.

Manolas, D. A., Gialamas, T. and Tsahalis, D. T., “A genetic algorithm for the simultaneous optimization of the sensor and actuator positions for an active noise and/or vibration control system”, *Proceedings of Internois’96,* pp 1187-1191, 1996.

Martin, T. and Roure, A., “Optimization of an active noise control system using spherical harmonics expansion of the primary field”, *Proceedings of Internois’96,* pp 1167-1170, 1996.

Martin, T. and Roure, A., “Optimization of an active noise control system using spherical harmonics expansion of the primary field”, *Journal of Sound and Vibration*, **201**(3), pp577-593, 1997.

Martin, T. and Roure, A., “Active noise control of acoustic sources using spherical harmonics expansion and a genetic algorithm: simulation and experiment”, *Journal of Sound and Vibration*, **212**(3), pp511-523, 1998.

McLoughlin, M., Hildebrand, S. and Hu, Z., “A novel active transformer quieting system”, *Proceedings of Internoise ’94,* 1323-1326, 1994.

Nelson, P. A. and Elliott, S. J., *Active Control of Sound* Academic Press, 1992.

Pope, L. D., “On the Transmission of Sound through Finite Closed Shell: Statistical Energy Analysis, Modal Coupling, and Non-resonant Transmission”, *Journal of the Acoustical Society of America*, **50**, pp1004-1018, 1971.

Qiu, X., Hansen, C. H. and Li, X., “A comparison of near-field acoustic error sensing strategies for the active control of harmonic free field sound radiation”, *Journal of Sound and Vibration* **215**(1), 81-103, 1998.

Qiu, X, Li, X and Hansen, C. H., “A decomposition of the sound field radiated by a large transformer”, *Proceedings of Internois’99*, pp1793-1796, 1999.

Qiu, X. and Hansen, C. H., “Secondary acoustic source types for active noise control in free field: monopoles or multipoles?”, *Journal of Sound and Vibration*, **232**(5), pp 1005-1009, 2000.

Simpson, M. T. and Hansen, C. H., “Use of genetic algorithms to optimize vibration actuator placement for active control of harmonic interior noise in a cylinder”, *Noise Control Engineering Journal*, **44**(4), pp169-184, 1996.

Soedel, *Vibrations of Shell and Plates*, second edition, Marcel Dekker, Inc. 1993.

Sommerfeldt, S. D. and Nashif, P. J., “An adaptive filtered-x algorithm for energy –based active control”, *Journal of the Acoustical Society of America,* **96** (1), pp 300-306, 1994.

Snyder, S. D. and Tanaka, N., “On feedforward active control of sound and vibration using vibration error signals”, *Journal of the Acoustical Society of America,* **94** (4), pp 2181-2193, 1993a.

Snyder, S. D., Hansen, C. H. and Tanaka, N., “Shaped vibration sensors for feedforward control of structural radiation”, *Proceedings of the Second Conference on Recent Advances in Active Control of Sound and Vibration*, Blacksburg, USA, pp 177-188, 1993b.

Snyder, S. D., and Hansen, C. H., “Using multiple regression to optimize active noise control system design”, *Journal of Sound and Vibration*, **148**(3), pp537-542, 1991.

Tanaka, N., Snyder, S. D. and Hansen, C. H., “Distributed parameter modal filtering using smart sensors”, *Transactions of the ASME*, Vol. 118, pp 630-640, 1996a.

Tanaka, N, Kikushima, Y. Kuroda, M. and Snyder, S. D., “Active control of acoustic power radiated from a vibrating planar structure using smart sensors (acoustic power suppression using adaptive feedforward control)”, *JSME International Journal,* series C, Vol. **39**, No. 1, pp 49-57, 1996b.

Tsahalis, D. T., Katsikas, S. K. and Manolas, D. A., “A genetic algorithm for optimal positioning of actuators in active noise control: results from the ASANCA project”, *Proceedings of Internois’93* pp83-88, 1993.

Varadan, V. V., Kim, J and Varadan, V. K., “Optimal design of enclosures for active noise control and isolation”, *SPIE* Vol. 2442, pp 470-475, 1995.

Varadan, V. V., Kim, J and Varadan, V. K., “Optimal placement of piezoelectric actuators for active noise control”, *AIAA Journal* Vol. 35, pp 526-533, 1997.

Wallace, E., “Radiation Resistance of a Rectangular Panel”, *The Journal of the Acoustical Society of America* **51**, pp 946-952, 1972.

Wang, B., Fuller, C. R. and Dimitriadis, E. K., “Active control of structurally radiated noise using multiple piezoelectric actuators”, *AIAA Journal*, Vol. 29, No II, pp 1802-1809, 1991a.

Wang, B., Fuller, C. R. and Dimitriadis, E. K., “Active control of noise transmission through rectangular plates using multiple piezoelectric or point actuators”, *Journal of the Acoustical Society of America* **90**, 2820-2830, 1991b.

Wang, B. and Fuller, C. R., “Near-field pressure, intensity, and wave-number distributions for active structural acoustic control of plate radiation: theoretical analysis”, *Journal of the Acoustical Society of America* **92**, pp 1489-1498, 1992.

Wang, B., “Applications of genetic algorithms to the optimum design of active control system”, *Noise-93*, pp231-236, 1993.

Wang, B., Burdisso, R. A. and Fuller, C. R., “Optimal placement of piezoelectric actuators for active structural acoustic control”, *Journal of Intelligent Material, Systems and Structures*, Vol. 5, pp 67-77, 1994.

Wang, B., “Optimal placement of microphones and piezoelectric transducer actuators for far-field sound radiation control”, *Journal of the Acoustical Society of America*, **99**, (5), pp 2975-2984, 1996.

APPENDIX A RESPONSE OF SHELLS TO EXCITATION BY PZT ACTUATORS

A.1 Equations of motion

The equations of motion for a shell may be written as (Soedel (1993)):

$$-\frac{\partial(N_{11}A_2)}{\partial\alpha_1}-\frac{\partial(N_{12}A_1)}{\partial\alpha_2}-N_{12}\frac{\partial A_1}{\partial\alpha_2}+N_{22}\frac{\partial A_2}{\partial\alpha_1}-A_1A_2\frac{Q_{13}}{R_1}+A_1A_2\rho h\ddot{u}_1$$

$$=A_1A_2\left(q_1+\frac{1}{2A_2}\frac{\partial T_n}{\partial\alpha_2}\right) \tag{A.1}$$

$$-\frac{\partial(N_{12}A_2)}{\partial\alpha_1}-\frac{\partial(N_{22}A_1)}{\partial\alpha_2}-N_{21}\frac{\partial A_2}{\partial\alpha_1}+N_{11}\frac{\partial A_1}{\partial\alpha_2}-A_1A_2\frac{Q_{23}}{R_2}+A_1A_2\rho h\ddot{u}_2$$

$$=A_1A_2\left(q_2-\frac{1}{2A_1}\frac{\partial T_n}{\partial\alpha_1}\right) \tag{A.2}$$

$$-\frac{\partial(Q_{13}A_2)}{\partial\alpha_1}-\frac{\partial(Q_{23}A_1)}{\partial\alpha_2}+A_1A_2\left(\frac{N_{11}}{R_1}+\frac{N_{22}}{R_2}\right)+A_1A_2\rho h\ddot{u}_3$$

$$=A_1A_2\left(q_3+\frac{1}{A_1A_2}\left(\frac{\partial(T_1A_2)}{\partial\alpha_1}+\frac{\partial(T_2A_1)}{\partial\alpha_2}\right)\right) \tag{A.3}$$

where T_1 is a distributed moment[*] component in the α_1 direction, T_2 is in the α_2 direction, and a twisting moment T_n is about the normal to the shell surface. q_i (i=1, 2 and

---

[*] In this thesis, the idea of a distributed moment is used. It has an unit of moment per unit area. Line and point moments are then formulated using the Dirac delta function.

3) are pressure loads. A_1 and A_2 are called the *fundamental form parameters* or *Lamé parameters*. α_1, α_2 and α_3 are curvilinear surface coordinates as shown in Figure A.1.

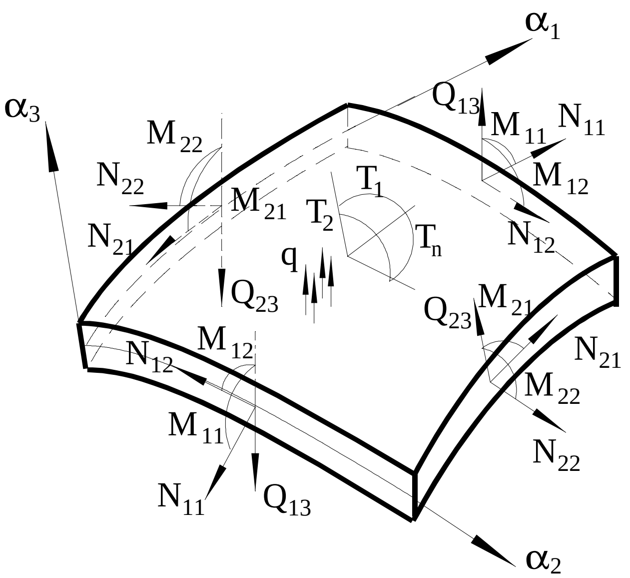

Figure A.1 A curvilinear coordinate system

In Figure A.1, N_{22} is a boundary force normal to the boundary in the tangent plane to the neutral surface; Q_{23} is a shear force acting on the boundary normal to the shell surface and N_{21} is a shear force acting along the boundary in the tangent plane; M_{22} is a moment in the α_2 direction and M_{21} is a twisting moment in the α_1 direction.

For a cylindrical shell, the curvilinear coordinates are $\alpha_1 = x$, $\alpha_2 = \theta$ and $\alpha_3 = w$, and $R_1 = R_x = \infty$, $R_2 = R_\theta = R$. R is the radius of the cylinder shell. A_1=1 and A_2=R.

A cylindrical shell excited by bending moments T_1 and T_2 is considered. In this case the twisting moment T_n and the pressure loads q_i are equal to zero. Thus N_{ij} (j=1, 2 and 3) are equal to zero. The equation of motion for a cylindrical shell corresponding to excitation by pure bending moments T_1 and T_2 may be written in the following form:

$$\frac{\partial Q_{xw}}{\partial x}+\frac{1}{R}\frac{\partial Q_{\theta w}}{\partial \theta}-\rho h\ddot{w}=-\frac{\partial T_x}{\partial x}-\frac{1}{R}\frac{\partial T_\theta}{\partial \theta} \tag{A.4}$$

where T_x is an external moment in the x direction and T_θ is in the θ direction (units of distributed moment per unit area). R is the radius of curvature of the shell; h is the thickness of the shell and ρ is the density of material.

To obtain Q_{xw} and $Q_{\theta w}$ in equation (A.4), the following equations are employed,

$$R\frac{\partial M_{xx}}{\partial x}+\frac{\partial M_{\theta x}}{\partial \theta}-Q_{xw}R=0 \tag{A.5}$$

$$R\frac{\partial M_{x\theta}}{\partial x}+\frac{\partial M_{\theta\theta}}{\partial \theta}-Q_{\theta w}R=0 \tag{A.6}$$

Rearranging equations (A.5) and (A.6) gives:

$$Q_{xw}=\frac{\partial M_{xx}}{\partial x}+\frac{1}{R}\frac{\partial M_{\theta x}}{\partial \theta} \tag{A.7}$$

$$Q_{\theta w}=\frac{\partial M_{x\theta}}{\partial x}+\frac{1}{R}\frac{\partial M_{\theta\theta}}{\partial \theta} \tag{A.8}$$

where M_{xx}, $M_{x\theta}$ ($M_{\theta x}$) and $M_{\theta\theta}$ are bending moments caused by external moments in the shell and they have units of moment per unit length. They can be expressed as:

$$M_{xx}=-D\left(\frac{\partial^2 w}{\partial x^2}+\mu_s\frac{1}{R^2}\frac{\partial^2 w}{\partial \theta^2}\right) \tag{A.9}$$

$$M_{x\theta}=M_{\theta x}=-\frac{D(1-\mu_s)}{R}\frac{\partial^2 w}{\partial x\partial \theta} \tag{A.10}$$

$$M_{\theta\theta}=-D\left(\frac{1}{R^2}\frac{\partial^2 w}{\partial \theta^2}+\mu_s\frac{\partial^2 w}{\partial x^2}\right) \tag{A.11}$$

where $D = \dfrac{E_s h^3}{12(1-{\mu_s}^2)}$, is the bending stiffness; E_s is Young's modulus of shell and μ_s is Poisson's ratio.

Substituting equations (A.9)~(A.11) into equation (A.4) and rearranging it gives:

$$D\nabla^4 w + \rho h \ddot{w} = \frac{\partial T_x}{\partial x} + \frac{1}{R}\frac{\partial T_\theta}{\partial \theta} \tag{A.12}$$

where $\nabla^4 = \dfrac{\partial^4}{\partial x^4} + 2\dfrac{1}{R^2}\dfrac{\partial^4}{\partial x^2 \partial \theta^2} + \dfrac{1}{R^4}\dfrac{\partial^4}{\partial \theta^4}$.

For line moments on a cylindrical shell, in Figure 1 the distributed moments per unit area, T_x and T_θ, may be written as follows:

$$T_x = M_x(\delta(x-x_1) - \delta(x-x_2))(u(\theta-\theta_1) - u(\theta-\theta_2)), \tag{A.13}$$

$$T_\theta = \frac{1}{R} M_\theta(\delta(\theta-\theta_1) - \delta(\theta-\theta_2))(u(x-x_1) - u(x-x_2)), \tag{A.14}$$

where $u(\ )$ and $\delta(\ )$ are the unit step function and the Dirac delta function respectively; and M_x and M_θ are bending moments caused by external line moments in the shell.

Substituting equations (A.13) and (A.14) into (A.12) gives:

$$\begin{aligned} D\nabla^4 w + \rho h \ddot{w} &= M_x(\delta'(x-x_1) - \delta'(x-x_2))(u(\theta-\theta_1) - u(\theta-\theta_2)) \\ &\quad + \frac{1}{R^2} M_\theta(\delta'(\theta-\theta_1) - \delta'(\theta-\theta_2))(u(x-x_1) - u(x-x_2)) \end{aligned} \tag{A.15}$$

Equation (A.15) is the general equation of motion of a thin cylindrical shell excited by external line moments.

A.2 Bending moments generated by piezoelectric actuators bonded to cylindrical shells

Generally, the bending moments generated in a cylindrical shell by a piezoelectric actuator can be approximated by external line moments acting on the structure at the edge of the piezoelectric layer. They can be expressed in terms of stresses in the shell as:

$$M_x = \int_{-h/2}^{h/2} \sigma_{xs} z dz \tag{A.16}$$

$$M_\theta = \int_{-h/2}^{h/2} \sigma_{\theta s} z dz \tag{A.17}$$

The stress σ_{xs} is given as:

$$\sigma_{xs} = \frac{2\sigma_{ixs} z}{h} \tag{A.18}$$

where σ_{ixs} is the stress in the shell at $z = h/2$.

Also the stress $\sigma_{\theta s}$ may be expressed in terms of $\sigma_{i\theta\theta}$ in a similar way to that described above because the thickness of the shell is much smaller compared with the other shell dimensions:

$$\sigma_{\theta s} = \frac{2\sigma_{i\theta\theta} z}{h} \tag{A.19}$$

Using the moment equilibrium condition about the neutral axes of the shell, the following equations may be given:

$$\int_0^{h/2} \sigma_{xs} z dz + \int_{h/2}^{h/2+t_g} \sigma_{xg} z dz + \int_{h/2+t_g}^{h/2+t_g+t_a} \sigma_{xa} z dz = 0 \tag{A.20}$$

$$\int_{0}^{h/2}\sigma_{\theta s} zdz + \int_{h/2}^{h/2+t_g}\sigma_{\theta g} zdz + \int_{h/2+t_g}^{h/2+t_g+t_a}\sigma_{\theta a} zdz = 0 \tag{A.21}$$

where σ_{xg} and $\sigma_{\theta g}$ are stresses in the glue in the x direction and the θ direction respectively; $\sigma_{\theta g}$ and $\sigma_{\theta a}$ are stresses in the actuator in the x direction and the 6 direction respectively.

To obtain expressions of σ_{xg}, $\sigma_{\theta g}$, σ_{xa} and $\sigma_{\theta a}$ in terms of σ_{ixs} and $\sigma_{i\theta\theta}$, respectively, an assumption is made that strain slope across the shell, glue and actuator is uniform:

$$\varepsilon_{xs} = \varepsilon_{xg} = \varepsilon_{xa} = k_x z \tag{A.22}$$

$$\varepsilon_{\theta s} = \varepsilon_{\theta g} = \varepsilon_{\theta a} = k_\theta z \tag{A.23}$$

where k_x and k_θ are strain slopes in the x direction and the θ direction respectively.

According to material mechanics concepts strains ε_{xs}, and $\varepsilon_{\theta s}$ may be expressed in terms of stresses σ_{xs} and $\sigma_{\theta s}$ respectively as:

$$\varepsilon_{xs} = \frac{1}{E_s}(\sigma_{xs} - \mu_s \sigma_{\theta s}), \tag{A.24}$$

$$\varepsilon_{\theta s} = \frac{1}{E_s}(\sigma_{\theta s} - \mu_s \sigma_{xs}). \tag{A.25}$$

Substituting equations (A.18) and (A.19) into (A.24) and (A.25), then substituting the results into (A.22) and (A.23) gives:

$$k_x = \frac{2}{hE_s}(\sigma_{ixs} - \mu_s \sigma_{i\theta\theta}) \tag{A.26}$$

$$k_\theta = \frac{2}{hE_s}(\sigma_{i\theta\theta} - \mu_s \sigma_{ixs}) \tag{A.27}$$

Stress-strain expressions in the actuator may be described in terms of the free strains Λ_x and Λ_θ due to the applied voltage:

$$\sigma_{xa} = \frac{E_a}{1-\mu_a^2}(\varepsilon_{xa} + \mu_a \varepsilon_{\theta a} - \Lambda_x) \tag{A.28}$$

$$\sigma_{\theta a} = \frac{E_a}{1-\mu_a^2}(\varepsilon_{\theta a} + \mu_a \varepsilon_{xa} - \Lambda_\theta) \tag{A.29}$$

Substituting equations (A.26) and (A.27) into equations (A.22) and (A.23) for ε_{xa} and $\varepsilon_{\theta a}$, and substituting the results into equations (A.28) and (A.29), expressions for σ_{xa} and $\sigma_{\theta a}$ in terms of σ_{ixs} and $\sigma_{i\theta\theta}$ may be written as:

$$\sigma_{xa} = \frac{2}{(1-\mu_a^2)h}\frac{E_a}{E_s}((1-\mu_a\mu_s)\sigma_{ixs} + (\mu_a - \mu_s)\sigma_{i\theta\theta})z - \frac{E_a}{1-\mu_a^2}\Lambda_x\,, \tag{A.30}$$

$$\sigma_{\theta a} = \frac{2}{(1-\mu_a^2)h}\frac{E_a}{E_s}((1-\mu_a\mu_s)\sigma_{i\theta\theta} + (\mu_a - \mu_s)\sigma_{ixs})z - \frac{E_a}{1-\mu_a^2}\Lambda_\theta\,. \tag{A.31}$$

where the free strains in the actuators Λ_x and Λ_θ due to the electric field may be expressed as (Hansen and Snyder (1997)):

$$\Lambda_x = \frac{d_{31}V}{t} \text{ and } \Lambda_\theta = \frac{d_{32}V}{t}$$

where *t* is the piezoelectric actuator thickness; d_{31} and d_{32} are charge or strain constants.

Similarly, expressions for σ_{xg} and $\sigma_{\theta g}$ may be obtained as follows:

$$\sigma_{xg} = \frac{2}{(1-\mu_g^2)h}\frac{E_g}{E_s}((1-\mu_g\mu_s)\sigma_{ixs} + (\mu_g - \mu_s)\sigma_{i\theta\theta})z \tag{A.32}$$

$$\sigma_{\theta g} = \frac{2}{(1-\mu_g^2)h}\frac{E_g}{E_s}((1-\mu_g\mu_s)\sigma_{i\theta\theta} + (\mu_g - \mu_s)\sigma_{ixs})z \tag{A.33}$$

Substituting equations (A.18), (A.30) and (A.32) into (A.20) and integrating gives:

$$\sigma_{ixs}\frac{h^2}{12}+\frac{2E_g}{hE_s}\alpha_g(\beta_g\sigma_{ixs}+\gamma_g\sigma_{i\theta\theta})t_g\left(\frac{1}{4}h^2+\frac{1}{2}ht_g+\frac{1}{3}t_g^2\right)$$

$$+\frac{2E_a}{hE_s}\alpha_a(\beta_a\sigma_{ixs}+\gamma_a\sigma_{i\theta\theta})\left(t_a\left(\frac{1}{4}h^2+\frac{1}{2}ht_a+\frac{1}{3}t_a^2\right)+t_at_g(h+t_g+t_a)\right)$$

$$-E_a\alpha_a\Lambda_xt_a\left(\frac{h}{2}+\frac{t_a}{2}+t_g\right)=0 \qquad \text{(A.34)}$$

where
$$\alpha_g=\frac{1}{(1-\mu_g^2)},\quad \beta_g=1-\mu_g\mu_s,\quad \gamma_g=\mu_g-\mu_s$$

$$\alpha_a=\frac{1}{(1-\mu_a^2)},\quad \beta_a=1-\mu_a\mu_s,\quad \gamma_a=\mu_a-\mu_s$$

Similarly:

$$\sigma_{i\theta\theta}\frac{h^2}{12}+\frac{2E_g}{hE_s}\alpha_g(\beta_g\sigma_{i\theta\theta}+\gamma_g\sigma_{ixs})t_g\left(\frac{1}{4}h^2+\frac{1}{2}ht_g+\frac{1}{3}t_g^2\right)$$

$$+\frac{2E_a}{hE_s}\alpha_a(\beta_a\sigma_{i\theta\theta}+\gamma_a\sigma_{ixs})\left(t_a\left(\frac{1}{4}h^2+\frac{1}{2}ht_a+\frac{1}{3}t_a^2\right)+t_at_g(h+t_g+t_a)\right)$$

$$-E_a\alpha_a\Lambda_\theta t_a\left(\frac{h}{2}+\frac{t_a}{2}+t_g\right)=0 \qquad \text{(A.35)}$$

Neglecting the effect of the bonding layer (Kim and Jones (1991)) in equations (A.34) and (A.35) and solving them for σ_{ixs} and $\sigma_{i\theta\theta}$ gives:

$$\sigma_{ixs}=\frac{\dfrac{E_a\alpha_at_a(h+t_a)}{2}\left(\left(\dfrac{h^2}{12}+\dfrac{2E_a}{hE_s}\alpha_a\beta_a\eta\right)\Lambda_x-\dfrac{2E_a}{hE_s}\alpha_a\gamma_a\eta\Lambda_\theta\right)}{(\dfrac{h^2}{12}+\dfrac{2E_a}{hE_s}\alpha_a\beta_a\eta)^2-(\dfrac{2E_a}{hE_s}\alpha_a\gamma_a\eta)^2} \qquad \text{(A.36)}$$

$$\sigma_{i\theta\theta}=\frac{\dfrac{E_a\alpha_a t_a(h+t_a)}{2}\left(\left(\dfrac{h^2}{12}+\dfrac{2E_a}{hE_s}\alpha_a\beta_a\eta\right)\Lambda_\theta-\dfrac{2E_a}{hE_s}\alpha_a\gamma_a\eta\Lambda_x\right)}{(\dfrac{h^2}{12}+\dfrac{2E_a}{hE_s}\alpha_a\beta_a\eta)^2-(\dfrac{2E_a}{hE_s}\alpha_a\gamma_a\eta)^2} \tag{A.37}$$

where $\eta=\frac{1}{4}h^2t_a+\frac{1}{2}ht_a^2+\frac{1}{3}t_a^3$.

Substituting equations (A.36) and (A.37) into (A.18) and (A.19) respectively, and then substituting results into (A.16) and (A.17) and integrating gives:

$$M_x=\frac{h^2}{6}\frac{\dfrac{E_a\alpha_a t_a(h+t_a)}{2}\left(\left(\dfrac{h^2}{12}+\dfrac{2E_a}{hE_s}\alpha_a\beta_a\eta\right)\Lambda_x-\dfrac{2E_a}{hE_s}\alpha_a\gamma_a\eta\Lambda_\theta\right)}{(\dfrac{h^2}{12}+\dfrac{2E_a}{hE_s}\alpha_a\beta_a\eta)^2-(\dfrac{2E_a}{hE_s}\alpha_a\gamma_a\eta)^2} \tag{A.38}$$

$$M_\theta=\frac{h^2}{6}\frac{\dfrac{E_a\alpha_a t_a(h+t_a)}{2}\left(\left(\dfrac{h^2}{12}+\dfrac{2E_a}{hE_s}\alpha_a\beta_a\eta\right)\Lambda_\theta-\dfrac{2E_a}{hE_s}\alpha_a\gamma_a\eta\Lambda_x\right)}{(\dfrac{h^2}{12}+\dfrac{2E_a}{hE_s}\alpha_a\beta_a\eta)^2-(\dfrac{2E_a}{hE_s}\alpha_a\gamma_a\eta)^2} \tag{A.39}$$

The equation of motion for a cylindrical shell can be obtained by substituting equations (A.38) and (A.39) into equation (A.15).

APPENDIX B CALIBRATION OF SOUND INTENSITY PROBE CONSTRUCTED USING TWO ELECTRET MICROPHONES

B.1 Introduction

In general, for sound intensity measurement, two highly phase-matched microphones are required if the p-p method is employed, which can imply a relatively high cost for the sensors. However, low cost microphones can be used to sense tonal noise, for instance the transformer noise. In this case, the amplitude and phase of each microphone on the sound intensity probe must be calibrated individually at each of the frequencies of interest.

B.2 Principle

The correction spectrum $c(\omega)$, which represents the amplitude and phase differences between the output of a calibrated microphone and that a standard microphone exposed to the same sound field, can be expressed as:

$$c(\omega) = \frac{b^*(\omega)a(\omega)}{b^2(\omega)} \tag{B.1}$$

$$b(\omega)c(\omega) = b(\omega)\frac{b^*(\omega)a(\omega)}{b^2(\omega)} = a(\omega) \tag{B.2}$$

where $a(\omega)$ and $b(\omega)$ represent complex spectra measured by the standard microphone and the calibrated microphone respectively; $c(\omega)$ is the correction spectrum for $b(\omega)$ to $a(\omega)$, which includes the effects of microphone preamplifiers.

From Equation (B.2) it can be seen that after calibrating, $b(\omega)$ is multiplied by $c(\omega)$ and $b(\omega)c(\omega)$ is equal to $a(\omega)$. In other words, if it is multiplied by the correction spectrum $c(\omega)$, the signal for the calibrated microphone is identical to the signal for the standard microphone. Thus all the calibrated microphones are identical to the standard microphone at the specified frequencies, so that two microphones on a sound intensity probe have an identical response to a sound field (highly phase-matched and sensitivity-matched microphone pair).

B.3 Calibration procedures

A high precision Brüel & Kjær type microphone on a Brüel & Kjær type 3519 sound intensity probe was selected as a standard microphone. Each electret microphone was calibrated against this high precision microphone by placing them into a UA0914 sound intensity coupler with ZI0055 sound source, which provided an identical sound field to both microphones. The channel A microphone on a Brüel & Kjær type 3519 sound intensity probe was connected to port 1 on the UA0914 sound intensity coupler and the electret microphone was connected to port 2. A dummy microphone was connected into port 3 (Figure B.1).

To generate the sound, a ZI0055 sound source in the intensity coupler was driven by a HP 3325B signal generator at 100 Hz, 200 Hz, 300 Hz and 400 Hz. The spectra measured by the microphones were recorded by a PC computer with a PC 30 interface board through microphone preamplifiers. The calibration was automatically calculated by means of a program representing equations (B.1) and (B.2). The block diagram of the calibration system is shown in Figure B.2.

Figure B.1 Configuration of UA0914 sound intensity coupler for calibrating electret microphones

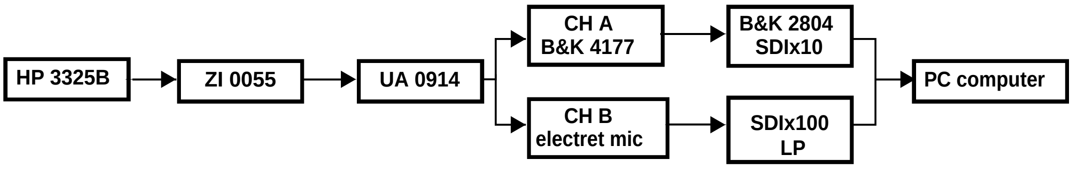

Figure B.2 A block diagram for calibration of the electret microphones

In Figure B.2, SDI is a microphone preamplifier which was specially designed for this project by The University of Adelaide. After the relative calibration of each electret microphone using the calibration system shown in Figure B.2, the absolute calibration (amplitude correction for electret microphone measurement) of the system was implemented. To do this, a high quality sound intensity measurement system, which consisted of a Brüel & Kjær type 4177 microphone pair and a Brüel & Kjær type 2144 analyzer, was selected for the absolute calibration procedure. This high quality measurement system was then calibrated using a Brüel & Kjær type 4228 calibrator. Outputs of both systems with the same input were recorded as shown in Figure B.3.

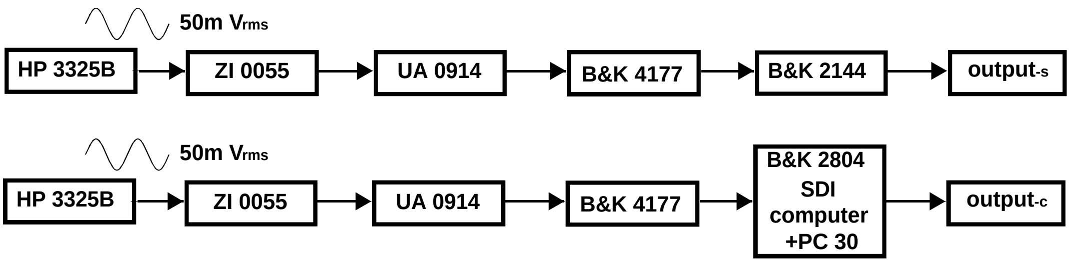

Figure B.3 A block diagram for measurement of sound pressure level in the calibration system

In Figure B.3, $\text{output}_{\text{-s}}$ and $\text{output}_{\text{-c}}$ are outputs of the standard system and the calibrated system respectively. Data which were used for absolute calibration are presented in Table B.1.

Table B.1 Calibration results of the system

frequency (Hz)	$\text{output}_{\text{-s}}$	$\text{output}_{\text{-c}}$	
	SPL (dB)	SPL (dB)	$V_{p\text{-}p}$ (V)
100	97.7	100.3	2.0
200	97.4	100.2	2.0
300	97.2	100.0	2.0
400	97.0	99.7	2.0

APPENDIX C FORCE SENSITIVITIES OF INERTIAL SHAKERS

In Chapter 6 several inertial shakers were used as control sources to minimize noise radiated from a small transformer. The specifications of the shakers were given in Chapter 4. In this appendix, the calibration results for shakers which were used in the experiment in Chapter 6 are presented. The calibration procedure follows the discussion of Chapter 4.

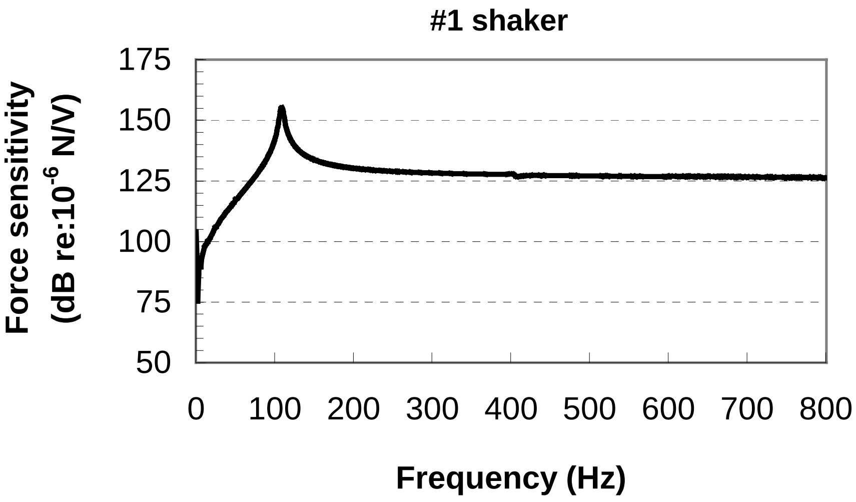

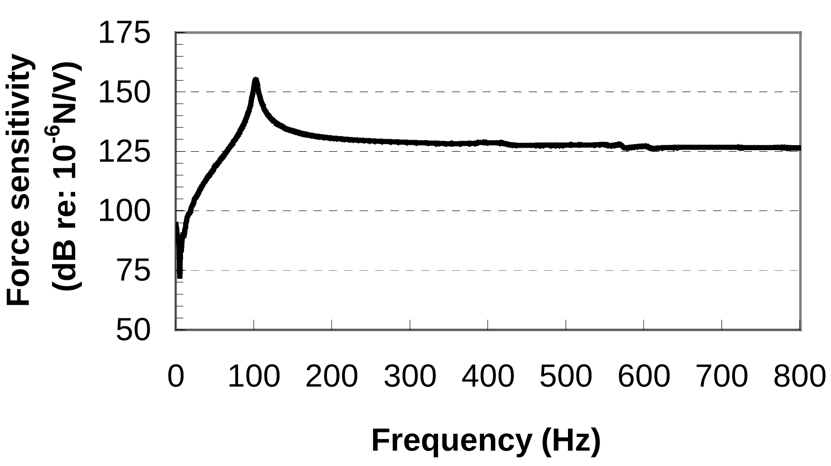

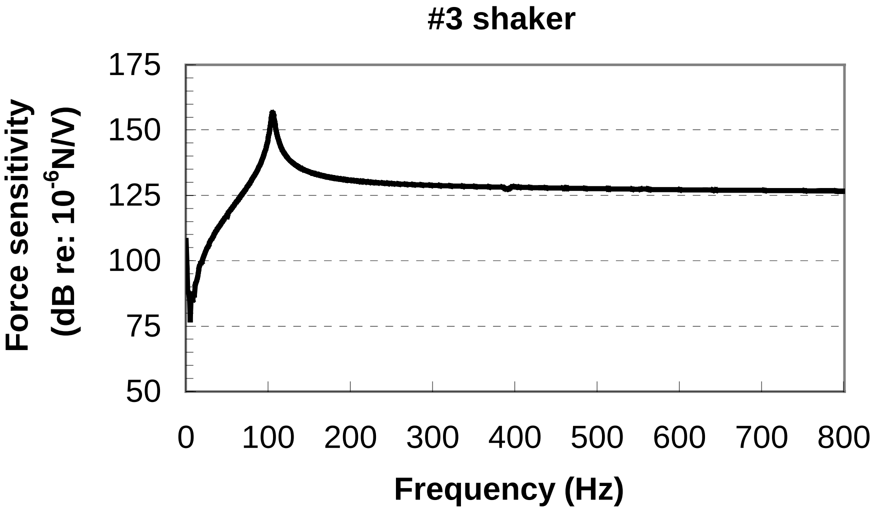
#3 shaker
Force sensitivity (dB re: 10^{-6}N/V)
175
150
125
100
75
50
0
100
200
300
400
500
600
700
800
Frequency (Hz)

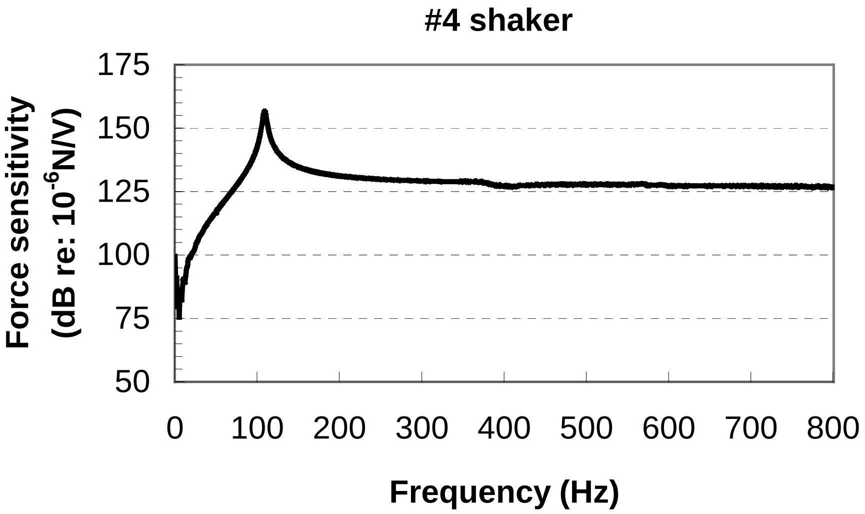
#4 shaker
Force sensitivity (dB re: 10^{-6}N/V)
175
150
125
100
75
50
0
100
200
300
400
500
600
700
800
Frequency (Hz)

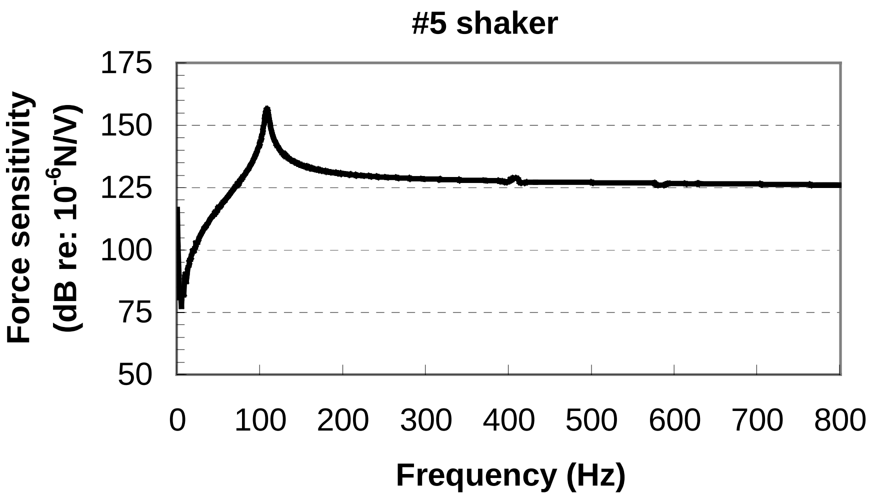
#5 shaker
Force sensitivity (dB re: 10^{-6}N/V)
175
150
125
100
75
50
0
100
200
300
400
500
600
700
800
Frequency (Hz)

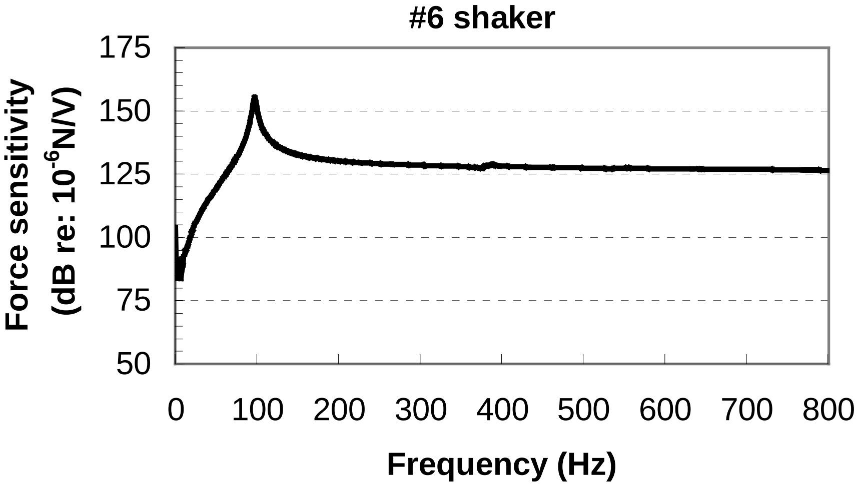
#6 shaker
Force sensitivity
(dB re: 10^-6N/V)
175
150
125
100
75
50
0
100
200
300
400
500
600
700
800
Frequency (Hz)

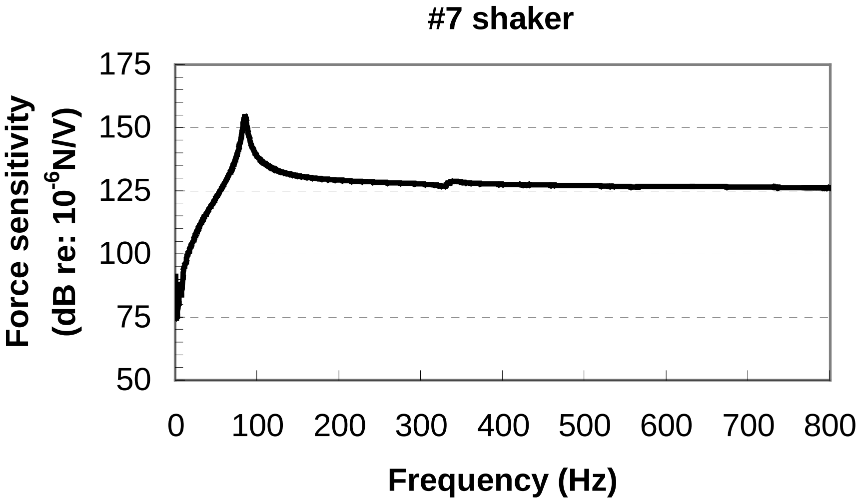
#7 shaker
Force sensitivity
(dB re: 10^-6N/V)
175
150
125
100
75
50
0
100
200
300
400
500
600
700
800
Frequency (Hz)

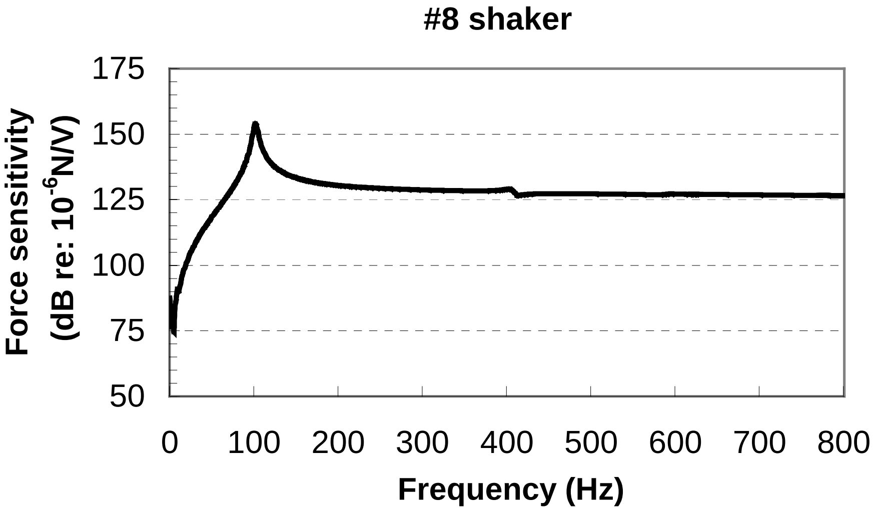
#8 shaker
Force sensitivity
(dB re: 10^-6N/V)
175
150
125
100
75
50
0
100
200
300
400
500
600
700
800
Frequency (Hz)

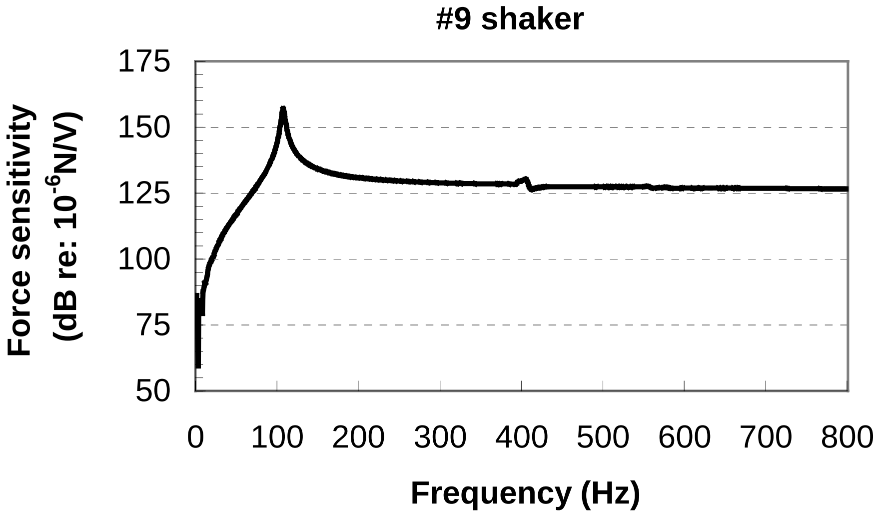
#9 shaker
Force sensitivity (dB re: 10^{-6}N/V)
175
150
125
100
75
50
0
100
200
300
400
500
600
700
800
Frequency (Hz)

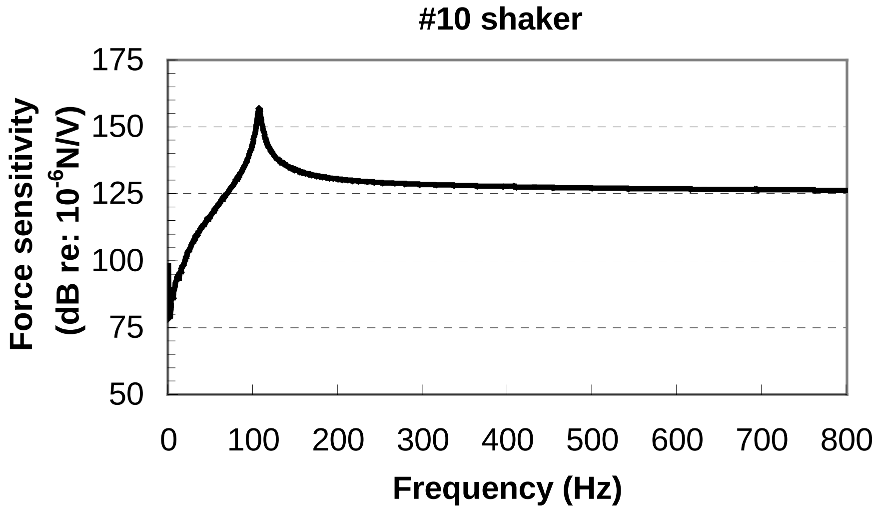
#10 shaker
Force sensitivity (dB re: 10^{-6}N/V)
175
150
125
100
75
50
0
100
200
300
400
500
600
700
800
Frequency (Hz)

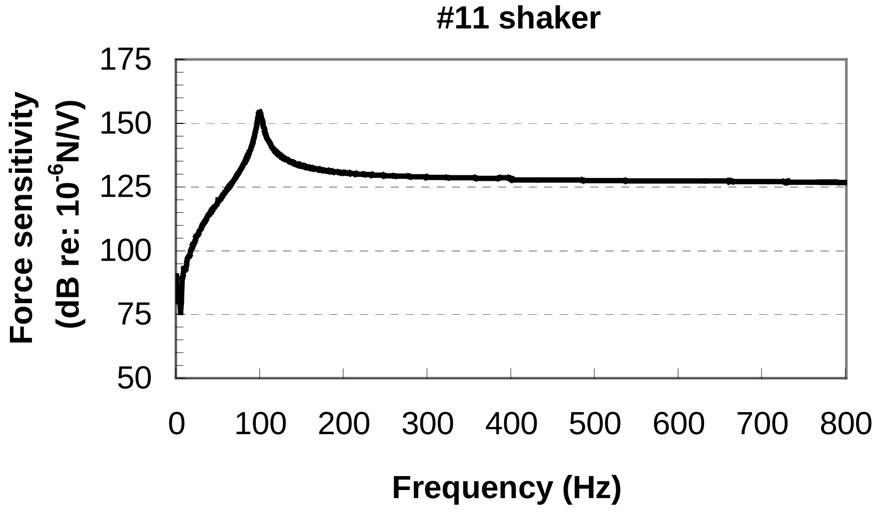
#11 shaker
Force sensitivity (dB re: 10^{-6}N/V)
175
150
125
100
75
50
0
100
200
300
400
500
600
700
800
Frequency (Hz)

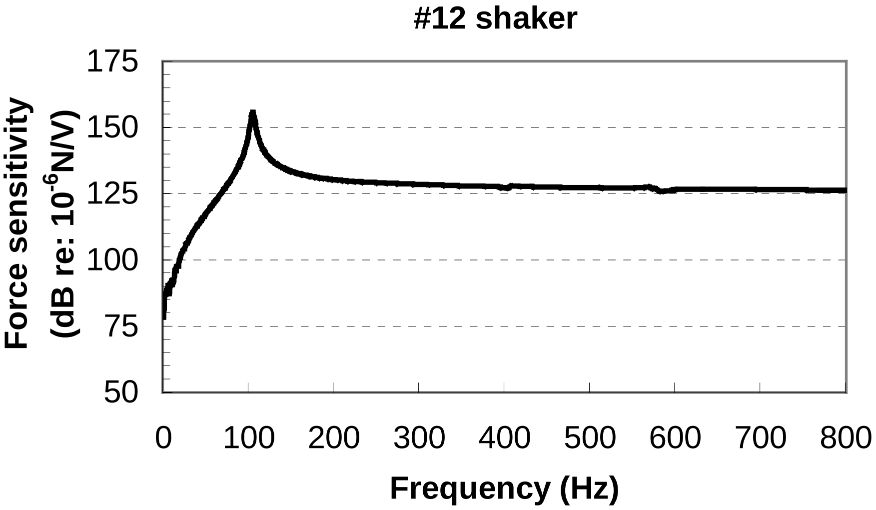
#12 shaker
Force sensitivity (dB re: 10^{-6}N/V)
175
150
125
100
75
50
0
100
200
300
400
500
600
700
800
Frequency (Hz)

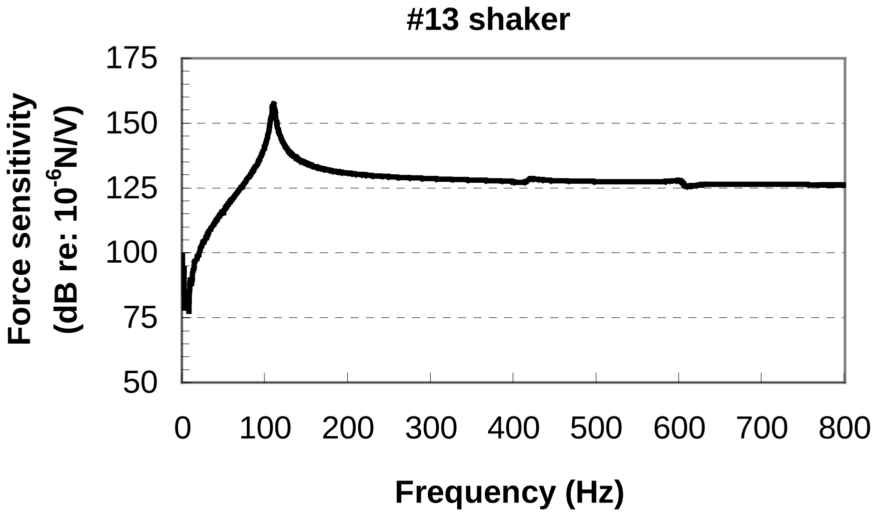
#13 shaker
Force sensitivity (dB re: 10^{-6}N/V)
175
150
125
100
75
50
0
100
200
300
400
500
600
700
800
Frequency (Hz)

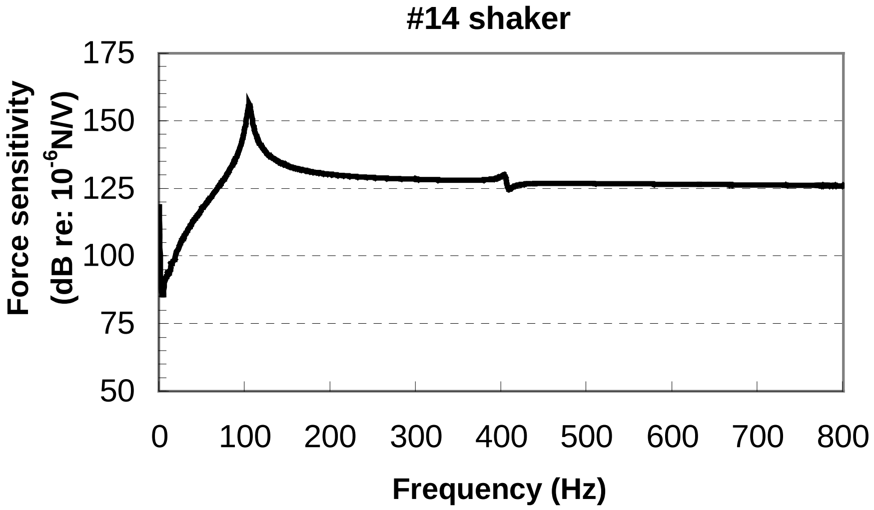
#14 shaker
Force sensitivity (dB re: 10^{-6}N/V)
175
150
125
100
75
50
0
100
200
300
400
500
600
700
800
Frequency (Hz)

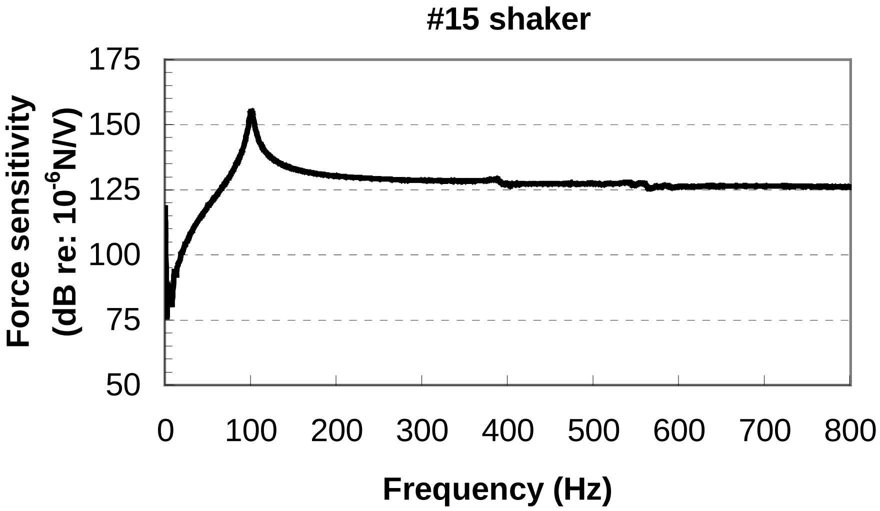

Figure C.1 Force sensitivity of the inertial shakers